Università degli Studi di Napoli Federico II

Dottorato di ricerca in Fisica

Ciclo XXXV

Coordinatore: Prof. Vincenzo Canale

Magnetic and plasmonic nanomaterials for biosensing applications

Settore Scientifico Disciplinare FIS/01-FIS/07

Tutori:
Prof. Vincenzo Iannotti
Prof. Raffaele Velotta

Dottoranda:
Emanuela Scardapane

Anno accademico 2019–2022

Contents

NOTATION

5-FAM	5-carboxyfluorescein
Ab	Antibody
Abs*	Fluorescently labelled antibody
ABS	Acrylonitrile butadiene styrene
AC	Alternating current
Anti *P*LDH	Pan malaria antibody
Apt	Aptamer
Apr*	Fluorescently labelled Aptamer
AuNP	Gold nanoparticle
BC	Boundary condition
BCMN	Block Copolymer Micelle Nanolithography
BSA	Bovine serum albumin
CTAB	hexadecyltrimethylammonium bromide
Cy5	Cyanine 5
Cys	Cystein
ELISA	Enzyme-linked Immunosorbent Assay
Fab	Fragment antigen-binding
FDTD	Finite-Difference Time-Domain
FE	Fluorescence Enhancement
Fe_3O_4@Au NPs	Iron oxide nanoparticles coated with gold
FRET	Förster Resonance Energy Transfer
Ig	Immunoglobin
LDOS	Local Density Optical States
LOD	Limit of Detection
LSP	Localized Surface Plasmon
LSPR	Localized Surface Plasmon Resonance
ME	Magnetoelastic
MNPs	Magnetic Nanoparticles
MOKE	Magneto-optic Kerr Effects
MOSPR	Magneto-optic Surface Plasmon Eesonance
OD	Optical Density
PCR	Polymerase Chain Reaction
PEF	Plasmon-Enhanced Fluorescence
PfLDH	Plasmodium falciparum lactate dehydrogenase
PIT	Photochemical Immobilization Technique
PvLDH	Plasmodium vivax lactate dehydrogenase
QY	Quantum Yield
SAM	Self-Assembled Monolayer
SEM	Scanning Electron Microscopy
SERS	Surface-enhanced Raman scattering
SPP	Surface Plasmon Polariton
SPR	Surface Plasmon Resonance
TEM	Transmission electron microscopy
TMOKE	Transversal Magneto-Optic Kerr effect
Trp	Tryptophan
UV	Ultraviolet
VNA	Vector Network Analyzer

List of Publications

In this thesis

[1] R. Campanile, **E. Scardapane**, A. Forente, C. Granata, R. Germano, R. Di Girolamo, A. Minopoli, R. Velotta, B. Della Ventura, and V. Iannotti. "Core-shell magnetic nanoparticles for highly sensitive magnetoelastic immunosensor". In: Nanomaterials 10.8 (2020), p. 15.

[2] A. Minopoli, **E. Scardapane**, B. Della Ventura, J. A Tanner, A. Offenäusser, D. Mayer, and R. Velotta. "Double-Resonant Nanostructured Gold Surface for Multiplexed Detection". In: *ACS Applied Materials & Interfaces* 14.5 (2022), pp. 6417–642.

Other publications

[3] A. Minopoli, **E. Scardapane**, A. Acunzo, R. Campanile, B. Della Ventura, and R. Velotta. "Analysis of the optical response of a SARS-CoV-2-directed colorimetric immunosensor". In: *AIP Advances* 11.6 (2021), p. 06531.

[4] A. Acunzo, **E. Scardapane**, M. De Luca, D. Marra, R. Velotta, and A. Minopoli. "Plasmonic Nanomaterials for Colorimetric Biosensing: A Review". In: *Chemosensors* 10.4 (2022).

[5] R. Campanile, A. Acunzo, **E. Scardapane**, A. Minopoli, V. C. Martins, R. Di Girolamo, S. Cardoso, R. Velotta, B. Della Ventura, and V. Iannotti. "Multifunctional Core@Satellite Magnetic Particles for Magnetoresistive Biosensors". In: *ACS Omega* 7.41 (2022), pp. 36543–36550.

Introduction

The birth of biosensors is historically ascribed to Leland C. Clark and his colleagues who in 1962 realized a device called the *enzyme electrode* in order to detect glucose oxidase [6]. Biosensors are analytical devices that allow detection of biochemical substances by the means of two main components: the bioreceptors and the transducer. The bioreceptors specifically recognize the target molecules and the transducer converts the molecular recognition into a detectable signal. Nowadays, there are several well-assessed laboratory techniques such as liquid chromatography-mass spectrometry, reverse transcriptase-polymerase chain reaction, high-performance liquid chromatography and the enzyme-linked immunosorbent assay, that exhibit impressive performance in terms of sensitivity, selectivity, and reliability.
However, the demand for biosensing devices is still increasing [7, 8]. Main reasons are that the gold standard laboratory techniques generally require well-equipped laboratories and trained personnel. Moreover the use of significant amounts of toxic solvents, time consuming and expensive procedures limit their adoption for mass screening and *in-situ* applications for contaminant monitoring or diagnostic purposes.
In this regard, biosensors offering the possibility of real-time, practical, and affordable applications are particularly attractive for point-of-care testing (POC) and high-throughput analysis. Therefore, the scientific community is spurred to face the challenges that still limit biosensors-based approaches, such as limited sensitivities, difficulties in functionalization with bioreceptors, and the complexity of the technology transfer from the academic research to the industry [9, 10]. In the last few decades, the outstanding progresses in nanotechnology have shown a tremendous potential to address the quests of biosensing field thanks to a wide variety of emerging nanomaterials [11]. The key properties of nanomaterials depend on nanoscale objects with at least one dimension smaller than 100 nm.

The aim of this thesis is exploring a class of metallic nanomaterials with magnetic and plasmonic features to investigate their great potentiality in biosensing applications. In particular, the nanomaterials here investigated are suspended core@shell magnetic nanoparticles, a two-dimensional plasmonic nanostructure consisting of branch pattern of gold nanoparticles and a magnetoplasmonic heterostructure of gold and cobalt thin layers. All the nanomaterial have been implemented in an immuno-assay scheme in which their surfaces are functionalized with antibodies (the bioreceptors). The functionalization is obtained with the Photochemical Immobilization Technique, a novel functionalization method developed in *Biosensing* research group at the Department of Physics of the University of Naples Federico II [12]. Remarkably, for all the above mentioned magnetic and plasmonic nanomaterials the PIT was tested and implemented in an immuno-assay

scheme for the first time.
Magnetic nanoparticles have gained popularity due the possibility of remote controlling through an externally applied magnetic field. In particular, iron oxide magnetic nanoparticles are appealing due to their higher biocompatibility and greater ease of synthesis as compared to other magnetic materials [13, 14]. In this work we showed how core@shell magnetic nanoparticles consisting of a magnetite (Fe_3O_4) core coated with gold can be used to enhance the sensitivity of magnetoelastic transducers that generally suffer from poor sensitivity, being much more effective than gold nanoparticles [1]. Remarkably, we find that core@shell magnetic nanoparticles can be easily functionalized with antibodies using the PIT. The magnetoelastic biosensor is described in Chapter 2.
The second nanostructure here presented is a plasmonic nanostructure consisting of an assembly of branch pattern of gold nanoparticles immobilized on a glass slice. Plasmonic nanostructures (i.e. nanostructures that sustain the excitation of surface plasmon polaritons SPP or localized surface plasmon polaritons LSPP) opened the possibility of controlling and manipulating the light at nanoscale below the diffraction limit. Upon the stimulation with an external radiation, plasmonic nanostructures allow a sub-wavelength confinement and a strong enhancement of the electromagnetic field. Thanks to these features these nanomaterials can be used to enhance the fluorescence in plasmon-enhanced fluorescence (PEF) based biosensors. We showed that our nanostructure obtained with an easy fabrication method allows to achieve a competitive fluorescence enhancement as compared to much more complicated nanostructure. With numerical simulations we demonstrated that the pattern architecture endowed the substrate with a large amount of intense electromagnetic hot spots in which fluorophores can be housed. We find that the theoretical results are in agreement with the experimental outputs obtained implementing the substrate in the detection of a malaria biomarker in human whole blood [2]. This work is described in Chapter 3.
Eventually, the third nanomaterial investigated in this work is a magnetoplasmonic heterostructure consisting of a trilayer of cobalt and gold [15, 16]. Multilayered structures of ferromagnetic and noble metals layers exhibit both plasmonics and magneto-optics properties. In these structures, the excitation of SPP modes produces a resonant enhancement of the magneto-optical effects both in reflectance (Kerr effects) and in transmission (Faraday effects). In recent years, the magnetoplasmonic modulation of the surface plasmon resonance (SPR) has been proposed as tool to overcome the sensitivity of the traditional SPR sensors [17, 18]. Our research fits in this context. In particular, my research contribution consisted in fabricating and characterizing the magnetoplasmonic heterostructures, devising the experimental setup for real-time monitoring of the magneto-optical-surface-plasmon effect, testing the PIT and conducting biosensing experiments. The experimental activity took place in the research center CIC nanoGUNE (San Sebastián, Spain) under the supervision of the professors Paolo Vavassori and Andreas Seifert. We showed as a proof of concept the implementation of this substrate in an immunosensing scheme where the novel above mentioned PIT is employed for functionalizing the multilayered nanostructures. The preliminary results obtained can be easily improved by optimizing the fluidic system. The immunosensor based on magneto-optic surface plasmon resonance effect is reported in Chapter 4.

Organization of the thesis

Chapter 1 begins with some basic concepts on biosensing that will be recalled throughout the whole thesis, including a description of the Photochemical Immobilization Technique, the novel functionalization method adopted in this work. The chapter contains also basics aspects of magnetic nanoparticles with special regard to their application to biosensing and an introduction to plasmonics that is the core of the biosensors presented in Chapters 3 and 4. Starting with basics on optics in metals, the concepts of volume plasmons, surface plasmons and localized surface plasmon are gradually introduced. Afterwards, the optical response of metal nanoparticles is investigated through the Mie theory and within a quasi-static framework. Eventually, a section is devoted to the description of coupled localized surface plasmon modes that can arise in two dimensional arrays of metal nanoparticles.

In **Chapter 2** basic concepts on theory of magnetoelasticity and magnetoelastic (ME) materials are presented, so to explain the main ME properties of the acoustic-wave transducers and the origin of the mass sensitivity. Afterwards, a novel protocol for enhancing the response signal of the ME sensors exploiting core@shell magnetic nanoparticles is presented. The effectiveness of the protocol is proved by the experimental application of ME biosensor in a real-time detection of an antigen in liquid matrix.

Chapter 3 is devoted to the plasmon-enhanced fluorescence. In this chapter, some sections depict the effects occurring when a fluorophore is in close proximity of metal nanoparticles. In the second part of the chapter, a biosensor based on plasmon-enhanced fluorescence is presented. The sensor platform is a double resonant nanostructure that allowed the implementation of multiplexed detection in whole blood down to the femtomolar level. A detailed analysis of the nanostructure deeply describes the origin of the double resonance and of the fluorescence amplification factors obtained.

Chapter 4 starts with a description the magneto-optical effects within a classical framework. Other theoretical sections are devoted to the flourishing field of magnetoplasmonics where plasmonics and magneto-optics are combined, opening novel possibilities for the light manipulation at the nanoscale. The chapter focuses on magnetoplasmonic effects arising from the simultaneous excitation of surface plasmon polaritons and magneto-optical effects within multilayered heterostructure of noble and ferromagnetic metals. In the second part of the chapter the biosensor based the gold-cobalt trilayer is presented. A section is devoted to the experimental optimization of the layers thicknesses. Finally the biosensing application in liquid environment is described, proving high sensitivity, reliable stability, and specificity of the immunosensor.

Chapter 1

Preliminaries

Contents

1.1 Basics on biosensing

Biosensors are analytical devices able to convert the recognition of a biochemical substance into a detectable signal. They mainly consist of three components:

- bioreceptors: the biological elements that selectively recognize the target molecules (e.g. bacteria, proteins, toxins, viruses). Examples of bioreceptors are enzymes, antibodies, nucleic acids, aptamers. When the bioreceptors are antibodies (immunoglobulins) the sensor goes under the name of immunosensor.

- physicochemical transducer: the element that converts the recognition of target biomolecules into a measurable signal. According to the transduction system biosensor can be classified as electrochemical, optical, acoustic-wave based;

- the electronic system that analyses the signal and displays the outcome.

Depending on the details of theirs components, biosensors have found a variety of applications in different fields including food and water safety, environmental monitoring, agriculture, and medical diagnosis [19].
The demand for biosensors has grown despite the existence of well-established conventional laboratory techniques such enzyme-linked immunosorbent assay (ELISA, [20]), polymerase chain reaction (PCR, [21]), and liquid chromatography (HPLC). The reason is that all of them generally require well-equipped laboratories, skilled personnel, sample pretreatments and complex chemical procedures. On the contrary, biosensors offer low-cost and user-friendly procedures, rapid response-signal, and thus the possibility of performing *in-situ* analysis and real-time environmental/diagnostic monitoring.
Some parameters that will be used throughout this work for describing the performances of biosensors are listed below for convenience:

- Limit of detection (LOD): the lowest concentration or amount of an analyte that can be measured and that is statistically different from the analyte blank;

- Dynamic (Linear) range is the range of analyte concentrations for which the sensor gives a different (linear) response;

- Sensitivity: the variation of the sensor signal as a function of the variation of the analyte concentration or amount;

- Selectivity: the ability of detecting a specific analyte in a sample containing other contaminants;

- Specificity: the capability of the sensor of not giving a response signal when exposed to molecules different from the target.

Some other important qualities to which one can refers are (i) the reproducibility, that is the coherence of the response signal that a sensor generates among different experiments, and (ii) the stability that describes how much the sensor's response is affected by external and environmental disturbances.

1.1.1 Surface biofunctionalization

A crucial factor affecting both the sensitivity and specificity of a biosensing device is the biofunctionalization [10]. This includes the choice of the bioreceptors and the methods for immobilizing them on the active surface of the sensors.
Ideal bioreceptors should have high selectivity and specificity against the target analyte. Among all the possible bioreceptors, antibodies (Abs) are considered prime candidates thanks to their inherent affinity with the antigen's molecules, high specificity and versatility.

Abs are characterized by two fragment antigen-binding (Fab) that are responsible for the selective recognition of the target biomolecules (Fig. 1.1). An efficient immobilization of the Abs on the active surface of a sensor should expose their Fab to the sample containing the target analyte.

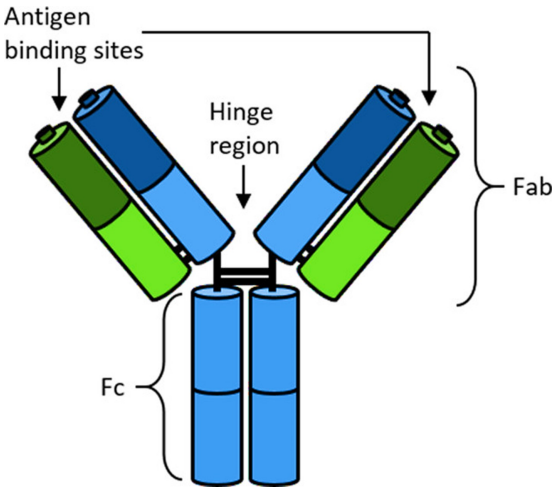

Figure 1.1: Sketch of a typical IgG structure. The heavy are in blue and the light chains are green, respectively. Adapted from [22].

However, the strategies for immobilizing antibodies with the right orientation and with an optimal surface density, is still an open issue [23].
Many functionalization methods have been so far explored. We list here the general idea of the main techniques known, before introducing the one adopted in this work for all the biosensors (Section 1.1.2). The simplest method is the physical adsorption that relies on weak intermolecular interactions (e.g. van der Waals bonds, electrostatic interactions) between antibodies and metal surfaces [24]. It is an easy strategy that does not require any chemical modification of the surface, however, resulting bonds are generally weak and with random orientation. Another strategy to immobilize Abs consist in exploiting intermediate proteins (protein A or protein G [25]) that bind to the Fc region of antibodies (Fig. 1.1) leaving the antigen binding sites free for the recognition of the antigen. The main advantage is promoting the best orientation (Fab exposed to the surrounding environment). However, the instability of non-covalent binding can cause the disassembling of the antibodies, especially during the regeneration step [26]. A covalent conjugation of Abs onto metal surface can be obtained by modifying the biosensor surface with reactive groups (e.g hydroxy, thiol, carboxy or amino groups). In this case the bindings are stable. The main drawback is that these procedure are usually time-consuming because of the complex chemical steps involved. Also, there is a concrete risk of modifying antigen binding sites, thus compromising the efficiency of the molecular recognition [27].

1.1.2 Photochemical Immobilization Technique

The photochemical immobilization technique (PIT) is a simple, fast and effective strategy to immobilize Abs on noble metal surfaces with one Fab free and exposed to the

surrounding environment [12]. The technique has been recently developed in the *Biosensing* research group at the Department of Physics of the University of Naples Federico II [12],[22]. The PIT consists in irradiating Abs with UV-light so to produce the selective photoreduction of the disulfide bridges in some cysteine-cysteine/tryptophan (Cys-Cys/Trp) triads [28] that are present in the Immunoglobulins G (IgG) structure [29]. The UV excitation of the Trp leads to the generation of solvated electrons that are captured by the nearby disulfide bridge resulting in its destabilization and in a subsequent breakage of the Cys-Cys bond. The process produces four free thiol groups, two of which interact with the noble metal surface forming a covalent binding (Fig. 1.2).

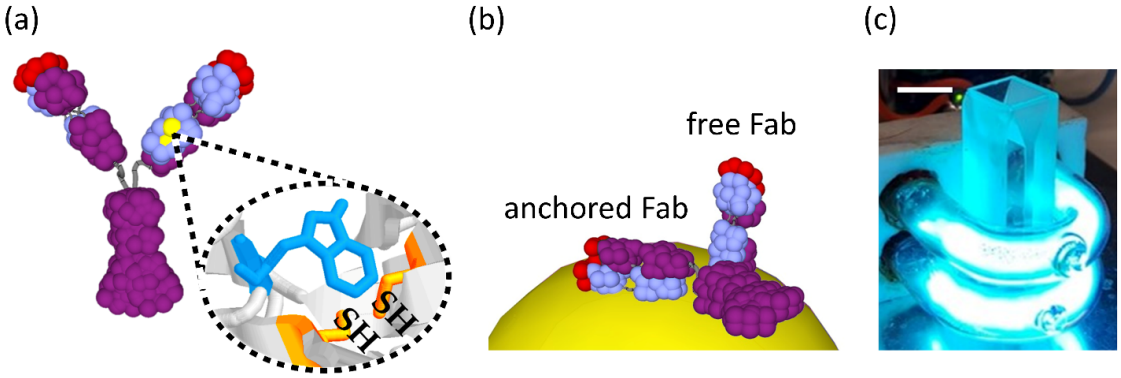

Figure 1.2: (a) UV irradiation of Abs leads to the selective production of four thiol groups, two of them are visible in the figure. (b) Schematic representation of an antibody linked to a gold surface. Thanks to the position of the thiols, the antibody is immobilized with the one Fab anchored on the gold surface, while the other is exposed to the environment. (c) Low pressure mercury U-shaped UV-lamp used to carry out the thiols activation in antibody Fabs. The length of the scale bar in the top-left corner is 1 cm. Adapted from [2, 30].

Besides the stability of the covalent binding, this functionalization ensures both close packing and an optimal orientation of the tethered Abs, with one of their binding sites free and exposed to the sample solution.
The protocol mainly consists in the irradiation of a Abs solution with a UV-lamp for $30 - 60$ s. The irradiation time depends on the power of the UV-lamp used and it has been established according to the results of the Ellman's assay [12]. The sensor's surface needs to be exposed to the solution of UV-activate antibodies for few minutes (details on the protocols employed in this work for each biosensor are reported in the corresponding chapter). This technique preserves the selectivity and efficiency of the antibodies while ensuring an optimal tail-on orientation. Compared to the conventional methods, PIT is a quick and user-friendly method, it does not require any chemical or surface modification. So far PIT has been adopted to develop several type of immunosensors based on different transduction systems such as quartz-crystal microbalances [31] and screen-printed electrodes for electrochemical sensing [32]. Moreover, it has been successfully employed to functionalize colloidal solutions of gold nanoparticles (AuNPs), for colorimetric transducers [33],[34] and gold coated magnetic nanoparticles [1], [5].

1.2 Basics on magnetic nanoparticles

Magnetic nanoparticles (MNPs) have been attracting increasing interest in scientific community as they provide the possibility to control and tune properties of nanoscale objects through an external magnetic field. Commonly MNPs consist of pure ferromagnetic materials or alloys, oxides, or composite structures based on ferromagnetic elements (Fe,Co,Ni). They can be fabricated via physical methods (e.g. condensation methods, mechanochemical dispersion) or chemical methods. The latter typically involve co-precipitation, thermal decomposition, sol-gel, and micro-emulsion methods [35]. Small magnetic particles exhibit many unique phenomena such as superparamagnetism and enhanced magnetic coercivity [36]. In Sections 1.2.1 and 1.2.2 we recall some fundamental properties of fine magnetic particles, in particular the size-dependence of coercivity and the superparamagnetic behaviour.

1.2.1 Coercivity of magnetic particles

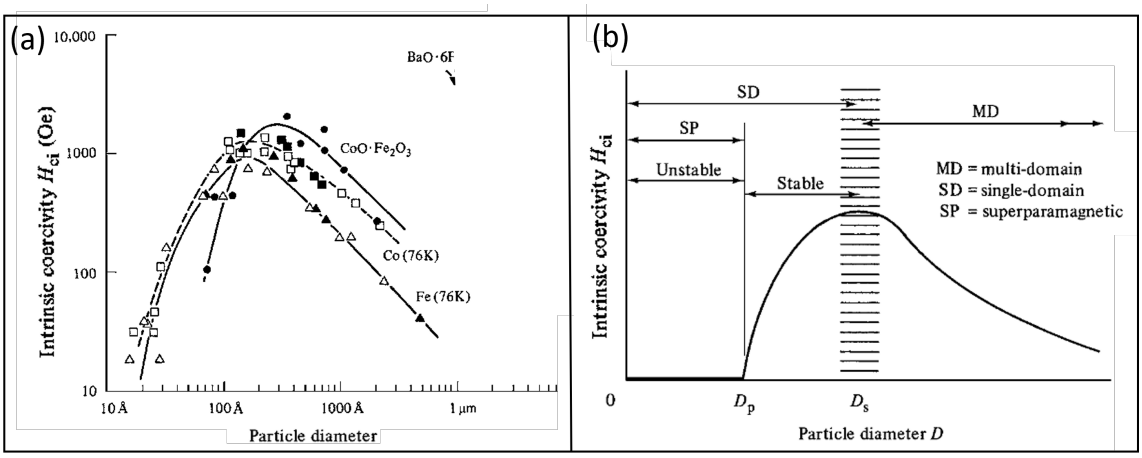

Figure 1.3: (a)Variation of intrinsic coercivity H_{ci} with particle size (b) Schematic representation of the size dependence of the intrinsic coercivity. The terms *stable* and *unstable* refer to particles with relaxation time $\tau < 100s$ and $\tau > 100s$ respectively. Adapted from [36, 37]

In magnetic materials, domain walls are interfaces between regions in which the spontaneous magnetization M_S has different directions (i.e. different easy crystallographic directions). Generally, the change of spin directions between adjacent domains does not occur abruptly. There are domains walls with nonzero width and a definite structure consisting of spins oriented in noneasy directions. The reason can be understood from an energetic argument. The minimization of the exchange energy requires the walls to be as wide as possible, so to make angle between adjacent spins as small as possible. On the other hand, thin walls require a smaller number of spins pointing in noneasy directions thus reducing the anisotropy energy. The formation of domains walls is associated to a certain energy cost per surface area. It can be shown that when the specimen size is less than a critical value a configuration with one single-domain is favored with respect to multi-domains configurations. In particular below a critical diameter D_s small magnetic

particle consist of a single domain. In this size range the coercivity reaches a maximum (Fig. 1.3(a)). As the particle size decreases below D_s the coercivity decreases as well (Fig. 1.3(a)). Finally below a critical diameter D_p the coercivity is zero because of thermal effects. In this state magnetic particles are called superparamagnetic (see Fig. 1.3(b) and Section 1.2.2).

1.2.2 Superparamagnetism

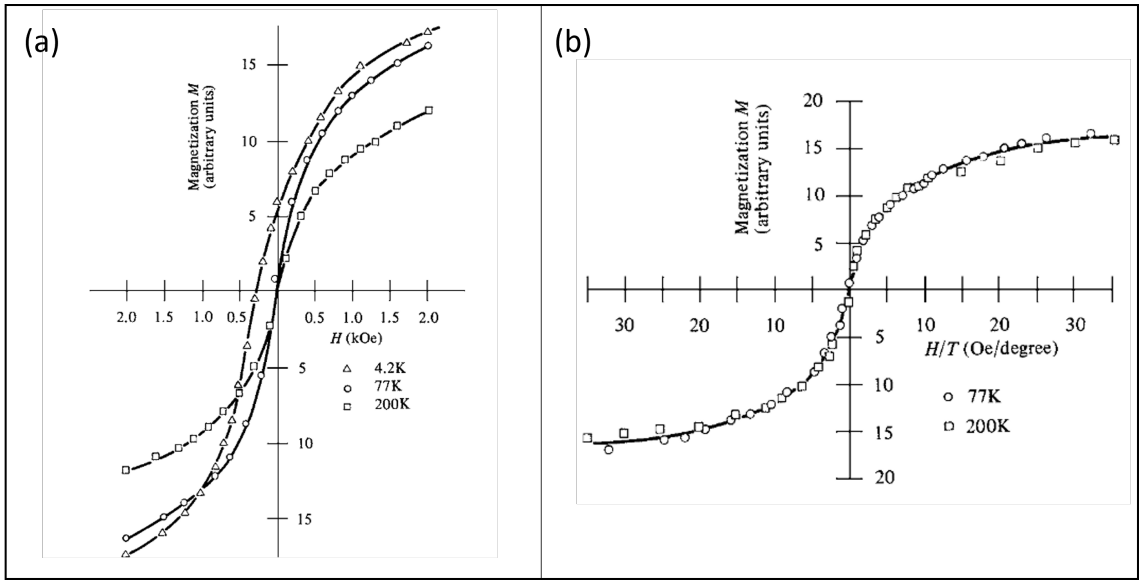

Figure 1.4: (a) Magnetization curves of an assembly of iron particles (4.4 nm in diameter) at different temperatures plotted against the applied field, (b) magnetization curves of the assembly measured at different temperatures superimpose when M is plotted as a function of the magnetic field divided by the temperature H/T. Reproduced from [36, 38].

Let us consider an assembly of uniaxial, single-domain particles with no applied magnetic field. The magnetization of each particle can be reversed overcoming the energy barrier given by the anisotropy energy. Assuming that the particle's surface makes no contribution to the anisotropy, the energy has the form $E = K \sin^2 \theta$ where K is the anisotropy constant and θ is the angle between the magnetic moment $\mathbf{m}$ of the particle and the anisotropy axis. Hence the energy barrier associated is $\Delta E = KV$ where V is the volume of the particle [36].
Below a critical dimension of the single-domain particles, the anisotropic energy becomes so small that that energy fluctuations happening at microscopic scale could overcome the anisotropy energy barrier causing the spontaneous reverse of the magnetization of a particle from one easy direction to the other. As for paramagnetic materials, if a field is applied to the assembly of nanoparticles, the field will tend to align their magnetic moments whereas the thermal energy will have the opposite tendency. However, the magnetic moment per nanoparticle is relatively enormous as compared to the magnetic moment per atom or ion in a normal paramagnetic material (few Bohr magnetons). This

is the reason why this phenomenon goes under the name of superparamagnetism [39]. Magnetization curves of the assembly measured at different temperatures superimpose when M (i.e. the magnetization of the assembly), is plotted as a function of the magnetic field divided by the temperature H/T (see Fig. 1.4). Since there is no hysteresis, both retentivity and coercivity are zero. However, the superparamagnetism disappears and the hysteresis appears when the assembly is cooled below a particular temperature or when the size of the particles go beyond the critical diameter for the zero coercivity, D_p. To determine these critical values of temperature or size, we must consider the rate at which the assembly approaches thermal equilibrium after the applied field H has been removed. Suppose an assembly of uniaxial particles has reached a magnetization value M_i due to the application of an external magnetic field and that the field is removed at $t = 0$. The magnetization M of the assembly will decrease as an effect of the demagnetization of the particles due to the thermal energy. The rate of decrease is given by:

$$-\frac{\partial M}{\partial t} = \frac{M}{\tau_0} e^{-\Delta E/k_B T} = \frac{M}{\tau}, \tag{1.1}$$

where ΔE is the energy barrier due to anisotropy, $e^{-\Delta E/kT}$ is the Boltzmann factor giving the probability that a particle has a thermal energy that exceeds the energy gap for magnetization reversal. The value of τ_0 is typically in the range $10^{-13} - 10^{-9}$ s [35]. The time τ is the relaxation time. The magnetization at any time is decreasing as $M_i e^{t/\tau}$. If the measuring time τ_{meas} is much larger than τ, a time average of the magnetization orientation is observed in the experimental time interval, and the assembly of particles behaves like a paramagnetic system. On the contrary, if $\tau_{meas} \ll \tau$, the system does not reach a new equilibrium state and its magnetisation does not change. If $\tau_{\text{meas}} = 100$ s that is characteristic value for the static magnetic measurements, and $\tau_0 = 10^{-9}$ s, the condition $\tau_{meas} = \tau$ in Eq. (1.1) gives that for uniaxial particles (i.e. $\Delta E = KV$) the transition to a stable behavior occurs when the energy barrier becomes equal to $25kT$ (Fig. 1.3(b)). For a given T, this implies that the volume of the particles assumes the value V_p:

$$V_p = \frac{25kT}{K}, \tag{1.2}$$

which gives for any particle's shape the corresponding diameter D_p that is the upper limit diameter of superparamagnetic behaviour.
At a given particles' size, there will be a temperature T_B below which the hysteresis will appear, called the blocking temperature. For uniaxial particles, proceeding as before, we get:

$$T_B = \frac{kV}{25k}. \tag{1.3}$$

1.2.3 Magnetic nanoparticles in biosensing

Iron-oxide nanoparticles, such as magnetite (Fe_3O_4) and maghemite (Fe_2O_3), are usually preferred for biomedical and environmental application due to the ease of synthesis, ease of surface modification [40], and relatively low toxicity [41]. Many applications are reported in biosensing [13, 42], nanomedicine and pharmacology (e.g. magnetic targeting,

drug delivery, magnetic resonance imaging, hyperthermia). Suspended magnetic particles offer a large active surface aria which encourage a rapid transfer of analytes onto their surfaces. As regarding the sensing applications, MNPs can be used in solid face extraction for collecting and separating the analytes of interest in the sample volume [43]. Beyond the techniques of samples preparations, an appropriate combination of MNPs with several transduction systems can amplify the detection signal and the interaction with applied magnetic fields may accelerate the process of target recognition [44]. To name few examples, in giant magnetoresistive sensors the magnetic field generated by magnetic nanoparticles is directly exploited [5], in optical sensing MNPs can be used to enhance the change of the refractive index for refractometric transducers [44].
Also, due to superparamagnetic properties they can be easily collected from sample solutions by applying an external magnetic field [40]. Generally, the use of MNPs in biosensing requires their surfaces to be functionalized with bioreceptors. However complex, expensive and time-consuming procedures may be needed to directly link the bioreceptors on the MNPs. Indeed, it is common to coat the magnetic core with a gold layer, a polymeric shell (e.g. poly (ethylene glycol) (PEG), 2,3-dimercaptosuccinic acid) or a silica shell on which bioreceptors can link more easily [45, 46]. The presence of a shell is also essential to protect the surface and improve the chemical stability [47].
In particular, gold decorated magnetic nanoparticles merge the magnetic properties of the cores with the oxidation resistance, the chemical stability, and the unique optical properties of gold. The optical and magnetic properties can be tailored by changing size, gold shell thickness, shape, charge, and surface modification [48]. However, the application of decorated magnetic nanoparticles is a relatively new topic and the protocols available in the literature for an effective coating require expensive laboratory equipment and may be complex and time-consuming [48].

Gold coated MNPs can be realized in several different configuration: core@shell, core@satellite, nanodumbbells and hybrid structures [48]. In this thesis, the core@shell type have been adopted in combination with a magnetoelastic transducer (Chapter 2). Core@shell nanoparticles are characterized by the presence of an approximately uniform gold coating around the magnetic core. The gold layer ensures high stability and allows to maximize the presence of Abs per particle linked via PIT (Section 1.1.2, Section 2.A.2). However, the magnetic properties of the core@shell structure are weakened by the diamagnetic nature of gold shell.

1.3 Basics on optics in metallic nanostructures

1.3.1 Optical properties of metals

The interaction between electromagnetic waves and metals can be understood in the classical framework based on the Maxwell's equations. When interacting with low-frequencies radiation, up to visible light's part of the spectrum, metals are highly reflective and only a negligible part of the incident radiation can penetrate trough them. At higher frequencies towards near infrared and visible part of the spectrum, the penetration of electromagnetic waves increases significantly and dissipation phenomena occur. In the ultra-violet part of the spectrum metals allow the propagation of electromagnetic waves with the occurrence

of attenuation and absorption phenomena depending on the electronic band structure. The dispersive properties of metals can be described by the mean of a complex dielectric function $\varepsilon(\omega)$ [49]. Thus to retrieve a convenient expression for $\varepsilon(\omega)$ and describe the optical phenomena of interest, we start from the three-dimensional Maxwell's equations for macroscopic electromagnetic fields [50, 49]:

$$\nabla \cdot \mathbf{D} = \rho_{ext}, \tag{1.4}$$

$$\nabla \cdot \mathbf{B} = 0, \tag{1.5}$$

$$\nabla \times \mathbf{E} = -\frac{\partial \mathbf{B}}{\partial t} \tag{1.6}$$

$$\nabla \times \mathbf{H} = \mathbf{J} + \frac{\partial \mathbf{D}}{\partial t}, \tag{1.7}$$

where $\mathbf{D}$, $\mathbf{E}$ are the dielectric displacement field and the electric field and $\mathbf{H}$,$\mathbf{B}$ are the magnetic field and the magnetic induction, respectively. As for the right side of the equations, ρ_{ext} is the external density charge and $\mathbf{J}_{ext}$ the external density current. Moreover the constitutive relations bind the macroscopic fields with the polarization $\mathbf{P}$ and the magnetization $\mathbf{M}$ fields:

$$\mathbf{D} = \varepsilon_0 \mathbf{E} + \mathbf{P}, \tag{1.8}$$

$$\mathbf{H} = \frac{1}{\mu_0}\mathbf{B} - \mathbf{M}, \tag{1.9}$$

where ε_0 and μ_0 are the electric permittivity and the magnetic permeability of vacuum, respectively.

Within this section, we assume to deal with nonmagnetic materials, for which the magnetization is zero. With this assumption we do not lose generality since the optical behaviour of the metals is driven by the by the electric polarization effect.

For isotropic and nonmagnetic media the constitutive relations can be rewritten as:

$$\mathbf{D} = \varepsilon_0 \varepsilon \mathbf{E}, \tag{1.10}$$

where ε is the relative permittivity. By inserting the expression in (1.8) into (1.10), it follows that the polarization field is linearly related with the electric field through the dielectric susceptibility χ:

$$\mathbf{P} = \varepsilon_0 \chi \mathbf{E}. \tag{1.11}$$

In the case of Ohmic and isotropic metals, the current density is proportional to the electric field by the conductivity σ:

$$\mathbf{J} = \sigma \mathbf{E}. \tag{1.12}$$

To take into account the dependence of the optical response of metals on the wave vector, we need to introduce the non-locality in time and space. Thus, assuming that the material is homogeneous (which means that length scales are larger than the lattice spacing) the equations (1.10) and (1.12) turn into the following:

$$\begin{aligned} \mathbf{D}(\mathbf{r}, t) &= \varepsilon_0 \int\int \varepsilon(\mathbf{r} - \mathbf{r}', t - t')\mathbf{E}(\mathbf{r}', t')\, d\mathbf{r}' dt', \\ \mathbf{J}(\mathbf{r}, t) &= \int\int \sigma(\mathbf{r} - \mathbf{r}', t - t')\mathbf{E}(\mathbf{r}', t')\, d\mathbf{r}' dt'. \end{aligned} \tag{1.13}$$

The Fourier transform of the previous relations gives:

$$\begin{aligned}\widetilde{D}(\mathbf{k},\omega) &= \varepsilon_0\widetilde{\varepsilon}(\mathbf{k},\omega)\widetilde{E}(\mathbf{k},\omega),\\ \widetilde{J}(\mathbf{k},\omega) &= \widetilde{\sigma}(\mathbf{k},\omega)\widetilde{E}(\mathbf{k},\omega),\end{aligned} \tag{1.14}$$

where the tilde symbol indicates the Fourier Transform, $\mathbf{k}$ is the wave vector and ω the frequency. From these relations we can easily retrieve an expression for the dielectric function $\widetilde{\varepsilon}(\mathbf{k},\omega)$:

$$\widetilde{\varepsilon}(\mathbf{k},\omega) = 1 + \frac{i\widetilde{\sigma}(\mathbf{k},\omega)}{\varepsilon_0\omega}. \tag{1.15}$$

As long as the wave length λ of the impinging radiation is much longer than the lattice spacing and the electrons mean free path, the equation (1.15) can be evaluated when $\mathbf{k} = 0$ which implies $\widetilde{\varepsilon}(\mathbf{k},\omega) = \widetilde{\varepsilon}(\omega)$. In general, the dielectric function is a complex function $\widetilde{\varepsilon}(\omega) = \varepsilon_1 + i\varepsilon_2$, where $\varepsilon_1 := \mathrm{Re}(\widetilde{\varepsilon})$ and $\varepsilon_2 = \mathrm{Im}(\widetilde{\varepsilon})$. The index of refraction is also a complex function defined as $\widetilde{n} = \sqrt{\widetilde{\varepsilon}(\omega)} := n + i\kappa$. The following equations follow by the definitions:

$$\begin{aligned}\varepsilon_1 &= n^2 - \kappa^2, \quad & n^2 &= \frac{\varepsilon_1}{2} + \frac{\sqrt{\varepsilon_1^2+\varepsilon_2^2}}{2},\\ \varepsilon_2 &= 2n\kappa, & \kappa &= \frac{\varepsilon_2}{2n}.\end{aligned} \tag{1.16}$$

The imaginary part of the index of refraction, κ, is the extinction coefficient that is related to the optical absorbance of the electromagnetic waves propagating trough the medium. More explicitly, the exponential attenuation of a beam of intensity I_0 propagating through a medium is given by the Beer's law [49]:

$$\begin{aligned}I(x) &= I_0 e^{(-\alpha x)},\\ \alpha &= \frac{2\kappa(\omega)\omega}{c},\end{aligned} \tag{1.17}$$

where c is the speed of light in the vacuum. Thus by considering the relations (1.16) stated above, the imaginary part of the the dielectric function ε_2 determines the optical absorption inside the medium. If $|\varepsilon_1| \gg |\varepsilon_2|$, the real part of the index of refraction, n, is mainly determined by ε_1. In absence of external stimuli the Maxwell's equations lead to the wave equation for the electric field:

$$\nabla \times \nabla \times \mathbf{E} = -\frac{\mu_0\partial^2\mathbf{D}}{\partial^2 t}, \tag{1.18}$$

and the corresponding equation in Fourier transform is

$$\mathbf{k}(\mathbf{k}\cdot\mathbf{E}) - k^2\mathbf{E} = -\widetilde{\varepsilon}(\mathbf{k},\omega)\mathbf{E}\frac{\omega^2}{c^2}. \tag{1.19}$$

This equation admits two different solutions, namely transversal and longitudinal waves. For transversal waves $\mathbf{k}\cdot\mathbf{E} = 0$, the equation (1.19) gives

$$k^2\mathbf{E} = \widetilde{\varepsilon}(\mathbf{k},\omega)\mathbf{E}\frac{\omega^2}{c^2}, \tag{1.20}$$

that is the usual Helmholtz wave equation. For longitudinally polarized waves ($\mathbf{k}\cdot\mathbf{E} \neq 0$), according to the equation (1.19) the allowed wave frequencies are only the zeros of the dielectric function:

$$\widetilde{\varepsilon}(\mathbf{k},\omega) = 0. \tag{1.21}$$

This relation defines the dispersion relation for the so-called plasmon excitations that are - as we will see more in detail - collective longitudinal oscillations. To simplify the notation from now on we will omit the Fourier transform symbol on the dielectric function.

1.3.2 Plasma model

The optical properties of metals can be explained by the plasma model at frequency ranges that come from the electron band transition energies. The basic assumption of the model is that the electrons of a metal are a gas of particles free to move in a background of relatively fixed ions of opposite charge. In this picture the electron-electron interactions and the effect of the lattice potential are both neglected. When a driving electromagnetic field is applied to the metals, the electrons of the gas oscillate. Taking into account that the motion is damped by individual electron collision, the dynamics is described by the following equations [49]:

$$m\frac{\partial^2\mathbf{r}}{\partial^2 t} + m\gamma\frac{\partial\mathbf{r}}{\partial t} = -e\mathbf{E}, \tag{1.22}$$

where $\gamma = 1/\tau$ is the characteristic collision frequency that corresponds to the inverse of the relaxation time τ of the free electron gas. Assuming harmonic time dependence of $\mathbf{E}$ upon time $\mathbf{E}(t) = \mathbf{E_0}e^{-i\omega t}$, a particular solution of the equations has the form

$$\mathbf{r}(t) = \mathbf{r_0}e^{-i\omega t} = \frac{e}{m(\omega^2 + i\gamma\omega)}\mathbf{E}(t). \tag{1.23}$$

The displacement of the electrons gives a contribution to the macroscopic polarization. If n_D is the electron number density, the polarization is $\mathbf{P}(t)$, since $\mathbf{P} = -n_D e\mathbf{r}(t)$, we get the following expression for the displacement field:

$$\begin{aligned} \mathbf{D}(t) &= \varepsilon_0\left(1 - \frac{\omega_p^2}{\omega^2 + i\gamma\omega}\right)\mathbf{E}(t), \\ \omega_p^2 &:= \frac{n_D e^2}{\varepsilon_0 m}, \end{aligned} \tag{1.24}$$

where ω_p is called plasma frequency. The resulting expression of complex dielectric function is

$$\varepsilon(\omega) = 1 - \frac{\omega_p^2}{(\omega^2 + i\gamma\omega)}, \tag{1.25}$$

whose real and imaginary part are $\varepsilon_1(\omega)$ and $\varepsilon_2(\omega)$ respectively:

$$\varepsilon_1(\omega) = 1 - \frac{(\omega_p\tau)^2}{1 + (\omega\tau)^2}, \qquad \varepsilon_2(\omega) = \frac{\omega_p^2\tau}{\omega(1 + \omega^2\tau^2)}. \tag{1.26}$$

At low-frequency $\omega\tau \ll 1$ the relations (1.26) become

$$\begin{aligned} \varepsilon_1(\omega) &\simeq 1 - \omega_p^2\tau^2 = 1 - \frac{\omega_p^2}{\omega^2}, \\ \varepsilon_2(\omega) &\simeq \frac{\omega_p^2\tau^2}{\omega\tau}, \end{aligned} \tag{1.27}$$

and the imaginary part of the dielectric function is dominant, $\varepsilon_2 \gg \varepsilon_1$. According to the equations (1.16):

$$n \approx k \approx \sqrt{\varepsilon_2/2}. \tag{1.28}$$

This implies that the real and the imaginary part of the index of refraction are of the same magnitude and very large so that the reflection coefficient $R = [(1-n)^2 + k^2]/[(1+n)^2 + k^2] \approx 1$. In this regime the radiation is mainly absorbed in a region very close to the metal interface preventing the wave propagation inside the metals (skin effect). On the contrary, at high-frequency $\omega\tau \gg 1$ the real part of the dielectric function results to be dominant ($\varepsilon_1 \gg \varepsilon_2$):

$$\varepsilon_1(\omega) \simeq 1 - \frac{\omega_p^2\tau}{\omega^2\tau}, \tag{1.29}$$

$$\varepsilon_2(\omega) \simeq \frac{\omega_p^2\tau^2}{\omega^3\tau^3}. \tag{1.30}$$

For frequencies higher than the plasma frequency $\omega \gg \omega_p$, according to the equation (1.25), $\varepsilon(\omega) \to 1$. In this transparent regime the electron plasma support the propagation of transversal waves through the metal. By inserting the equation (1.29) into (1.20) we get the dispersion relation and the group velocity of the propagating transversal waves (Fig. 1.5):

$$\begin{aligned} \omega^2 &= \omega_p^2 + k^2c^2, \\ v_g &= d\omega/dk = \frac{c^2k}{\gamma}. \end{aligned} \tag{1.31}$$

Noble metals

For noble metals in the region $\omega > \omega_p$ an extension of this model is needed. At high frequency the dielectric function tends to values different from the unit predicted by the equation (1.25). This is corrected adding a parameter ε_∞ that takes into account the net contribution from the positive ions:

$$\varepsilon(\omega) = \varepsilon_\infty - \frac{\omega_p^2}{(\omega^2 + i\gamma\omega)}. \tag{1.32}$$

Typical values of ε_∞ for metals lie into the range $1 - 10$ and depend on the inter-band response [51]. A contribution to the dielectric function is also given by inter-band transitions from lower-lying bands to the conduction band. These contributions can be accounted for by adding the description of the bound electrons into the equation (1.22). In the classic

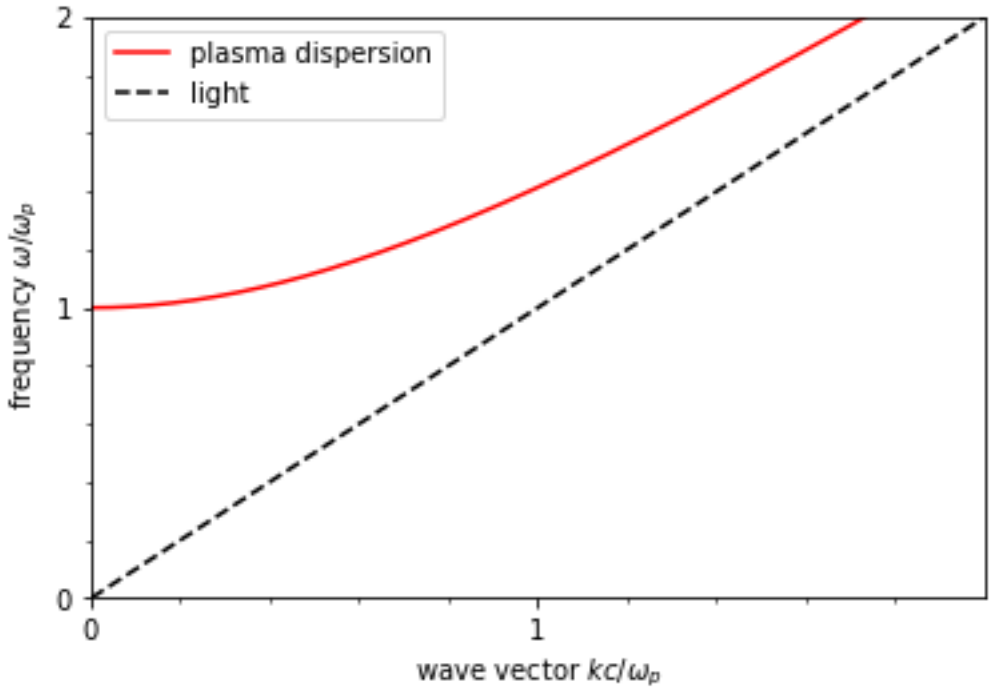

Figure 1.5: The dispersion relation of the free electron gas (red solid line). The propagation of transversal waves is only allowed for frequencies higher than the ω_p. The dashed black line is the dispersion relation of light in air $\omega = kc$.

pictures the bound electrons are linked to the nucleus by an atomic force represented as a spring force. Thus the equation (1.22) is replaced with the following

$$m\frac{\partial^2 \mathbf{r}}{\partial^2 t} + m\gamma\frac{\partial \mathbf{r}}{\partial t} + m\omega_0^2\mathbf{r} = -e\mathbf{E}, \tag{1.33}$$

where ω_0 is the resonance frequency.

1.3.3 Volume plasmons

We saw in the previous sections that the plasma frequency ω_p defines a threshold between the reflected and transmitted wave frequencies. The plasma frequency can also be understood in another way. At frequencies close to the plasma frequency the condition (1.21) is realized and, according to the equations (1.8) and (1.10), the electric field is a pure depolarization field with $\mathbf{E} = -\mathbf{P}/\varepsilon_0$. Let us consider a metal slab to which an external electric perturbation at a frequency close to ω_p is applied. Assuming that the free electron gas moves as a rigid entity, the external perturbation causes a collective displacement by a distance u from the equilibrium position. The electron gas experiences a restoring force due to the unbalanced charge of the positive ion cores and a surface density charge $\sigma = neu$ appear on the slab's sides (n is the electron volume density and e the electron charge). The equation of motion of the electron cloud is:

$$nm\frac{\partial^2 u}{\partial^2 t} = -neE = -\frac{n^2e^2u}{\varepsilon_0}, \tag{1.34}$$

where m is the electron mass and $E = \sigma/\varepsilon_0$. Manipulating the previous equations we get:

$$nm\frac{\partial^2 \mathbf{u}}{\partial^2 t} + \omega_p^2 \mathbf{u} = 0, \tag{1.35}$$

which implies that the plasma frequency naturally appears as a frequency of the collective oscillation of the free electron gas. It is worth noticing that the coherent in-phase oscillation of the conduction electrons is possible only if the condition $\mathbf{k} = 0$ is satisfied. The quanta of these collective oscillations are called volume plasmons in order to distinguish them from "localized" and "surface" plasmons. Because of their longitudinal nature, volume plasmons do not couple to transverse electromagnetic perturbations. In general for metals ω_p assume values that vary in the range of $1 - 15eV$ depending on the electronic band structure [52].

1.3.4 Surface Plasmon Polaritons

Surface Plasmon Polaritons (SPP) are electromagnetic oscillations propagating at the interface between a dielectric and a conductor and evanescently confined in the direction perpendicular to the surface. These modes arise from the coupling of the electromagnetic field with the electron plasma of the conductor.

The main properties of SPPs can be retrieved from a classical approach, by applying the Maxwell's equations to the interface between a dielectric and a conductor. The equations have to be solved in two separate regions of constant dielectric function (the dielectric and the conductor), and the obtained solutions must match appropriate boundary conditions. In absence of external stimuli the equations (1.6),(1.7) lead to the wave equation:

$$\Delta E - \frac{\varepsilon}{c^2}\frac{\partial^2 E}{\partial^2 t} = 0, \tag{1.36}$$

where it is assumed that the spatial variation of ε are negligible. For simplicity we can consider a one dimensional geometry (Fig. 1.6) in which $z = 0$ is the interface between the dielectric and the conductor and in the y-direction the system is homogeneous. We also assume that electric field propagates along the x direction and that it has the harmonic dependence on time $\mathbf{E}(\mathbf{r}, t) = \mathbf{E}(z)e^{ik_{sp}x}e^{-i\omega t}$ where $\mathbf{k_{sp}} = \kappa\hat{x}$ is the component of the wave vector along the propagation direction.

The equation (1.36) becomes

$$\frac{\partial^2 \mathbf{E}}{\partial^2 z} + (\kappa_0^2\varepsilon - k_{sp}^2)\mathbf{E} = 0, \tag{1.37}$$

where $\kappa_0 = \omega/c$ is wave vector in the vacuum. Making the equivalent assumptions for the magnetic field $\mathbf{H}(\mathbf{r}, t)$ for the three component of both field one easily retrieves the following set of equations:

$$-\frac{\partial E_y}{\partial z} = i\omega\mu_0 H_x, \qquad \frac{\partial E_x}{\partial z} - \frac{\partial E_z}{\partial x} = i\omega\mu_0 H_y, \qquad \frac{\partial E_y}{\partial x} = i\omega\mu_0 H_z, \tag{1.38}$$

$$-\frac{\partial H_y}{\partial z} = i\omega\varepsilon_0\varepsilon E_x, \qquad \frac{\partial H_x}{\partial z} - \frac{\partial H_z}{\partial x} = i\omega\varepsilon_0\varepsilon E_y, \qquad \frac{\partial H_y}{\partial x} = i\omega\varepsilon_0\varepsilon E_z, \tag{1.39}$$

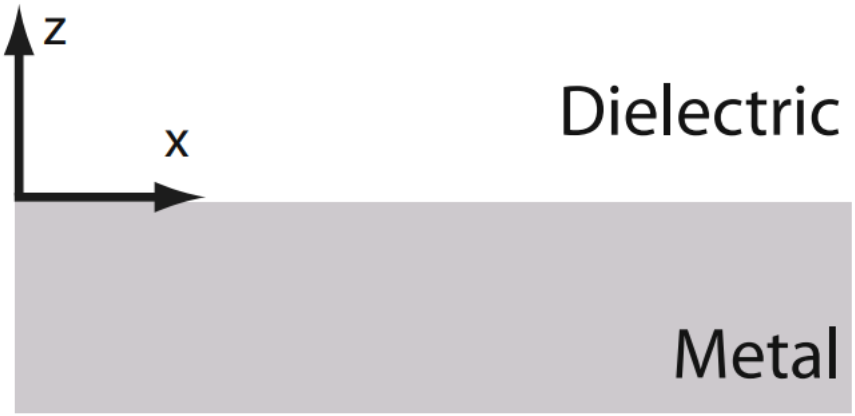

Figure 1.6: Configuration for SPP propagation at a single interface between a metal and a dielectric medium (from [49]).

where it has been used that the partial derivative with respect to the y-direction $\partial/\partial y$ is null for each component because of the assumption on the homogeneity of the system. This system admits two sets of solutions with different solutions: the so-called transverse electric mode (TE or s modes) and transverse magnetic mode (TM or p modes). The two sets of self-consistent solutions and the corresponding wave equations are the following: for TM modes

$$E_x = -\frac{i}{\omega\varepsilon_0\varepsilon}\frac{\partial H_y}{\partial z}, \qquad E_z = -\frac{k_{sp}}{\omega\varepsilon_0\varepsilon}H_y, \qquad \frac{\partial^2 H_y}{\partial z^2} + (k_0^2\varepsilon - k_{sp}^2)H_y = 0, \tag{1.40}$$

and for TE modes

$$H_x = \frac{i}{\omega\mu_0}\frac{\partial E_y}{\partial z}, \qquad H_z = \frac{k_{sp}}{\omega\mu_0}E_y, \qquad \frac{\partial^2 E_y}{\partial z^2} + (k_0^2\varepsilon - k_{sp}^2)E_y = 0. \tag{1.41}$$

We know that SPPs are propagating wave solutions confined to the interface between a dielectric and a conductor with evanescent decay in the direction perpendicular to the interface. Let $\varepsilon_d(\omega)$ be the dielectric function of the dielectric medium and a $\varepsilon_m(\omega)$ the one of the metal. The two media are separated by a single flat interface coinciding with the plane $z = 0$. For TM modes a solution is

$$\begin{aligned} H_y &= A_d e^{ik_{sp}x}e^{-k_{zd}}, \\ E_x &= \frac{iA_d}{\omega\varepsilon_0\varepsilon_d(\omega)(\omega)(\omega)}k_{zd}e^{ik_{sp}x}e^{-k_{zd}}, \\ E_z &= \frac{iA_d}{\omega\varepsilon_0\varepsilon_d(\omega)(\omega)(\omega)}k_{sp}e^{ik_{sp}x}e^{-k_{zd}}, \end{aligned} \tag{1.42}$$

for $z > 0$ and

$$\begin{aligned} H_y &= A_m e^{ik_{sp}x} e^{k_{zm}}, \\ E_x &= -\frac{iA_m}{\omega\varepsilon_0\varepsilon_m(\omega)} k_{zm} e^{ik_{sp}x} e^{-k_{zd}}, \\ E_z &= -\frac{iA_m}{\omega\varepsilon_0\varepsilon_m(\omega)} k_{sp} e^{ik_{sp}x} e^{k_{zm}}, \end{aligned} \tag{1.43}$$

(1.44)

for $z < 0$. The subscript m, d refer to the medium, k_{zm}, k_{zd} are the $\hat{z}$-component of the wave vectors in the two media. The inverse of the real part of these wave vectors k_{zm}^{-1}, k_{zd}^{-1} are the evanescent decay lengths (or depth penetration length) of the fields in the direction perpendicular to the interface. The continuity of the tangential component of the fields E_x and H_y and of the normal components D_z leads to the conditions $A_d = A_m$ and

$$\frac{k_{zm}}{k_{zd}} = -\frac{\varepsilon_d(\omega)}{\varepsilon_m(\omega)}. \tag{1.45}$$

According to the last condition the existence of SPPs solution at the interface implies that the dielectric functions of the medium have real parts with opposite signs. The condition is fulfilled in case of dielectric-metal interface. In particular, for metals we saw in the equation (1.27) that the real part of the dielectric function is negative at frequencies lower than the plasma frequency ω_p. Imposing that H_y is also a solution of the wave equation we get the two relation

$$\begin{aligned} k_{zm}^2 &= k_{sp}^2 - k_0^2\varepsilon_m(\omega), \\ k_{zd}^2 &= k_{sp}^2 - k_0^2\varepsilon_d(\omega), \end{aligned} \tag{1.46}$$

that lead to the dispersion relation for SPPs propagating at the interfaces between two media:

$$k_{sp} = k_0 \sqrt{\frac{\varepsilon_m(\omega)\varepsilon_d}{\varepsilon_m(\omega) + \varepsilon_d(\omega)}}, \tag{1.47}$$

where $\mathrm{Re}(\varepsilon_m(\omega)) < 0$ and $\mathrm{Re}(\varepsilon_d(\omega)) > 0$ as required by the equation (1.45).

Following the same procedure for TE modes leads to the conclusion that no surface mode can exist for TE polarization. Fig. 1.7 shows plot of the dispersion relation (1.47) of SPPs modes at the interface between a metal with negligible damping (i.e. $\mathrm{Im}(\varepsilon_\mathrm{m}(\omega)) \approx 0$) and air.

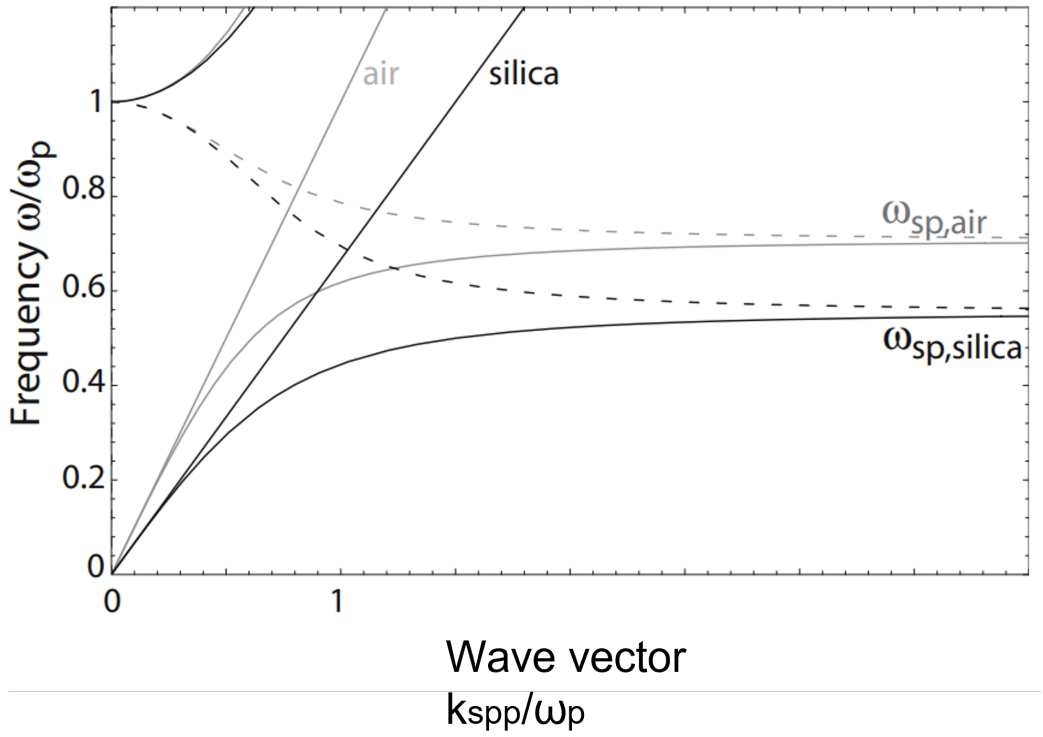

Figure 1.7: Dispersion relation of SPPs modes at the interface between a Drude metal with $\gamma \approx 0$ and air (gray curves) or silica (black curves.) Adapted from [49].

Since SPPs are bound modes, their excitation can only occur at frequencies lower than the plasma frequency $\omega \ll \omega_p$ for which metals are not transparent (Section 1.3.2), so that the SPPs dispersion curve lies on the right side of the light line in air. An important consequence is that special phase-matching techniques are required for the SPPs excitation via three-dimensional beams as we will further see in Section 1.3.5.

For large wave vectors $k_{sp} \to \infty$, the dispersive relation (1.47) admits two asymptotes that can be obtained by using the real part of the free electron dielectric function (eq.(1.25)) and assuming that the collision frequency of the metal, γ, is negligible. One branch solution is $\omega = ck_{sp}$ ($\omega \to \infty$ when $k_{sp} \to \infty$) and the other one, that correspond to the surface plasmon solutions, is the branch with ω that approaches a finite value ω_{sp} when $k_{sp} \to \infty$:

$$\omega_{sp} = \frac{\omega_p}{\sqrt{1+\varepsilon_d}}. \tag{1.48}$$

The value ω_{sp} is the so-called surface plasmon frequency. In this region the group velocity tends to zero $v_g \to 0$ and the SPPs modes have an electrostatic behaviour which is known as surface plasmon. The confinement of the surface plasmon occur in both media since

$$k_{sp} > \frac{\omega}{c}\sqrt{\varepsilon_j}, \tag{1.49}$$

with $j = m, d$ and the $\hat{z}$-components of the wavevectors have purely imaginary values

$$k_{zm} = \sqrt{\varepsilon_m k_0^2 - k_{sp}^2}, \qquad k_{zd} = \sqrt{\varepsilon_d k_0^2 - k_{sp}^2}, \tag{1.50}$$

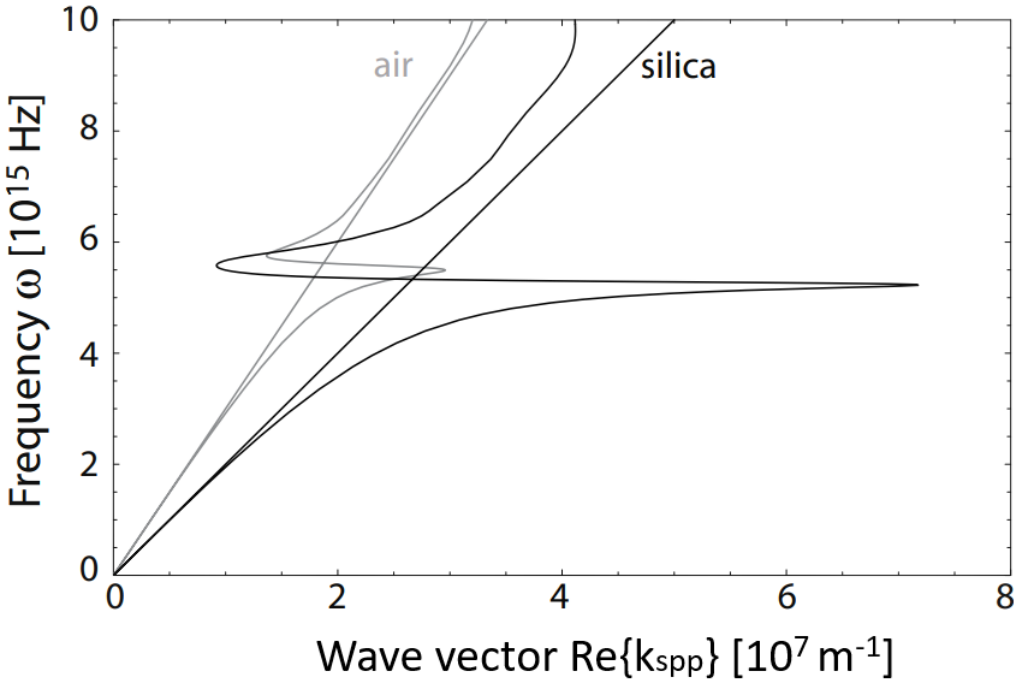

Figure 1.8: Dispersion relation of SPPs at a silver/air (gray curve) and silver/silica (black curve) interface. For real metal, the wave vector k_{sp} of the bound SPPs reaches a finite maximum value at the surface plasmon frequency ω_{sp}. Adapted from [49].

which implies that the fields decay exponentially away from the interface.

In the case of real metal, the imaginary part of the dielectric function is not null $\mathrm{Im}(\mathrm{e_m}) \neq 0$ for both from free-electron and interband damping. As a result, the SPPs are damped and the attenuation length $L = (2\mathrm{Im}(\mathrm{k_{sp}}))^{-1}$ lies typically in the range of $10 - 100\mu m$ in the visible regime depending on the metal/dielectric couple considered. In Fig. 1.8 it is shown as an example the dispersion relation of SPPs propagating at a silver/air and silver/silica interface. Compared to the previous undamped case, now the wave vector of the bound SPPs approaches a finite value at the surface plasmon frequency. The corresponding finite wavelength is $\lambda_{sp} = 2/(\mathrm{Re}(\mathrm{k_{sp}})$.

1.3.5 Configurations sustaining Surface Plasmon Polaritons

The excitation of SPPs modes requires the conservation of energy and momentum. On a flat metal/dielectric interface, at any frequency, the SPPs wave vector $k_{sp} > k \sin\theta$, where k is the wave vector of light on the dielectric side of the interface and θ the incidence angle. Thus, the phase matching is prohibited in this way but it is still possible in a three-layer system consisting of a thin metal film sandwiched between two insulators of different dielectric constants.

Let one of the insulators be the air ($\varepsilon = 1$). A beam reflected at the interface between the insulator of higher dielectric constant $\varepsilon_p(\omega)$ (usually a prism) and the metal will have an in-plane momentum $k_x = k\sqrt{\varepsilon_p}\sin\theta$ sufficient to excite SPPs at the metal/air interface. The phase-matching to SPPs cannot occur at prism/metal interface since the correspond-

ing SPP dispersion lies outside the prism light cone (Fig. 1.9).

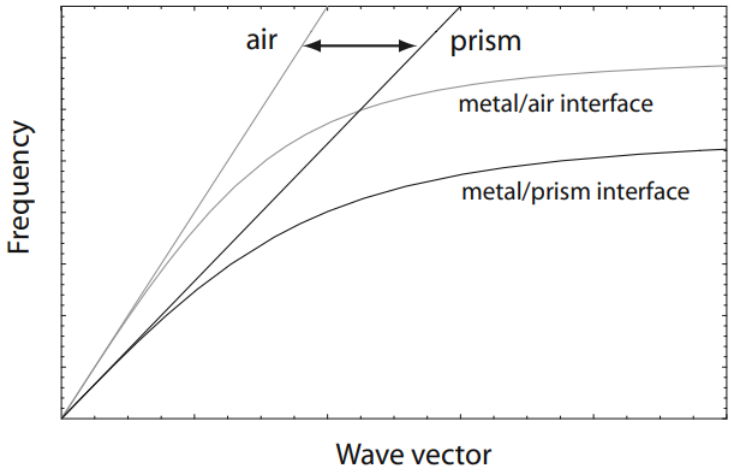

Figure 1.9: Dispersion relation of SPP at metal/air and metal/prism interface for the typical ATR coupling scheme. Only propagation constants between the light lines of air and that of the prism are accessible: the SPPs can be excited at metal/air interface where their propagation constants lies inside the prism light cone (from [49]).

The phase-matching with prisms can be realized with two different configurations: the Otto and Kretschmann configurations (Fig. 1.10).
In the Otto configuration [53], the prism is separated from the metal film by a thin air gap. Total internal reflection takes place at the prism/air interface exciting SPPs through tunnelling of the field to the metal/air interface.
In the Kretschmann configuration [54], a thin metal film is evaporated on the prism surface. The incidence angle of the exciting beam at the prism/metal interface is greater than the critical angle of total internal reflection. The tunnel effect occurs through the metal film so that SPPs are excited at the metal/air interface. Thus, the matching condition can be written as:

$$\mathrm{Re}\{\mathrm{k_{spp}}\} = \frac{\omega}{c}\sin(\theta)n_p, \tag{1.51}$$

where n_p is the index of refraction of the prism, ω the exciting frequency and θ the coupling angle.

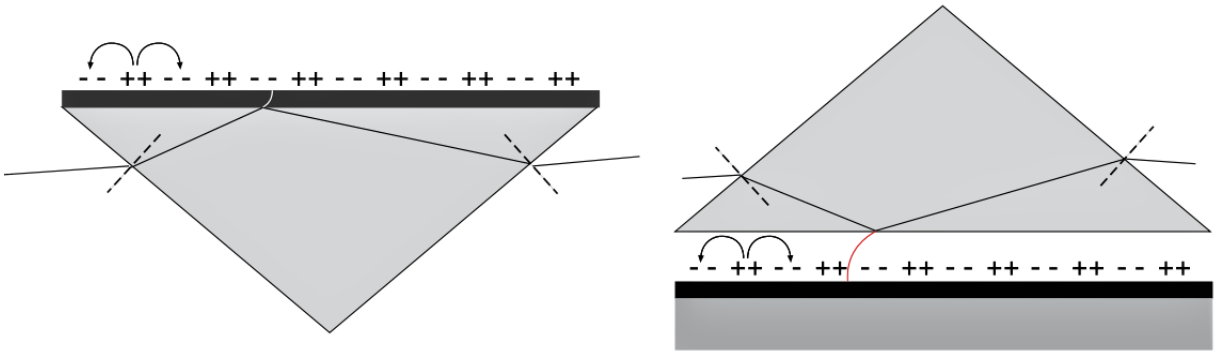

Figure 1.10: Phase-mathing SPPs using prism coupling with attenuated total internal reflection according to the Kretschmann-Raether (left) and Otto (right) configuration (from [49]).

The coupling scheme described is also called attenuated total internal reflection (ATR), and it is not the only possibility to exctice SPPs. The phase-matching can also be achieved with a grating of grooves or holes. For a one-dimensional grating of grooves (Fig. 1.11), the phase-matching requires

$$k_{spp} = \frac{\omega}{c} \sin\theta + \nu g, \tag{1.52}$$

where $g = 2\pi/a$ is the vector of the reciprocal space, a is the period of the diffraction grating and $\nu \in \mathbb{Z}$.

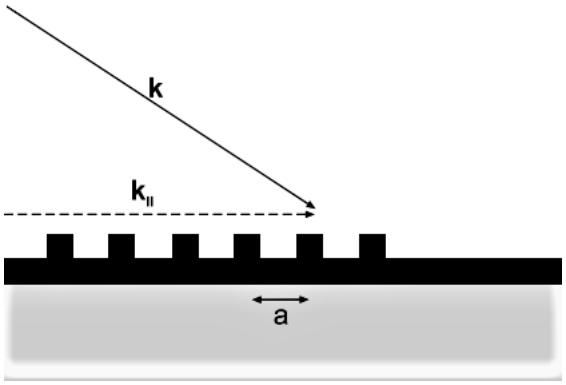

Figure 1.11: One dimensional grating: a is the grating vector, $k_{\|} = k \sin\theta$ where θ is the angle of incidence (from [49]).

Observing SPR

A direct method for observing the excitation of SPPs in ATR experiments is detecting the reflected light, measuring the dependence of the p-polarized light reflection coefficient R_{pp} on the incidence angle or wavelength. Ideally, in resonance condition, $R_{pp} = 0$, all energy of light wave transforms to surface plasmons.
It is worth noting that the modes excited with ATR configurations are leaking modes that lose energy due to intrinsic losses in the metal and the leakage of the radiation inside the

prism. The minimum of R_{pp} measured occurs due to the destructive interference between this leaking emission and the reflected part of the excitation beam. When the thickness of a metal film is optimal, the destructive interference causes the reflected beam to vanish, thus preventing the detection of the leaking field.

1.3.6 Localized Surface Plasmon Resonance

The interaction of an oscillating electromagnetic field and nanoparticles with small or subwavelenght dimension gives rise to propagating excitations of the conduction electrons of metallic nanostructures, called Localized surface plasmons (LSPR).

For describing this phenomenon we start considering the scattering problem for a small and spherical particle interacting with an oscillating electromagnetic field. If the dimension d of the nanoparicle is much smaller than the wavelenght of the electromagnetic field $d \ll \lambda$, the phase of the harmonically oscillating electromagnetic field is constant over the whole particle volume, and the problem can be reduced to the electrostatics (quasi-static approximation). Thus, we consider a homogeneous, isotropic, spherical nanoparticle of radius a located at the origin of the system and subjected to a static electric field $E = E_0\hat{z}$ (Fig. 1.12). The surrounding medium is isotropic and non-absorbing with dielectric constant ε_m, while $\varepsilon(\omega)$ is the dielectric response of the particle.

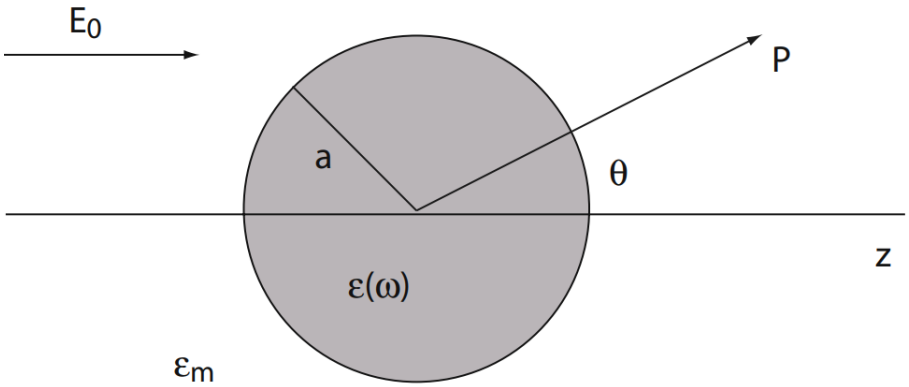

Figure 1.12: Homogeneous spherical particle placed into an electrostatic field $\mathbf{E_0}$ (from [49]).

In this geometric configuration, the solutions of the Laplace equation for the electric potential $\Delta\phi = 0$, are the following [50]:

$$\begin{aligned} \Phi_{in} &= -\frac{3\varepsilon_m}{\varepsilon + 2\varepsilon_m} E_0 r \cos\theta, \\ \Phi_{out} &= -E_0 r \cos\theta + \frac{\varepsilon - \varepsilon_m}{\varepsilon + 2\varepsilon_m} E_0 a^3 \frac{\cos\theta}{r^2}, \end{aligned} \tag{1.53}$$

where the proper boundary conditions for the normal and tangential component of the electric field are taken into account. We note that Φ_{out} can be written as:

$$\Phi_{out} = -E_0 r \cos\theta + \frac{\mathbf{p}\cdot\mathbf{r}}{4\pi\varepsilon_0\varepsilon_m r^3}, \tag{1.54}$$

where $\mathbf{p}$ is the electric dipole moment:

$$\mathbf{p} = 4\pi\varepsilon_0\varepsilon_m a^3 \frac{\varepsilon - \varepsilon_m}{\varepsilon + 2\varepsilon_m} = \varepsilon_0\varepsilon_m \alpha \mathbf{E_0}, \tag{1.55}$$

where α is by definition the polarizability. This means that when a small spherical nanoparticle is illuminated by light, the electric field causes that its conduction electrons to oscillate coherently with the field. The applied electric field induces a dipole moment inside the sphere of magnitude proportional to $|E_0|$. We note that the polarizability α defined in (1.55):

$$\alpha = 4\pi a^3 \frac{\varepsilon - \varepsilon_m}{\varepsilon + 2\varepsilon_m}, \tag{1.56}$$

experiences a resonant enhancement under the condition that $|\varepsilon + 2\varepsilon_m|$ is a minimum. For the case of small or slowly-varying $\mathrm{Im}\,\varepsilon$ this simplifies to the Fröhlich condition:

$$\mathrm{Re}\{\varepsilon(\omega)\} = -2\varepsilon_m. \tag{1.57}$$

The mode associated to this resonant condition in an an oscillating field is called dipole surface plasmon of the metal nanoparticle (Fig. 1.13 (a)).

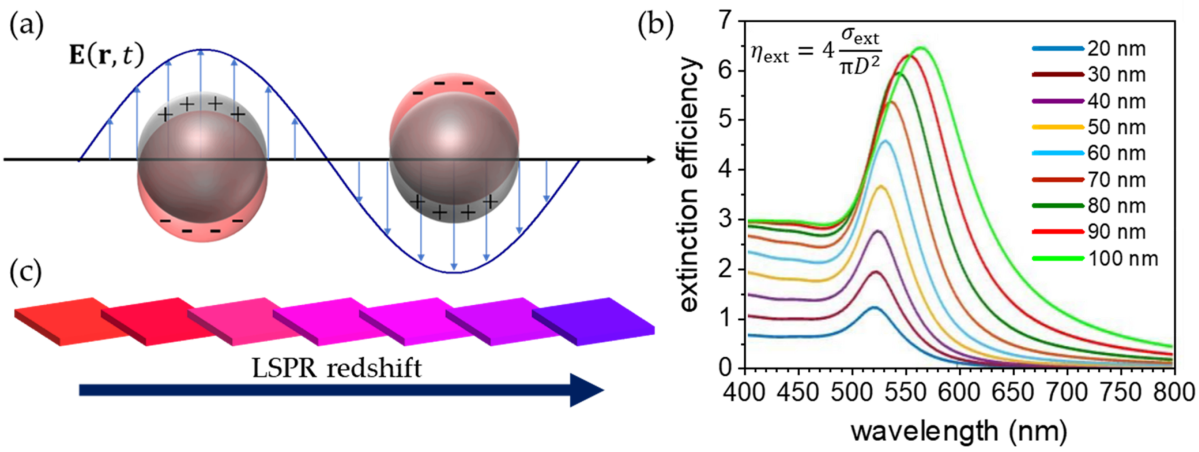

Figure 1.13: (a) Schematic illustration of the localized surface plasmon excitation. (b) Extinction efficiency as a function of NP diameter. (c) Sketch of the visual colour change of a nanostructured substrate as a consequence of the LSPR redshift. Adapted from [2].

It is worth to notice that in real cases the magnitude of the polarizability α is limited by $\mathrm{Im}(\varepsilon) \neq 0$. The electric field distribution is given by $\mathbf{E} = -\nabla\phi$:

$$\begin{aligned} \mathbf{E_{in}} &= \frac{3\varepsilon_m}{\varepsilon + 2\varepsilon_m}\mathbf{E_0}, \\ \mathbf{E_{out}} &= \mathbf{E_0} + \frac{3\mathbf{n}(\mathbf{n}\cdot\mathbf{p}) - \mathbf{p}}{4\pi\varepsilon_0\varepsilon_m r^3}. \end{aligned} \tag{1.58}$$

Thus, resonant condition in α implies an enhancment for both the internal and the external electric field. Now we can restore the harmonic time dependence of the electric field, keeping in mind that the spatial retardation effects over the whole nanoparticle volume

are neglected because of the quasi-static approximation. Thus, from (1.55) the oscillating electric field $\mathbf{E} = \mathbf{E_0} e^{-i\omega t}$ induces an oscillating dipole moment $\mathbf{p} = e p_0 \varepsilon_m \alpha \mathbf{E_0} e^{-i\omega t}$. The radiation of this dipole leads to scattering of the plane wave by the sphere, which can be represented as radiation by a point dipole. We recall that the total fields $\mathbf{H}(t) = \mathbf{H} e^{-i\omega t}$ and $\mathbf{E}(t) = \mathbf{E} e^{-i\omega t}$ emitted by an oscillating dipole are [50]:

$$\begin{aligned} \mathbf{H} &= \frac{ck^2}{4\pi}(\mathbf{n}\times\mathbf{p})\frac{e^{ikr}}{r}\left(1-\frac{1}{ikr}\right), \\ \mathbf{E} &= \frac{1}{4\pi\varepsilon_0\varepsilon_m}\left\{k^2(\mathbf{n}\times\mathbf{p})\times\mathbf{n}\frac{e^{ikr}}{r} + [3\mathbf{n}(\mathbf{n}\cdot\mathbf{p})-p]\left(\frac{1}{r^3}-\frac{ik}{r^2}\right)e^{ikr}\right\}, \end{aligned} \tag{1.59}$$

with $k = 2\pi/\lambda$ and $\mathbf{n}$ is the unit vector. In the near region $kr \ll 1$ the magnetic field is:

$$\mathbf{H} = \frac{i\omega}{4\pi}(\mathbf{n}\times\mathbf{p})\frac{1}{r^2}, \tag{1.60}$$

and the electric field reduces to the static solution

$$\mathbf{E} = \frac{3\mathbf{n}(\mathbf{n}\cdot\mathbf{p})-\mathbf{p}}{4\pi\varepsilon_0\varepsilon_m r^3}. \tag{1.61}$$

In the near field region, the electric field is predominant since the magnitude of the magnetic field is smaller of a factor $\sqrt{\frac{\varepsilon_0}{\mu_0}}kr$. In the radiation zone where $kr \gg 1$ the dipole fields have the typical spherical-wave form:

$$\mathbf{H} = \frac{ck^2}{4\pi}(\mathbf{n}\times\mathbf{p})\frac{e^{ikr}}{r}, \tag{1.62}$$

$$\mathbf{E} = \sqrt{\frac{\mu_0}{\varepsilon_0\varepsilon_m}}\mathbf{H}\times\mathbf{n}. \tag{1.63}$$

Under these circumstances, the nanoparticle acts as an electric dipole, absorbing and scattering electromagnetic fields in a resonant condition. In the quasi-static approximation, the scattering and absorption cross sections assume the following form:

$$\sigma_{sca} = \frac{k^4}{6\pi}|\alpha|^2 = \frac{8\pi}{3}k^4\alpha^6\left|\frac{\varepsilon-\varepsilon_m}{\varepsilon+2\varepsilon_m}\right|^2, \tag{1.64}$$

$$\sigma_{abs} = k\mathrm{Im}[\alpha] = 4\pi k a^3\,\mathrm{Im}\left\{\frac{\varepsilon-\varepsilon_m}{\varepsilon+2\varepsilon_m}\right\}, \tag{1.65}$$

where in the first equalities the relation between α and the absorption and scattering cross sections is provided through the Optical Theorem [55]. The extinction cross section given by $\sigma_{ext} = \sigma_{sca} + \sigma_{abs}$ is (Fig. 1.13(b)):

$$\sigma_{ext} = 9V\frac{\omega\varepsilon_m^{3/2}}{c}\frac{\mathrm{Im}\{\varepsilon\}}{[\mathrm{Re}\{\varepsilon\}+2\varepsilon_m]^2+\mathrm{Im}\{\varepsilon\}^2}, \tag{1.66}$$

where V is the volume of the spherical nanoparticle. All these cross sections are valid for metal as well as dielectric scatters.

For a sphere consisting of a Drude metal with a dielectric function (1.25) located in a medium of dielectric constant ε_{medium}, the Fröhlich's criterion is fulfilled at the frequency:

$$\omega_{LSPR} = \sqrt{\frac{\omega_p}{2\varepsilon_{medium} + 1}}. \tag{1.67}$$

The equation (1.67) states that the LSPR resonance strongly depends on the dielectric environment. In particular, the ω_{LSPR} red-shifts as the dielectric constant of the medium ε_{medium} increases. The dependence on ε_{medium} is approximately linear over small ranges of the refractive index at optical frequencies [56].

We finally observe that the LSPR strong dependence on the refractive index of the surrounding medium is the reason why the effect is employed for colorimetric plasmonic sensors [1]. Fig. 1.13(c) shows the sketch of the typical color change of colloidal solutions of gold nanoparticles caused by the red-shift of the LSPR and exploited by colorimetric plasmonic biosensors.
The effect of the LSPR is also concentrating the incident electromagnetic field in proximity of the nanostructure. The concentrated local electromagnetic field can interact with some optical processes such as fluorescence. In this case the resulting effect is the plasmon-enhanced fluorescence as we will see in Chapter 3.

1.3.7 Mie theory

When particle dimensions are comparable with the wavelength of the incident radiation we have to take into account that electromagnetic field experienced by the particle is not constant over its whole volume. Thus, the quasi-static approximation fails. An alternative approach is given by the Mie's theory. It consists in studying the scattering fields produced by a plane wave incident on a conducting sphere in a linear, isotropic, and homogeneous medium. To do that is convenient to introduce the spherical harmonics and the spherical vector harmonics, in order to decompose the incident field and then derive an expression for the field in proximity of the spherical particle. Let ψ the scalar wave function that solve the Helmholtz equation:

$$\Delta\psi(\mathbf{r}) + k^2\psi(\mathbf{r}) = 0 \tag{1.68}$$

Every solution of this equation can be written a series of the ψ^{even} and ψ^{odd} that indeed are basis of solutions:

$$\psi^{even}_{\ell m} = \cos(m\phi)P^m_\ell(\cos\theta)z_l(kr) \tag{1.69}$$
$$\psi^{odd}_{\ell m} = \sin(m\phi)P^m_\ell(\cos\theta)z_l(kr) \tag{1.70}$$

where P^ℓ_m are Legendre functions of the first kind of degree ℓ and order m and the symbol z_l refers to the spherical Bessel functions j_n, y_n, $h^{(1)}_n$, $h^{(2)}_n$. In particular, two possible solutions of the equation (1.68), restoring the harmonic time dependence, can be written

as:

$$u = e^{-i\omega t}\cos(\phi)\sum_{\ell=1}^{\infty}(-i)^{\ell}\frac{2\ell+1}{\ell(\ell+1)}P_{\ell}^{1}(\cos\theta)j_{\ell}(kr), \tag{1.71}$$

$$v = e^{-i\omega t}\sin(\phi)\sum_{\ell=1}^{\infty}(-i)^{\ell}\frac{2\ell+1}{\ell(\ell+1)}P_{\ell}^{1}(\cos\theta)j_{\ell}(kr). \tag{1.72}$$

The Mie solution inside and outside the sphere can be found by imposing the boundary conditions on the sphere's surface at infinite distance. In the two sets of solution different type of Bessel functions appear. This comes from the imposition of the proper boundary conditions. Thus we have outside the sphere [57]:

$$u = e^{-i\omega t}\cos(\phi)\sum_{\ell=1}^{\infty}a_{\ell}(-i)^{\ell}\frac{2\ell+1}{\ell(\ell+1)}P_{\ell}^{1}(\cos\theta)h_{\ell}(kr), \tag{1.73}$$

$$v = e^{-i\omega t}\sin(\phi)\sum_{\ell=1}^{\infty}b_{\ell}(-i)^{\ell}\frac{2\ell+1}{\ell(\ell+1)}P_{\ell}^{1}(\cos\theta)j_{\ell}(kr), \tag{1.74}$$

where h_ℓ are the Hankel functions, and inside the sphere:

$$u = e^{-i\omega t}\cos(\phi)\sum_{\ell=1}^{\infty}c_{\ell}(-i)^{\ell}\frac{2\ell+1}{\ell(\ell+1)}P_{\ell}^{1}(\cos\theta)j_{\ell}(kr), \tag{1.75}$$

$$v = e^{-i\omega t}\sin(\phi)\sum_{\ell=1}^{\infty}d_{\ell}(-i)^{\ell}\frac{2\ell+1}{\ell(\ell+1)}P_{\ell}^{1}(\cos\theta)j_{\ell}(kr), \tag{1.76}$$

where a_ℓ, b_ℓ, c_ℓ, d_ℓ are the Mie's coefficients.

We can introduce two vectors $\mathbf{M}$ and $\mathbf{N}$ that solve the vector wave equation

$$\nabla\nabla\cdot\mathbf{C} - \nabla\times\nabla\mathbf{C} + k^2\mathbf{C}^2 = 0, \tag{1.77}$$

so that in the end the electric and the magnetic fields can be expressed in terms of these solutions. These vector wave functions are defined as:

$$\mathbf{M} = \nabla\times(r\psi), \qquad \mathbf{N} = \frac{1}{k}\nabla\times\mathbf{M}. \tag{1.78}$$

The time factor is reintroduced with the harmonic time dependence by writing $\mathbf{M} = \mathbf{m}e^{-i\omega t}$ and $\mathbf{N} = \mathbf{n}e^{-i\omega t}$. With these definitions we find the spherical vector wave functions [57]:

$$\mathbf{m}_{01n} = \frac{j_n(kr)}{\sin\theta} P_n^1(\cos\theta)\cos\phi\mathbf{e}_\theta - j_n(kr)\frac{\partial P_n^1}{\partial\theta}\sin\phi\mathbf{e}_\phi, \tag{1.79}$$

$$\mathbf{m}_{e1n} = -\frac{j_n(kr)}{\sin\theta} P_n^1(\cos\theta)\sin\phi\mathbf{e}_\theta - j_n(kr)\frac{\partial P_n^1}{\partial\theta}\sin\phi\mathbf{e}_\phi, \tag{1.80}$$

$$\begin{aligned}\mathbf{n}_{e1n} =& \frac{n(n+1)}{kr} j_n(kr) P_n^1(\cos\theta)\sin\phi\mathbf{e_r} + \frac{1}{kr}[krj_n(kr)]'\frac{\partial P_n^1}{\partial\theta}\mathbf{e}_\theta \\ &+ \frac{[krj_n(kr)]}{kr\sin\theta} P_n^1(\cos\theta)\cos\phi\mathbf{e}_\phi,\end{aligned} \tag{1.81}$$

$$\begin{aligned}\mathbf{n}_{01n} =& \frac{n(n+1)}{kr} j_n(kr) P_n^1(\cos\theta)\cos\phi\mathbf{e_r} + \frac{1}{kr}[krj_n(kr)]'\frac{\partial P_n^1}{\partial\theta}\mathbf{e}_\theta \\ &+ \frac{[krj_n(kr)]}{kr\sin\theta} P_n^1(\cos\theta)\sin\phi\mathbf{e}_\phi,\end{aligned} \tag{1.82}$$

where $\mathbf{e}_r$, $\mathbf{e}_\theta$, $\mathbf{e}_\phi$ are the unit vectors in spherical coordinates and the labels 0, e stand for *odd* and *even*, and the prime indicates the derivative with respect to the argument kr. From the previous equations, the incident field $\mathbf{E_i}$ and the fields inside the sphere E_t and outside the sphere E_r expressed in spherical harmonics are [57]:

$$\mathbf{E_i} = E_0 e^{-i\omega t}\sum_{n=1}^{\infty} i^n \frac{2n+1}{n(n+1)}[\mathbf{m_{01n}^{(1)}} - \mathbf{n_{e1n}^{(1)}}], \tag{1.83}$$

$$\mathbf{E_t} = E_0 e^{-i\omega t}\sum_{n=1}^{\infty} i^n \frac{2n+1}{n(n+1)}[a_n^t\mathbf{m_{01n}^{(1)}} - b_n^t\mathbf{n_{e1n}^{(1)}}], \tag{1.84}$$

$$\mathbf{E_r} = E_0 e^{-i\omega t}\sum_{n=1}^{\infty} i^n \frac{2n+1}{n(n+1)}[a_n^r\mathbf{m_{01n}^{(3)}} - ib_n^r\mathbf{n_{e1n}^{(3)}}]. \tag{1.85}$$

The functions $\mathbf{m_{01n}^{(3)}}$ and $\mathbf{n_{e1n}^{(3)}}$ are obtained by the expressions in (1.80) and (1.82) by replacing $j_n(kr)$ with Hankel functions $h_n(kr)$. The corresponding scattering, extinction, and absorption cross sections result from the Optical Theorem [58]:

$$\begin{aligned}\sigma_{sca} &= \frac{2\pi}{|k|^2}\sum_{l=1}^{\infty}(2l+1)(|a_l|^2 + |b_l|^2), \\ \sigma_{ext} &= \frac{2\pi}{|k|^2}\sum_{l=1}^{\infty}(2l+1)\mathrm{Re}\{a_l + b_l\}, \\ \sigma_{abs} &= \sigma_{ext} - \sigma_{sca},\end{aligned} \tag{1.86}$$

where l represents the multipole order of the scattering.

1.3.8 Coupled Localized Surface Plasmons

In an assembly of proximal metal nanoparticles, the LSPR is strongly affected by the near-field coupling of the resonances of the individual particles.
The arising coupled modes are called coupled-LSPs (c-LSPs) and can offer a strong electric field enhancement and confinement at the inter-particle gaps whenever they resonate

with the external perturbation [59].
Generally, the resonant conditions for c-LSPR take place for wavelengths that are red-shifted or blue-shifted with respect to LSPR wavelengths of the corresponding individual-nanoparticle. These phenomena have been described by applying the plasmon hybridization method to dimers of nanoparticles [60],[61]. According to the model, when the inter-particle gap is of few nanometers, the LSPs modes of individual particle mix and give rise to bonding and anti-bonding hybrid plasmon modes [62].

When the external radiation is linearly polarized along the dimer axis (longitudinal polarization), a lower energy (or bonding) mode σ results from the in-phase coupling of the individual particle dipoles, whereas a higher energy (or anti-bonding) mode $\sigma*$ results from the out-of-phase dipolar coupling [62]. Thus, σ ($\sigma*$) modes occur at c-LSPR wavelengths λ_{c-LSP} that are red-shifted (blue-shifted) with respect that of the individual particle LSPR [63].
Furthermore, the σ mode is associated with a strong enhancement of electric field (hot spots) at the dimer gap while the $\sigma*$ mode exhibits a stronger field confinement at the dimer edges.

Conversely, if the polarization is orthogonal to the dimer axis (transverse polarization), a lower energy (or bonding) mode π (red-shifted) is associated to the out-of-phase dipolar coupling, whereas a higher energy (or anti-bonding) mode $\pi*$ (blue-shifted) is associated to the in-phase dipolar coupling [63].

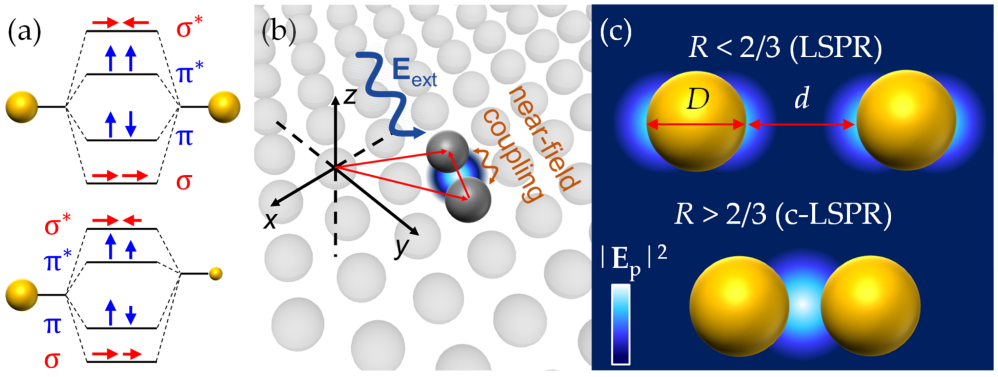

Figure 1.14: (a) Schematic representation of the plasmon hybridization model. (b) Sketch of the near-field coupling among two neighbouring nanoparticles in a two-dimensional hexagonal lattice. (c) Schematic illustration of the electric field enhancement in the case of LSPR mode and c-LSPR mode for a homodimer configuration (from [4])

Fig. 1.14(a) shows a graphical representation of the plasmon hybridization model in the case of a homodimer (i.e., two equivalent nanoparticles) as well as a heterodimer (i.e., two non-equivalent nanoparticles).
It is worth noting that a linearly polarized light cannot excite the out-of-phase modes $\sigma*$ and π in a homodimer (dark modes), but specific illuminations such as a focused cylindrical vector beam can [64].
However, $\sigma*$ and π modes are allowed by the heterodimer configuration (under linearly polarized light) and, in this case, they are characterized by weaker intensities than σ and

$\pi*$ in-phase modes. These facts can readily be addressed by the dipole-dipole model (in the quasi-static approximation): the oppositely oriented dipole moments neutralize each other (dark modes) in the case of homodimers while an incomplete cancellation takes place for heterodimer (Fig. 1.14(a)) [62].

In the case of a 2D nanoparticle array, the plasmonic behavior in a first approximation depends on the ratio between the nanoparticle diameter D and the inter-particle distance d, $R = D/d$ (Fig. 1.14b)).
In particular, when $R > 2/3$ their LSPs do couple through near-field interactions and give rise to c-LSP modes [65](Fig. 1.14(c)). On the contrary, if $R < 2/3$ the couplings are negligible and the optical response of the array is well-described by a system of decoupled LSPs [65]. These properties can be recovered from the following semi-empirical relation for resonance shift of a nanoparticle dimer Δ/λ_{c-LSPR} [66]:

$$\frac{\Delta\lambda_{c-LSP}}{\lambda_{c-LSP}} = ke^{\frac{d}{\ell_d}}, \tag{1.87}$$

where k is the maximum c-LSPR shift for the dimer and ℓ_d is the decay length of the c-LSP. By varying the inter-particle distance between two metal nanoparticles through lithographic techniques, it resulted that c-LSP decay length ℓ_d can be approximated as $\ell_d \sim D/5$ [67]. Therefore, there is the concrete possibility to tune the optical response of a nanostructure by tailoring the array pattern. This potentially makes the c-LSPR-based platforms a versatile tool for biosensing applications [4, 68].

Chapter 2

Magnetoelastic biosensor

Contents

2.1 Introduction

Recently, among the magnetic biosensors [69], magnetoelastic materials (ME) have emerged as interesting acoustic-wave transducers for development of high-sensitive biosensors [70]. ME sensors can be placed in a vibration condition due to magnetostriction effect, at the characteristic resonance frequency f_0, employing time-varying magnetic fields.
The attaching of a small mass to the surface of the material involves a shift of the resonance frequency, which can therefore be used as sensing parameter. In fact, the mass addition dampens the resonance behavior of the resonant sensor.
The principal competitive advantage of ME biosensors is that they are wireless, namely there is no physical connection between the detection electronics and the sensor. Wireless sensing turns out to be a very interesting feature for applications as point of care testing, especially by considering that most of the other devices require complex wiring for power and measurement.
Furthermore, ME transducers are composed by a low-cost raw material, and their compact size make them suitable for multiplexing schemes. However, sensitivity remains the main drawback of these transducers. Recent attempts to enhance sensitivity rely on several strategies such as the reduction of the size of ME platforms [71], and the amplification of the signal response by using gold nanoparticles [72].
It should be noted that the attempt of reducing the dimension of sensor platforms is limited by manufacturing difficulties and loss of the intensity of the signal that occur when the microscale is reached [73, 74].
Gold nanoparticles (AuNPs) are widely used in biosensing due to their high chemical stability, biocompatibility and large specific surface area on which bioreceptors such as Abs can be properly immobilized. In the case of a ME sensor, the amplification of the response signal via AuNPs exploits the typical sandwich-assay scheme, in which AuNPs, functionalized with bioreceptors (e.g., Abs), bind to the target-bioreceptor pair (e.g., antigen-Ab) on the sensor surface. Thus, the mass loading on the ME sensor surface increases, enhancing its sensitivity of detection.
Besides AuNPs, magnetic nanoparticles have also found application as signal labels in biosensing systems, such as molecular detection and related strategies that rely on ligand-receptor binding. In particular, iron oxide magnetic nanoparticles (NPs) are particularly appealing due to their magnetic properties, tunable size, biocompatibility, and greater ease of synthesis than other magnetic materials [13, 14]. Indeed, recent studies have shown how to use magnetic nanoparticles to improve the efficiency of the functionalization process [75], to realize multiplexing immunoassays [76] and for magnetic detection [69, 77, 78].

In this chapter, we describe how core@shell magnetic nanoparticles, Fe_3O_4@AuNPS, i.e., made of gold nanoflower grown on a magnetic core, can be used to amplify the signal from a ME biosensor for wireless detection of contaminants in liquid [1].
The use of the magnetic properties of nanoparticles is a current and relevant topic for scientific community, although the tendency to aggregation is an obstacle to their applications. In our case, gold coating and the functionalization protocols employed for signal amplification have also the effect to prevent the Fe_3O_4NPS aggregation, so that other complex and time-consuming techniques can be avoided [78, 79].
The sensor platform is a inexpensive and commercially available ME material (Metglas

2826), shaped in a ribbon of small size (6mm x1mm x30μm). We propose the synergy of two strategies to increase the performance of this sensor:

- a new amplification procedure that exploits gold coated nanoparticles with magnetic core;
- the use of reliable, quick and easy-to-use antibody functionalization procedure.

We observed that the signal amplification obtained with gold coated nanoparticles with magnetic core (Fe_3O_4@AuNPS) was significantly higher than that obtained using AuNPs, although the nanoparticles' mass was the same. The fact that in our case both the magnetic sensitive platform and magnetic nanoparticles contribute to the measurements process is an element of novelty in comparison with standard configurations widely discussed in literature [80, 81].
It should be noted that the amplification of the shift of the resonance frequency of the ME sensor is due to the mass of magnetic nanoparticles and does not depend directly on their magnetic properties. Indeed, the advantage of the magnetic core of the nanoparticles relies in its coupling with the local magnetic field, which in turn leads to an increase of the local density at proximity of the ribbon surface. Such an effect can be well understood by working out the magnetic field produced by the magnetized ribbon and comparing its action on a magnetic nanoparticle with the thermal energy (Brownian motion).
Regarding the functionalization procedure, the photochemical immobilization technique (PIT) recently introduced [12] not only was used for the first time to functionalize a ME material (coated with gold), but also the gold nanoflowers grown on the magnetic nanoparticles.

The experimental results show that the proposed ME biosensor has a reliable stability in liquid, a quick response to antigen exposure and exhibits a limit of detection (LOD) lower than 1 nM.

2.2 Magnetoelasticity

2.2.1 Origin of magnetoelasticity

Elastic and magnetic properties of materials are related. When a material is exposed to a magnetic field its dimension changes; on the other hand when a stress is applied to the material, a change in its magnetization occurs. The previous effects go under the name of magnetoelastic (magnetostrictive) effect and inverse magnetoelastic (magnetomechanical) effect. While these effects are usually negligible in most materials, their entity is particularly evident in some types of metallic glasses. We shall focus on the magnetostrictive effect.
The magnetostrictive effect is due to the spin-orbit coupling of the electrons [36]. The rough picture is that the magnetoelastic strain $\lambda = \Delta L/L$ follows from the reorientation of the electrons' spins according to the orientation of the external magnetic field together with a deformation of the electrons' clouds, as schematically depicted in Fig. 2.1.

The order of magnitude of the magnetostriction is 1-10 of parts per million (ppm). For example, for the ME material employed in this work (Metglas 2826) λ is about $1.1 \cdot 10^{-5}$,

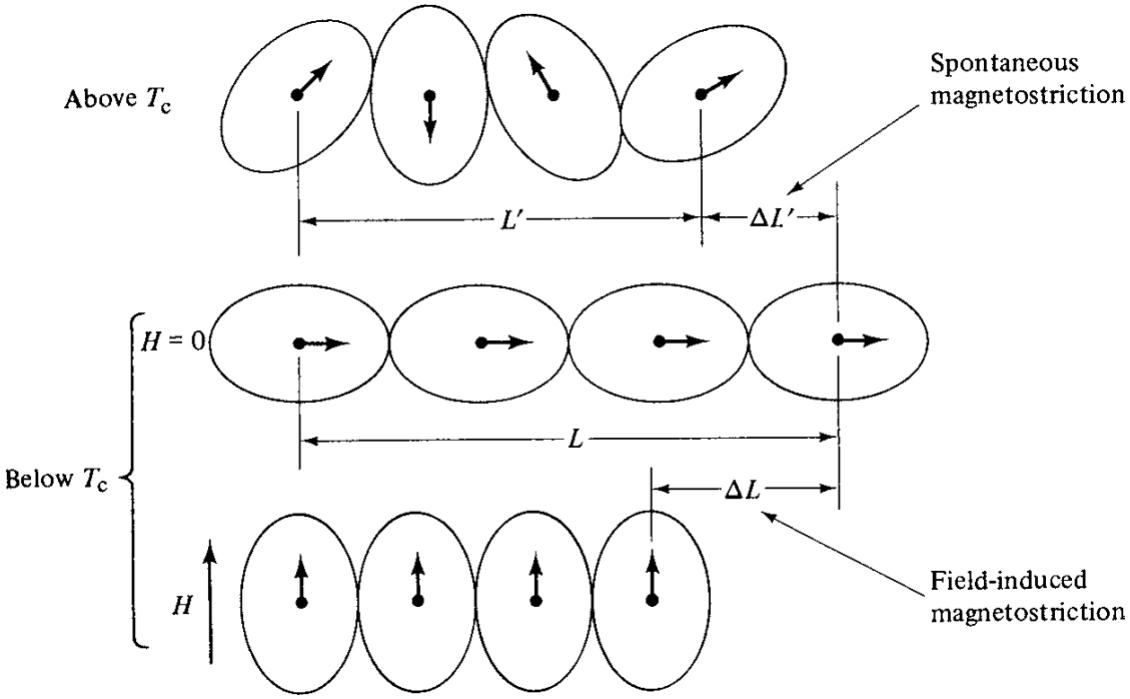

Figure 2.1: The relation between magnetostriction and spin-orbit coupling. The black dots represent atomic nuclei, the oval line the electrons' clouds, the arrows the net magnetic moment per atom. The upper figure shows the row of atom in the paramagnetic state above the Curie temperature T_C. Assuming for simplicity that the spin orbit coupling is very strong, the spontaneous magnetization occurring below T_C would cause a rotation of the spins and the electron clouds in accordance with the crystal anisotropy. Then applying a field $\mathbf{H} \neq 0$ strong enough the spins and the electron clouds would rotate causing a magnetostrictively strain by an amount $\Delta L/L$. Adapted from [36].

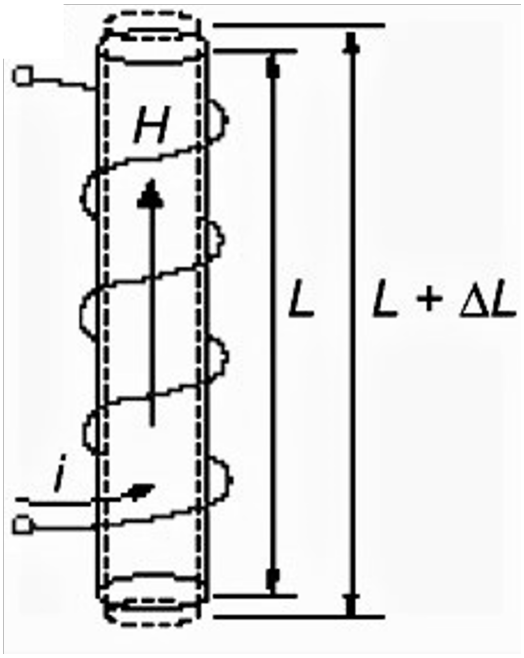

Figure 2.2: Schematic representation of the magnetostrictive effect. A ME ribbon is subjected to an external magnetic field generated by a coil. The ME strain is $\lambda = \Delta L/L$. Adapted from [82].

that is 66 μm for a 6 mm long ribbon as the ones we used in this this work [1].
When a time depending magnetic field is applied to a ME ribbon, longitudinal elastic vibrations occur due to the time varying strain (Fig. 2.2).

We will illustrate in the next section the thermodynamic description of the magnetostriction aiming at deriving the acoustic wave equations and the characteristic resonant frequencies of the ME ribbon.

2.2.2 Metallic glasses

ME transducers are generally thick film strips made from amorphous ferromagnetic alloys. Amorphous metallic solids are noncrystalline materials generally obtained by cooling down a liquid alloy quickly enough to avoid crystallization.

The usual production method is called melt spinning, and employs very high cooling rate of about $10^5 - 10^6$ K/sec that are essential to reach the glassy state [36]. The microscopic structure that emerges from the rapid solidification reveals the absence of any long-range order, almost like the snapshot of a liquid phase. Generally, the final product resulting from industrial fabrications is a thin ribbon about $20 - 50\,\mu$m thick with meters or kilometers of length (Fig. 2.4). Typical compositions are given $70 - 90\%$ of transitions metals and $10 - 20\%$ additional substances. For magnetic applications the transition metals preferred are Fe, Co and Ni. The other components may be metalloids as Si and B that are necessary for the glass formation and refractory metals like Nb, Mo [84].

Metallic glasses are distinguished in two main categories, the Co-based and the Fe-based amorphous alloys. The former have a superior soft magnetic behaviour and for some compositions almost zero magnetostriction, the latter are characterized by high saturation

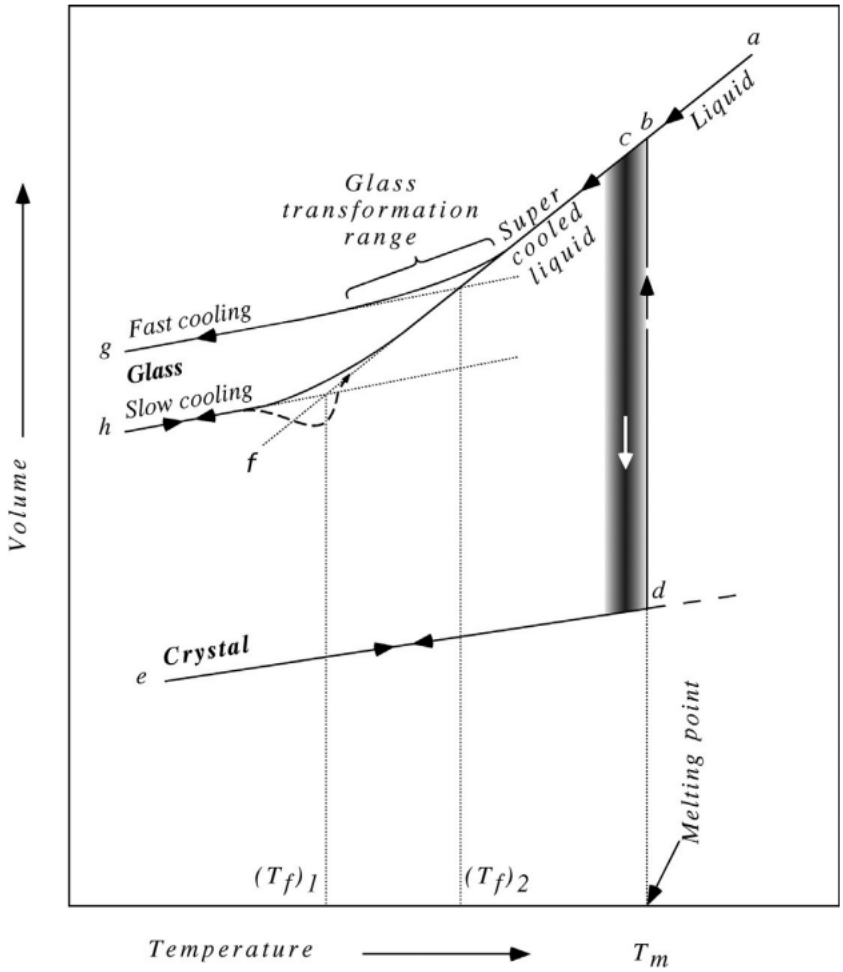

Figure 2.3: Volume-Temperature diagram. From right to left, T_m is the melting temperature of the liquid. Lowering the temperature, if the cooling rates are high enough, the crystallization does not occur and the material enter the *supercooled liquid* phase. T_{f1} and T_{f2} are two fictive temperature at which the liquid enter the *glassy state*. These temperatures are by definition the intersections between the glassy state line and the liquid line. (Adapted from [83])

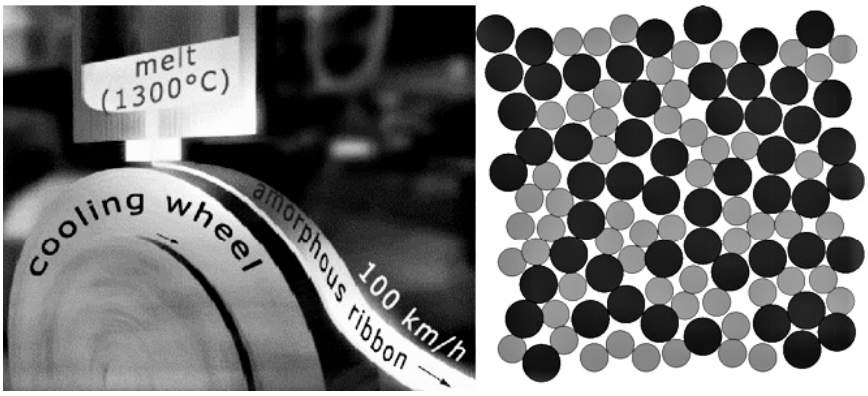

Figure 2.4: On the left: fabrication of an amorphous metallic shaped in a thin ribbon. On the right: schematic representation of the noncrystalline atomic structure. (Adapted from [84])

magnetization and a relevant magnetostriction [84]. ME sensors are based on Fe-based amorphous alloys. In this work we adopted the Metglas 2826 alloy whose composition is $Fe_{40}Ni_{40}P_{14}B_6$. A detailed description of the amorphous solids metals and their fabrication goes beyond the scope of this work. For a complete discussion on amorphous metals we refer the reader to [85].

2.2.3 Acoustic wave equation of magnetoelastic ribbons

Following the classical elasticity theory, we describe a ME material as a deformable and continuous medium subjected to a magnetic field $\mathbf{H}$ and to a mechanical force for unit volume $\mathbf{F}$ that causes a shear stress. Generally, when the body is deformed the coordinates $\mathbf{x}$ of each point of the body go under a transformation $\mathbf{x} \rightarrow \mathbf{x}'$. We call *deformation vector* $\mathbf{u}$ the vector that represents the difference between the object's configuration under a deformation and its natural state whose coordinates are $u_i = x_i' - x_i$ with $i = x, y, z$.
Let $U(S, \gamma, B)$ be the internal energy of the ME material and $\{S,\ \gamma,\ B\}$ the entropy, the strain and the flux density of the magnetic field, respectively. From the first law of thermodynamics:

$$dU = \delta L + \delta Q \tag{2.1}$$

where δL is the infinitesimal work done by an external force applied to the system per unit volume and δQ the heat absorbed per unit volume by the system. For a reversible transformation, $dQ = TdS$ where T is the temperature. The force $\mathbf{F}$ acting on the material and causing the shear stress can be written as the divergence of the shear tensor $F_i = \frac{\partial \tau_{ij}}{\partial x_j}$ by using the typical definition of stress tensor [86]. The infinitesimal work of the force applied to the material can be shown to be $\tau_{ij} d\gamma_{ij}$ where γ_{ij} is the symmetric part of the Jacobian matrix of the deformation vector $\mathbf{u}$:

$$dU = T\delta S + \tau_{ij} d\gamma_{ij} + H_i dB_i, \tag{2.2}$$

and

$$\left(\frac{\partial U}{B_i}\right)_{\gamma_{kl}} = H_i, \quad \left(\frac{\partial U}{\gamma_{ij}}\right)_{B_k} = \tau_{ij}. \tag{2.3}$$

The third-order tensors known *ME coefficients* can now be defined as follows:

$$\left(\frac{\partial H_k}{\partial \gamma_{ij}}\right)_{B_l} = \left(\frac{\partial \tau_{ij}}{\partial B_k}\right)_{\gamma_{mn}} = -h_{ijk}, \tag{2.4}$$

$$-\left(\frac{\partial H_k}{\tau_{ij}}\right)_{B_l} = \left(\frac{\partial \gamma_{ij}}{B_k}\right)_{\tau_{mn}} = g_{ijk}, \tag{2.5}$$

$$\left(\frac{\partial B_k}{\tau_{ij}}\right)_{H_l} = \left(\frac{\partial \gamma_{ij}}{H_k}\right)_{\tau_{mn}} = d_{ijk}, \tag{2.6}$$

$$\left(\frac{\partial B_k}{\gamma_{ij}}\right)_{H_l} = \left(\frac{\partial \tau_{ij}}{H_k}\right)_{\gamma_{mn}} = e_{ijk}. \tag{2.7}$$

By sing the previous relations one can retrieve all the constitutive equations of magnetoelasticity under the hypothesis of small perturbations. Here we only report the ones that will be further needed for deriving the acoustic wave equations [87]:

$$\begin{aligned} \gamma_{ij}(\tau_{mn}, H) &= s^{H_k}_{ijmn}\tau_{mn} + d_{ij}H_l, \\ B_i(\tau_{mn}, H) &= d_{imn}\tau_{mn} + \mu^{\gamma_{kh}}_{il}H_l, \end{aligned} \tag{2.8}$$

where $s^{H_k}_{ijmn}$ and $\mu^{\gamma_{kh}}_{il}$ are called the specific elastic compliance and permeability, respectively, and by definition:

$$s^{H_k}_{ijmn} = \frac{\partial \gamma_{ij}}{\partial \tau_{mn}}_{B_k}, \qquad \mu^{\gamma_{kh}}_{il} = \frac{\partial B_i}{\partial H_l}.$$

These equations describe small magnetostrictive deformations induced by magnetic fields and stresses for which the material's response is linear and quasi reversible. The amorphous ferromagnetic materials can verify this condition due to their soft magnetic properties [88]. In particular, the linearity condition for the magnetoelastic effect is satisfied for values of the external polarizing field $\mathbf{H}$ close to the inflection point of the magnetoelastic strain curve $\lambda(\mathbf{H})$ (Fig. 2.5).

From the constitutive equations (2.8) we can derive the equations of motion for the displacement vector $\mathbf{u}$. For simplicity we assume that the ME material is thin road lying along the $\hat{z}$-axis and $\mathbf{H} = H_z\hat{z}$ [87] [89]:

$$(s^{-1}_{zz})\left(\frac{\partial^2 u_z}{\partial z^2} - d_{zz}\frac{\partial H}{\partial z}\right) = \rho\frac{\partial^2 u_z}{\partial t^2}, \tag{2.9}$$

where ρ is the density of the ME material. Considering the relations (2.3), we get the wave equation:

$$(s^{-1}_{zz})(1 - e_{zz}gzz)\frac{\partial^2 u_z}{\partial z^2} = \rho\frac{\partial^2 u_z}{\partial t^2}. \tag{2.10}$$

The velocity of propagation for these longitudinal vibrations is:

$$v = \sqrt{\frac{(s^{-1}_{zz})(1 - e_{zz}gzz)}{\rho}} = \sqrt{\frac{E}{\rho}}, \tag{2.11}$$

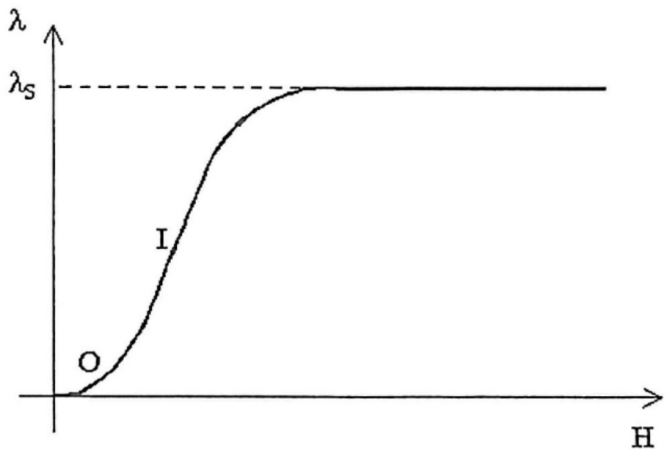

Figure 2.5: Sketch of of the magnetoelastic strain λ versus the applied magnetic field H for an amorphous ferromagnetic material. The strain at saturation is λ_S. I is the inflection point of the curve.

where E is the Young modulus. By imposing the free-standing boundary conditions $\partial_z u_z = 0$ the following harmonic frequencies are obtained:

$$f_n = \frac{n}{2L}\sqrt{\frac{E}{\rho}}, \tag{2.12}$$

where L is the length of the rod and n is an integer. When the thin rod approximation fails but still the thickness and the width of the ME material are significantly smaller than the length, we can rather use the plane strain approximation. In plane strain approximation the Young's modulus becomes $E/(1-\nu^2)$ where ν is Poisson's ratio ([90]) yielding to the following expression for the harmonic frequencies :

$$f_n = \frac{n}{2L}\sqrt{\frac{E}{\rho(1-\nu^2)}}. \tag{2.13}$$

For instance, for the ME material used in this work (Metglas alloy 2826) the Poisson's ratio ν is approximately 0.33 .

Oscillations in liquids

In this work we use a ribbon shaped ME material immersed in liquid environment. In air the fundamental resonance frequency of a ribbon for which the plane strain approximation applies is:

$$f_0 = \frac{1}{2L}\sqrt{\frac{E}{\rho(1-\nu^2)}}. \tag{2.14}$$

When immersed in a viscous liquid, the frequency and the amplitude of vibrations reduce due to dissipative shear forces [70]:

$$f_{liq} = f_{air} - \sqrt{\frac{\eta_{liq}\rho_{liq}}{\pi}}\frac{\sqrt{f_{air}}}{2\rho d}, \tag{2.15}$$

where η_{liq} and ρ_{liq} are the dynamic viscosity and density of the liquid and d is the thickness of the ME ribbon.

2.2.4 Effect of mass loading

If a coating of mass ΔM is uniformly applied on the surface of the ME ribbon, the resonance frequency of the mass loaded ribbon with respect to the frequency of the bare (mass M) can be obtained substiting the density of the bare ribbon $\rho = M/(Ad)$ with the density of the loaded ribbon $\rho = (M + \Delta M)/(Ad)$, where A is the cross sectional area and M the mass. Thus, assuming $\Delta M \ll M$ and deriving the expression (2.15) with respect to the mass M, the frequency shift results:

$$\Delta f = f_{loaded} - f_0 = \frac{5f_{liq} - 3f_{air}}{4M}, \tag{2.16}$$

where f_{liq} is the frequency of the bare ribbon in liquid and f_{air} is the frequency of the bare ribbon in air. When temperature, humidity and other environmental parameters cam be considered constant, the resonance frequency change of the ME sensor depends only on the mass loading on its surface.

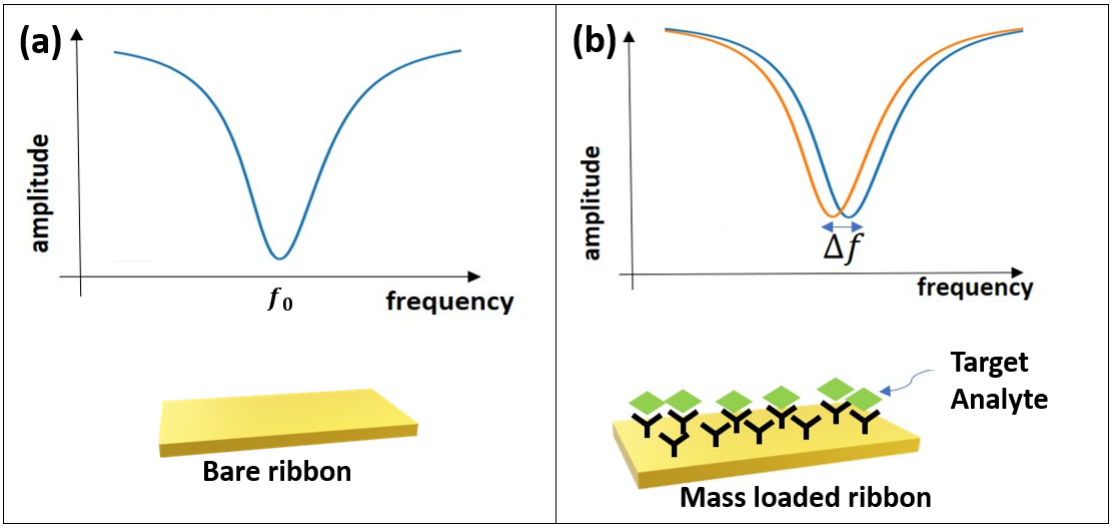

Figure 2.6: Schematic representation of the resonance shift of caused by the mass loading. A bare ribbon has a characteristic f_0 resonance frequency (a) and after the mass loading (represented here by antibodies and antigens) experiences a resonance shift Δf.

2.3 Materials and methods

2.3.1 Magnetoelastic platform

The sensor's platforms composed of Metglas alloy 2826 ($Fe_{40}Ni_{40}P1_4B_6$) were purchased from Honeywell Corporation (Morriston, NJ, USA) in the form of roll and cut in ribbon form with the dimensions 6 mm × 1 mm × 30 μm using a computer-controlled laser cutting machine.

The ME ribbons were ultrasonically cleaned sequentially in ethanol and distilled water each for 20 min, then dried in an inert atmosphere. The surfaces of the cleaned ME ribbons were covered with a layer of titanium (Ti) in thickness of 30 nm, followed by a layer of gold (Au) in thickness of 100 nm. The titanium inner layer was used to improve the adhesion of the gold film on the sensor surfaces, while the gold layer was exploited to enhance the immobilization process of sensing-elements (i.e., antibodies in this study) on the sensor surfaces and also to protect the ME ribbons from corrosion. Compared with other works found in literature [91] polishing and annealing of the ME ribbons were not needed in our procedure.

2.3.2 Surface biofunctionalization

The ME sensor surfaces coated with gold and washed sequentially in ethanol and ultra-pure water were functionalized by means of Abs human IgG produced in Goat, purchased by ImmunoReagents Inc. (Raleigh, NC, USA). The adopted functionalization procedure was the photochemical immobilization technique (PIT) [12] a powerful and rapid methodology based on an appropriate UV-activation of Abs, whose effectiveness was already confirmed in several application for biosensing [92] [31] [32] [33].

The functionalization procedure via PIT involved the following steps: the ME sensor was mounted into a fluidic circuit and immersed in MilliQ water; a quartz cuvette containing 1 mL of Abs dissolved in ultra-pure water 25 μg/mL was irradiated by UV light (lamp Trylight) for 30 s, which is the optimal irradiation time for PIT; since the Abs binding sites remain active for about five minutes, immediately after the irradiation, the activated Abs solution was placed in the fluidic circuit and conveyed onto the ME sensor surfaces.

The solution flowed into the closed fluidic circuit for several minutes.In this study gold nanoparticles AuNPs and core@shell Fe_3O_4@AuNPs were used to amplify the biosensor response, in order to determine, for the same mass of the nanoparticles, whether the magnetic action produces an improvement in the sensitivity of the biosensor.

The functionalization was again achieved by PIT for both types of NPs. A volume of 1 ml of suspended NPs in MilliQ water was prepared, whereas a volume of 100 μl of Abs solution 25 μg/ml irradiated by UV-light for 30 s, was added in twenty spikes (5 μl each) to the NPs solution and gently stirred in order to avoid aggregation. The absorbance spectra of the functionalized NPs, characterized by the UV/vis spectrophotometer (model 6715 Jenway, Cole-Parmer Company, Illinois USA), showed a red-shift of 3 nm of the LSPR wavelength, in accordance with the change of both types of NPs refractive index due to immobilization of antibody onto gold layer [33].

2.3.3 Experimental setup

The ME biosensor was mounted into a fluidic circuit by inserting it in a 3D printed acrylonitrile butadiene styrene (ABS) cell that was subsequently placed in a glass tube to be connected to a fluidic continuous pump (Fig. 2.7). Two identical home-made Helmholtz coils were mounted at a distance equal to their radius and employed to produce a static and uniform magnetic field in the central region between them, where the glass tube, enclosing the ME sensor, was placed. During the experiments the applied static field was

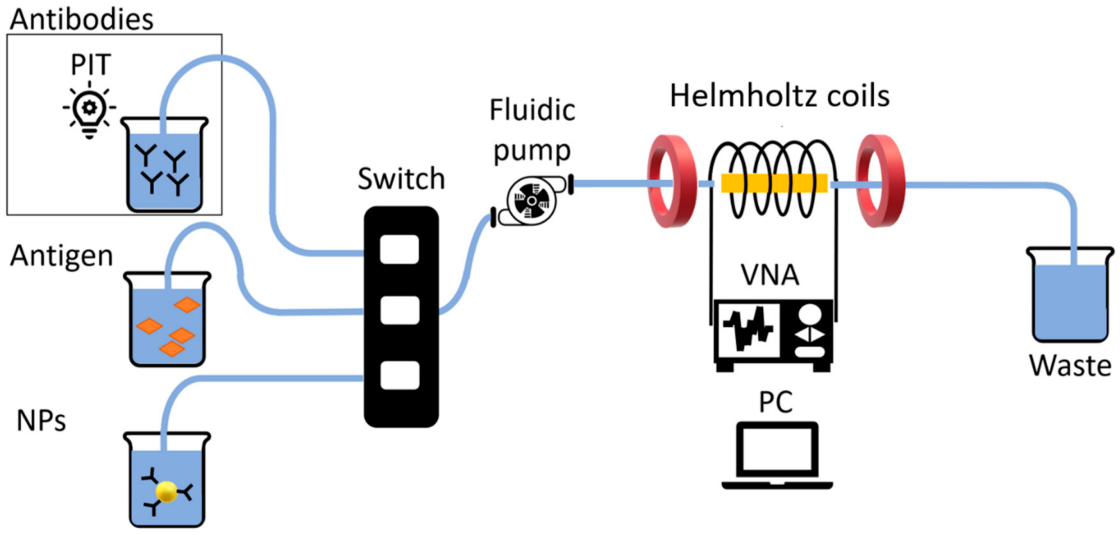

Figure 2.7: Schematic representation of the experimental setup. From left to right: the solution containing antibodies (activated via PIT), antigens and functionalized nanoparticles, fluidic channels and switch, fluidic (continuous) pump, Helmholtz coils, the ribbon enclosed by the cylindrical coil, the VNA connected to the PC and the flash out container (waste). A flow rate of $5\,\mu\text{ls}^{-1}$ was used in order to ensure laminar flow over the ME sensor. Resonance frequencies were continuously monitored and recorded by the analyzer (VNA) and computer system (PC). Finally, the waste analyte was collected in the flush out container for disposal. Reproduced from [1]

approximately 50 Oe (for details see **??**). A vector network analyzer (VNA) (E5071C ENA series, Keysight Technologies, California, USA) was connected to a home-made cylindrical coil wound around the glass tube containing the ME sensor. The cylindrical single layer coil was made with 80 consecutive windings, using a copper wire (diameter of 0.1 mm), for a length of 8 mm and a diameter of 3.5 mm. The VNA operating using S-parameters, was employed to provide an AC field to excite the ribbon and monitor the reflected signal from the cylindrical coil around the sensor. The reflection coefficient S11, i.e., the ratio between the amplitude of the reflected signal and the amplitude of the incident one, is commonly used to monitor the resonance frequency of a ME resonator [70]. In fact, S11 signal reaches its minimum at a frequency corresponding to the resonance frequency, f_0, of the sensor. The error of the experimental setup on a resonance frequency measure, extracted by fitting the signal obtained by the VNA, is of the order of 10^{-2} Hz, much smaller than the error related to stability fluctuation over time of f_0 (3 Hz as estimated in Section 2.3.4).

2.3.4 Experimental procedure

Before starting the sample injection, the fluidic circuits (flow rate of about $5\mu\text{l}\cdot\text{s}^{-1}$) and the ME sensor were rinsed with MilliQ water. A typical sensorgram reporting all the measurement steps is shown in Fig. 2.8. In first step (I) a solution of $25\,\mu\text{l}\cdot\text{s}^{-1}$ of UV-activated antibodies (anti-human IgG produced in goat) was conveyed to the cell for the

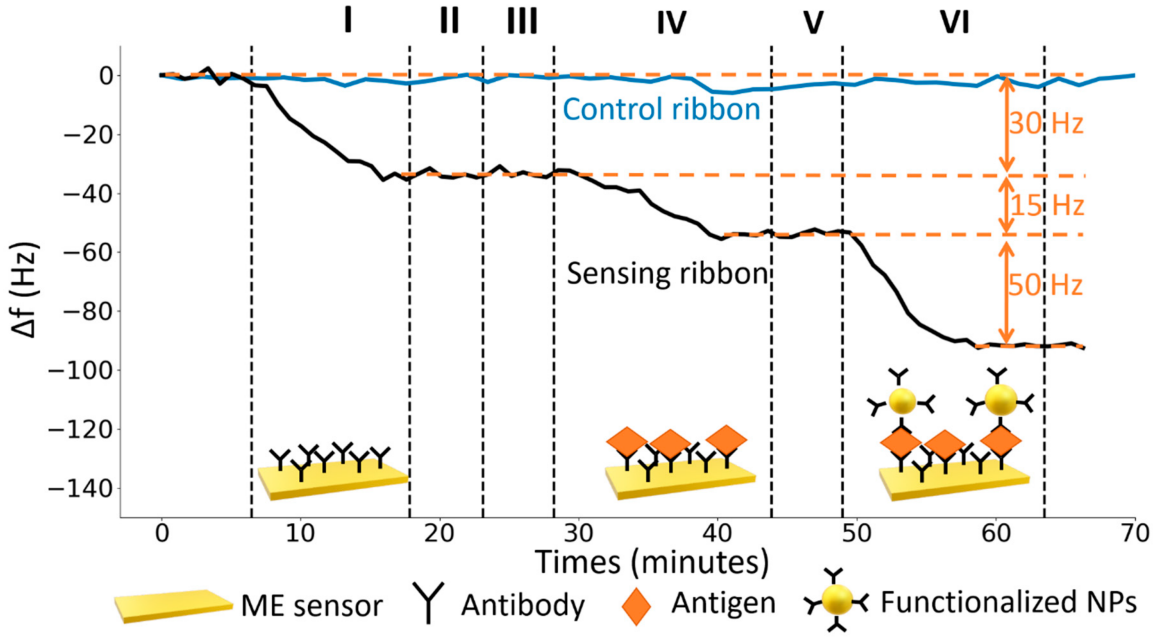

Figure 2.8: Typical dynamic response of the ME biosensor. On the y axis the shift of the resonance frequency f_0 due to the mass loading and on the x axis the time interval. The black line represents the response of the sensing ribbon in each of the following steps: (I) functionalization with a solution of 25 μg/ml of UV-activated antibodies, (II) rinse with MilliQ water, (III) flowing of bovine serum albumin solution (50 μg/ml), (IV) flowing of target antigen solution (5μg/ml), (V) rinse with MilliQ water, (VI) amplification with core@shell magnetic NPs (Fe_3O_4@Au). The control ribbon, that was employed to estimate the noise level, is represented by a blue line. Reproduced from [1].

surface functionalization with the PIT. The decrease of the resonance frequency of the sensor makes evident that the functionalization took place correctly in just ten minutes.

After the stabilization, the fluidic circuit was rinsed for five minutes with MilliQ water to remove the unbound Abs (II). Subsequently, a bovine serum albumin solution (50 μg/ml) flowed into the fluidic circuit for five minutes to fill possible free space left by Abs on the gold surface (blocking, step III). In the step IV a solution of target antigen (Human IgG) flowed into the circuit for fifteen minutes. After the rinse (step V) a solution (1ml) of functionalized core@shell nanoparticles was conveyed to the cell (step VI). As it can be noticed looking at Fig. 2.8, the Fe_3O_4@AuNPs play an important role since the ME sensor response is eventually amplified by a factor slightly greater than three at this intermediate concentration. We highlight that all the steps were carried out until the equilibrium condition was reached thereby making more robust the whole approach. For each detection step the time to achieve a reliable stability was approximately five minutes, thus we carried out long term stability measurements (blue line in Fig. 2.8), which we used to analyze the distribution of the means of the resonance frequency measured over intervals of five minutes. It turned up that the standard deviation ($\bar{\sigma}$) of such a distribution was 1Hz so that 3 Hz (3 SD) was used to determine the threshold to establish the occurrence of a signal (limit of detection).

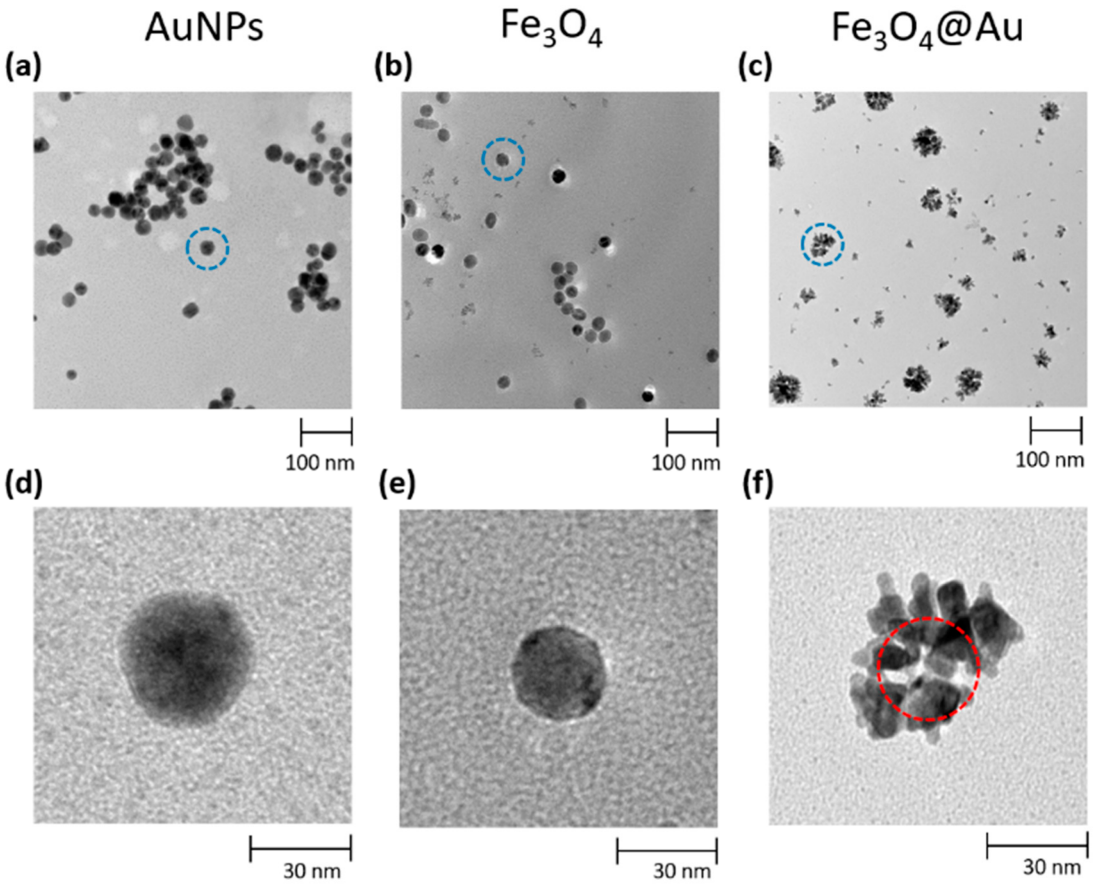

Figure 2.9: TEM micrographs of (a) AuNPs, (b) Fe_3O_4NPsand (c) Fe_3O_4@AuNPs (gold nanoflower grown on a magnetic core). In the lower part of the figure the circled portions in panels (a,b,c) are respectively reported in detail in panels (d,e,f). In panel (f) the magnetic core is highlighted with a red circle. Reproduced from [1].

2.3.5 Charaterization of gold and magnetic nanoparticles

Transmission electron microscopy (TEM) micrographs were collected using a FEI Tecnai G2 S-twin apparatus (University of Naples Federico II, Italy) operating at 200 kV (LaB6 source). The particle powder samples were transferred on carbon-coated copper grids (200 mesh) by dispersing them in ethanol and then adding one drop on the copper grid and evaporating the solvent. Fig. 2.9 shows the TEM micrograph of AuNPs synthesized according to the above mentioned protocol (a) as well as the Fe_3O_4 magnetic nanoparticles before (b) and after (c) the gold coating (Fe_3O_4@AuNPs).

The mass distribution of the AuNPs and Fe_3O_4@AuNPs, which was crucial in order to construe the results related to signal amplification, was assessed by applying the software SPIP Mountains 8 to the TEM micrographs (Fig. 2.10 a,b). The nanoparticle of interest was considered and extracted from the collective TEM micrograph (I), the contour of the nanoparticles was detected and distinct by the background (II), then the particle surface (III) together with its 3D rendering (IV) were generated. The latter was employed to estimate the volume of the object. Once the volume of the nanoparticle had been estimated, its mass was obtained by multiplying by the density of the material. In Figure 2c the mass

distribution of AuNPs (blue histogram) and of core@shell nanoparticles (red histogram) are compared. Each nanoparticle employed for the mass analysis was extracted randomly from collective TEM micrographs. The two mass distributions (Fig. 2.10c) turned out to be unimodal distributions with the picks around the value 0.4 fg for Fe_3O_4@AuNPs (red histogram) and 0.63 fg for AuNPs (blue histogram). The standard deviations are respectively 0.2 fg and 0.09 fg. Thus, the masses of AuNPs and Fe_3O_4@AuNPs result to be of the same order of magnitude.

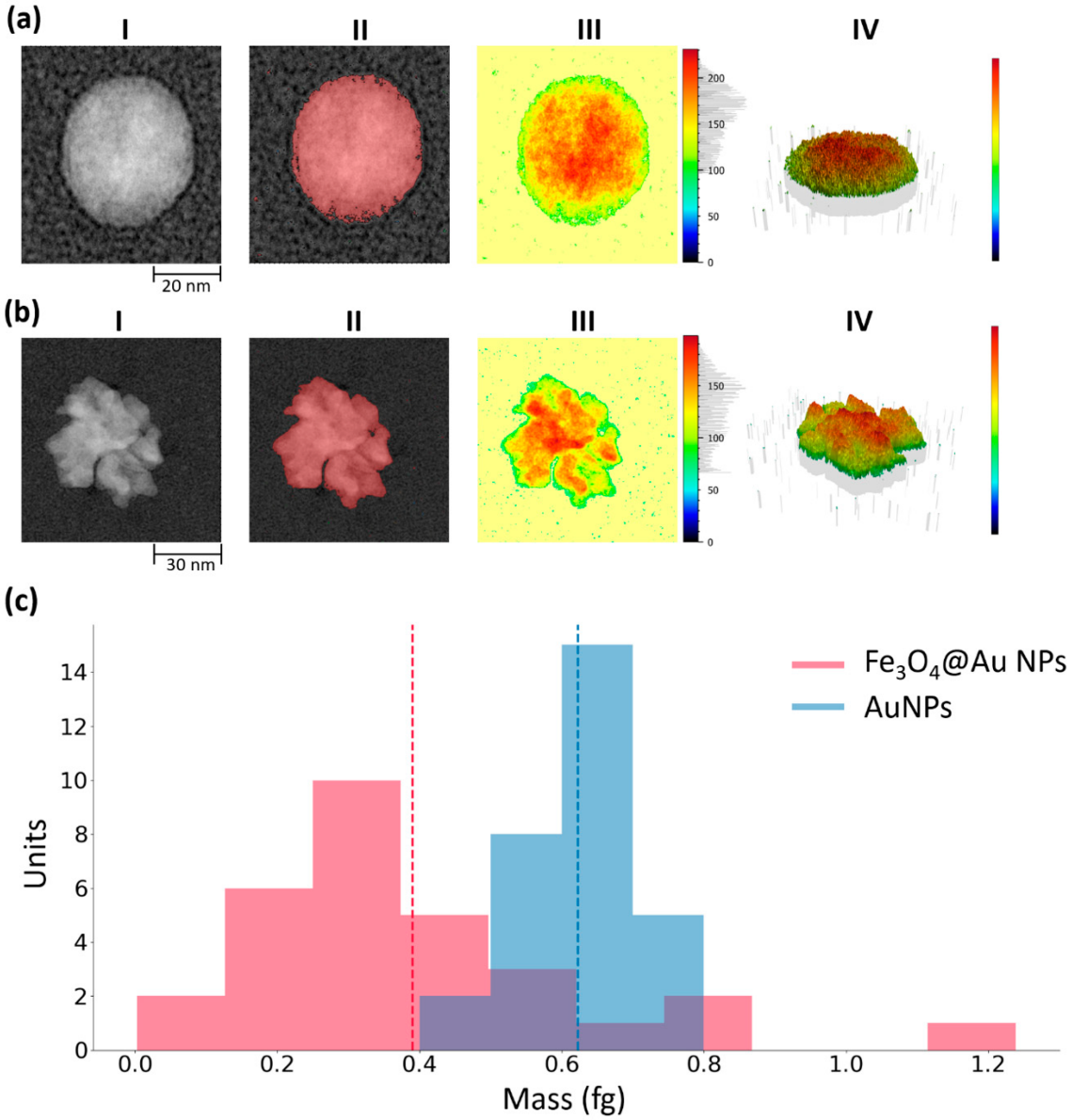

Figure 2.10: The steps of the protocol employed to estimate the mass of AuNPs (a) and Fe_3O_4@AuNPs (b) using the software SPIP Mountains 8. The nanoparticle of interest was considered and extracted from the collective TEM micrograph (I), the contour of the nanoparticles was detected and distinct by the background (II), then particle surface (III) and its 3D rendering (IV) were generated. The latter was employed to estimate the volume of the object. (c) Mass distribution of AuNPs and Fe_3O_4@AuNPs (core@shell NPs). The mean and the standard deviation for the mass distributions were 0.4 ± 0.2 fg for Fe_3O_4@AuNPs and 0.63 ± 0.09 fg for AuNPs. Each nanoparticle employed for the mass analysis was extracted randomly from collective TEM micrographs. Reproduced from [1].

2.4 Biosensing application

2.4.1 Comparison between AuNPs and Fe_3O_4@AuNPs

The idea of taking advantage of the magnetic interaction between magnetite nanoparticles and ME ribbons has already been employed in the past to detect bacteria [93]. In that case, Fe_3O_4 nanoparticles were modified by using chitosan, a linear polysaccharide, so that their surface was charged positively. In this way, in specific conditions, the nanoparticles bind to negatively charged bacteria as Escherichia coli and therefore, thanks to magnetic attraction, they also bind to the surface of the ME sensor giving rise to a signal enhancement. This approach has several drawbacks. Firstly, the chitosan coating and the Escherichia coli binding process are expensive and time consuming (several hours); and furthermore, the whole procedure must be carried out under controlled conditions, this preventing the application to complex matrices. Secondly, since the adhesion between bacteria and nanoparticles results from the electrostatic interaction between bacteria and the chitosan, it is expected that the specificity will be greatly compromised when other gram-negative bacteria are present in the sample. To circumvent such limitations, we functionalized the gold surface of Fe_3O_4@AuNPs with the antibodies targeting antigen, in this way achieving high specificity for the nanoparticle-antigen interaction.

Moreover, the magnetic core of the nanoparticles still played an important role since the (specific) nanoparticle-antigen bond is somehow catalyzed and enforced by the interaction between the magnetic dipole moment of the core@shell NPs and the strong local magnetic field. The occurrence of the latter process can be deduced by the results shown in Fig. 2.11, in which the response signals obtained by exposing the sensor to 1 μg/ml of antigen solution and amplifying once with AuNPs (blue line) and once with core@shell NPs (red line) are reported. Even though their mass was smaller (Fig. 2.10), core@shell magnetic NPs were able to amplify the frequency shift by a larger amount (Fig. 2.11) thereby demonstrating the higher sensitivity that can be achieved when the additional tool provided by magnetic moment is exploited.

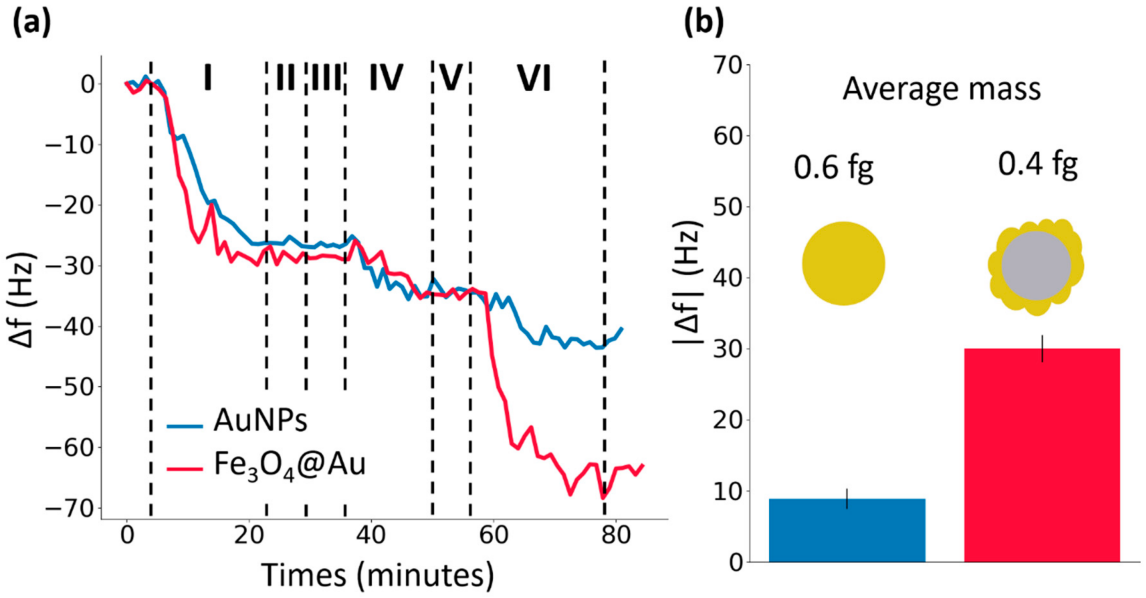

Figure 2.11: Comparison between the amplification effects due to AuNPs and core@shell magnetic NPs. (a) The blue and the red lines represent the response of the sensing ribbon to the following steps: (I) functionalization with $25\mu g/ml$ of UV-activated antibodies (anti-human IgG) which causes a shift of the resonance frequency $\Delta f \approx 30$Hz; (II) rinse with MilliQ water; (III) flowing of bovine serum albumin solution ($50\,\mu$g/ml); (IV) exposure to the antigen solution (human IgG) which causes a shift Δf $\approx$ 10Hz; (V) rinse with MilliQ water; (VI) amplification with AuNPs for the blue line and amplification with core@shell magnetic NPs for the red line. The former causes a shift $\Delta \mathrm{f} = 9 \pm 1\,\mathrm{Hz}$ while the latter causes a shift $\Delta \mathrm{f} = 30 \pm 2\,\mathrm{Hz}$. (b) A direct comparison between the amplification of the response signal due to AuNPs (blue) and core@shell magnetic NPs (red). Reproduced from [1].

2.4.2 Detection of human IgG

The dose-response curve is reported in Fig. 2.12 together with the best fit of the experimental data provided by a Langmuir isotherm curve [94]:

$$f(x) = a\frac{x}{x+c}, \tag{2.17}$$

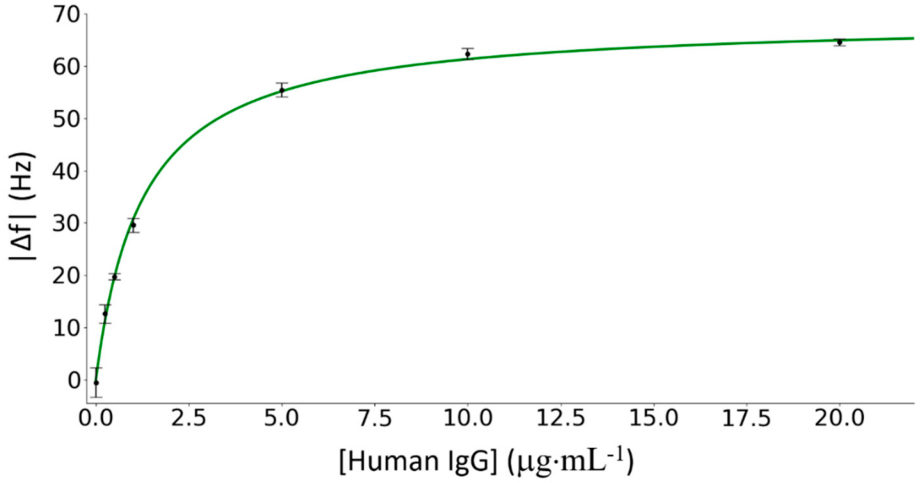

Figure 2.12: Dose–response curve, i.e., resonance frequency shifts Δf versus human IGg concentrations. Experimental data are fitted by Langmuir isotherm curve (Equation (2.17)). The range of tested concentrations varies from the zero concentration to 20μ g/ml. Each concentration has been tested using different ribbons. Reproduced from [1].

where a $= 68.9 \pm 0.5$ Hz and C $= 1.25 \pm 0.04\,\mu$g/ml are the asymptotic value, and the concentration at which the frequency shift reaches the 50 % of its maximal value, respectively. We carried out every experiment with a different ribbon obtaining coherent results. This is a strong confirm of the robustness of the experimental setup with respect to fluctuations related to differences in the fabrication process of ME sensors. The dose-response curve exhibits signal saturation at concentrations larger than 10 μgml, thus showing that the ME immunosensor is able to provide a quantitative measurement over two decades. The error on each experimental point of the dose response curve was estimated by propagating the errors of the resonance frequency values in the equilibrium states before and after the amplification with core@shell NPs. The error of the resonance frequency of an equilibrium state was estimated as the standard deviation of the measured values in a time interval of five minutes. The limit of detection (LOD) was assessed inserting the error estimated in Section 2.3.4 ($3\bar{\sigma} = \pm 3$ Hz) in (2.17) and turned up to be lower than 0.1μg/ml (0.66nM).

2.4.3 Specificity test

To ascertain the sensor specificity, the same experimental procedure was used to test the ME sensor with similar compounds. In the present case, we measured the response of the

immunosensor to a mixture rabbit IgG produced in sheep and mouse IgG produced in goat at a concentration of 20μg/ml each, whose sensorgram is shown in Fig. 2.13. As it is clearly visible, only the shift resulting from the surface functionalization is visible, whereas no additional frequency shift is measured as a result of the presence of rabbit and mouse IgGs. This is true even when core@shell magnetic NPs are conveyed into the interaction cell (step VI). The high specificity of the immunosensor is largely a consequence of the excellent biorecognition properties of the antibodies.

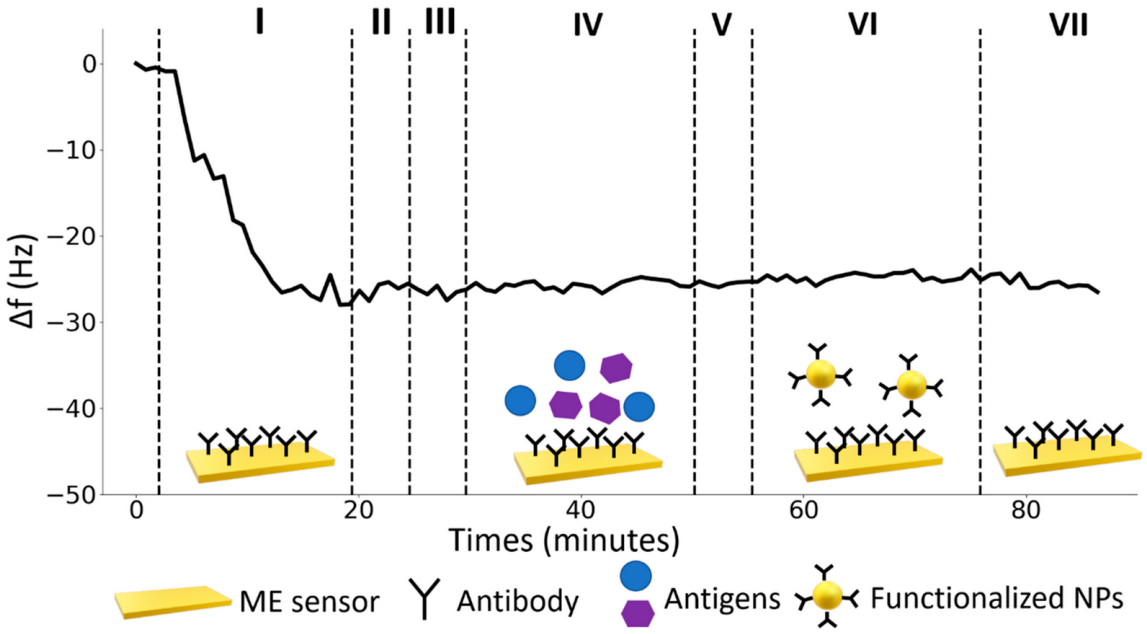

Figure 2.13: Sensor specificity. ME sensor responses to a mixed solution of rabbit IgG produced in sheep and mouse IgG produced in goat. The black line represents the response of the sensing ribbon in each of the following steps: (I) functionalization with a solution of 25 μg/ml of UV-activated antibodies, (II) rinse with MilliQ water, (III) flowing of bovine serum albumin solution ($50\mu g ml^{-1}$), (IV) flowing of Rabbit IgG produced in sheep and Mouse IgG produced in goat solution both at a concentration of 20μg/ml, (V) rinse with MilliQ water, (VI) amplification Fe_3O_4@AuNPs), (VII) rinse with MilliQ water. Reproduced from [1].

2.4.4 Magnetic interaction among the ME sensor and Fe_3O_4@AuNPs

The magnetic force acting on each core@shell Fe_3O_4@AuNP is:

$$\mathbf{F}(\mathbf{r}) = \nabla(\mathbf{m} \cdot \mathbf{B}_{tot}), \tag{2.18}$$

where $\mathbf{m}$ is the magnetic moment of a core@shell magnetic nanoparticle and $\mathbf{B}_{tot} = \mathbf{B}_H + \mathbf{B}$ is the magnetic induction field generated by the Helmholtz coils ($\mathbf{B}_H$) and the ME ribbon ($\mathbf{B}$), respectively. The magnetic induction field produced by Helmholtz coils is directed along the z axis (Fig. 2.15) and can be considered uniform in the region around the ribbon. On the contrary, the magnetic induction field produced by the ME ribbon is not uniform

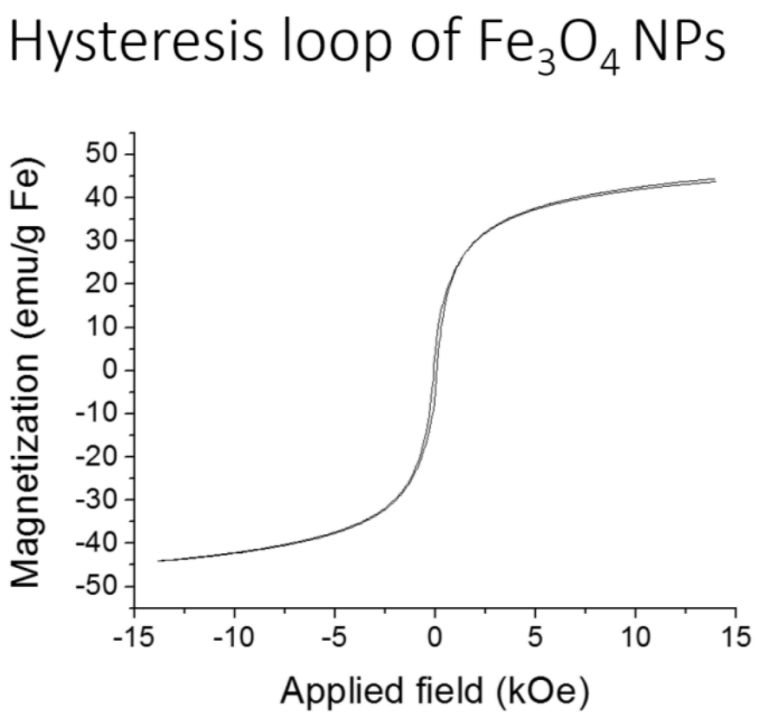

Figure 2.14: Room-temperature $M-H$ curve of the magnetite samples (supplied by the nanoparticles manufacturer Ocean Nano Tech, LLC) measured by cycling the external magnetic field between -14000Oe and 14000Oe. This magnetization curve shows a very weak hysteresis and exhibits small values of coercive field and residual magnetization. Reproduced from [1].

and can be worked out by considering the ribbon as rectangularly shaped permanent magnet whose significant components can be written as [95] [96]:

$$B_x(x,y,z) = \frac{\mu_0 M}{4\pi}\sum_{k=1}^{2}\sum_{m=1}^{2}(-1)^{k+m}\ln\left[\frac{(y-y_1)[(x-x_m)^2+(y-y_1)^2+(z-z_k)^2]^{1/2}}{(y-y_2)[(x-x_m)^2+(y-y_2)2+(z-z_k)^2]^{1/2}},\right] \tag{2.19}$$

$$B_z(x,y,z) = \frac{\mu_0 M}{4\pi}\sum_{k=1}^{2}\sum_{m=1}^{2}(-1)^{k+m}\tan^{-1}\left[\frac{(x-x_n)(y-y_m)}{(z-z_k)[(x-x_n)^2+(y-y_m)2+(z-z_k)^2]^{1/2}}\right], \tag{2.20}$$

where μ_0 is the magnetic permeability of free space, $x_1, x_2, y_1, y_2, z_1, z_2$ are the positions of the edges of the ribbon with respect to x, y and z axis (Fig. 2.14(a)).

The magnetization $\mathbf{M} = M\hat{z}$ of the ribbon is oriented along the z axis and the value of $\mu_0 M$ is approximately $0.2T$ for Metglas [97]. The component B_y, can be neglected since it is always much smaller than B_x and B_z while the latter are of the same order of magnitude and reach their maximum nearby the ribbons ends (Fig. 2.15,(c)). The dependence of B_x and B_z on x, y and z variables in Fig. 2.15 suggests that the significant magnetic interaction is limited to a region with volume $S_{xyz} = 100\,\mu\text{m} \times 1\,\text{mm} \times 100\,\mu\text{m}$ close to the ends of the ribbon. In this region B_H is negligible with respect to B_x and B_z and does not contribute significantly to the nanoparticles' magnetization.

The magnetic moment, $\mathbf{m}$, of a core@shell magnetic NP is the product of its magnetization, M_{NP}, and volume, $V_m = \frac{4\pi R_m^3}{3}$, where R_m is the radius of its magnetic core, $m = M_{NP}\ V_m$. The volumetric magnetization induced by the external magnetic induction field, $M_{NP} = \frac{\Delta\chi}{\mu_0}\mathbf{B}$, where $\Delta\chi = \chi_{M_{NP}} - \chi_{water} \approx \chi_{M_{NP}}$ is the effective susceptibility of a magnetic nanoparticle with respect to the medium (water). Since the component of the magnetic induction field along the y axis is negligible, the magnetic moment of a core@shell NP lies on the $x - z$ plane.
The order of magnitude of the magnetic moment can be retrieved by the hysteresis cycles of Fe_3O_4 superparamagnetic nanoparticles provided by the seller and reported in Fig. 2.14, also considering the effect of the gold shell that weakens magnetic properties [98].

The intensity of external magnetic induction field was high enough to induce significant magnetization, but only in the linear range of the magnetic response so the magnetic susceptibility could be considered constant in our case. Thus, the attractive magnetic force between the ribbon and a core@shell NP is:

$$F_x(x,y,z) = \frac{\partial \mathbf{m}\cdot\mathbf{B}}{\partial x} = \frac{V_m\Delta\chi}{\mu_0}\left(2B_x\frac{\partial B_x}{\partial x} + 2B_z\frac{\partial B_z}{\partial x}\right). \tag{2.21}$$

From the analysis of Equations (2.19) and (2.20), along the x axis, we have $B_x \approx B_z$ (Fig. 2.15 (c)) which entails $\frac{\partial B_x}{\partial x} \approx \frac{\partial B_z}{\partial x} \approx 1\ T\cdot mm^{-1}$; thus equation (2.21) can be approximated as follows

$$F_x(x,y,z) = 4\frac{V_m\Delta\chi}{\mu_0}B_x(x,y,z)\left(\frac{\partial B_x}{\partial x}\right), \tag{2.22}$$

The force in Equation (2.22) bends the nanoparticles velocity field lines towards the ribbon thereby increasing the local density of the core@shell magnetic NPs. The order of magnitude of the bending can be estimated as the displacement induced by $F_x(x,y,z)$acting on a nanoparticle in the region where the force is non-vanishing, i.e., the region S_{xyz} previously defined. The mean force F_x acting on core@shell magnetic NPs can be evaluated by averaging $F_x(x,y,z)$ in the region S_{xyz}. According to Stokes' law, for a spherical particle with radius r, the displacement caused by the mean force F_x is

$$\Delta s_m \approx \mu\hat{F}_x t_l, \tag{2.23}$$

where $\mu = (6\pi\eta r)^{-1}$ is the mobility, t_l the time during which the interaction takes place. It should be noted that this approach is valid in the approximation that the motion is uniform along x, a condition well satisfied in our case since the limit velocity is reached within a very short time-interval ($\tau \approx 10^{-6}s$).
The time t_d in which the magnetic interaction takes place can be estimated as $t_d = d\ v_{flux}^{-1} \approx 1\ s$, where $v_{flux} \approx 100\ \mu\mathrm{m}\cdot\mathrm{s}^{-1}$ is the the longitudinal velocity of the liquid inside the channel and $d \approx 100\mu m$ the size of S_{xyz} along $z$axis. Eventually, (2.23) provides $\Delta s_m \approx 30\,\mu$m that leads to an increase of the frequency collision between nanoparticles and the ribbon surface whereby more antigens (human IgGs) captured on the surface are ballasted by nanoparticles.
The significance of such a bend arises from its comparison to the Brownian motion displacement

$$\Delta s_B = \sqrt{2Dt_D}, \tag{2.24}$$

where D is the diffusion coefficient ($D = \mu k_B T \approx 10^{-11}$ $\mathrm{m}^2 \cdot \mathrm{s}^{-1}$) and t_D the diffusion time, which we can estimate by requiring $\Delta s_B \approx \Delta s_m$. Thus, from equations (2.23) and (2.24), we obtain $t_D \approx 45\,\mathrm{s}$, a time much longer than the transit time of the core@shell NPs over the ME ribbon, which implies that the velocity field lines remain bent by magnetic force along the whole length of the ribbon.
This view is confirmed by the analysis of the energy scales involved. The binding energy between the antibodies and the antigen is of the order of $1.6\ 10^{-19}\,\mathrm{J}$ (eV), which is larger than the thermal energy at room temperature ($k_B T = 0.0410^{-19}\,\mathrm{J} = 0.025\,\mathrm{eV}$).

Interestingly, the potential well due to the magnetic induction field averaged over the region of interest S_{xyz}, is of the order of $k_B T$ thus making consistent the description about the role played by the strong magnetic induction field at the edge of the ribbon in bending the velocity field lines and increasing the "effective" nanoparticle density, but without giving rise to any non-specific interaction with nanoparticles and the surface of the ribbon.

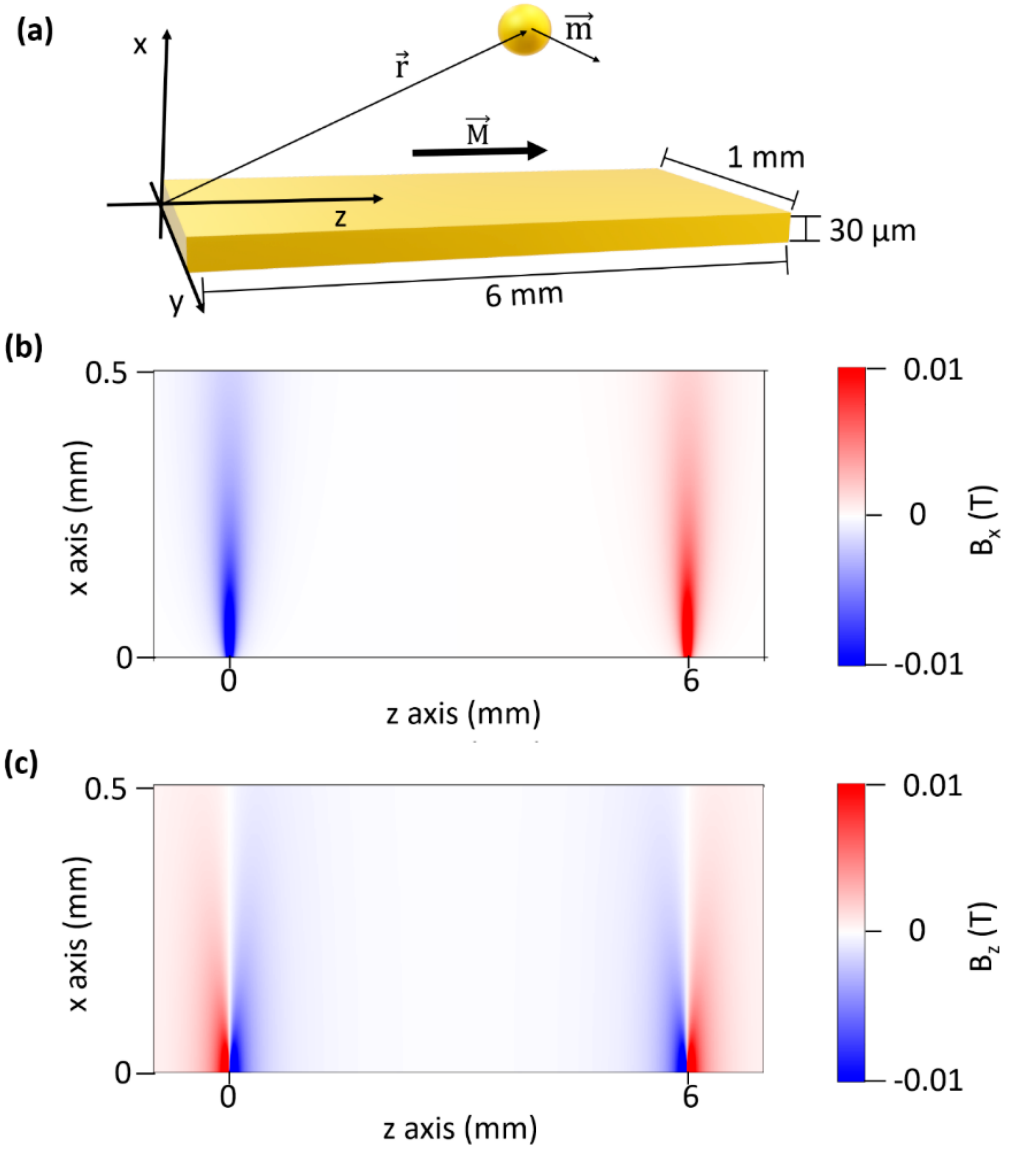

Figure 2.15: (a) Schematic representation of the interaction among the core@shell magnetic nanoparticle and the ME ribbon. **M** is the magnetization of the ME ribbon, m is the magnetic moment of the core@shell nanoparticle and **r** indicates the position in the chosen reference system. (b,c) Intensity of the x and z components x of the magnetic induction field (B_x and B_z) in the symmetry plane xz of the ribbon ($y = 0.5\,\mathrm{mm}$).

2.5 Conclusions

In this chapter we presented a high-performance ME biosensor for wireless recognition of antigens in liquid. An innovative signal amplification method has also been introduced based on core@shell magnetic nanoparticles (Fe_3O_4@AuNPs). The results obtained with magnetic nanoparticles have been compared with those obtained with gold nanoparticles, showing that the magnetic character of the former plays a crucial role for improving the performance. The ME biosensor exhibits a LOD of 0.66 nM against human IgG in water. Generally, ME sensors are simple in design and can be produced in small size using standard manufacturing procedures; the raw material are quite inexpensive so that the cost of manufacturing of these sensors is mainly the sensing element (i.e., antibody in this study). Furthermore, the sensing mechanism is wireless, so that there is no the need for direct physical contacts, thus favoring their use in real-time applications such as detection in conductive liquids or in sealed and opaque containers, and biological experiments such as monitoring of blood flow chemistry. In addition to these features, the ME biosensor presented in this thesis, profits from the synergy with PIT that allows a fast and efficient functionalization, thus contributing to the rapidity of the detection measure, which lasts approximately 1 hour (including the functionalization). Moreover since the PIT does not need a laboratory, there is a better chance of turning the sensor into a portable device. The stability in water of the ME biosensor, the rapidity of sample analysis and the possibility of turning the sensor into a portable device are essentials characteristics for environmental control and food safety applications. As a possible application, the LOD achieved against human IgG would be appropriate for detecting glyphosate [(N-(phosphonomethyl)glycine)] in water. Indeed European Union settled the maximum residue limit of glyphosate in drinking water to $0.1\,\mu g \cdot l^{-1}$ (i.e., 0.5 nM) while in the United State of America the established limit is $700\,\mu g \cdot l^{-1} = 4\,\mu M$ (Directive 2006/118/EC, Directive 2006/118/EC, USEPA. EPA 816-F-09-004).

Appendix

2.A Protocols

2.A.1 Synthesis of gold nanoparticles

The AuNPs were synthesized by chemical reduction of tetrachloroauric (III) acid trihydrate ($HAuCl_4 \cdot 3H_2O$) through sodium citrate ($Na_3C_6H_5O_7$) [99]. A solution of 50 ml of ultra-pure water and 0.5 ml solvated $Na_3C_6H_5O_7$ (24 mM) was heated up at 150 C and stirred constantly. Afterwards, 6 ml of sodium citrate dihydrate (39 mM) was added into the boiling solution to achieve particle nucleation. To further increase particle growth, another 4.2 mL of $HAuCl_4 \cdot 3H_2O$ (24 mM) was added after 2 min. The color of the solution changed from transparent to black to finally move to bright red in few minutes. As final step, the solution was let cool down for two hours keeping the same stirring.
In order to employ AuNPs as signal amplification factor, it was necessary to remove the sodium citrate, in which they were suspended to avoid aggregation, during the functionalization of the surface with Abs. The centrifuge protocol working conditions for 1 mL of citrate AuNPs (the dilution: 200 μl of citrate AuNPs and 800 μl of ultra-pure water) was achieved through two steps: (a) 15 min at 9000 $\times$ g, and (b) 10 min at 5000 $\times$ g. After each centrifugation, the pellet was re-suspended in 1 ml ultra-pure water.
The resulting optical density (OD) was ≈ 1 that corresponds to $\approx 10^{11}$ AuNPsml^{-1} with diameter of 40 nm [100].

2.A.2 Coating of magnetic nanoparticles

The magnetic Fe_3O_4 nanoparticles (average diameter 30 nm) were purchased by MERCK (catalog number 747327) and gold coated as follows: 100 μl of magnetic nanoparticles were added to a solution containing 50 ml of MilliQ water and sodium citrate (10 mg/ml) and they were heated until 90C with vigorous stirring. Once the temperature was reached, 50 μl of $HAuCl_4 \cdot 3H_2O$ (10mg/ml) was added to the solution for four times every ten minutes. At this point the solution was let to cool down until it reached the room temperature keeping the same stirring. As a result of such a procedure a colloidal solution of 50ml of Fe_3O_4@AuNPs was obtained.

2.B Static magnetic field

The static field applied to the ME ribbon is produced by two Helmholtz coils mounted at a distance equal to their radius (5.7 cm). The uniform magnetic field in the central region

between the coils where the ME ribbon is assumes the following value:

$$B = \frac{4}{5}^{3/2} \frac{\mu_0 i N}{R} \tag{2.25}$$

where B è is the magnetic field, R is the radius of the coils, N è number of winding, i is the current. The linear relation is experimentally verified as shown in Fig. 2.16(a).

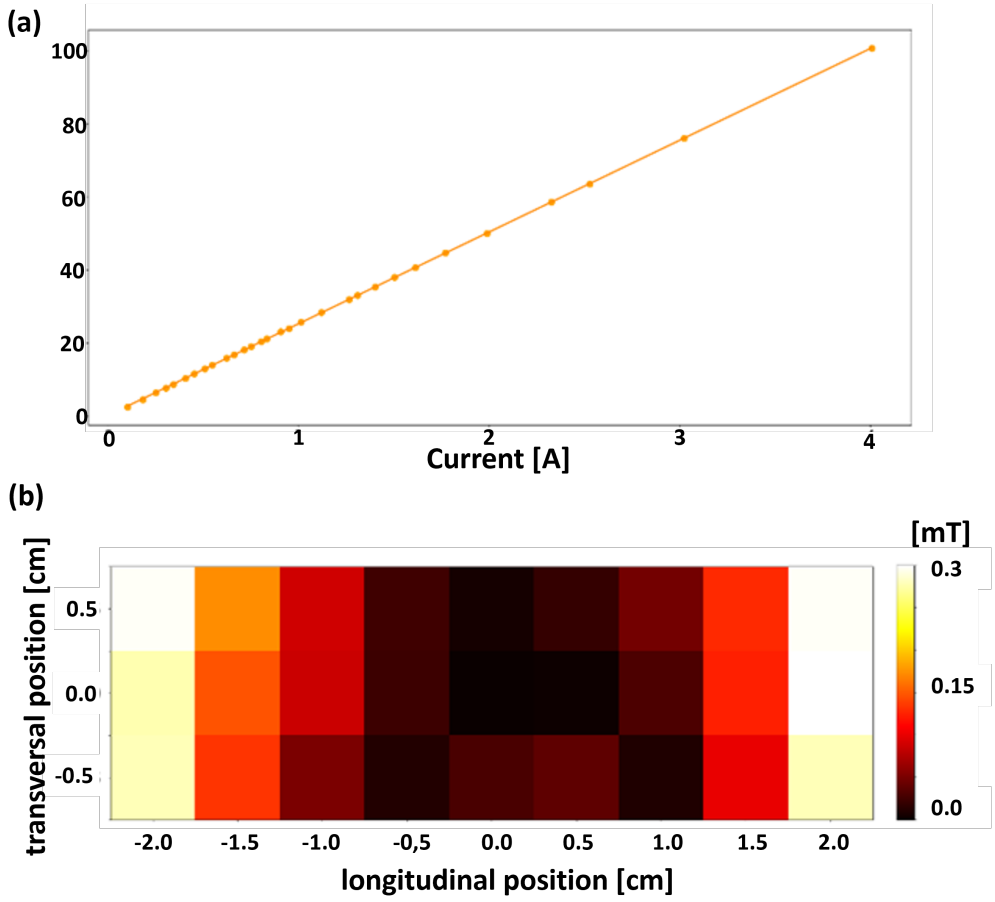

Figure 2.16: Uniformity of the static magnetic field produced by the Helmholtz coils in the plane containing the ME ribbon, where the origin of the system is placed in the middle of the Helmholtz coil. The longitudinal positions is the coordinate parallel to the longest side of the ME ribbon (6 mm).

Fig. 2.16(b) depicts the variation of value the magnetic field in the whole region between the coils with respect to value measured in central region (30 Oe). The measurements are performed in the plane containing the ribbon.

Chapter 3

Plasmon-Enhanced Fluorescence biosensor

Contents

3.1 Introduction

In the last few decades, plasmonic nanostructures have been routinely used to amplify the signal in plasmon-enhanced fluorescence (PEF) [101], surface plasmon-coupled emission (SPCE) [102], surface-enhanced Raman scattering (SERS) [103], and surface-enhanced infrared absorption (SEIRA) applications [104]. In particular, the fluorescence amplification is highly desirable in biosensing applications to remarkably lower the detection limits, notably in complex biological systems exhibiting significant interfering background (e.g., autofluorescence, crosstalk, competing signals) [105].
Even though the physics underlying the PEF phenomenon is still to be fully understood [106, 107], the fluorescence enhancement (FE) can be ascribable to the optical coupling between the nanostructure and the fluorescent molecules [101]. The particular enhancement mechanism (i.e. excitation rate enhancement, emission rate enhancement, dual-mechanism enhancement) is determined by the (i) fluorophore-nanostructure spectral overlap and (ii) fluorophore-nanostructure separation distance [108, 109] (Section 3.2.2).

Rough metal surfaces constitute one of the simplest tool to realize a fluorescence enhancer for biosensing applications since they generally offer high densities of randomly distributed electromagnetic hot spots on macroscopic areas. Additionally, employing a sensing area with no discontinuities provides the substrate with a multitude of anchoring sites for biomolecules to make the bioreceptor-substrate binding easier. Nevertheless, their moderate FEs limit their applicability to bioassays whose interest concerns concentrations larger than tens of picomolar [92].
Thus, a wide variety of nanostructured platforms have been recently explored to devise high-performance fluorescence enhancers apt to realize ultrasensitive bioassays such as nanoassemblies [110, 111], nanocages [112, 113], and nanopatterns [114, 115, 116]. Particularly, Soret colloids realized through thermo-driven self-assembly [117] represent an intriguing approach to achieve not only remarkable FEs (up to thousands-fold) [118, 119], thanks to the collective and coherent coupling between localized surface plasmons and surface plasmon polaritons [118, 120], but also highly directional and p-polarized emission enhancements ($> 97\,\%$) when implemented on SPCE platforms [121, 118]. Even larger FEs (up to 106-fold) [122] were measured by using particular designs sustaining strong inter-plasmon coupling such as nanocavities [114, 123], and nanoantennas [124, 125]. However, such architectures require a nanoscale positioning of the fluorescent molecules at electromagnetic hot spots to make their adoption in real biosensing applications unpractical [126].

Two-dimensional (2D) patterns of metal nanoparticles represent a smart solution to simultaneously augment both the FEs via inter-plasmon coupling and the hot spot density.

Their optical properties crucially depend on lattice parameters and on the size, shape, material, and immediate environment of nanoparticles [56]. In fact, modifications in the index of refraction of the immediate environment entail a variation of the optical response so that nanostructured surfaces can be effectively used for bulk refraction index sensing and molecular sensing [127]. As it concerns the material, silver is generally preferred to gold in fluorescence-based assays because of the lower quenching entailed by silver at nanoscale distance ($< 5\,\text{nm}$). However, the significant chemical reactivity of silver makes it prone to oxidation and dissolution, which is detrimental for some applications in real matrices [128].
On the other hand, gold exhibits high biocompatibility and inertness [129]. Innovative strategies have been recently explored for dequenching the fluorophore emission, such as adopting photonic crystal [130] and graphene oxide as substrates [131].

Patterns of AuNPs are valid candidates as a signal enhancer since they combine tunable plasmonic features with simple fabrication [132]. In a first approximation, their optical behavior depends on the ratio D/d between the particle diameter and the center-to-center distance (see Section 1.3.8). Additionally, multi-resonant plasmonic modes can be activated by properly tailoring the pattern architecture so that these structures are suitable for multiplexed bioanalytical assays. Multiplexing-based assays are highly appealing in diagnostics since they benefit from lower detection time, sample volume, and costs despite generally suffering from low sensitivity and specificity, also requiring complex microfluidic systems, sample pretreatment, and purification steps [133, 134]. When fabrication affordability and scalability as well as optical tunability are required, block copolymer micelle nanolithography (BCMN) stands out over other methods thanks to its capability to easily produce large-scale periodic arrays of AuNPs whose lattice parameters can be modified by simply choosing the appropriate diblock copolymers [135].
In recent studies, two plasmonic substrates consisting of hexagonally arranged (BCMN) and randomly positioned AuNPs (electrostatic immobilization) were implemented in a PEF-based assay for detecting malaria biomarker Plasmodium falciparum lactate dehydrogenase (PfLDH) down to femtomolar and picomolar levels, respectively, without any sample preconcentration and pretreatment [136, 137].

The quest for multiplexed detection, while preserving high quality performances, spurred us to devise a double-resonant plasmonic nanostructure suitable for simultaneously detecting two different analytes in the matrix of interest [4]. Thus, we tailored BCMN in such a way to fabricate branch patterns made of plasmon-coupled hexagonally arranged AuNPs, which gives rise to a coupled mode whose resonance lies in the far-red region, and sprinkled plasmon-uncoupled AuNPs that exhibit an LSPR at 524 nm.
As a case study, we implemented the proposed plasmonic nanostructure in a PEF-based malaria apta-immunosensor for detecting PfLDH in spiked whole blood. The PfLDH is a biomarker secreted by the Plasmodium falciparum parasite, the most common and lethal among the malaria parasites (90 % of malaria-related mortality worldwide [138]).
The PEF-based apta-immunoassay herein described combines the intrigued optical properties of a double-resonant plasmonic nanostructure with the photochemical immobilization technique (PIT) (Section 1.1.2).
While Abs were preferred as a capture bioreceptor layer since the simple and effective func-

tionalization carried out via PIT, fluorescently labeled aptamers (Apts*) were employed as the top bioreceptor layer in the sandwich configuration to (i) significantly increase the specificity, (ii) enable optimal separation distance between fluorophore and nanostructure (approximately 10 nm), and (iii) accomplish a versatile and affordable fluorescent labeling of the analytes of interest.
It is worth mentioning that our approach allowed us to not be overly concerned about dequenching strategies since fluorophores were inherently positioned beyond the FRET region (Section 3.2.2).

3.2 Plasmon-Enhanced Fluorescence

3.2.1 Fluorescence spectral modification

In free-space conditions, the absorption of a photon of energy $h\omega$ typically sends the fluorophore to the first excited singlet state S_1, from which it can relax to the ground state S_0 by emitting a photon of a lower energy $h\omega'$ or by non-radiative decay processes including heating and quenching mechanisms. The emission from an isolated fluorophore is described in terms of two observables: the quantum yield QY and the lifetime τ. The lifetime is the average time the molecule spend in the excited state before returning in the ground state. The QY is the number of emitted photons relative to the number of absorbed photons. The process is governed by the rate constants of radiative and non-radiative processes, namely $\gamma^{(r)}$ and $\gamma^{(nr)}$, that depopulate the excited state. We will indicate with Q_0 and τ_0 the QY lifetime, respectively, of a fluorophore in free-space conditions [101]:

$$Q_0 = \frac{\gamma_0^{(r)}}{\gamma_0^{(r)} + \gamma_0^{(nr)}}, \tag{3.1}$$

$$\tau_0 = \frac{1}{\gamma_0^{(r)} + \gamma_0^{(nr)}}, \tag{3.2}$$

where $\gamma_0^{(r)}$ and $\gamma_0^{(nr)}$ are the radiative and non-radiative decay rates in free-space conditions, respectively.

Although $\gamma_0^{(r)}$ does not significantly depend on the external conditions, fluorescence QY, lifetime and intensity are strongly affected by the surrounding environment due to the changes in $\gamma_0^{(nr)}$. Thus, the fluorophore spectral properties can by modified by altering $\gamma_0^{(nr)}$. However the enhancement of the fluorescence observables is inherently limited since a decrease of τ_0 implies not only an increase of $\gamma^{(r)}$ but also a decrease of QY strongly decreasing a probability to emit a photon. On the contrary, when a fluorophore is nearby a metal surface, the metal introduces an additional radiative rate ($\gamma_p^{(r)}$) yielding to both an increase of the quantum yield QY_p and a reduction of the lifetime τ_p [139]:

$$Q_p = \frac{\gamma_0^{(r)} + \gamma_p^{(r)}}{\gamma_0^{(r)} + \gamma_0^{(nr)} + \gamma_p^{(nr)} + \gamma_p^{(r)}}, \qquad \tau_p = \frac{1}{\gamma_0^{(r)} + \gamma_0^{(nr)} + \gamma_p^{(nr)} + \gamma_p^{(r)}}, \tag{3.3}$$

where $\gamma_p^{(nr)}$ is the rate of the quenching processes introduced by the nearby metal.

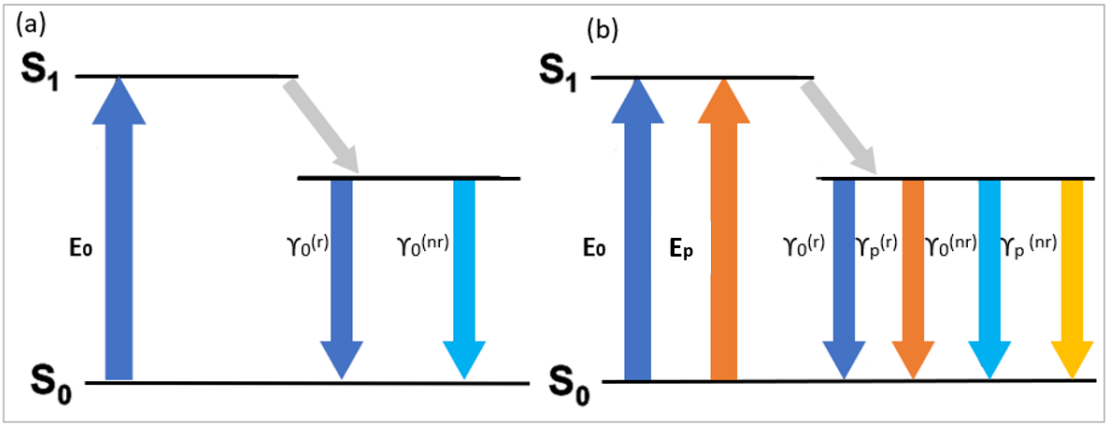

Figure 3.1: (a) Jablonski diagram for the free-space conditions and (b) modified from the presence of a conductive nanostructure.

3.2.2 Mechanisms of plasmon-fluorescence interaction

The energy transfer between the plasmon and the fluorophore is dominated by dipole-dipole interactions. If the fluorophore is in close proximity of the nanostructure surface ($1 - 10\,\text{nm}$), the non radiative local field of one dipole can excite the other. This is called Förster resonance energy transfer (FRET). The efficiency of the energy transfer in FRET strongly depends on the separation distance [140]:

$$\eta_{FRET} = \frac{1}{1 + \left(\frac{R}{R_0}\right)^6}, \tag{3.4}$$

where R is the fluorophore-nanostructure. It decays as $1/R^6$ because each dipole has a $1/R^3$ near field.

The distance behavior is scaled by the factor R_0, which depends on the spectral overlap between the emission of the donor's excited state and the acceptor's ground state absorption. Since the value of R_0 lies usually in the range of $3 - 8\,\text{nm}$ in plasmon-fluorophore FRET the enhancement is very efficient only for small separation distances $R < R_0$.
A second mechanism that the plasmon has to enhance the radiative rate of the fluorophore is the Purcell effect. To understand the Purcell effect we can consider what happens to a radiative dipole when it is placed in a resonant cavity. According to the Fermi's Golden Rule, the spontaneous emission rate from a set of final states $|f\rangle$ to the initial state $|i\rangle$ is generally written as:

$$\gamma = \frac{2\pi}{\hbar^2} \sum_f \langle g|\hat{H}|i\rangle \delta\left(\omega_i - \omega_f\right). \tag{3.5}$$

Equation (3.5) for a dipole emitter ($\hat{H} = -\hat{p} \cdot \hat{E}$) becomes [141]:

$$\begin{aligned} \gamma(\mathbf{r}, \omega) &= \frac{2\omega}{3\hbar\varepsilon_0} |\mathbf{p}|^2 \rho_{LDOS}(\mathbf{r}, \omega), \\ \rho_{LDOS}(\mathbf{r}, \omega) &= \frac{6\omega}{\pi c^2} \left[\mathbf{n} \cdot \text{Im}\mathbf{G}(\mathbf{r}, \mathbf{r}, \omega) \cdot \mathbf{n}\right], \end{aligned} \tag{3.6}$$

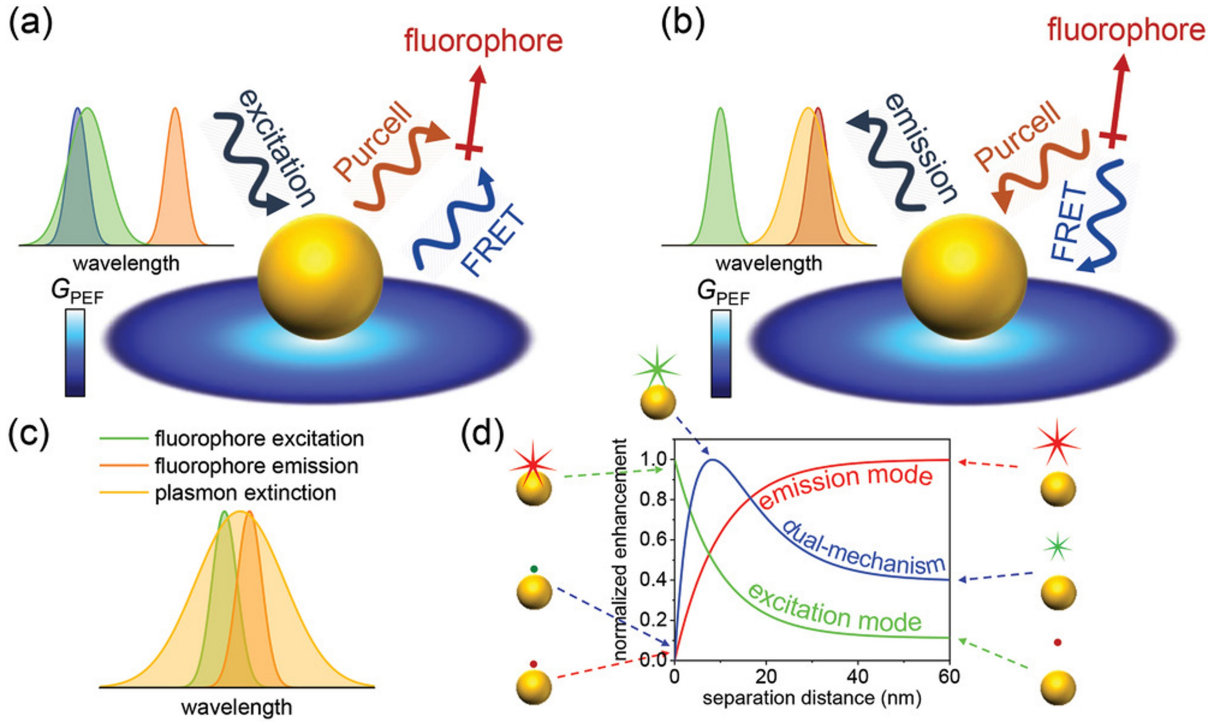

Figure 3.2: (a) Enhancement of the excitation mode through either FRET and Purcell effect due to the spectral overlap between the plasmon extinction and the fluorophore absorption. (b) Emission mode enhancement through either FRET and Purcell effect due to the spectral overlap between the plasmon extinction and the fluorophore emission. Adapted from [68].

where $\mathbf{p}$ is the transition dipole moment of the emitter, $\mathbf{n}$ the unit vector of the orientation of $\mathbf{p}$, $\mathbf{r}$ is the position vector, ω the emission frequency, ρ_{LDOS} the local density of the states, $\mathbf{G}(\mathbf{r}, \mathbf{r}, \omega)$ is the Green's dyadic which is the electric field interacting with the emitter due to its own radiation. We recall that the so-called dyadic Green's function $\mathbf{G}(\mathbf{r}, \mathbf{r}')$ is in general the electric field at the field point $\mathbf{r}$ due to a single point source $\mathbf{j}(\mathbf{r})$ at the source point $\mathbf{r}'$. It is the solution of the equations:

$$\nabla \times \nabla \, \mathbf{G}_i(\mathbf{r}, \mathbf{r}') - k^2 \mathbf{G}_i(\mathbf{r}, \mathbf{r}') = \delta(\mathbf{r} - \mathbf{r}') n_i,$$

for $i = x, y, z$, with n_i unit vector in i-direction.

From the eq. (3.6) we have that [109]:

$$\rho_{loc}(\mathbf{r}, \omega) \sim |E_{loc}(\mathbf{r}, \omega)|^2, \tag{3.7}$$

where and E_{loc} is the local electric field of the cavity normalized to the incident intensity. A consequence of the modification of the LDOS entailed by the cavity is that the emission intensity will be amplified on-resonance and quenched off-resonance with respect to free space emission. The plasmon acts on the nerby fluorophore as a resonant cavity. Its local field $|E_{loc}|^2$ (in proximity of the nanoparticle's surface) is stronger than the free space light incident on the nanoparticle, so it increases the LDOS with respect to the free-space conditions. If the plasmon's absorption or scattering spectrally overlaps with the

fluorophore's emission, the fluorophore's emission rate will be enhanced by the plasmon due to the change in the LDOS.

The spectral overlap between the plasmon extinction and the fluorophore excitation and emission determines if the FRET or Purcell effect take place and which one is predominant. In particular, if the plasmon overlaps with the fluorophore absorption spectrum, the fluorophore excitation rate is enhanced through FRET mechanism at separation distances of a few nanometers. A weaker coupling would take place at longer fluorophore-nanostructure distances (Fig. 3.2, (a)). On the other hand, if the plasmon overlaps with the fluorophore emission an enhancement or quenching of the emission intensity is possible. In particular a large fluorescence enhancement will take place through the Purcell effect for separation distances from the nanoparticles' surface beyond FRET region. For smaller distances of a few nanometers, the fluorophore's emission will be quenched by FRET mechanism [109] (Fig. 3.2, (b)). Usually it not feasible to obtain a pure excitation or emission enhancement the relatively broad extinction line width of the plasmon and the Stokes shift of the fluorophore (spectral difference between the wavelength of the absorption pick and the wavelength of the emission pick) [109]. Thus, the two mechanism take place together realizing the so-called dual-mechanism enhancement. As a result, an intense fluorescence enhancement arises at distances of about $1 - 30\,\text{nm}$ while a strong quenching is present at shorter separation distances.

3.2.3 Fluorescence amplification

The fluorescence amplification of a molecule due to the proximity of a plasmonic nanostructure arises from three different contributions: the enhancement of the fluorophore excitation rate $G(\omega)$, the enhancement of the fluorophore radiative decay rate $Y(\omega')$, and the gain of the luminescence collection efficiency $K(\omega')$ [142, 143, 144]:

$$FE(\omega, \omega') = G(\omega)Y(\omega')K(\omega') \tag{3.8}$$

where ω is the excitation frequency and ω' the emission frequency. In the next section we will discuss each of these factors.

3.2.4 Intensity enhancement factor

To calculate the field enhancement factor G, we consider a spherical particle illuminated by a plane wave, linearly polarized electromagnetic (EM) wave. We assume that the plane wave is propagating along the positive z axis and the electric field is polarize along the x axis. The center of the particle is located at the origin of the coordinate system. The ambient medium is vacuum. The incident field in vector spherical wave functions is given by (see Section 1.3.7):

$$\mathbf{E_i} = \hat{\mathbf{u}}_\mathbf{x} E_0 e^{ikz - i\omega t} = E_0 e^{-i\omega t} \sum_{n=1}^{\infty} i^n \frac{2n+1}{n(n+1)} (\mathbf{m}_{01n}^{(1)} - i\mathbf{n}_{e1n}^{(1)}), \tag{3.9}$$

here E_0 is the incident wave amplitude; k is the wavenumber, ω is the incident wave frequency; c is the speed of light in vacuum; $\hat{\mathbf{u}}_\mathbf{x}$ is the unit vector along the x axis, and

$\mathbf{m}^{(1)}_{01n}$, $\mathbf{n}^{(1)}_{e1n}$ are the spherical vectorial functions [57] (see Section 1.3.7):

$$\mathbf{m}^{(1)}_{01n} = \frac{j_n(kr)}{\sin\theta} P^1_n(\cos\theta)\cos\phi\,\mathbf{e}_\theta - j_n(kr)\frac{\partial P^1_n}{\partial\theta}\sin\phi\,\mathbf{e}_\phi, \tag{3.10}$$

$$\begin{aligned}\mathbf{n}^{(1)}_{e1n} = {} & \frac{n(n+1)}{kr} j_n(kr) P^1_n(\cos\theta)\sin\phi\,\mathbf{e}_\mathbf{r} + \frac{1}{kr}[krj_n(kr)]'\frac{\partial P^1_n}{\partial\theta}\mathbf{e}_\theta + \\ & + \frac{[krj_n(kr)]}{kr\sin\theta} P^1_n(\cos\theta)\cos\phi\,\mathbf{e}_\phi,\end{aligned} \tag{3.11}$$

where $\mathbf{e}_r$, $\mathbf{e}_\theta$ and $\mathbf{e}_\phi$ are unit vectors of the spherical coordinate system; $r = |\mathbf{r}|$ is the length of the radius vector from the particle center to a point of interest; θ and ϕ are the spherical angles, $\theta \in [0, \pi]$ and $\phi \in [0, 2\pi]$, $j_n(kr)$ are the Bessel function; $P^1_n(\cos\theta)$ are the Legendre functions and the prime indicates the derivative with respect to its argument. The electric field which is induced near a particle in subjected to the electromagnetic field (3.9) can be written as [57] (see Section 1.3.7):

$$\mathbf{E}_p(\omega, \mathbf{r}) = E_0 e^{-i\omega t}\sum_{n=1}^{\infty} i^n \frac{2n+1}{n(n+1)}(a_n \mathbf{m}^{(3)}_{oln} - ib_n \mathbf{n}^{(3)}_{eln}) \tag{3.12}$$

where $\mathbf{m}^{(3)}_{oln}$ and $\mathbf{n}^{(3)}_{eln}$ are the spherical vector functions whose form can be obtained substituting the Bessel function $j_n(kr)$ with the Hankel functions $h^1_n(kr)$ in the equations (3.10), e a_n and b_n are the Mie coefficients [144], [57]:

$$a_n = -\frac{\psi_n(ka\sqrt{\varepsilon})\psi'_n(ka) - \sqrt{\varepsilon}\psi'_n(ka\sqrt{\varepsilon})\psi_n(ka)}{\psi_n(ka\sqrt{\varepsilon})\xi'_n(ka) - \sqrt{\varepsilon}\psi'_n(ka\sqrt{\varepsilon})\xi_n(ka)}, \tag{3.13}$$

$$b_n = -\frac{\sqrt{\varepsilon}\psi_n(ka\sqrt{\varepsilon})\psi'_n(ka) - \psi'_n(ka\sqrt{\varepsilon})\psi_n(ka)}{\sqrt{\varepsilon}\psi_n(ka\sqrt{\varepsilon})\xi'_n(ka) - \psi'_n(ka\sqrt{\varepsilon})\xi_n(ka)}, \tag{3.14}$$

where a is the radius of the metal spherical particle and $\varepsilon = \varepsilon(\omega)$ is its dielectric permittivity and we introduced the so-called Riccati-Bessel functions:

$$\psi_\ell(r) = rj_\ell(r), \quad \xi_\ell(r) = rh^1_\ell. \tag{3.15}$$

To calculate the field enhancement in proximity of the particle, we need to calculate the following ratio [144]:

$$G(\omega, \mathbf{r}) = \frac{|\mathbf{E_i}(\omega, \mathbf{r}) + \mathbf{E_p}(\omega, \mathbf{r})|^2}{|\mathbf{E_i}(\omega, \mathbf{r})|^2} \tag{3.16}$$

where $\mathbf{E_i}(\omega, \mathbf{r}) + \mathbf{E_p}(\omega, \mathbf{r})$ is the total electric field nearby the particle. Averaging $G(\omega, \mathbf{r})$ over all the spatial direction we get [144]:

$$\begin{aligned}\langle G(\omega, \mathbf{r})\rangle = {} & \frac{1}{(kr)^4}\sum_{n=1}^{\infty} n(n+1)(2n+1)|\psi_n(kr) + b_n\xi_n(kr)|^2 + \\ & + \frac{1}{2(kr)^2}\sum_{n=1}^{\infty}(2n+1)(|\psi_n(kr) + a_n\xi_n(kr)|^2 + |\psi'_n(kr) + b_n\zeta'_n(kr)|^2).\end{aligned} \tag{3.17}$$

In the case of particles whose size is negligibly small when compared to the wavelength of the incident line, the problem just seen simplifies to an electrostatic problem where the oscillating electric field is approximated by a constant field (quasi-static approximation). In particular, the electric field $\mathbf{E_p}$ for $ka \to 0$ reduce (1.61) and we get [144]:

$$\begin{aligned} G_{norm}(\omega, r) &= \left| 1 + 2\frac{\varepsilon(\omega) - 1}{\varepsilon(\omega) + 2} \left(\frac{a}{r}\right)^3 \right| \\ G_{tang}(\omega, r) &= \left| 1 - \frac{\varepsilon(\omega) - 1}{\varepsilon(\omega) + 2} \left(\frac{a}{r}\right)^3 \right| \end{aligned} \tag{3.18}$$

where G_{norm} and G_{tang} correspond to the normal and tangential orientation with respect to the nanoparticle's surface.

3.2.5 Enhancement of the fluorophore quantum yield

To get the enhancement of the quantum yield $Y(\omega, \mathbf{r})$ one needs to calculate radiative and nonradiative components of a molecule decay rate of a fluorophore in proximity of a metal nanoparticle [145]:

$$Y(\omega, \mathbf{r}) = \frac{Q_p(\omega', \mathbf{r})}{Q_0} = \frac{\gamma^{(r)}}{\gamma_0^{(r)}} \left[1 + Q_0 \left(\frac{\gamma^{(r)} + \gamma_p^{(nr)}}{\gamma_0^{(r)}} - 1 \right) \right]^{-1}, \tag{3.19}$$

where $Q_p(\omega', \mathbf{r})$ (3.3) and Q_0 (3.1) are the emitter quantum yield in the presence of a metal nanoparticle and in free space, respectively, ω' is the emitted frequency, $\gamma^{(r)} = \gamma_0^{(r)} + \gamma_p^{(r)}$. Decay rates can be computed in the classical electrodynamics framework [146, 147]. For radiative spontaneous decay rate the following expressions can be obtained:

$$\begin{aligned} \left(\frac{\gamma^{(r)}(\omega', \mathbf{r})}{\gamma_0^{(0)}} \right)_{norm} &= \frac{3}{2(kr)^4} \sum_{n=1}^{\infty} n(n+1)(2n+1) |\psi_n(kr) + b_n \xi_n(kr)|^2, \\ \left(\frac{\gamma^{(r)}(\omega', \mathbf{r})}{\gamma_0^{(r)}} \right)_{tang} &= \frac{3}{4(kr)^4} \sum_{n=1}^{\infty} n(n+1)(2n+1) |\psi_n(kr) + a_n \xi_n(kr)|^2 + \\ &\quad + |\psi_n'(kr) + b_n \xi_n'(kr)|^2), \end{aligned} \tag{3.20}$$

where γ_0 is the radiative decay rate in a free space (in absence of the spherical particle); r is the length of radius vector plotted from a particle center to the molecule position; the *norm* (*tang*) subscript refer to the the cases when the molecule dipole orientation is normal (tangent) to a particle surface. For the nonradiative decay rate a similar calculation can be performed. However it is more convenient to find out the full rate of spontaneous decay γ^{tot}, which is the sum of the radiative and nonradiative rates $\gamma^{tot} = \gamma^{(r)} + \gamma_p^{(nr)}$ [145]:

$$\begin{aligned} \left(\frac{\gamma^{(tot)}(\omega', \mathbf{r})}{\gamma_0^{(r)}} \right)_{norm} &= 1 + \frac{3}{2(kr)^4} \sum_{n=1}^{\infty} n(n+1)(2n+1) \mathrm{Re}\{b_n \xi_n^2(kr)\}, \\ \left(\frac{\gamma^{(tot)}(\omega', \mathbf{r})}{\gamma_0^{(r)}} \right)_{tang} &= 1 + \frac{3}{2(kr)^4} \sum_{n=1}^{\infty} n(2n+1) \mathrm{Re}\{a_n \xi_n^2(kr) + b_n (\xi_n'(kr))^2\}. \end{aligned} \tag{3.21}$$

Radiative decay in quasi-static approximation

In the quasi-static approximation $ka \to 0$ the equations (3.20) adopt the form:

$$\begin{aligned}\left(\frac{\gamma^{(r)}(\omega', \mathbf{r})}{\gamma_0^{(r)}}\right)_{norm} &= \left|1 + 2\left(\frac{\varepsilon_(\omega') - 1}{\varepsilon(\omega') + 2}\right)\left(\frac{a}{3}\right)^3\right|^2, \\ \left(\frac{\gamma^{(r)}(\omega', \mathbf{r})}{\gamma_0^{(r)}}\right)_{tang} &= \left|1 + \left(\frac{\varepsilon_(\omega') - 1}{\varepsilon(\omega') + 2}\right)\left(\frac{a}{3}\right)^3\right|^2,\end{aligned} \tag{3.22}$$

where the *norm* (*tang*) subscript indicates the radial (tangential) orientation of a molecule dipole moment with respect to a spherical nanoparticle surface. The quasi-static limit value (3.22) can also be calculated starting from the following relation [145]:

$$\frac{\gamma^{(r)}}{\gamma_0^{(r)}} = \frac{|\mathbf{p_0} + \delta\mathbf{p}|^2}{|\mathbf{p_0}|^2}, \tag{3.23}$$

where $\mathbf{p_0}$ is the is the molecule dipole moment in vacuum, and $\delta\mathbf{p}$ is the induced dipole moment which a nanoparticle acquires in the presence of a molecule.

Noteworthy, the equations (3.22) adopt the same of form of the equations (3.18). However, *norm* and *tang* subscript are referred to the orientation of the dipole with respect to the nanoparticle surface in (3.22) and to the orientation of the incident field in (3.18). Also there is a dependence on different frequencies. In (3.18) ω is the frequency of the impinging radiation whereas in (3.22) ω' is the frequency of the light emitted.

Non-radiative decay in quasi-static approximation

As regard the equations (3.21) in the quasi-static limit we get [145]:

$$\begin{aligned}\left(\frac{\gamma^{(nr)}(\omega', \mathbf{r})}{\gamma_0^{(r)}}\right)_{norm} &= \frac{3}{2(kr)^3}\sum_{n=1}^{\infty}(n+1)^2\left(\frac{a}{r}\right)^{2n+1}\mathrm{Im}\left\{\frac{\varepsilon(\omega') - 1}{\varepsilon(\omega') + \frac{n+1}{n}}\right\}, \\ \left(\frac{\gamma^{(nr)}(\omega', \mathbf{r})}{\gamma_0^{(r)}}\right)_{tang} &= \frac{3}{4(kr)^3}\sum_{n=1}^{\infty}n(n+1)\left(\frac{a}{r}\right)^{2n+1}\mathrm{Im}\left\{\frac{\varepsilon(\omega') - 1}{\varepsilon(\omega') + \frac{n+1}{n}}\right\}.\end{aligned} \tag{3.24}$$

From equations in (3.24) it results that the $\gamma_p^{(nr)}/\gamma_0^{(r)}$ diverges when the emitter molecule is approaching the nanoparticle surface. If non-radiative spontaneous decay rate tends to infinity, the quantum yield will tend to zero. This means that the luminescence quenching will occur. In this case, an excited molecule will lose energy by means of Joule heating process.

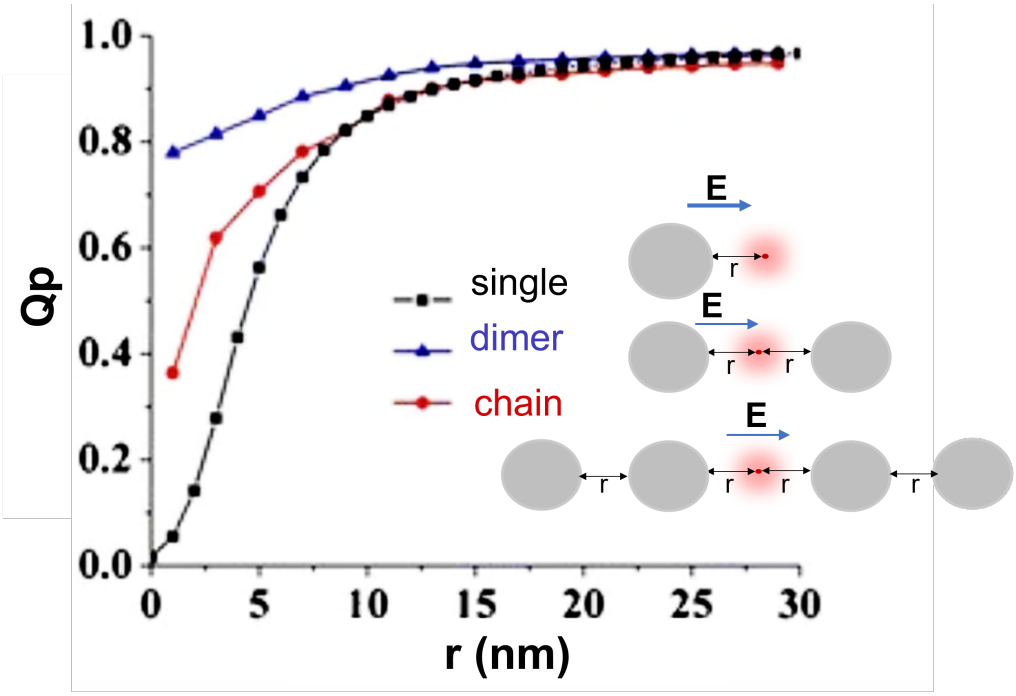

Figure 3.3: Calculated quantum yield of a fluorophore emitting ($\lambda = 480\,\text{nm}$) in proximity of a Ag spherical nanoparticle of 90 nm diameter (single, black curve), in the gap between two Ag spherical nanoparticles (dimer, blue curve), and in the gap of a chain (red curve) as a function of the separation distance from the nanoparticles surface r (adapted from [148]).

So far we assumed the emitter molecule is affected by the presence of a single metal nanoparticle. However, it has been demonstrated that a significant difference emerges when the emitter is placed in the gap of a nanoparticle dimer [148]. In particular the quenching effect occurs only for distance from the nanoparticle surface smaller than those predicted for a single nanoparticle. A comparison between the cases of an emitter molecule in proximity of a single nanoparticle, a dimer, or a chain of nanoparticles are depicted in Fig. 3.3 [148].

3.2.6 Luminescence collection efficiency

The fluorescence enhancement factor is proportional to the gain in luminescence collection efficiency $K(\omega')$ since the detected fluorescence can only receive the contribution of the photons that are actually collected by the setup [142]:

$$K(\omega') = \frac{\kappa_p}{\kappa_0}, \tag{3.25}$$

where κ_p and κ_0 are the collection efficiency in presence of the nanostructure and in free-space conditions, respectively. The luminescence collection efficiency is dependent on the directivity of the emission. We can enhance the gain by maximizing the directivity and by minimizing the collection efficiency κ used for the reference. An objective with low numerical aperture should be used in accordance with the peak angular emission of the

radiation pattern of the antenna [142], [149]. Moreover, it has been demonstrated that the nanostructures can be designed so to tune the directivity of light emission [150].

3.3 Materials and methods

3.3.1 Double-resonant nanostructure: morphology and optical response

The sensing chip is a substrate that consists of an assembly of plasmon-coupled and plasmon-uncoupled gold nanoparticles (AuNPs) immobilized onto a glass slide. Plasmon coupled AuNPs are hexagonally arranged along branch patterns whose resonance lies in the red band ($\sim 675\,\text{nm}$). Plasmon- uncoupled AuNPs are sprinkled onto the substrate, and they exhibit a narrow resonance at 524 nm. Details on the fabrication with BCMN are reported in Section 3.C.1. We describe below the morphological and optical characterizations of the substrate.

Morphology

The morphological characterization of the substrate was accomplished by scanning electron microscopy (SEM) (details are reported in Section 3.A). Fig. 3.4(a) depicts a SEM image at high magnification of the nanostructured pattern. Aiming to activate the plasmonic coupled modes of the AuNPs arranged along the branches, the particle growth was carried out to increase value of the ratio between the nanoparticle diameter and the center-to-center distance D/d (Fig. 3.4). A higher number of isolated AuNPs appears as a by-product of the growth process. Instead of representing a detriment, such isolated AuNPs trigger a localized resonance mode in addition to the coupled mode.

The histogram of the nanoparticle size before the growth process includes two Gaussian distributed populations: patterned AuNPs whose distribution is peaked at 27 nm with a standard deviation of 5 nm and isolated larger gold by-products randomly distributed onto the substrate whose size is $45 \pm 7\,\text{nm}$ (Fig. 3.4 (c)). The histogram after the nanoparticle growth includes three populations: isolated AuNPs whose diameter is $31 \pm 6\,\text{nm}$, larger AuNPs of $56 \pm 10\,\text{nm}$ diameter arranged along the branches, and isolated gold by-products of $90 \pm 15\,\text{nm}$ (Fig. 3.4 (d)).
The center to center distance distribution of patterned AuNPs did not significantly change after the nanoparticle enlargement meaning that the growth process does not alter the patter architecture (Fig. 3.4 (e),(f)). An average center to center distance of 80 nm was large enough to sustain a plasmonic coupled mode for patterned AuNPs of approximately $50 - 60\,\text{nm}$ diameter.

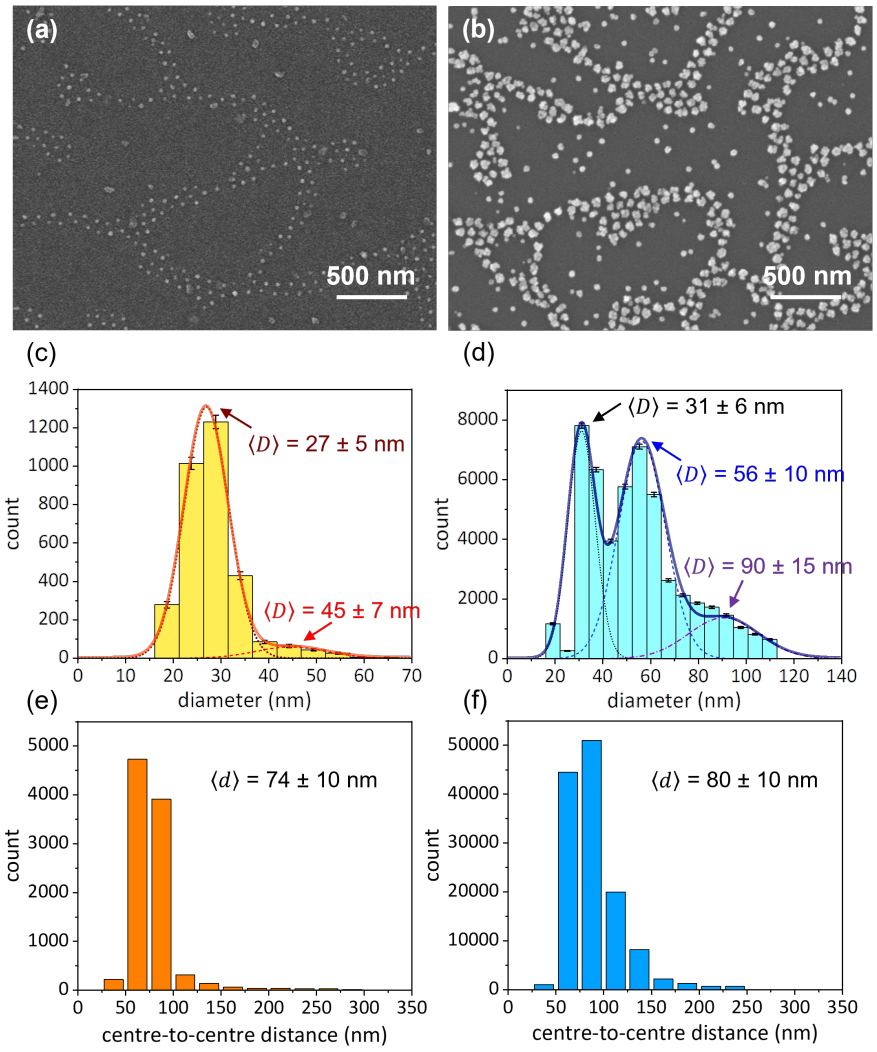

Figure 3.4: SEM images of the substrate (a) before and (b) after the nanoparticle growth. Histograms of the nanoparticle diameter (c) before and (d) after the nanoparticle growth. The solid orange and blue lines are the fits obtained by considering the histograms as the sum of (c) two and (d) three Gaussian distributed populations, respectively. Histograms of the center to center distance (e) before and (f) after the nanoparticle growth. Reproduced from [2].

Optical Response

The experimental extinction spectrum of the substrate exhibits two resonances at (i) 524 nm and (ii) 675 nm (solid black line in Fig. 3.5).

Isolated AuNPs give rise to the localized mode at 524 nm, as expected of AuNPs of 30 nm diameter in air, [151],[152] whereas (ii) patterned AuNPs entail a coupled mode at 675 nm [151]. The finite-difference time-domain (FDTD) method was adopted to solve Maxwell's equations in order to retrieve the theoretical response of the substrate when stimulated by an external electromagnetic perturbation. The simulated curve (solid gold line in Fig. 3.5) consistently reproduces that experimentally observed (solid black line in

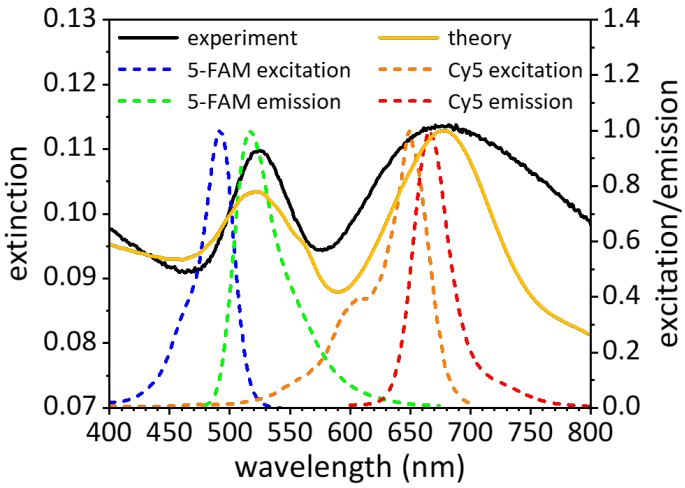

Figure 3.5: Experimental (solid black line) and theoretical (solid gold line) extinction spectrum of the substrate. Plasmon-fluorophore spectral overlap with 5-FAM (emission coupling, dashed green line) and Cy5 (dual-mechanism coupling, dashed orange and red lines) dyes. From [2]

Fig. 3.5) (technical details on FDTD simulations are reported in Section 3.B). For comparison, we also worked out the extinction spectra of the nanostructure without combination of AuNPs with different sizes (Section 3.E)

Once the substrate was optically characterized, the fluorophore should be generally chosen so that its excitation/emission peaks overlap with the plasmon extinction [109, 101].
Given the large variety of organic fluorophores apt to this aim, the spectral overlap may be virtually accomplished at any wavelengths in the visible range. In this regard, we selected 5-carboxyfluorescein (5-FAM) and cyanine 5 (Cy5) dyes whose excitation/emission spectra are reported in Fig. 3.5. While the narrow resonance at 524 nm restricts the spectral overlap to the only radiative coupling with 5-FAM dye (emission peak at 520 nm, dashed green line), the broad resonance band at higher wavelengths leads to a dual-mechanism coupling with Cy5 dye (excitation/emission 650 nm/665 nm, dashed orange and red lines).

It is worth mentioning that the choice of 5-FAM dye was not optimal since its excitation peak lay off-resonance (490 nm). In such a way, we did not fully exploit the amplification potential of the plasmonic resonance at 524 nm. Indeed, a fluorophore whose excitation peak was in the green band may experience a higher FE as compared to the 5-FAM dye.

3.3.2 Surface biofunctionalization

The substrates were PIT-functionalized with pan malaria Abs (anti-PLDH). First, the anti-PLDH concentration was varied over a large range to optimize the surface covering (Fig. 3.6(a)). Both the plasmonic resonances red-shifted as the anti-PLDH concentration

increased up to 50 μg/ml, above which the substrate is unable to house more Abs. Thus, an anti-PLDH concentration of 50μg/ml was used throughout all the experiments yielding a plasmon red-shift of approximately 4.5 nm due to the dielectric protein layer surrounding the AuNPs (Fig. 3.6(b)). The efficient surface filling is also demonstrated by the lack of significant optical change in the extinction spectrum after the blocking step (dashed red line in Figure S4b). Since the steric hindrance of a PIT-immobilized Ab is approximately 150 nm^2 [31]) the average number of Abs per nanoparticle of 60 nm (30 nm) diameter was $\sim$ 75 ($\sim$ 20). Details on the biofunctionalization protocol are reported in Section 3.C.2.

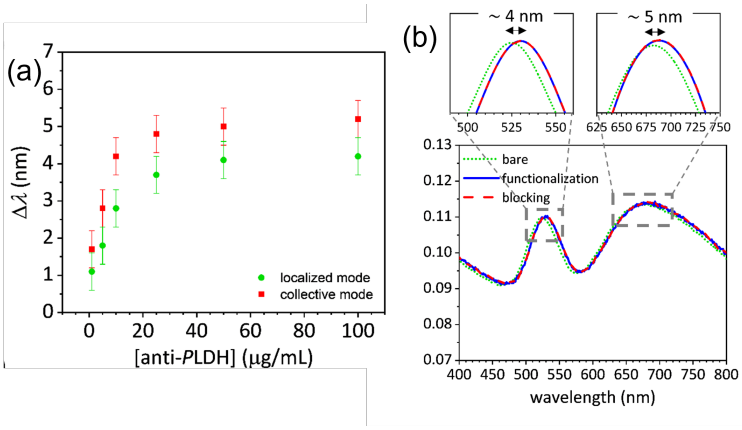

Figure 3.6: Shift of the plasmon resonance wavelengths as a function of anti-PLDH concentration for the localized (green circles) and collective (red squares) modes. Both the resonances red-shift as the anti-PLDH concentration increased up to 50 μg/ml that corresponds to a maximum redshift of approximately $4-5$ nm . (b) Experimental extinction spectrum of the substrate before (dotted green line) and after functionalization (solid blue line) and blocking (dashed red line). The insets show the Gaussian fits used for evaluating the plasmon resonance wavelength. Reproduced from [2].

3.3.3 Detection scheme

The biosensing application was conceived as a case study for evaluating the performance of the proposed substrate as a fluorescence enhancer in a PEF-based biosensor in multiplexed measurements for simultaneously detecting two different analytes.
The multiplexed detection was obtained by adopting the sandwich configuration Ab-analyte-Apt* shown in Fig. 3.7(a). Fig. 3.7(b) shows some representative fluorescence pictures at different analyte concentrations. Notably, the bright spot number is clearly distinct from the control (i.e., uninfected human whole blood) down to the picomolar level for both the fluorophores (details about acquisition and processing of fluorescence pictures are reported in Section 3.D.1).
Note that the fluorescence of each bright spot is likely to arise from one single fluorophore as explained in detail in Section 3.3.4.

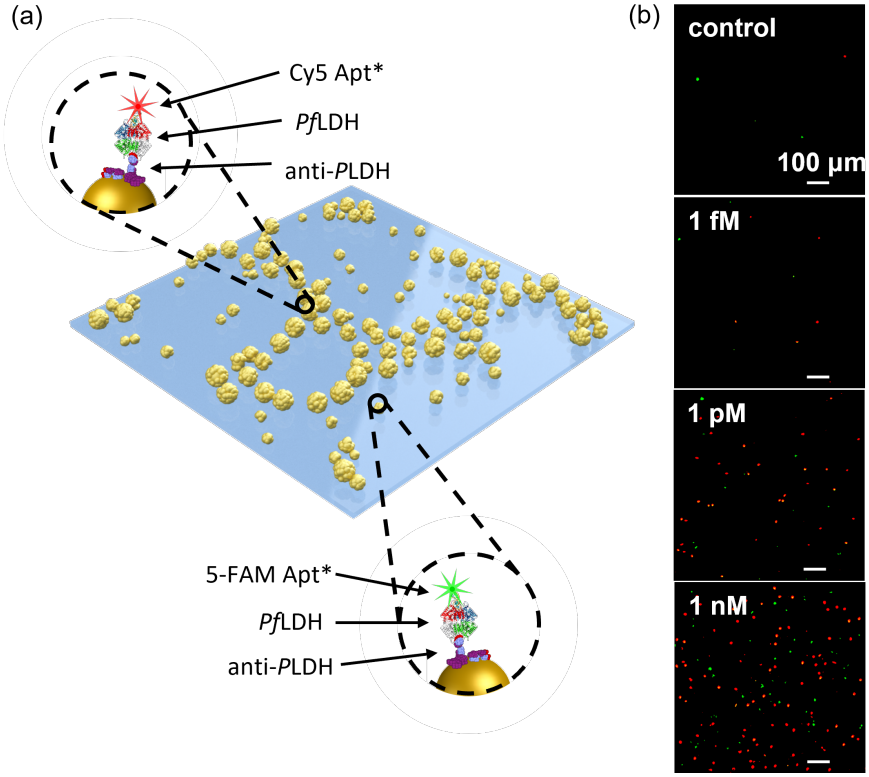

Figure 3.7: a) Sketch of the pattern architecture consisting of branch hexagonally arranged and sprinkled AuNPs. The insets show the Ab-PfLDH-Apt* sandwich schemes in the case of 5-FAM and Cy5 labels. (b) Example of fluorescence images recorded at different PfLDH concentrations spiked in human whole blood. From [2].

3.3.4 Analysis of the bright spots

In order to demonstrate the assumption that the fluorescence of each bright spot corresponds to the light emitted by one single fluorophore, we firstly considered the lowest PfLDH concentrations (1 fM) we investigated (Fig. 3.7). The corresponding number of analytes in 1 mL volume (i.e., the volume we used throughout the work) is 6×10^5. Thus, in principle we can have 6×10^5 PfLDH proteins over the whole substrate ($10 \times 8\,\mathrm{mm}^2$) and, hence, 2×10^4 analytes can be virtually housed in the microscope field of view (FOM) ($1.66 \times 1.40\,\mathrm{mm}^2$). In ideal conditions, 2×10^4 fluorophores bind the analytes in the FOM. The photodetector contains 5.51×10^6 pixels (Section 3.D.1). We can now evaluate the probability that two fluorophores lie on an area of the substrate whose fluorescence would be collected by one pixel ($, 0.650 \times 0.650\,\mu\mathrm{m}^2$, see Section 3.D.1). Since the number of fluorophores (2×10^4) is much smaller than the number of pixels (5.5×10^6), we can adopt the Poisson statistics to retrieve the probability $P(k)$ that k fluorophores are placed in one pixel4

$$P(k) = e^{\frac{m}{n}} \frac{(m/n)^k}{k!},$$

where m is the number of fluorophores and n is the number of pixels. It results $P(2) = 0.0005\,\%$. Therefore, we can safely assert that bright spots appearing in fluorescence

images at very low PfLDH concentration (femtomolar level) arise from individual fluorophores.
Moving to the next PfLDH concentrations we explored 1 pM, 1 nM, and 1 μM, the number of fluorophores housed in the FOM in ideal conditions is 2×10^7, 2×10^{10}, and 2×10^{13}, respectively. Since $m > n$, we evaluated the probabilities $P(0)$ that one pixel is vacant. Since $P(0) = e^{-m/n}$, it results 43% at 1 pM and negligible values at 1 nM and 1 μM. However, considering l dark pixels, the probabilities are much lower $P^{(l)}(0) = e^{-ml/n}$. For instance, $P^{(10)}(0) = 0.02\%$ at 1 pM. Nevertheless, in real measurements a much larger number of dark pixels were present as compared to the number of bright spots even at the largest PfLDH concentration (Fig. 3.7(b)). This result can be reasonably achieved only if $m \ll n$.
Such a discrepancy can be justified considering a low system efficiency that depends on

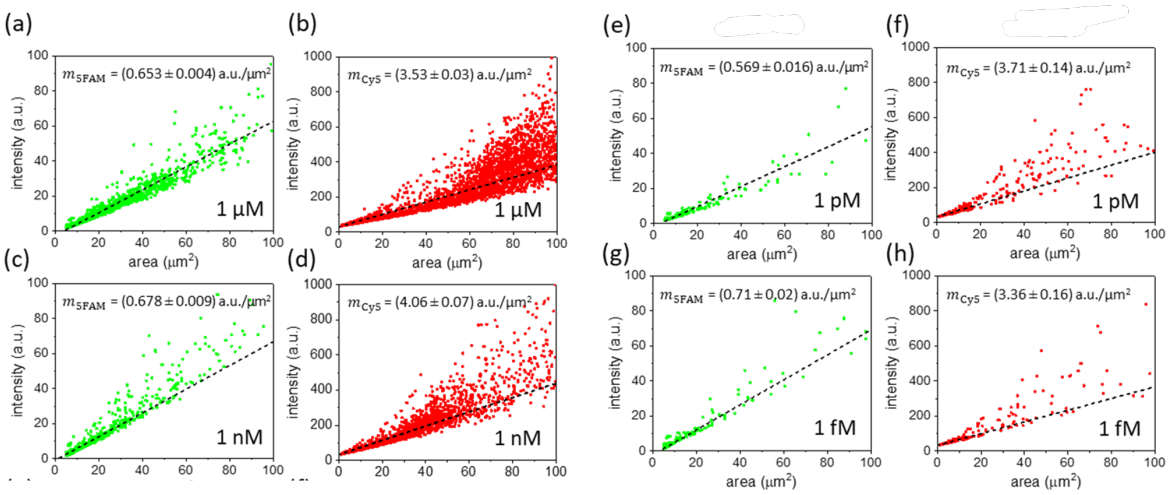

Figure 3.8: Correlation intensity vs spot area explored by (a) 5-FAM dye and (b) Cy5 dye at different PfLDH concentration spiked in whole blood (Pearson's $r = 0.95$). From [2].

(i) the binding affinities between Abs-Au, Abs-PfLDH and Apts*-PfLDH and (ii) the fluidic efficiency in each step. Thus, only a small amount of the available fluorophores would be housed on the substrate and only a tiny fraction of them would experience a significant FE. Therefore, we can assume that the condition $m < n$ is hold even at large concentrations (up to micromolar level) and, hence, the probability $P(l)$ that $l \geq 2$ fluorophores lie on one pixel is low.
The previous argumentation is coherent with the linearity exhibited by the correlation curves fluorescence versus spot area (Fig. 3.8). The slope of the linear regressions is independent from the PfLDH concentration revealing that the mean fluorescence intensity per pixel at low analyte concentrations (femtomolar level) is hold even at high concentrations (micromolar level).
In addition, the number of bright spots whose intensity/area ratio lies outside the linear regression is relatively low even if it enlarges as the analyte concentration increases.
In particular, these spots arose from nearby fluorophores whose light was collected by the same pixels of the photodetector so to increase the spot brightness while holding the spot

size. In conclusion, we can safely assert that most of the observed bright spots arise from individual fluorophores.

3.4 Biosensing application

Calibration Curve

The dependence of the fluorescence intensity F on the analyte concentration is shown in Fig. 3.9 (details about fluorescence analysis are reported in Section 3.D.1). The data are fitted by the four-parameter Hill equation [153]:

$$F([Pf\text{LDH}]) = F_1 + \frac{F_2 - F_1}{1 + \left(1 + \frac{K}{[Pf\text{LDH}])^n}\right)}, \tag{3.26}$$

where F_1 and F_2 are the minimum and maximum value of the fluorescence intensity, respectively, K is the concentration at which the fluorescence is equal to half of its maximum value, and n is the so-called Hill's coefficient [154]. Table 1 reports the best-fit parameter values, the linear range (LR), and the limit of detection (LOD), estimated as 3σ above the control value, for both the fluorescent dyes used in this work.

parameters	5-FAM	Cy5
F_1	7 ± 1 arb. units	6 ± 2 arb. units
F_2	66 ± 3 arb. units	154 ± 2 arb. units
K	$(0.36 \pm 0.15)10^3$ pM	6 ± 1.7 pM
n	0.36 ± 0.05	0.44 ± 0.06
χ^2	1.2	1.8
LR	10 pM − 1 μM	100 kM − 1 nM
LOD	50 pM (1.6 ng/ml)	260 fM (8.6 pg/ml)

Table 3.1: Best-Fit Parameter Values and LOD obtained by fitting the experimental data in (3.26).

Specificity

The specificity of the proposed apta-immunosensor was tested against the Plasmodium vivax lactate dehydrogenase (PvLDH) (90% residue identity with the PfLDH) [155]. To this aim, the desired amount of PvLDH (1 μM referred to undiluted blood) was spiked into the diluted specimens (human whole blood from healthy donors 1 : 100 diluted in 1 ml of 25 mM Tris buffer). Fig. 3.9(b) illustrates the fluorescence intensity measured in human whole blood with no analyte (control), competitive analyte (PvLDH), and analyte of interest (PfLDH). Although the bottom bioreceptor layer, consisting of pan malaria anti-PLDH, can capture any Plasmodium malaria marker, the high selectivity of malaria aptamers warranted a negligible cross-reaction with PvLDH [156].

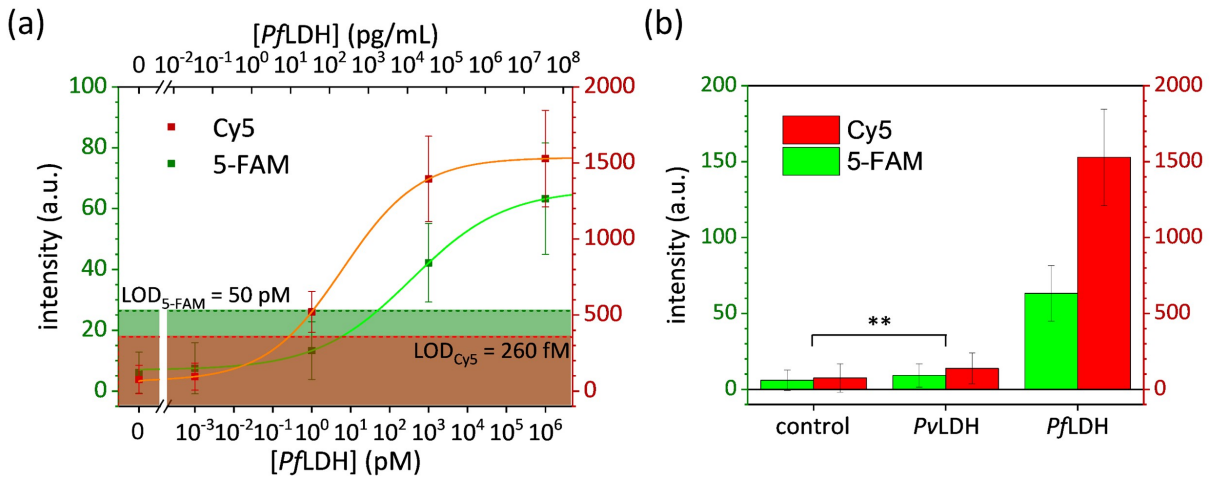

Figure 3.9: Fluorescence intensity as a function of PfLDH concentration spiked in human whole blood (calibration curve). The best fit curves (solid green and orange lines) are the four-parameter Hill eq.(3.26). The shaded regions represent the 3σ noise level measured in uncontaminated whole blood. (b) Specificity of the apta-immunoassay against the PvLDH ($**$ p $-$ value < 0.001). The data are averaged on ten measurements and are reported as mean value $\pm$ standard deviation. From [2].

3.5 Simulations

3.5.1 Fluorescence Enhancement: electromagnetic simulations

We investigated the electromagnetic response of the substrate when interacting with a plane wave radiation E_0. The ratio between the intensity of the electric field induced by the nanostructure, E, and the intensity of the incident radiation is defined as the gain factor G where ω is the frequency of the impinging perturbation and r is the position vector (Section 3.2.4):

$$G = \frac{|\mathbf{E}(\omega, \mathbf{r})|}{|\mathbf{E_0}(\omega, \mathbf{r})|}. \tag{3.27}$$

We modeled the nanostructure according to the architecture morphology provided by SEM images. In addition, we implemented a surface roughness onto each nanoparticle to approach the observed nanoparticle shape (Section 3.B for details).
Since the size of the fluorophores we used is $\sim 1\,\mathrm{nm}^3$ [157], we discretized the substrate over a mesh with 1 nm spatial resolution so that a dye can fit in a unit cell. Fig. 3.10(a)-(c) shows the intensity distributions of the electric field at the emission peak of 5-FAM (520 nm) and at the excitation/emission peaks of Cy5 (650/665 nm), whereas those off-resonance (490 nm and 575 nm) are depicted in Fig. 3.11.

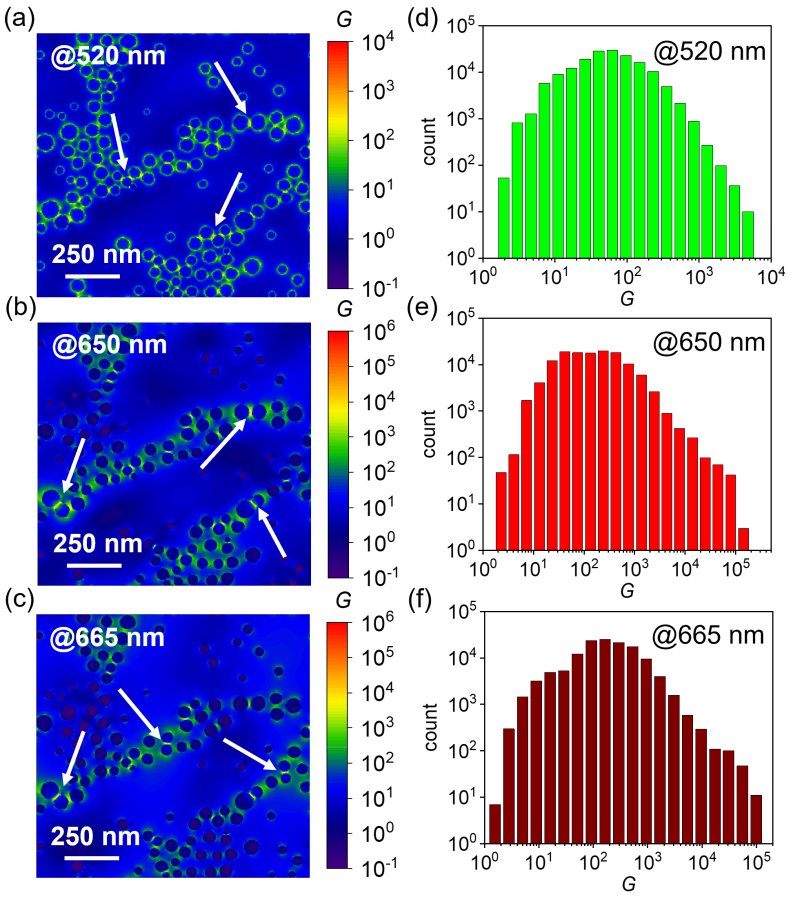

Figure 3.10: Simulated electric field intensity of the substrate worked out at wavelength (a) 520 nm, (b) 650 nm, and (c) 665 nm. The white arrows point to some plasmonic hot spots of the nanostructure. Histograms of the G value distribution evaluated in annulus-shaped regions around nanoparticles (5 nm thickness, 5 nm offset from particle surface) at wavelength (d) 520 nm, (e) 650 nm, and (f) 665 nm. From [2].

Regions surrounding nanoparticles exhibit higher G values as compared to the free space as a result of the strong confinement of the electric field: these regions are generally called hot spots [144].
At 520 nm wavelength, the main contribution to the electric field arose from the dipolar modes of nanoparticles. In this case, the electric field was mainly enhanced at the nanoparticle edges (along the polarization direction) or confined at the nanoparticle dimer junctions (Fig. 3.10(a)). However, such a plasmonic mode (i.e., not coupled mode) yielded a relatively low amplification (G values do not exceed few thousand).
On the contrary, much higher G values (up to hundreds of thousands) were observed at 650 nm and 665 nm wavelengths as a result of the strong inter-plasmon coupling among nearby AuNPs (Fig. 3.10(b),(c)).
A possible way to capture the physics underlying the coupled modes relies on the so-called plasmon hybridization method, [61, 60] according to which the modes resulting from a single nanoparticle mix (hybridize) with those from the nearby nanoparticles giving rise

to bonding and anti bonding plasmonic modes (see Section 1.3.8).
Since we aimed at using this platform for sensing applications where fluorophores are placed at a distance of $5-10$ nm from the surfaces of the nanoparticles, we focused our analysis on these annulus-shaped regions around each nanoparticle.

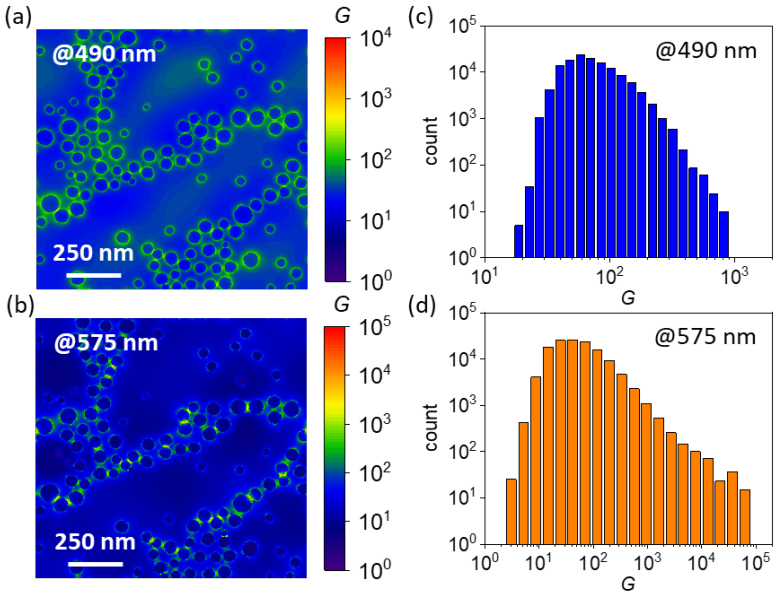

Figure 3.11: Simulated electric field intensity of the substrate worked out at wavelength (a) 490 nm and (b) 575 nm. Histograms of the G value distribution evaluated in annulus-shaped regions around nanoparticles (5 nm thickness, 5 nm offset from particle surface) at wavelength (c) 490 nm and (d) 575 nm. From [2].

In particular the electric field E_n around the n-th nanoparticle was evaluated in the $x-y$ plane in annuluses of 5 nm thickness and 5 nm offset from the nanoparticle surface via $E_n(r,\phi) = E(x_n + r\cos\phi, y_n + r\sin\phi)$ where r is the distance from the nanoparticle centroid (1 nm spatial resolution), ϕ is the azimuthal angle (1 degree of angular resolution), and (x_n, y_n) are the centroid coordinates. Note that r values range from $D_n/2 + 5$ nm to $D_n/2 + 10$ nm, in which D_n is the diameter of the n-th nanoparticle measured by SEM micrographs (Section 3.A). We implemented the E_n in a Python code that excluded multiple counting in overlapping annuluses.
Fig. 3.12 shows two representative magnifications of the electric field intensity worked out with perfectly spherical gold nanoparticles and rough gold nanoparticles, in which the shaded red annuli highlight the only regions where the G values were evaluated.

Fig. 3.10 shows the G value distributions in these regions at wavelengths of 520, 650, and 665 nm , respectively. The histograms reveal that only a tiny fraction of fluorophores would experience a relatively high G value meaning that most of them were positioned in places whose local amplification may not be strong enough to yield a measurable fluorescence. Additionally, we worked out the electromagnetic response of the substrate

with perfectly spherical nanoparticles (see Section 3.B for details).
In this case, much lower G values were attained revealing that the surface roughness was a crucial feature to augment the local field [158].

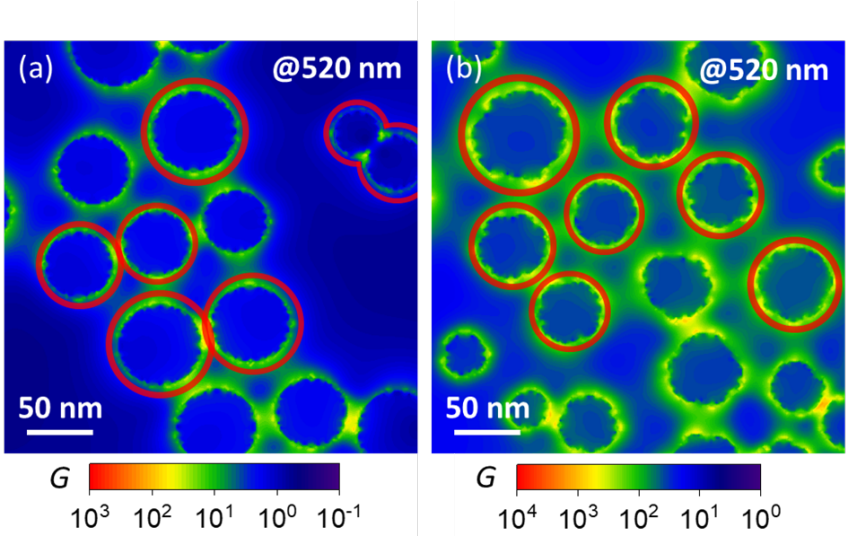

Figure 3.12: Electric field intensity distributions of (a) perfectly spherical gold nanoparticles and (b) rough gold nanoparticles worked out at 520 nm wavelength. The shaded red annuluses (5 nm thickness, 5 nm offset from the nanoparticle surface) highlight the regions where the G values were evaluated. Note that in the case of rough nanoparticles, the annulus offset is determined by considering an ideal spherical surface embedding the nanoparticle roughness. From [2].

3.5.2 Comparison between theoretical and measured Fluorescence Enhancement

The theoretical fluorescence enhancement factor is defined as

$$FE^{th}(\omega,\omega') = G(\omega)\frac{Q(\omega'}{Q_0} \tag{3.28}$$

where Q is the fluorophore quantum yield in PEF conditions, Q_0 is the fluorophore quantum yield in free-space, ω and ω' are the excitation and emission frequency, respectively. We aimed at comparing the FE^{th} values at excitation/emission wavelengths of the fluorophores with those experimentally measured (later described).
Since Q_0 is an inherent parameter of the fluorophore, the ratio Q/Q_0 is bounded above due to the constraint $Q <= 1$. Considering $Q^0_{5-\mathrm{FAM}} = 0.83$ at 520 nm wavelength for 5-FAM dye [159] and $Q^0_{Cy5} = 0.27$ at 665 nm wavelength for Cy5 dye [160], the ratio Q/Q_0 cannot exceed 1.2 for 5-FAM dye and 3.7 for Cy5. For simplicity, we firstly investigated the case $Q = Q_0$.
Thus, the G value distributions shown in Fig. 3.11(c) and Fig. 3.10(e) can be immediately converted into (FE^{th}) distributions at 490/520 nm and 650/665 nm excitation/emission,

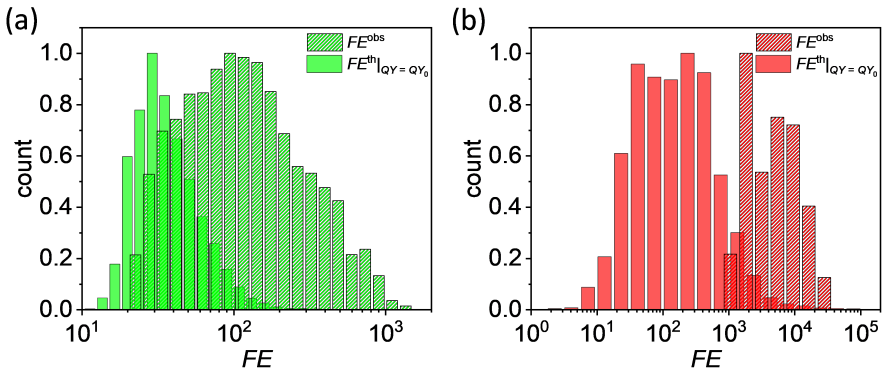

Figure 3.13: Experimental (top sub-panels) and theoretical (bottom sub-panels) FE distributions for (a) 5-FAM and (b) Cy5 dyes. Theoretical distributions are worked out at (a) 490/520 nm and (b) 650/665 nm excitation/emission wavelengths in the case $Q = 1$. The experimental histograms were obtained over an area of $1.66 \times 1.40\,\mathrm{mm}^2$, whereas the theoretical histograms were worked out over an area of $1.25 \times 1.25\,\mu\mathrm{m}^2$. From [2].

respectively. As it concerns the measured FE factor, it can be estimated as [161]:

$$\mathrm{FE}^{obs} = \frac{I_{PEF}}{\langle I_0 \rangle}, \tag{3.29}$$

where I_{PEF} is the fluorescence intensity provided by fluorophores in the presence of the nanostructure and $\langle I_0 \rangle$ is the mean fluorescence signal of fluorophores under non-PEF conditions (details are reported in Section 3.D.2). Fig. 3.13(a),(b) shows the FE^{obs} distributions for 5-FAM and Cy5 dyes, respectively (top sub-panels). Thus, we can compare such distributions with FE^{th} distributions worked out in the case $Q = 1$ (bottom sub-panels).

A slight discrepancy emerges between FE^{obs} and FE^{th} distributions in both the fluorophore channels probably ascribable to an underestimated nanoparticle roughness in the simulation modeling. Note that such a discrepancy would rise if perfectly spherical nanoparticles were considered (Fig. 3.14) rather than rough nanoparticles, thus corroborating the crucial role played by the nanoparticle roughness in enhancing the fluorescence. An estimation of the average FE factor, $\langle \mathrm{FE}^{obs} \rangle$, can be retrieved by [161]:

$$\langle \mathrm{FE}^{pbs} \rangle = \frac{\sum_{k=1}^{N_{PEF}} (I_{PEF})_k}{\langle I_0 \rangle N_{PEF}}, \tag{3.30}$$

where N_{PEF} is the number of bright spots. Equation (3.29) yields $\langle \mathrm{FE}^{obs}_{5FAM} \rangle = 160$ for 5-FAM dye and $\langle \mathrm{FE}^{obs}_{Cy5} > = 4500$ for the Cy5 dye. It is worth mentioning that the ratio between $\langle \mathrm{FE}^{obs}_{Cy5} \rangle$ and $\langle \mathrm{FE}^{obs}_{5FAM} \rangle$ of approximately 28 is consistent with the ratio between the slopes of the corresponding correlation curves (fluorescence vs spot area, see Section 3.3.4).

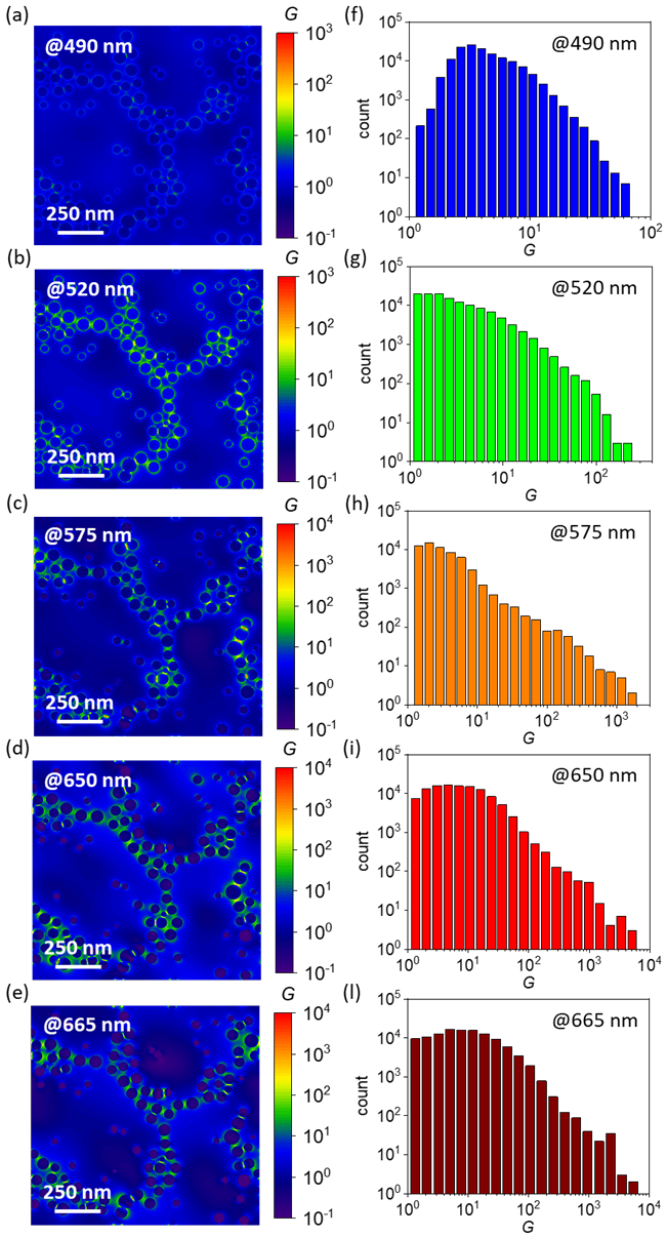

Figure 3.14: Simulated electric field intensity of the substrate in the case of perfectly spherical AuNPs worked out at wavelength (a) 490 nm, (b) 520 nm, (c) 575 nm, (d) 650 nm, and (e) 665 nm. Histograms of the G value distribution evaluated in annulus-shaped regions around nanoparticles (5 nm thickness, 5 nm offset from particle surface) at wavelength (f)490 nm, (g) 520 nm, (h) 575 nm, (i) 650 nm, and (l) 665 nm. From [2].

3.6 Conclusions

We presented a novel double-resonant plasmonic substrate for potential multiplexed and high-throughput analysis in PEF-based biosensing [2]. The substrate consists of an assembly of hexagonally arranged and sprinkled AuNPs, which gives rise to a double resonance at 524 nm and 675 nm wavelengths. The former was coupled with the emission peak of the 5-FAM dye and the latter with both the excitation and emission peaks of the Cy5 dye.
Numerical simulations demonstrated that the pattern architecture endowed the substrate with a large amount of intense electromagnetic hot spots in which fluorophores can be housed.

As a case-study, the substrate was implemented in a malaria apta-immunoassay for detecting PfLDH in human whole blood. We adopted Abs as capture bioreceptor layer and Apts* as the top fluorescently labeled layer. The PfLDH was simultaneously detected by both the fluorophores as proof of concept for multiplexed analysis. Additionally, the simultaneous detection of two fluorescent probes can provide high signal redundancy and an extension of the detection range. The LODs achieved are 260 fM with the Cy5 dye and 50 pM with the 5-FAM dye. No complex sample pretreatments are required making such a device suitable for point of care tests.
The measured average values of the fluorescence enhancement FE were 160 with 5-FAM dye and 4500 with Cy5 dye. We proved that these results are consistent with those simulated by considering branch patterns of rough AuNPs and that the roughness is crucial. As futuristic scope, multi-resonant devices may be also conceived by properly tailoring the pattern architecture or combining different metal nanoparticles in such a way to active additional plasmonic modes. Moreover, sharp nanoparticles may further augment the electromagnetic field by at least one order of magnitude as compared to smooth nanoparticles as simulations revealed. The potential biosensing applications of the proposed approach are far-reaching, for not only multi-analyte detection but also biomarker panel identification with double signal redundancy.

Appendix

3.A Analysis of scanning electron micrographs

SEM images were acquired by Zeiss LEO 1550VP field emission scanning electron microscope with a nominal resolution of 1 nm at 20 kV acceleration voltage by collecting secondary electrons with an In-Lens detector. The morphology of the substrate was analysed processing the micrographs by *ImageJ* software. Firstly, objects were isolated from the background by thresholding the raw image (Fig. 3.15(a),(b)), then adjacent nanoparticles were segmented by watershedding (Fig. 3.15(c)). *Analyze Particles* tool implemented in *ImageJ* was run to retrieve information about the object perimeter p, area S, shape descriptors, and centroid coordinates. Figure S1d shows an example of processed micrograph in which the nanoparticles are decomposed in outline and inner area. Afterwards, nanoparticle diameter was estimated as $D = 2\sqrt{(S/\pi)}$, whereas the centre-to-centre distance distribution was carried out by calculating the distance of each centroid from its nearest neighbours.

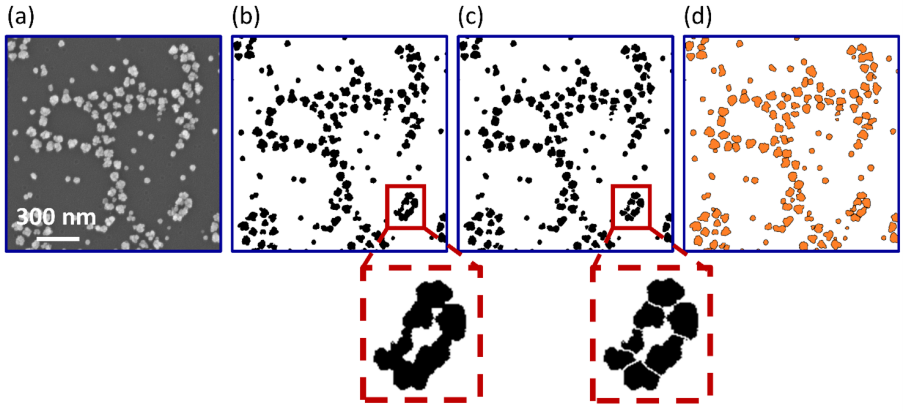

Figure 3.15: (a) Example of raw SEM micrograph at high magnification. Corresponding (b) thresholded and (c) segmented image. The insets show a magnification of a nanoparticle cluster highlighting the capability to effectively segment adjacent objects by the watershedding algorithm. (d) Processed image in which the nanoparticles are decomposed in outlines (black line) and inner region (orange filling). From [2].

3.B Numerical simulations

The optical response of the nanostructured substrate was simulated by using the finite-difference time-domain (FDTD) method implemented in *FDTD solutions* tool of Lumerical software. The Maxwell's equations are numerically solved in the time domain within a Mie problem-like framework by discretizing the space over a mesh and evaluating the evolution of the electric and magnetic fields in each cell.

Branch pattern of spherical AuNPs

An illustration of the simulation workspace is shown in Fig. 3.16(a).

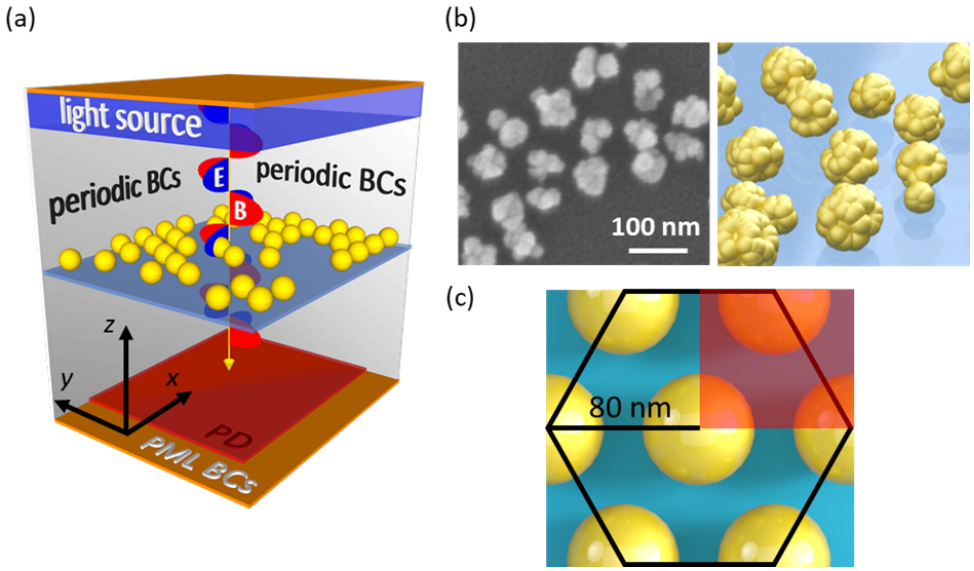

Figure 3.16: (a) Sketch of the simulation workspace consisting of light source, plasmonic nanostructure, dielectric substrate, photodetector (PD), and appropriate boundary conditions (BCs). (b) Comparison between the real morphology of the substrate observed by SEM (left panel) and a representative model employed in FDTD simulations (right panel). (c) Example of Au spheres arranged in a hexagonal cell. The shaded red rectangle represents the region in which the Maxwell's equations are numerically solved. Then, the solutions are symmetrically/anti-symmetrically extended to the whole hexagonal cell. From [2].

The optical behaviour of the substrate was explored through linearly polarized waves ($400-800$ nm wavelength, $0-180°$ polarization angle with angular step of $15°$) propagating along z direction. A photodetector placed in the $x-y$ plane was dedicated to measure the electric field over time ($1.25 \times 1.25 \mu m^2$ size) (not shown in Fig. 3.16(a)), whereas a second photodetector positioned on the opposite side of the workspace was set to collect the transmitted photons to work out the extinction spectrum of the nanostructure ($400-800$ nm wavelength, 1 nm spectral resolution). The nanostructure was realized by positioning homogeneous gold spheres1 onto a layer of silicon dioxide2 (200 nm thickness) according to the real morphology provided by SEM images. Nanoparticle centroids and

diameters were retrieved by raw SEM images as described in Section 3.A.

Then, homogeneous gold spheres were shaped in the Lumerical environment using *addsphere* script command. The refractive index of surrounding environment was set equal to 1. Periodic boundary conditions (BCs) were set along x and y directions to extend the simulation over an infinite array.
Bloch BCs were used for simulations with non-zero polarization angles in order to compensate the phase shift arising when an electromagnetic disturbance with a non-zero angle should be re-injected at the opposite workspace site. Perfect matched layer BCs along z direction (steep angle profile, 12 layers) warranted the complete absorption of the wave backscattered through the light source and that traveling beyond the photodetector [162].

The spatial resolution of the mesh was set equal to 1 nm to warrant high accuracy of the results while holding the simulation time within few hours.

Branch pattern of rough AuNPs

Technical parameters of simulations were set as in the Section S2.A. In addition, we implemented a degree of roughness onto the surface of spheres. Firstly, homogenous gold spheres were placed onto a layer of silicon dioxide2 (200 nm thickness) according to the real morphology. The diameters were reduced of 20 nm as compared to the real size (see Section 3.A). Secondly, gold hemispheres of radius 20 nm were randomly arranged onto the spherical surfaces allowing interpenetration. More precisely, 20 (40) (80) (120) (160) (200) gold hemispheres were placed onto spheres whose real diameter lied in the range $10-20$ nm $(20-30$ nm$)$ $(30-40$ nm $)$ $(40-60$ nm$)$ $(60-80$ nm$)$ $(>80nm)$. The size of the resulting rough spheres as well as their degree of roughness was comparable with the real one observed by electron microscopy (Fig. 3.16(b)).

3.C Protocols

3.C.1 Substrates fabrication

BCMN was adopted to fabricate branch patterns of hexagonally arranged AuNPs over a large area [135]. The procedure included four steps sequentially shown in Fig. 3.17.

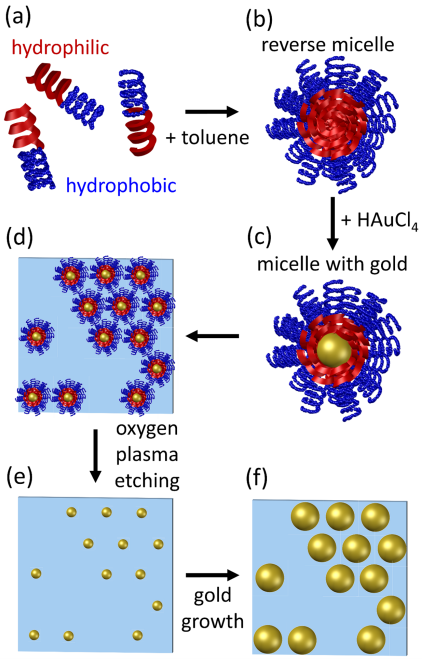

Figure 3.17: Fabrication scheme of the branch pattern of AuNPs by BCMN. (a) Dispersion of amphiphilic diblock copolymers in nonpolar solvent. (b) Self-assembly of reverse micelles. (c) Formation of Au seeds inside the hydrophilic core. (d) Laying of PS-AuNPs on the substrate. (e) Sticking of the AuNPs onto the glass slide after the copolymer etching. (f) Enlargement of the nanoparticle size. From [2].

An amount of 24.3 mg of diblock copolymer P3807-S2VP (Fig. 3.17(a)) was dispersed into 15 ml of toluene. The solution was kept under vigorous stirring for 72 h to obtain a homogeneous monodisperse solution of reverse micelles (Fig. 3.17(b)).
An amount of 13.1 mg of $HAuCl_4 \cdot 3H_2O$ was loaded into the solution under vigorous stirring for 72 h to allow the inception of Au seeds (inside the micelle core) covered by polystyrene shells (PS-AuNPs) (Figure 7c). The solution appears yellowish.
Then, possible copolymer aggregates were removed by filtering the solution. Diblock copolymers and gold(III) chloride trihydrate were handled in a glovebox under inert gas (argon) and controlled conditions ($O_2 < 1$ppm , $H_2O < 0.1$ ppm).
Before the PS-AuNP deposition onto the substrate, glass coverslips ($10 \times 8\,mm^2$) were sonicated for 5 minutes in acetone, 2-propanol, and ethanol sequentially to remove dust and impurities.
Afterward, the cleaned substrates were dipped in a nonpolar solvent (toluene) to enable the sticking of hydrophobic polystyrene shells. Then, the substrates were vertically dipped into the solution of PS-AuNPs by means of a dip-coater to warrant an extremely fine positioning and speed control. The dipping speed was set to 0.8 mm/s. Such a speed is low enough to warrant PS-AuNP laying onto the substrate while preventing the maximum close-packing (Fig. 3.17(d)).
Finally, an oxygen plasma treatment (0.8 mbar , 200 W , 30 min) was used to etch the copolymers so to leave the AuNPs immobilized onto the substrates (Fig. 3.17(e)).
Afterward, the substrates were incubated with 2 ml of gold growth solution (CTAB 190 mM, $HAuCl_4 \cdot 3H_2O$ mM ,$AgNO_3$ 8 mM, ascorbic acid 100 mM) for 2 h enabling the

increase of AuNP size while holding center-to-center distances (Fig. 3.17) [163].

3.C.2 Biofunctionalization and detection

Gold surface functionalization with pan malaria anti-PLDH was realized through the well-established PIT (Section 1.1.2). The aqueous solution containing anti-PLDH (50 μg/ml concentration, 1 ml volume) was UV irradiated for 30 s (6 W at 254 nm) and conveyed onto the substrate. The latter was integrated in a microfluidic system consisting of an interacting cell housing the substrate, a 2 ml syringe, and Tygon tubes with a diameter of 1 mm (for both the input and output channel) designed for biological samples (Fig. 3.18).

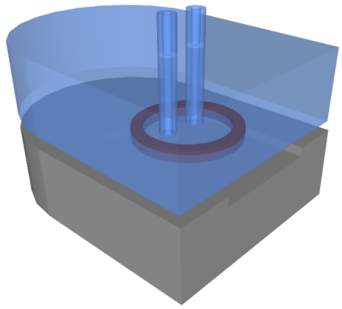

Figure 3.18: Sketch of the fluidic cell used to promote an effective interaction of the irradiated Abs contained into the aqueous solution with the nanostructured substrate. From [2]. From [2].

The volume of the solution in contact with the substrate was $\sim 30\,\mu l$, whereas the total volume flowing into the circuit was approximately $200\,\mu l$. The syringe was used to repeatedly draw $250\,\mu l$ from the fresh solution containing the irradiated Abs (4 draws separated by a time interval of 3 min). Then, ultrapure water was copiously flowed into the circuit to remove the unbound Abs from the substrate. The blocking step was carried out by flowing into the circuit an aqueous solution of 50 μg/ml BSA (4 draws of 250 μl separated by a time interval of 1 min). Afterward, ultra-pure water was copiously flowed into the circuit to remove unbound BSA molecules. Finally, the substrates were stored in PBS solution at room temperature.

Ab-Analyte-Apt* Stacking

Blood specimens were drawn from the healthy donors via monovette tubes. Ethylenediaminetetraacetic acid (EDTA) was added to prevent blood coagulation. Whole blood was diluted 1 : 100 in 25 mM Tris buffer to reduce the turbidity of the specimen.
The analyte was spiked into 1 ml of the diluted specimen to achieve a PfLDH concentration in the range 1 fM $-$ 1 μM(referred to undiluted whole blood). Control experiments were performed in uncontaminated specimens (diluted whole blood).
The functionalized substrates stored in the buffer solution (ready-to-use) were slightly rinsed by ultra-pure water and then incubated with PfLDH-spiked specimens (diluted whole blood) by gently shaking the sample for 2 h to improve the PfLDHcapture efficiency

by immobilized Abs. Afterward, the substrates were abundantly rinsed by ultra-pure water and Tris buffer to remove blood residues and unbound PfLDH molecules.
5-FAM- and Cy5-labeled malaria Apt* were added in the ratio 1 : 1 into 1 ml of PBS (10 mM) to achieve a final Apt* concentration of 0.1 μM. Thus, the substrates were transferred into the solution by gently shaking the bowl for 2 h h in dark conditions, thereby realizing the Ab-PfLDH-Apt* sandwich scheme shown in Fig. 3.7(a). Then, the substrates were copiously rinsed by ultra-pure water and PBS to remove unbound Apts*.

3.D Fluorescence Pictures

3.D.1 Acquisition and Analysis

Fluorescence images were acquired by Zeiss Axio Observer Z1 inverted phase contrast fluorescence microscope equipped by Zeiss Colibri.2 LED light source (modules 470 and 625 nm), Zeiss Plan-Apochromat $10x/0.45$ Ph1 M27 (FWD = 2.1 mm) objective, 38 HE filter (excitation $450-490$ nm/emission $500-550$ nm) and cube 50 Cy5 filter (excitation $625-655$ nm/emission $665-715$ nm), and pco.edge 5.5 sCMOS photodetector (scaling $0.650\,\mu$m $\times$ 0.650μm per pixel, image size 2560×2160 pixels, scaled image size 1.66 mm $\times$ 1.40 mm, 16 bit dynamic range). The camera exposure time was set to 2 s for recording every image. Raw fluorescence images were processed by *ImageJ* to measure the whole intensity arising from the bright spots. Firstly, RGB images were split into two channels containing the green and red components so to separately analyse the contribution of the two fluorophores used in this work. Since the raw images contained a smooth continuous background, the rolling ball algorithm was used to flatten any spatial variations of the background by evaluating the average value over a ball around each pixel and then by locally subtracting such a value from the image. Aiming at carrying out a reliable and robust analysis, one different substrate was used for each analyte concentration (rather than exploit additive concentrations on the same substrate), and ten fluorescence images were randomly acquired over each sample thereby obtaining an average value of the whole fluorescence intensity $\pm$ standard deviation.

3.D.2 Fluorescence intensity in non-PEF conditions

To measure the intensity $\langle I_0 \rangle$, a volume of 100 μl containing 250 fmol of Apts* (approximately 1.5×10^11 fluorophores) was drop-casted onto a microscope slide. After drying, the 5-FAM (Cy5) fluorophores resulted to be confined within a circular region of 12 nm (13 nm) diameter surrounded by an annulus (i.e., coffee ring) of 0.15 mm (0.10 mm) thickness whose intensity was 10-fold (4-fold) higher than that measured in the inner region (Fig. 3.19).

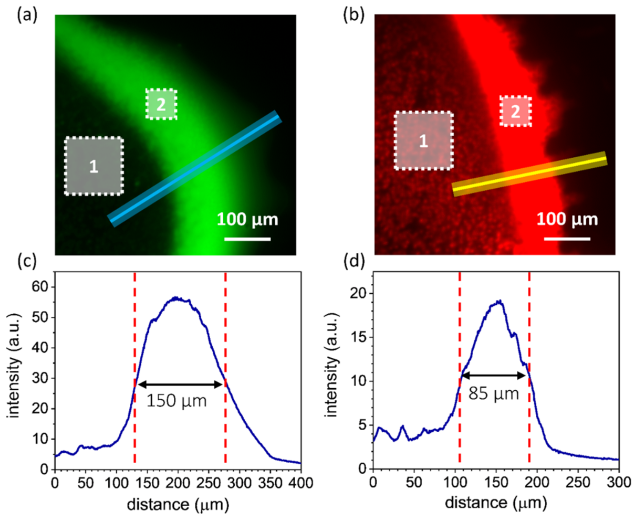

Figure 3.19: Fluorescence image of (a) 5-FAM-Apts* and (b) Cy5-Apts* dried drops. The drop was sampled in 100 regions of size $350 \times 350\,\mu m^2$ in the inner area (white squares 1, not in scale) and $70 \times 70\,\mu m^2$ on the annulus (white squares 2). (c,d) Ring thickness measured as FWHM of the intensity profile evaluated along the light blue and yellow lines highlighted in panels (a) and (b), respectively (from [2]).

The whole fluorescence intensity F_0 of the dried drop was measured by sampling the drop area in 100 regions of size $350 \times 350\,\mu m^2$ in the inner region and $70 \times 70\,\mu m^2$ on the annulus. Then, the resulting averages were scaled to the whole inner region ($\sim 113\,mm^2$ for 5-FAM dye and $\sim 133\,mm^2$ for Cy5 dye) and coffee ring area ($\sim 5.7\,mm^2$ for 5-FAM dye and $\sim 4.1\,mm^2$ for Cy5 dye).
Thus, the mean intensity $\langle I_0 \rangle$ provided by individual fluorophores in free-space condition is

$$\langle I_0 \rangle = \frac{F_0}{N_0},$$

where N_0 the number of fluorophores contained in the drop.

3.E Optical response of homogeneously sized gold nanoparticles

Numerical simulations worked out with homogeneously sized AuNPs confirmed that the measured double resonance of the real substrate is due to not only the branch architecture, but also the combination of heterogeneously sized AuNPs. Actually, the optical response of a pattern made of 30 nm diameter AuNPs conveys a broad peak in the extinction spectrum at 540 nm wavelength. This plasmonic mode may contain both the response of isolated nanoparticles (at ~ 520 nm) and that of plasmon-coupled nanoparticles (Fig. 3.20(a), Fig. 3.20(b) and Fig. 3.20(c)). On the contrary, the pattern made of 60 nm diameter AuNPs exhibits two resonances at 540 nm and 675 nm. Plasmon-uncoupled AuNPs contribute to the first plasmonic mode, whereas plasmon-coupled AuNPs produce the second mode (Fig. 3.20(d), Fig. 3.20(e) and Fig. 3.20(f)). Note that we coded the

script for placing homogeneously sized 60 nm diameter AuNPs in such a way to avoid particle interpenetration.

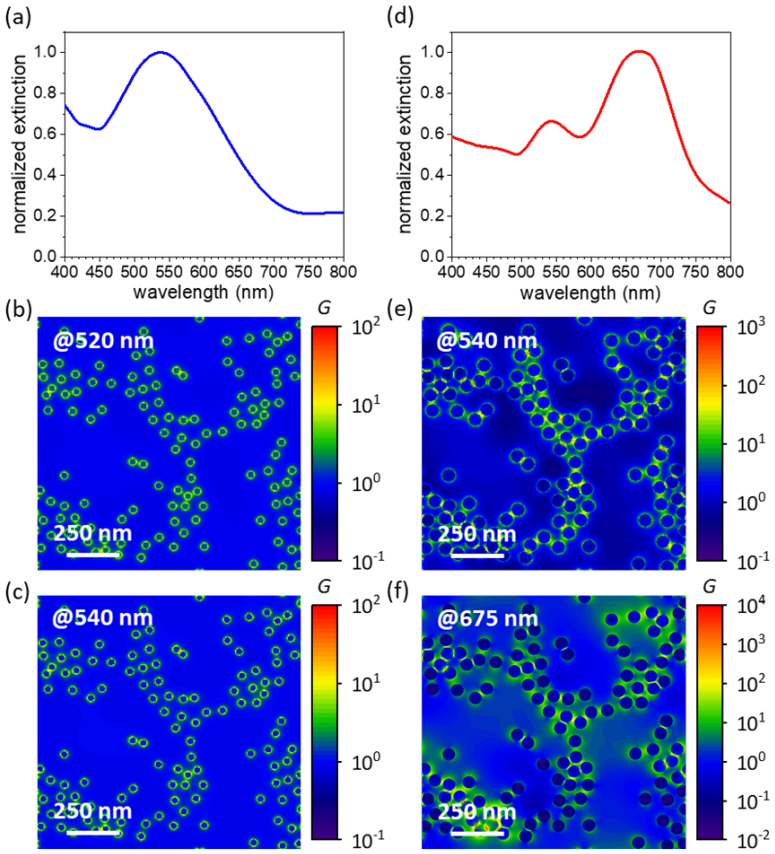

Figure 3.20: Simulated extinction spectrum of the substrate in the case of homogeneously sized AuNPs of (a) 30 nm diameter and (d) 60 nmdiameter. Simulated electric field intensity of the substrate worked out at wavelengths (b) 520 nm and (c) 540 nm in the case of 30 nm diameter AuNPs, and (e)540 nm and (f) 675 nm in the case of 60 nm diameter AuNPs (from [2] Supporting Information).

Chapter 4

Magneto-Optic Surface Plasmon Resonance biosensor

Contents

4.1 Introduction

The magnetoplasmonics is a blossoming field where concepts from plasmonics and magneto-optics are combined, opening novel possibilities for the light manipulation at the nanoscale [164, 165, 166]. The magnetoplasmonic modulation arises from the simultaneous excitation of SPPs modes and magneto-optic effects in plasmonic structures with a magneto-optical activity. In these structures, the excitation of SPP modes produces a resonant enhancement of the magneto-optic effects both in reflectance (Kerr effects) and in transmission (Faraday effects, see Section 4.2).
Notoriously, the excitation of SPPs modes in plasmonic devices has been extensively applied as biosensing technology [167, 18]. When SPPs are excited along the metal/dielectric surface, a change in the RI of the dielectric medium gives rise to a change in the propagation constant of the surface plasmon (see equation (1.51)). Through the coupling conditions, this modification entails a change of the characteristics of the light wave coupled to the SPPs that can be used as sensing parameters (Fig. 4.1). SPR sensors are based on this principle [18].

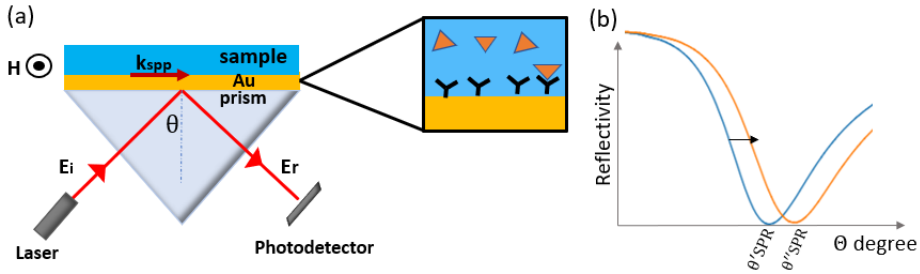

Figure 4.1: (a) Schematic representation of the experimental setup for SPR sensing. In the Kretschmann configuration, the dielectric medium that is in contact with the metal surface where SPPs are excited corresponds to the sample. The inset depicts the surface of the gold layer functionalized with bioreceptors and the biorecognition of the antigen (orange triangle). (b) The excitation of the SPPs causes a minimum intensity of the reflected beam in the angular scanning (solid blue line). The minimum of the reflectivity, θ'_{SPR}, shifts after the recognition of the antigen: $\theta'_{SPR} \rightarrow \theta''_{SPR}$ (the SPR curve shifts from the solid blue curve to the solid orange curve).

Recently, the magnetoplasmonic modulation that exploits SPP excitation has been proposed as tool to overcome the sensitivity of the traditional SPR sensors [17]. We will refer to the sensor based on simultaneously excitation of magneto-optic effects and SPPs modes as MOSPR (Magneto-Optic Surface Plasmon Resonance) sensors. For these sensors the adopted transducers are multilayered nanostructures composed of noble and ferromagnetic metals. These structures combine the extensive magneto-optical activity of ferromagnetic materials with the well-known plasmonic properties of noble metals (see Section 4.3.1).
The sensing process of MOSPR sensors may involve the measurement of the signal of the Transversal Magneto-Optic effect (TMOKE) at a fixed angle in proximity of the resonant condition (see Section 4.3.2) and for a fixed wavelength.

The enhancement of the magneto-optic effect in the multilayered structure relies on the excitation conditions of the SPPs, but it also dependent on the RI of the dielectric medium in contact with the metal-interface where SPP are excited. The scenario is quite similar to the traditional SPR systems, but in this case the plasmons are modulated by the magnetic field, giving rise to a sharp resonant enhancement of the TMOKE that has been exploited to solve small RI variation [17, 168].
So far a threefold improvement in the sensitivity with respect to traditional plasmonic-based sensing devices has been demonstrated in a biosensing application [169]. A similar result was also obtained in a novel class of devices conceived for gas sensing [170, 171].
Several studies have been devoted to define an optimal configuration for the noble metals/ferromagnetic multilayer used as sensing device both with theoretical and experimental approaches [172, 173, 174, 175, 176].
From these studies we can conclude that the enhancement of the MOSPR signal arises from balancing the magneto-optical activity (higher for thicker ferromagnetic layer) with the resonant condition of the SPPs modes. The latter results in a much lower value of the reflectivity at the minimum of the SPR curve ($R(\theta_{min})$) and a sharper resonant-like behaviour for the TMOKE signal (see Section 4.2.3). These aspects are strongly affected by the detailed composition of the multilayered structures, i.e. the thickness of all the metallic layer involved and their relative positions in the multilayer.
Even though most of these works ([172, 173, 174, 175, 176]) assume to deal with the same type of multilayered structures (e.g. Au/Co/Au, Au/Fe/Au) it is difficult to determine which is the ideal trilayer or bilayer. For instance, in some cases the thickness of the top noble metal layer (the one exposed to the sample solution) is assumed to be as subtle as convenient for enhancing the MOSPR signal. However, since this layer prevents the oxidation of the internal ferromagnetic layer, choosing a thickness of $1 - 2$nm or even less can be unpractical or unfeasible. Moreover, the optimal magneto-optical enhancement depends on the bulk medium, so that the configurations that give the greatest enhancement in air are generally not the same in the liquid environment. Another crucial aspect is that the magneto-optic effect and the SPPs are also dependent on the choice of the adhesive layers added to attach the metal nanostructure on the glass substrates. Commonly, few nanometers of chromium (Cr) or titanium (Ti) are used as adhesive layers even if their presence can add dumping effects, thus broadening the SPR resonance [177] and worsening the sensitivity of the MOSPR sensors [17]. Finally, it worth mentioning that some others works have explored different magnetoplasmonic nanostructure to enhance the RI sensitivity of MOSPR based sensors. We refer the interested reader to [178, 168, 166].

In this chapter we propose a MOSPR immunosensor whose sensing platform is a multilayered nanostructure composed of a thin cobalt layer sandwiched between two gold layers: Au/Co/Au/TiO_2. The thickness of the layers have been selected according to an optimization of the MOSPR signal as explained in Section 4.4.2 (details on fabrication are given in Section 4.B.2). We adopted the Photochemical Immobilization Technique (PIT) (see [12], Section 1.1.2) for the first time in a MOSPR sensor.
The RI sensitivity of MOSPR sensors (and SPR sensors) relies on the evanescent field that probes the dielectric medium at the metal interface where SPPs are excited. Thus, the sensitivity of these devices is also affected by the thickness of the protein layer built on the sensing surface in order to functionalize the chip with bioreceptors. In this regard

the PIT allowing a well-oriented tethering of the antibodies on metal surfaces ensures that only thin layer of antibodies ($\sim 5\,\mathrm{nm}$) is formed on the surface of the MOSPR chip [12]. Such a thickness cannot be guaranteed by other functionalization techniques ([27, 25]) except the physical adsorption which anyway suffers from having no control on antibodies orientation (see Section 1.1.1). To the best of our knowledge, the influence of the biofunctionalization on the MOSPR sensitivity has not been considered yet.
We successfully adopted the PIT for the MOSPR sensor for the real-time monitored detection of the antigen (human IgG) at several concentrations in water, achieving a LOD of $1.6nM$. These preliminary results can be easily improved by optimizing the fluidic system Section 4.4.4.
The application shows that the MOSPR immunosensor has a reliable stability in water and a specific response to the analytes.

Before deepening the description of the MOSPR immunosensor, we give a basic overview of the magneto-optic effects (Section 4.2) and the intertwined magneto-optic and surface plasmon properties (Section 4.3.2) focusing on 2D multilayered noble metal/ferromagnetic nanostructures.

4.2 Magneto-optic effects in metals

Magneto-optics is the branch of the physics that study the effects of an external magnetic fields on the optical properties of a system. The first discovery of magneto-optic effects dates back to 1845. It was Michael Faraday to observe that when a linearly polarized light passes through a glass under an applied magnetic field, its plane of polarization rotates [179]. The reflection analog of the Faraday effect was discovered in 1876 by John Kerr [180]. The magneto-optic Kerr effect (MOKE) consists in the alteration of the polarization state of the light reflected from the surface of a magnetized material. A complete description of the magneto-optical phenomena involves the Zeeman effect. However the classical description based on Lorentz's classical theory provides a useful insight [181] to show how the permittivity and susceptibility tensors change in presence of a magnetic field.

4.2.1 Physical origins of magneto-optic effects: classical description

Let us consider a system of electrons harmonically bound in an oscillating electric field and with a static magnetic field applied along the z axis. The equation of motion of each electron is:

$$m\frac{\partial^2 \mathbf{r}}{\partial t^2} + b\frac{\partial \mathbf{r}}{\partial t} + kr = -e\mathbf{E_0}e^{-i\omega t} - e\mu_0\frac{\partial \mathbf{r}}{\partial t} \times \mathbf{H}, \tag{4.1}$$

where b is the damping coefficient, $\sqrt{k/m} = \omega_0$ is the natural frequency of the electron, r is the displacement of the electron from its equilibrium position and the term on the right side is the Lorentz force. Looking for a solution as $\mathbf{r} = \mathbf{r_0}e^{-i\omega t}$, where the electrons

displacement has the same time dependence as the electric field, the eq. (4.1) becomes

$$-\omega^2\mathbf{r_0} - i\omega\gamma\mathbf{r_0} + \omega_0\mathbf{r_0} = -e\mathbf{E_0} - i\omega\frac{\varepsilon\mu_0}{m}\mathbf{r}\times\mathbf{H}, \tag{4.2}$$

where $\gamma = b/m$ is the damping parameter. For an assemblage of N oscillators the polarizability is $\mathbf{P} = -Ne\mathbf{r_0}$ where $-e\mathbf{r_0}$ is the amplitude of the each electric dipole moment and it is a linear function of the electric field $\mathbf{E_0}$. The linear dependence is expressed trough the polarizability tensor $\hat{\chi}$ and it reads $\mathbf{P} = \varepsilon_0\hat{\chi}\mathbf{E_0}$ (see eq. (1.11)) where

$$\hat{\chi} = \begin{pmatrix} \chi_{xx} & \chi_{xy} & \chi_{xz} \\ \chi_{yx} & \chi_{yy} & \chi_{yz} \\ \chi_{zx} & \chi_{zy} & \chi_{zz} \end{pmatrix}. \tag{4.3}$$

From the equation (4.2) we can calculate the coefficients of the polarizability tensor which result to be the following:

$$\chi_{xx} = \chi_{yy} = \frac{Ne^2}{\varepsilon_0 m}\frac{\omega_0^2 - \omega^2 - i\gamma\omega}{(\omega_0^2 - \omega^2 - i\gamma\omega)^2 - 4\omega^2\omega_L^2}, \tag{4.4}$$

$$\chi_{xy} = -\chi_{yx} = \frac{Ne^2}{\varepsilon_0 m}\frac{i\omega\omega_L}{(\omega_0^2 - \omega^2 - i\gamma\omega)^2 - 4\omega^2\omega_L^2}, \tag{4.5}$$

where $\omega_L = e\mu_0 H/2m$ is the cyclotron frequency known as Larmor's frequency.
The presence of the magnetic field causes the non-diagonal antisymmetric terms to appear, (4.5). In the absence of the magnetic field, the off-diagonal elements vanish and in the case of isotropic media, the susceptibility tensor is diagonal with all the elements equal to each other. Thus the magnetic field induces an anisotropy in the system that is manifest in the non-diagonal form of the susceptibility $\hat{\chi}$ and the dielectric tensor $\hat{\varepsilon}$, where $\hat{\varepsilon} = \mathbb{I}_{3x3} + \hat{\chi}$ and $\mathbb{I}_{3x3}$ is the identity tensor.

4.2.2 Dielectric tensor in ferromagnets

As we saw in Section 4.2.1, in absence of magnetic fields the dielectric tensor $\hat{\varepsilon}$ is symmetric but the application of a magnetic field makes this tensor asymmetric. Generally, the effect of the magnetic permeability tensor μ in the optical phenomena is small, so that we can assume $\hat{\mu} = \mu_0\mathbb{I}_{3x3}$. Thus, the macroscopic property of the material are contained in the dielectric tensor $\hat{\varepsilon}(\omega)$:

$$\hat{\varepsilon} = \begin{pmatrix} \varepsilon_{xx} & \varepsilon_{xy} & \varepsilon_{xz} \\ -\varepsilon_{xy} & \varepsilon_{yy} & \varepsilon_{yz} \\ -\varepsilon_{xz} & -\varepsilon_{yz} & \varepsilon_{zz} \end{pmatrix}, \tag{4.6}$$

where the components ε_{ij} may be complex, depend on the magnetization M, and satisfy the following Onsager relations [182]:

$$\varepsilon_{ij}(-\mathbf{M}, \omega) = \varepsilon_{ji}(-\mathbf{M}, \omega). \tag{4.7}$$

The displacement vector $\mathbf{D}$ adopts the following form:

$$\mathbf{D} = \varepsilon_0\mathbf{E} + i\mathbf{g}\times\mathbf{E} \tag{4.8}$$

where $\mathbf{g}$ is the gyration vector, that is a function of the magnetization $\mathbf{M}$ and describes the gyrotropic effects (the magnetic gyrotropic birefringence and the magnetic circular dichroism). Let us limit our description to the case of an isotropic ferromagnetic materials [183] for which $\varepsilon_{xx} = \varepsilon_{yy} = \varepsilon_{zz} = \varepsilon$. The magneto-optical constants or Voigt parameters are defined as $Q_j = i\varepsilon_{ji}/\varepsilon_{ii} = g_j/\varepsilon$ with $i, j = x, y, z$. If the magnetization is zero Q and g vanish. In the linear approximation the off-diagonal terms of $\hat{\varepsilon}$ are proportional to $\mathbf{M}$.

In terms of Voigt parameters the dielectric tensor of an optically isotropic ferromagnet can be written as:

$$\hat{\varepsilon} = \begin{pmatrix} \varepsilon & iQm_z & iQm_y \\ -iQm_z & \varepsilon & -iQm_x \\ -iQm_y & iQm_x & \varepsilon \end{pmatrix}, \tag{4.9}$$

where $\mathbf{m} = (m_x, m_y, m_z) = \mathbf{M}/M_S$ and M_S is the magnetization at saturation. For paramagnetic and diamagnetic materials the off-diagonal terms of $\hat{\varepsilon}$ depend on the applied magnetic field and unless high magnetic fields are applied they result to be much smaller than the optical constants.

4.2.3 Magneto-Optic Kerr Effects (MOKE)

The Kerr effects consist in a change in the polarization and intensity of the light reflected by a material induced by the presence of a magnetic field. The general condition for every type of Kerr effect is that the incident electric field has a component perpendicular to the sample magnetization.

Let us consider a plane wave propagating through the medium with a dielectric tensor ε [182]:

$$\mathbf{E} = \mathbf{E}_0 e^{i(k\cdot r - \omega t)}, \qquad \mathbf{H} = \mathbf{H}_0 e^{i(k\cdot r - \omega t)}. \tag{4.10}$$

Taking the curl of the equation (1.6) and using the equations (1.7), (1.11) we get:

$$\mathbf{k}(\mathbf{k}\cdot\mathbf{E}) - k^2\mathbf{E} + \frac{\omega^2}{c^2}\varepsilon\mathbf{E} = 0. \tag{4.11}$$

Recalling that $k_0^2 = \omega^2/c^2$ and $\mathbf{N} = \mathbf{k}/k_0$ and assuming that light propagates along z-direction ($\mathbf{k} = (0, 0, k)$, $\mathbf{N} = (0, 0, N)$) we get the following set of equations for the electric field $\mathbf{E}$:

$$\begin{pmatrix} N^2 - \varepsilon_{xx} & -\varepsilon_{xy} & 0 \\ \varepsilon_{xy} & N^2 - \varepsilon_{xx} & 0 \\ 0 & 0 & N^2 - \varepsilon_{zz} \end{pmatrix} \begin{pmatrix} E_x \\ E_y \\ E_z \end{pmatrix} = 0, \tag{4.12}$$

which implies $E_z = 0$ and

$$\begin{aligned} (N^2 - \varepsilon_{xx})E_x - \varepsilon_{xy}E_y = 0, \\ \varepsilon_{xy}E_x - (N^2 - \varepsilon_{xx})E_y = 0- \end{aligned} \tag{4.13}$$

Requiring a non-zero solution, we get:

$$N_{R,L}^2 = k_0(\varepsilon_{xx} \pm i\varepsilon_{xy}), \qquad \pm iE_x = Ey. \tag{4.14}$$

The condition on the right implies that the eigenstates of light are circularly polarized states and the two values of N obtained are the complex index of refraction for left (L) and right (R) circularly polarized light eigenmodes inside the material.

Since Kerr effects occur in reflection, we consider the case where the light hits the sample surface and it is reflected. The circularly polarized eigenstates of light exist in both media, inside and outside the material. By using the the Fresnel relations the reflection coefficients for left and right circularly polarized light are r_L, r_R given by

$$r_R = \frac{N_R - 1}{N_R + 1}, \qquad r_L = \frac{N_L - 1}{N_L + 1}. \tag{4.15}$$

If we consider a linearly polarized light with $E_{in} = (E_x, 0, 0)$ incident on the surface of a ferromagnet, then the components of the reflected field E_r will be given by $(r_x E_x, r_y E_x, 0)$ with:

$$r_x = \frac{r_R + r_L}{2}, \quad r_y = \frac{r_R - r_L}{2} \tag{4.16}$$

Now we can define the complex rotation Φ_K as

$$\Phi_K = \theta_k + i\eta_K = -\frac{r_y E_x}{r_x E_x} = i\frac{N_R - N_L}{N_R N_L - 1}. \tag{4.17}$$

In general for linearly polarized incident light, the reflected light will be elliptically polarized. According to the definition, the quantity θ_K indicates the rotation of the major axis of the elliptically polarized light while η_K is the ellipticity, i.e., the ratio of the length of the minor axes to length of the major axes of the ellipsoid. If the off-diagonal terms of the dielectric tensor $\hat{\varepsilon}$ are zero (i.e. $Q = 0$), then $r_y = 0$ and the Kerr effect does not take place. On the contrary, if these terms are not null ($Q \neq 0$), three types of MOKE can take place depending on the relative orientation of the magnetization vector with respect to the sample plane and the plane of incidence of light.

Assuming that xy-plane is the plane of incidence of light, xz-plane is the sample plane and that the incident light is p-polarized (TM) we have that:

- the polar Kerr effect occurs when $\mathbf{M} = M_y\hat{y}$ (Fig. 4.2(a));
- the longitudinal Kerr effect occurs when $\mathbf{M} = M_x\hat{x}$ (Fig. 4.2(b)) ;
- the transversal Kerr effect occurs when $\mathbf{M} = M_z\hat{z}$ (Fig. 4.2(c)).

The polar and the longitudinal effects produce a rotation of the plane of polarization together with an ellipticity of the light reflected from the sample surface. In this thesis we use the transversal Kerr effect (TMOKE), which is characterized by a modulation of the reflectance of an incident p-polarized light.

Transversal magneto-optic Kerr effect (TMOKE)

The transversal magneto-optic Kerr effect (TMOKE) is observed when the magnetization vector, $\mathbf{M}$ is parallel to the sample plane and perpendicular to the plane of incidence of the light. It results in a variation of the intensity and a phase shift of the linearly p-polarized light impinging on the sample. According to the considerations made previous sections, the dielectric tensor is of the form:

$$\hat{\varepsilon} = \begin{pmatrix} \varepsilon & iQm_z & 0 \\ -iQm_z & \varepsilon & 0 \\ o & 0 & \varepsilon \end{pmatrix}. \tag{4.18}$$

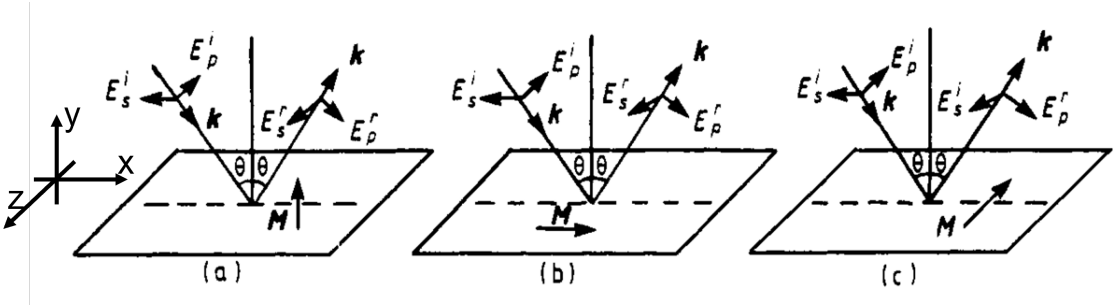

Figure 4.2: In the figure xy-plane is the plane of incidence of light, xz-plane is the sample plane. E_s^i and E_p^i are the s- and p- polarized components of the incident electric field, respectively. Analogously E_s^r and E_p^r are the s- and p- polarized components of reflected electric field. $\mathbf{k}$ is the wave vector, $\mathbf{M}$ the magnetization vector of the sample. According to the direction of the magnetization vector, the MOKE configurations are classified as: (a) polar (b) longitudinal,(c) transversal. Adapted from [183].

The intensity change of the p-component of the reflected light is described by $\Delta R_{pp}/R_{pp}$:

$$\frac{\Delta R_{pp}}{R_{pp}(0)} := 2\,\frac{R_{pp}(\mathbf{M}) - R_{pp}(-\mathbf{M})}{R_{pp}(\mathbf{M}) + R_{pp}(-\mathbf{M})}, \tag{4.19}$$

where R_{pp} is the square of the Fresnel coefficient $|r_{pp}|^2$ for p-polarized light and the quantity $R_{pp}(\mathbf{M}) - R_{pp}(-\mathbf{M})$ measures the change of the reflectivity R_{pp} when the orientation of the magnetization vector $\mathbf{M}$ switches from $+\mathbf{M}$ to $-\mathbf{M}$. By definition $R_{pp}(0)$ is the reflectivity in a demagnetized state (i.e. $\mathbf{M} = 0$) for an ideal demagnetized sample, experimentally represented by the average value of $R(\mathbf{M})$ and $R(-\mathbf{M})$.

4.3 Magneto-Optic Surface Plasmons

4.3.1 Magnetoplasmonic materials

We already described the SPPs as modes depending on the optical and geometrical properties of the system (see Section 1.3.4). However, the magnetic field has also the ability of affecting the SPPs properties. This has opened the possibility of tuning the characteristics of SPPs with the application of an external control agent (i.e. the magnetic field). The effects of the magnetic field on of the SPP is governed by the off-diagonal terms of the dielectric tensor $\hat{\varepsilon}$ which are responsible of the magneto-optical activity of the material (see Section 4.2.1, Section 4.2.2, [184]).
When the magnetic field is applied in a direction perpendicular to the propagation of the SPPs and parallel to the sample surface, the dispersion relation of the SPP modes (equation (1.47)) is modified and a dependence on k_{spp} orientation appears. This nonreciprocity effect induced by the magnetic field has been observed firstly in semiconductors [185] and then in ferromagnetic/metallic systems [15].

The advantage of using ferromagnetic materials is that the magneto-optical activity of these material is much higher, making the nonreciprocity effect in principle much more evident. However, due to the high values of their absorption losses the associated SPR

curves are too broad. On the other hand, plasmonic materials as noble metals exhibit a poor magneto-optical activity so that very high magnetic fields (tens of Tesla) are required to observe the induced nonreciprocity on SPPs modes [186]. Given that there are no materials that simultaneously exhibit good plasmonics features and significant magnetic and magneto-optical properties, a magnetoplasmonic material is generally a combination of ferromagnets and noble metals. The easiest way to devise a magnetoplasmonic material is a multilayered systems containing a ferromagnetic layer and a noble metal layer whose surface is involved in the propagation of SPPs modes.

We restrict our further considerations to the type of magnetoplasmonic structure adopted in this work, that is a multilayered planar structure of noble metals and ferromagnets (in our case gold/cobalt/gold) that sustains SPPs modes. We refer the reader to [166] for an overview on magnetoplasmonic nanostrucures sustaining LSPP.
An exact derivation of the optical properties of the multilayered systems (noble metals/ferromagnets) requires a general formulation for the propagation of electromagnetic waves of arbitrary polarization in a multilayered systems. The planar magnetic multilayers are represented by Yeh's (4x4) matrices and each layer is characterized by its own complex dielectric tensor $\hat{\varepsilon}$. The typical boundary conditions for the fields must be imposed at all the interfaces to determine the electric and magnetic field distributions in the multilayer [187, 188]. We will not deepen this description. Instead, we will give the main experimental and theoretical results that allow to describe the intertwined magneto-optic and surface plasmon effects (Section 4.3.2).

4.3.2 MOSPR in metals/ferromagnetic heterostructures

The excitation of SPPs modes can be used for the resonant enhancement of magneto-optic effects both in reflectance (Kerr effects) or in transmission (Faraday effect). In the following, we will offer examples from literature where the excitation of SPPs modes is combined with the TMOKE for some noble metals/ferromagnetic multilayers. Due to the presence of the magnetic layer, the optical properties of the noble metal-ferromagnetic heterostructure correspond to that of an anisotropic system described by a dielectric tensor with non-zero off-diagonal terms which are functions of the **M**. In particular, the dispersion relation of SPP in anisotropic media depends on these terms [189].

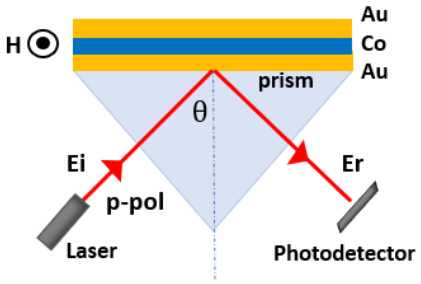

Figure 4.3: Schematic representation of a magnetoplasmonic multilayer where the ferromagnetic film (cobalt, Co) is sandwiched between two film of noble metal films (gold, Au). The sample is placed above a glass-prim in ATR configuration. The cobalt film is magnetized parallel to the sample surface.

In the case of the TMOKE, the SPP wave vector is modified as $k^0_{spp} \rightarrow k^0_{spp} + \Delta K_{spp}(\mathbf{M})$ and the modification adopts the following form in the limit of very thin ferromagnetic layer [184]:

$$\Delta K_{spp}(\pm\mathbf{M}) \approx \pm 2d \frac{(k_0 \varepsilon_d \varepsilon_m)^2}{(\varepsilon_d + \varepsilon_m)(\varepsilon_d^2 - \varepsilon_m^2)} \left(i \frac{\varepsilon_{mo}}{\varepsilon_{xx}} \right) e^{h/\delta_{skin}}, \tag{4.20}$$

where ε_{xx} and ε_{mo} represent the optical and magneto-optical constants of the magnetic layer, respectively (i.e. the diagonal and off-diagonal terms of the dielectric tensor), ε_m is the dielectric constant of the noble metals and ε_d that of the dielectric, k_0 is the light wave vector in vacuum, d is the thickness of the ferromagnetic layer, h is the distance of the ferromagnetic layer from the dielectric/noble metal interface, δ_{skin} is the skin depth of light inside the noble metal. The expression is valid under the condition $d \ll \delta skin$ and $\varepsilon_{mo} \ll \varepsilon_{xx}$.
Let us consider the case in which the SPPs are excited in the ATR geometry as the one depicted in Fig. 4.3 (see also Section 1.3.5). The SPP excitation causes the appearance of a minimum of the reflectivity $R_{pp}(\theta)$ at a specific angle of incidence θ_{min} above the critical angle for total internal reflection. The angle for SPP excitation θ_{min} is the angle at which the matching between the in-plane component of the wave vector of the incident radiation and that of the SPP (k_{spp}) occur and hence the following relation is valid:

$$k_{spp} = \frac{2\pi}{\lambda} \sin(\theta_{min}), \tag{4.21}$$

where λ is the wavelenght of the exciting radiation. Therefore when the magnetization of

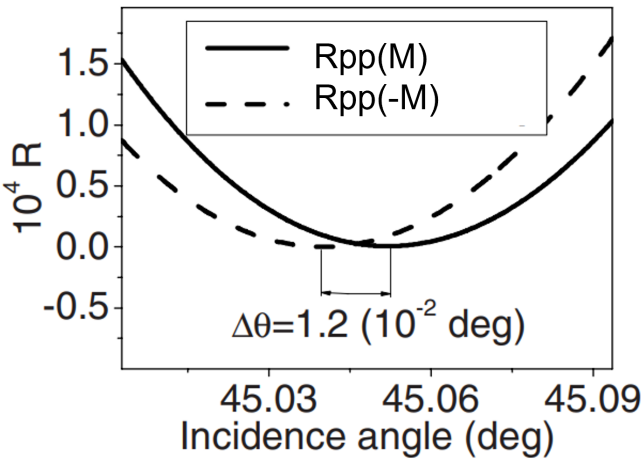

Figure 4.4: Simulated reflectivity R_{pp} for a geometrical configuration ATR as the one in Fig. 4.3 obtained for a multilayer Au5 nm/Ag 5 nm/Co7 nm/Ag7 nm/glass with the magnetization parallel to the sample surface. The dielectric medium above the Au top layer is air. $\Delta\theta$ is the angular shift of the minimum of the SPR caused by the switch of the magnetization from $-\mathbf{M}$ (dashed line) to $\mathbf{M}$ (solid line). Reproduced from [16].

the ferromagnetic film is flipped from $\mathbf{M}$ to $-\mathbf{M}$ or vice versa, the minimum of the SPR consequently shifts $\theta_{min} \rightarrow \theta_{min} \pm \Delta\theta$.
For typical magnepolasmonic multilayers with noble metals and ferromagnets $\Delta\theta \approx 10^{-3} - 10^{-2}$ degree [16, 15] (see Fig. 4.4). The TMOKE signal in the range of incident angles θ where the SPR is observed exhibits a typical resonant-like shape as shown in the plots in Fig. 4.5(d) obtained for Au 6 nm/Co 4.7 nm/Au 16 nm/glass structure (black-dots). The peak of the $\Delta R_{pp}/R_{pp}(\theta)$ signal is around the minimum of the $R_{pp}(\theta)$ (Fig. 4.5(c)).

When no SPP excitation is present, the TMOKE signal exhibits a monotone increase with the thickness of the ferromagnetic layer (see (Fig. 4.5(e)). However, when the SPR is excited, a maximum is observed for a certain thickness, that gradually decrease for thicker layers (Fig. 4.5(f)). The reason of this behaviour is that the TMOKE signal $\Delta R_{pp}/R_{pp}$ reaches a maximum for the Co thickness at which R_{pp} reaches a minimum which corresponds to the optimum SPP-light coupling conditions.

The resonant shape of the TMOKE signal can be approximated as follows:

$$\frac{\Delta R_{pp}(\theta, \mathbf{M})}{R_{pp,M=0}(\theta)} = \frac{\partial R_{pp,M=0}(\theta)}{\partial\theta} \frac{\Delta\theta_{min}(\mathbf{M})}{R_{pp}(0)}. \tag{4.22}$$

We can observe that Δk_{spp} goes linearly with the magnetization (eq. (4.20)) and so does $\Delta\theta_{min}$ as we can easily see from the relation (4.21):

$$\delta\theta_{min} = \frac{k_{spp}(M) - k^0_{spp}}{nk_0 \cos\theta_{min}} = \frac{\Delta k_{spp}}{nk_0 \cos\theta_{min}}. \tag{4.23}$$

Thus, in the eq. (4.22) the variation of the $R_{pp,M=0}(\theta)$ when the magnetization is flipped is approximated by $(\partial R_{pp,M=0}(\theta)/\partial\theta)\,\Delta\theta_{min}$. All of this is strictly valid in the approximation

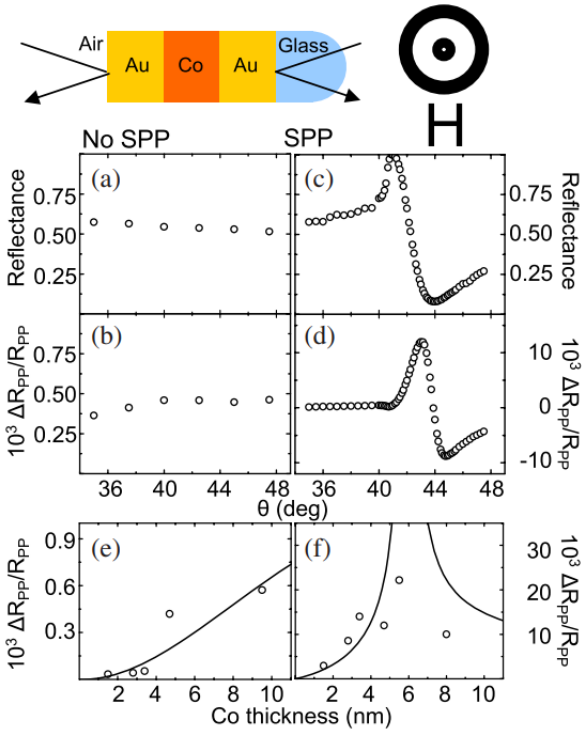

Figure 4.5: Top: schematic view of the sample configuration in ATR geometry (Kretschman configuration). The incident light is TM polarized with $\lambda = 632nm$. The magnetic field H is parallel to the sample surface. In (a), (b), (c), (d) the experimental behavior of the reflectivity $R_{pp}(\theta)$ and the TMOKE signal $\Delta R_{pp}/R_{pp}(\theta)$ as a function of the incidence angle for a trilayer with Co thickness of 4.7 nm is reported. No surface plasmon modes are excited in the left hand panels (a), (b), (e), whereas the right hand panels show the corresponding data with SPP excitation. In (e) and (f) dots correspond to experimental data and solid line to theoretical values calculated by the authors. Reproduced from [15].

in which the the equation (4.20) was retrieved, however it is in good approximation with the experimental results obtained for Au/Co/Au multilayers with Co thickness in the range of about $0 - 10$ nm in [15] (see Fig. 4.6).

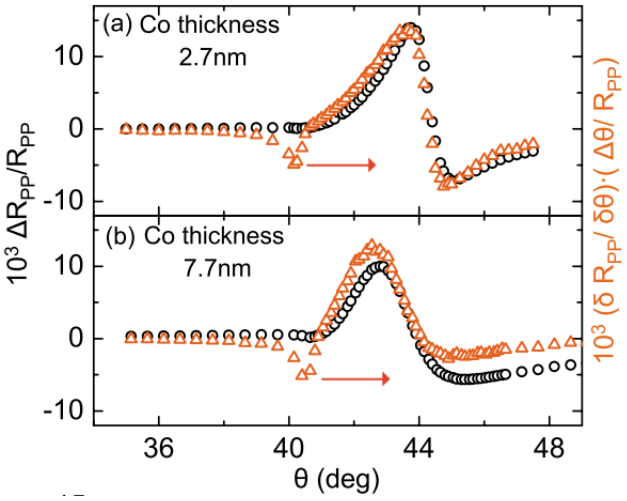

Figure 4.6: TMOKE effect measured (black circles) and approximated with the derivative of the reflectivity (orange triangles) for two different samples Au/Co/Au with Co thicknesses of (a) 2.7 nm and (b) 7.7 nm. The thickness of the gold layers is the same for both samples. Reproduced from [15].

4.4 Materials and methods

4.4.1 Experimental setup

Experimental configuration of SPR system

The setup is a prism-coupled SPR system in Kretschmann configuration (Fig. 4.7). The system consists of a diode laser (ULN, 635 nm, 5 mV, Coherent) a Faraday rotator (IO-2D-633-VLP, Thorlabs), a beam shaping refractive component (LB1904 biconvex lens, Thorlabs), a beam splitter for a reference signal, a reflectivity detector and a reference detector (CCM1-BS013/M, Thorlabs), and a semicylindrical coupling prism (Schott N-SF57, Crysmit Photonics, China) with index of refraction $n_{BK7} = 1.5168$, transparent at λ= 633 nm. The prism is placed on a rotating platform (M-060.DG DC, PI miCos, Spain). The reflectivity photodetector is housed on a second rotating platform (OSMS-60YAW, OptoSigma, France) (PDA100A-EC, Thorlabs) and the two rotating platforms are built on three linear translational stages (PLS-85, Pi miCos), which allow the optical alignment of the system.
The beam splitter provides two identical beams, whose intensities are measured by the two photodetectors in order to calculate the reflectivity. The beam component that reaches the sensor surface is further reflected and the emerging beam is collected by one of the photodetectors. The measured reflectivity R_{pp} is the ratio between reflected light intensity I_1 and the incident light intensity I_0. By rotating the system it is possible to reconstruct the reflectivity as a function of the incident angle $R(\theta)$.
A 3D printed holder was fabricated to attach the plasmonic devices on the prism's surface (Fig. 4.7, inset). The devices are deposited on 170 μm BK7 glass substrate which can be attached to the prism's surface with a matching oil.
The fabricated devices are also integrated into microfluidic chambers (Fig. 4.7, inset) that

are manufactured by lamination of polymer layers using an origami-based self-alignment method (details in Section 4.A). A syringe pump was used for injecting the samples and for controlling the flux velocity.

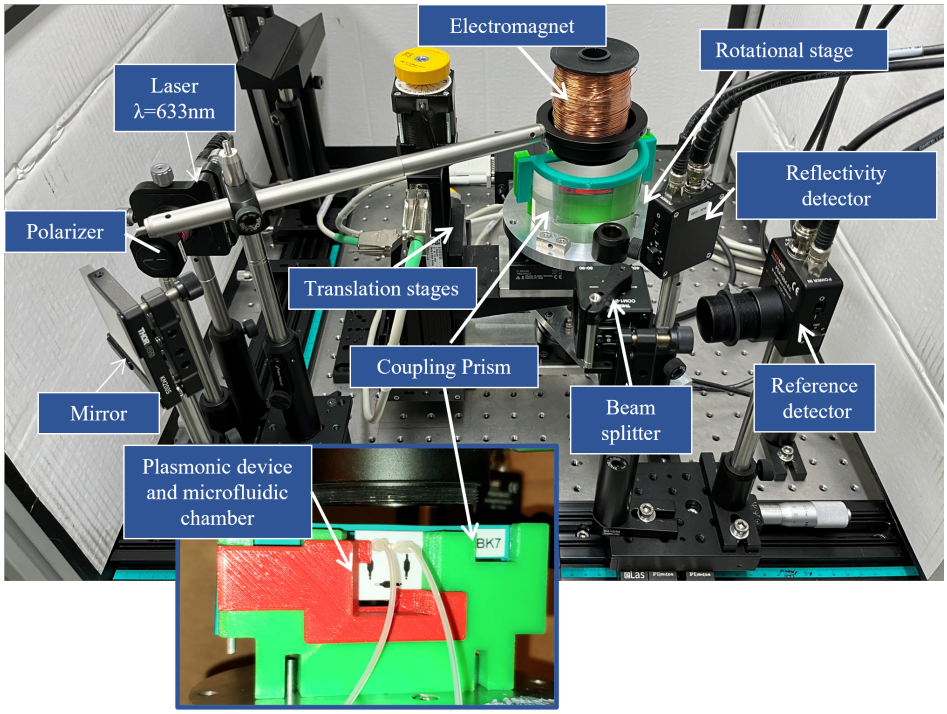

Figure 4.7: Customized SPR system in Kretschmann configuration with a cylindrical coupling prism. The system is equipped with an electromagnet in TMOKE configuration. The inset shows the back of the prism where a plasmonic chip is integrated in a fluidic chamber (white) and attached to the planar surface of the cylindrical prism.

Experimental configuration of MOSPR measurements

The SPR system is equipped with an electromagnet in TMOKE configuration. The magnetoplasmonic device is a gold-cobalt trilayer.
If the electromagnet is as close as possible to the magnetoplasmonic device, the magnetic field $\mathbf{H}$ produced can be considered approximately homogeneous in the area of interest of the device. With the appropriate intensity of the magnetic field, the magnetic domains of the cobalt layer can be saturated in such way that the magnetization vector $\mathbf{M}$ results parallel to the sample surface and perpendicular to the plane of incidence of the light.
When the impinging radiation is p-polarized, we can observe the TMOKE signal

$$\frac{\Delta R_{pp}}{R_{pp}} = 2\frac{R_{pp}(\mathbf{M}) - R_{pp}(-\mathbf{M})}{R_{pp}(\mathbf{M}) + R_{pp}(-\mathbf{M})},$$

by measuring the reflectivity variation occurring when the orientation of the magnetization vector is flipped from $+\mathbf{M}$ to $-\mathbf{M}$.
In order to measure the TMOKE signal, an external magnetic field with a frequency oscillation of 130 Hz is used. The magnetic field intensity must be sufficient to saturate the

magnetic domains of the ferromagnetic layer. In this case the switching of the direction of the magnetization vector is obtained by switching the direction of the magnetic field **H**. A sinusoidal function digitally generated with 130 Hz is generated to both modulate the magnetic field and give a reference signal to the lock-in (7225 Dual Phase DSP Lock-in Amplifier, Ametek).
For modulating the magnetic field, the signal is transmitted to the power supply (BOP $20-5$MM, 20 V, Kepco) connected with the electromagnet. A data acquisition board (USB-6212, National Instrument) receives the output signal of the lock-in, that is the amplitude of the first harmonic of the reflectivity signal $R_{pp}(t)$. Finally, a data acquisition board allows the conversion of the analog input signal into a 16 bits digital signal with a sampling rate 250 Ksample/s (the rate has to be divided by the number of the channels used).
It is worth noticing that the reflectivity $R_{pp}(t)$ is measured at a fixed angle and as a function of time it is a square signal where the maximum and the minimum values correspond to $R_{pp}(\mathbf{M})$ and $R_{pp}(-\mathbf{M})$. Thus, the amplitude of this signal represents the difference $|R_{pp}(\mathbf{M}) - R_{pp}(-\mathbf{M})|$, while the average value is $(R_{pp}(\mathbf{M}) + R_{pp}(-\mathbf{M}))/2$. For the real-time sensing experiments we used the first harmonic of the reflectivity $R_{pp}(t)$ which is generally not equal to $|R_{pp}(\mathbf{M}) - R_{pp}(-\mathbf{M})|$. However, the first harmonic gave the higher contribution.
These considerations do not apply to the angular-scan measurements of the TMOKE signal that were performed without the lock-in (see Section 4.4.3).

4.4.2 Optimization of metal thicknesses in Au/Co/Au trilayers

The plasmonic material chosen for the experiments is a trilayer of gold-cobalt-gold (Au/Co/Au) deposited on glass with an intermediate adhesive layer of TiO_2. The top gold layer can prevent the oxidation of Co and also offers a proper surface for the biofunctionalization with the PIT (Section 1.1.2). Details on the fabrication are given in Section 4.B.2. Here we report an experimental study on the dependence of MOSPR effect on the metals layers' thicknesses performed over a set of Au/Co/Au trilayers. The selected set of samples is listed in Table 4.1.

sample	configurations
1	Au 4.9 nm /Co 5.2 nm/Au 17 nm /TiO_2 3 nm
2	Au 9.9 nm/Co 5.2 nm/Au 15.5 nm /TiO_2 3 nm
3	Au 10 nm/Co 2 nm/Au 26 nm/TiO_2 3 nm
4	Au 10 nm/Co 3 nm/Au 26 nm /TiO_2 3 nm
5	Au 10 nm/Co 7 nm/Au 11 nm /TiO_2 3 nm

Table 4.1: Set of Au/Co/Au trilayers with different layers' thickness, deposited on glass substrate (details of fabrication in Section 4.B.2).

The range of Co thickness explored are chosen in accordance with literature [15]. The thickness of TiO_2 was chosen as the minimal at which the adhesion on glass substrate was satisfactory. Thus, it is the same for every chip. It worth noticing that Cr and Ti have been preferred in literature as regarding the MOSPR sensing, despite their damping

effects [190, 191, 177]. Thus, the studies about the optimization of the layers' thickness have been so far performed using Cr or Ti as adhesive layers or alternatively with out any adhesive layer. We will discuss the comparison of the experimental results with the theoretical expectations, using the approximations depicted in Section 4.3.2.

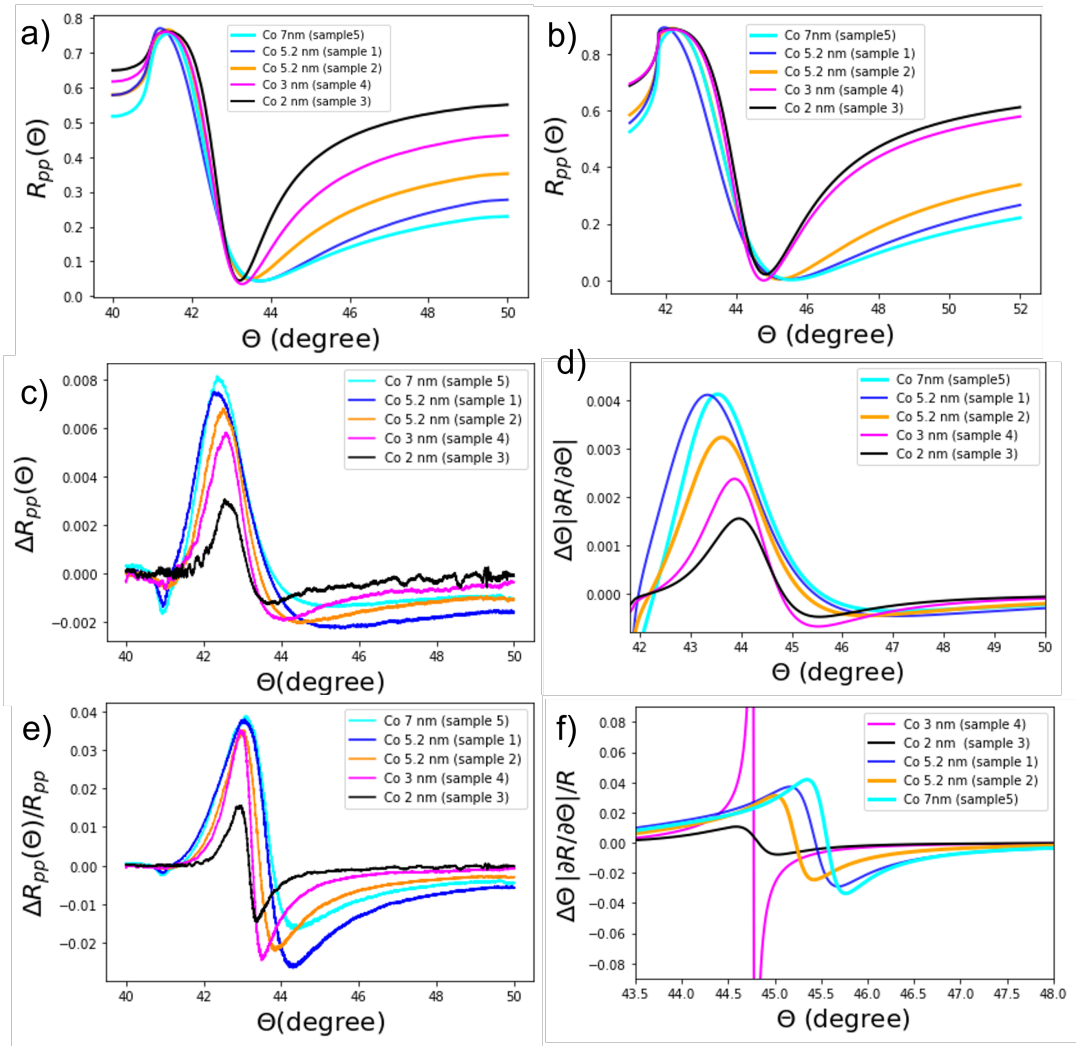

Figure 4.8: (a) Experimental SPR curves of all the chips in Table 4.1 measured in air, (b) theoretical SPR curves calculated for the same chips (Winspall software) in air, (c) experimental $\Delta R_{pp}(\theta)$ angular scan in air, (d) theoretical curves calculated as $\Delta R_{pp}(\theta) \approx \Delta\theta \frac{\partial R_{pp}}{\partial\theta}$ using the R_{pp} theoretical curves in the panel above, (e) experimental MOSPR curves, (f) calculated MOSPR curves using $\frac{\Delta R_{pp}}{R_{pp}}(\theta) \approx \frac{\partial R_{pp}}{\partial\theta}\frac{\Delta\theta}{R_{pp}}$.

Fig. 4.8(a) depicts the experimental SPR curves of all the chips in Table 4.1 measured in air. Fig. 4.8(b) shows the theoretical SPR curves calculated for the trilayers with the Winspall software using the RI values reported in the databases ($n_{Au} = 0.121965 + i3.29194$, $n_{Co} = 2.2129 + i4.17010$ [192], $n_{TiO_2} \approx 2.2813$ [193]). Comparing Fig. 4.8(a) with Fig. 4.8(b) we notice that in both experimental and theoretical plots the trilayers with the smallest content of Co (2 nm and 3 nm) exhibit the narrowest SPR, i.e. much similar

to the typical SPR curve of a gold chip. On the contrary the SPR curves of the others chips are broadened. In particular, the chip with 7 nm of Co has the broadest SPR resonance. The difference between the chips with the same Co content of 5.2 nm can be ascribed to the different thicknesses of the gold top layers. In fact, sample 1 has 5 nm of gold top layer and hence the Co layer affect more the SPP properties with respect to the the case of the sample 2, where the gold top layer is 10 nm. For estimating the $\Delta R_{pp} = R_{pp,M}(\theta) - R_{pp,-M}(\theta)$ we can use the approximation (4.22) together with the expressions in (4.20) and (4.21) that allow to compute the angular shift $\Delta\theta$ caused by the switching of the orientation of the magnetization vector Fig. 4.8(d)). The experimental data, reported in Fig. 4.8(c) and the theoretical curves in Fig. 4.8(d) exhibit again a similar behaviour. Since the shift of the propagation constant of the SPPs is proportional to the thickness of the ferromagnetic layer (eq. (4.20)) the chips with higher Co content generally present greater $\Delta R_{pp}(\theta)$ values, however the angular shift is also exponentially dependent on distance between the Co layer and the surface at which the SPPs modes are excited (eq. (4.20)). This explains the difference between sample 1 (blue curve) and sample 2 (orange curve) in Fig. 4.8(c) in agreement with the respective curves in Fig. 4.8(d).

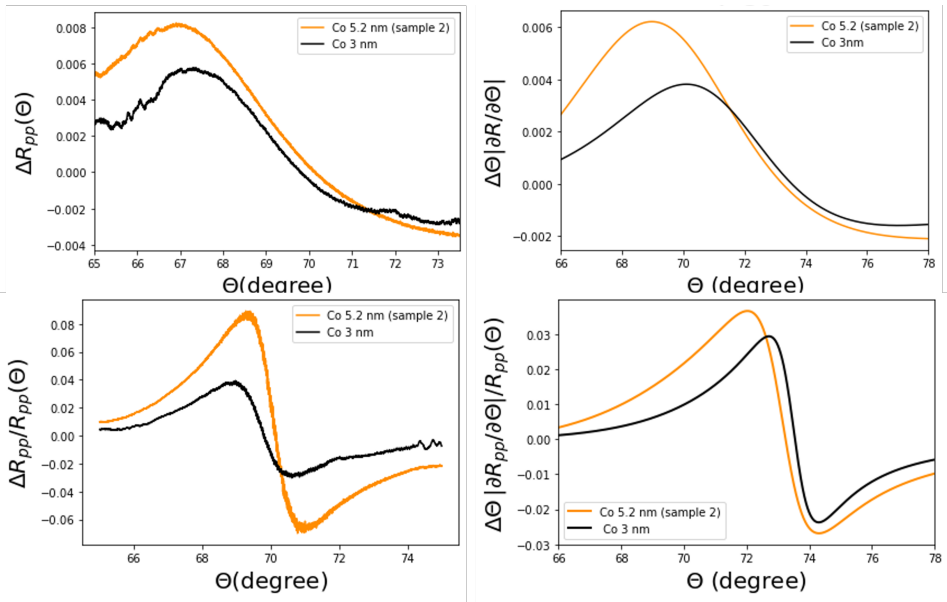

Figure 4.9: On the left: $\Delta R_{pp}(\theta)$ (upper panel) and the MOSPR signal $\Delta R_{pp}/R_{pp}(\theta)$ (bottom panel) of the sample 2 (9.9 nm/Co 5.2 nm/Au 15.5 nm /$TiO_2$3 nm) and the sample 4 (Au 10nm//Co 3nm/Au 26 nm /$TiO_2$3 nm) collected in pure water. On the right: the theoretical curves $\Delta R_{pp}(\theta) \approx \Delta\theta \frac{\partial R_{pp}}{\partial\theta}$ (upper panel) and $\frac{\Delta R_{pp}}{R_{pp}}(\theta) \approx \frac{\partial R_{pp}}{\partial\theta}\frac{\Delta\theta}{R_{pp}}$ (bottom panel) for the same sample 2 and 4.

Finally we can compare the experimental MOSPR curves (i.e. the TMOKE signal in presence of excited SPP). The theoretical curves are calculated from the $\Delta R(\theta)$ in Fig. 4.8(d) dividing by the reflectivity curves in Fig. 4.8(b). The difference between the theoretical expectation for the chip with 2 nm of Co and the actual experimental curves can be mainly ascribed to the minimum of the respective reflectivity curves. In fact, the minimum of the reflectivity curves can be several order of magnitude smaller than the

ones actually measured, thus giving rise to a very big and sharp MOSPR signal (magenta curve in Fig. 4.8(f)). Looking at the experimental curves in Fig. 4.8(e), it is clear that the sharpest signal arise from the samples whose SPR curves are narrower (black, magenta and orange curves) as expected from the derivative-like behaviour of the MOSPR ((4.22)).

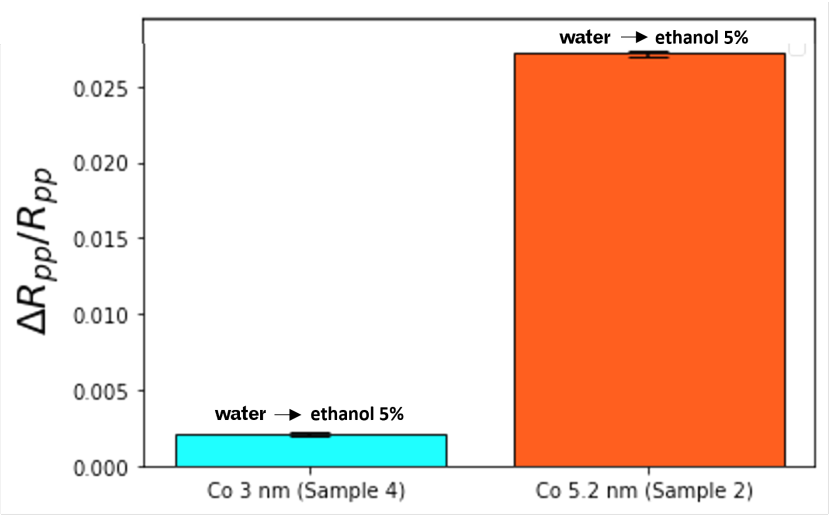

Figure 4.10: The shifts of the $\Delta R_{pp}(\theta)$ signal due to the change of the bulk environment around the Au/Co/Au trilayers from pure water to a aqueous solution of ethanol (5%) for sample 4 and sample 2. The shifts were measured real-time at a fixed angle corresponding to the inflection point of the respective $\Delta R_{pp}(\theta)$ signal ($\theta = 69.4$ degree for the sample 4 and to 69.9 degree for the sample 2).

From this analysis we can select sample 2 and sample 4 as preferred sample balancing the magnitude of the signal with the sharpness of the curve that is expected to positively influence the sensitivity of the chip. The sample with the gold layer thickness ≈ 10 nm is preferred to the sample with more subtle top layer (sample 1) for better preventing the Co oxidation.
However all the SPR curves are broaden in water environment with respect to the air, and also the minimum of the reflectance changes. Comparing the $\Delta R_{pp}(\theta)$ signal and the MOSPR signal $\Delta R_{pp}/R_{pp}(\theta)$ of the sample 2 and the sample 4 in water, we see that the sample 2 gives a greater MOSPR signal (Fig. 4.9, left panels). The curves can also be compared with theoretical counterparts which show a similar behaviour (Fig. 4.9, right panels).

The difference between the functions $\Delta R_{pp}(\theta)$ for the two samples (1,2) determines a different response signal to the change of the bulk refractive index. The shift of the function due to the change of the bulk environment around the Au/Co/Au trilayer from pure water to a aqueous solution of ethanol (5 %) was measured for each of the two chips at the θ angle equal to the inflection of the respective $\Delta R_{pp}(\theta)$ signal in water. The response signal is more than 10 times greater for the sample 2 (Fig. 4.10). For the biosensing experiments reported in this work we selected the sample 2: Au 9.9 nm/Co 5.2 nm/Au 15.5 nm/TiO_2 3 nm.

4.4.3 Experimental procedure

The realized Au/Co/Au multilayer has been used as transducer both in the traditional SPR sensing configuration and in the MOSPR configuration. The angular dependence of the reflectivity $R_{pp}(\theta)$ where θ is the incidence angle, is measured in Kretshmann configuration described in Section 4.4.1 and in Section 1.3.5. The angular interrogation on the appropriate angle range has a resonance-like shape (SPR) because of the excitement of the SPPs modes (Fig. 4.11(a)).
Generally, in the SPR sensing measurements, the shift of the curve caused by the changing of the effective RI is the sensing parameter. In this case, one can observe the shift of the θ_{min}, the angle at which the minimum of the reflectivity occurs, or the shift of any other angle. A typical choice in sensing is the angle of maximum slope for the reflectivity curve (Fig. 4.11(a)).
The real-time measurement of every step of the sensing process, from the immobilization of the bioreceptors to the detection of the analyte, can be performed at a fixed angle observing the variation of the reflectivity, that is retrieved as explained in Section 4.4.1 as the ratio between the intensity received by the reflectivity photodetector (I_1) and the intensity of the reference photodetector (I_0), i.e. $R_{pp}(\theta) = I_1(\theta)/I_0$ where I_1 and I_0 are simultaneously recorded.

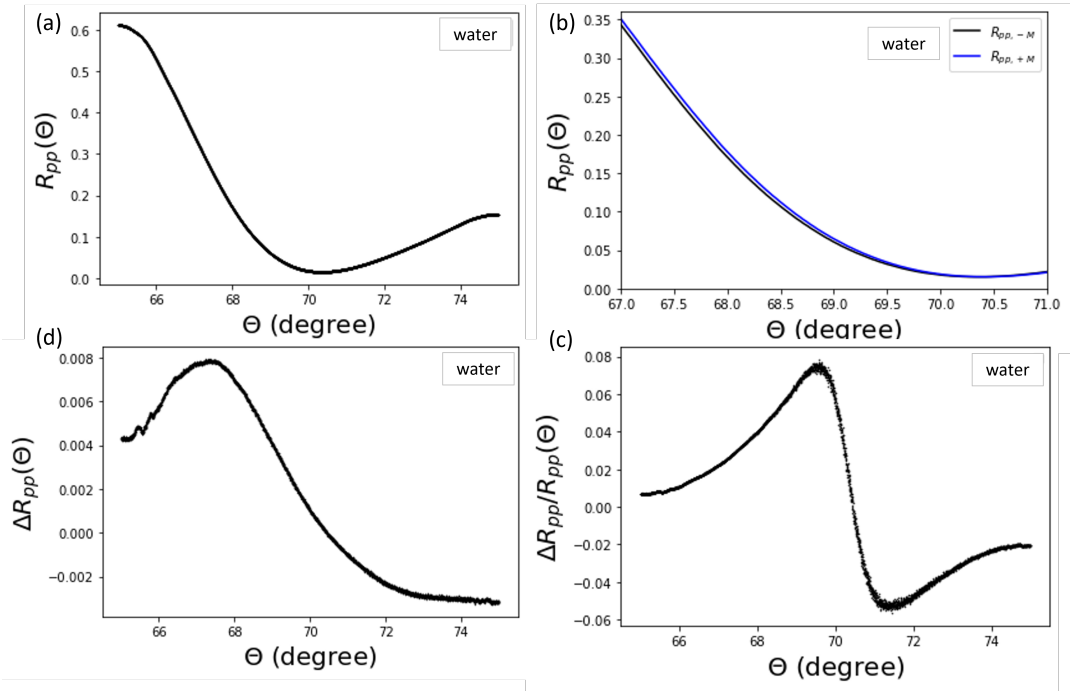

Figure 4.11: Measurements performed with the chip Au 9.9 nm/Co 5.2 nm/Au 15.5 nm/TiO_2 3 nm. The angular-scans of (a) the reflectivity in pure water, (b) the reflectivity in pure water with two different orientation of the magnetization vector at saturation (c) the signal $\Delta R_{pp}(\theta)$ and (d) the TMOKE signal $\Delta R_{pp}(\theta)/R_{pp}$.

For the MOSPR sensing, before starting a real-time monitoring of the detection (or

the functionalization), we measure the TMOKE signal as a function of the incident angle. This step is performed in the following way: the reflectivity curve is measured $R_{pp}(\theta)$ repetitively (≈ 20 times) with an angular resolution of about 0.002 while a magnetic field H that saturates the trilayer is applied. The magnetic field is produced by the means of an electromagnet connected to a power supply. Thus, the same measurement is repeated changing the direction of the magnetic field (i.e. changing the sign of the applied voltage). An example of the experimental shift of the reflectivity caused by the switch of the magnetization is reported in Fig. 4.11(b).
From the two curves $R_{pp,M}(\theta)$, $R_{pp,-M}(\theta)$ obtained switching the orientation of the magnetization vector at saturation, we retrieve the angular dependence of the TMOKE signal $\Delta R_{pp}/R_{pp,M=0}(\theta)$ where $R_{pp,M=0}(\theta)$ is obtained as $(R_{pp,M}(\theta) + R_{pp,-M}(\theta))/2$ as we saw in Section 4.2.3 (see Fig. 4.11(d), Fig. 4.11(c)).

Then we fix the angle at which the slope of the TMOKE signal is maximum $\bar{\theta}$ and performed the real-time measurement at the selected angle.
For the real-time measurement the orientation of the magnetic field varies with 130 Hz as explained in Section 4.4.1, and the amplitude of the signal emerging from the reflectivity photodetector $I_{1,\bar{\theta}}(t)$ is retrieved by the lock-in over an integration time of 2 s. The difference $\Delta R_{pp}(t) = R_{pp,M}(\bar{\theta}) - R_{pp,-M}(\bar{\theta})(t)$ is obtained by dividing for the intensity of the reference photodetector, $I_0(t)$, that is simultaneously monitored. The sum $(R_{pp,M}(\bar{\theta}) + R_{pp,-M}(\bar{\theta})(t))/2$ is the average value of $I_1(t)$ over a finite number of periods (again divided by the intensity I_0).

Biosensing experiments

The sample is mounted on the system and the fluidic circuits are connected to a syringe pump with flux velocity 15 μl/min. We measure the angular scan of the TMOKE signal in pure water. The real-time measurements take place at a fixed angle, chosen as the angle at which the slope of the function $\Delta R_{pp}/R_{pp}(\theta)$ is maximum. Once the angle is fixed we can monitor the functionalization of the gold surface of the sensor:

(i) a solution of antibodies (anti-human IgG) activated with the PIT flows for approximately 15 min (details in Section 4.4.4, Section 4.B.1);

(ii) the chip is rinsed with water to remove the excess of not bound antibodies;

(iii) the casein solution for the blocking is injected in the fluidic system (details on the blocking in Section 4.4.4, Section 4.B.1) for 40 min;

(iv) the sensor chip is rinsed with water again.

Since the casein solution is in PBS buffer, the changing of the signal observed is also related to the change of the RI of the bulk solution. After the bio-functionalization and the blocking, the TMOKE signal as function of the incident angle of the p-polarized light is measured again in pure water so to find the new angle at which the function has a maximum slope (see **??**, red line). Finally:

(v) a solution containing the target analyte is conveyed on the sensor surface and while sensing signal monitored;

(vi) when the binding dynamics reaches the equilibrium state, the chip is rinsed with water again in order to remove the excess of not bound analytes. This step ends when an equilibrium state is reached again.

In the experiments in which different concentrations of the antigen solutions are inserted subsequently (from the lower concentration to the highest one) the steps (v), (vi) must be repeated for each concentration.

4.4.4 Surface biofunctionalization

The magnetoplasmonic devices were functionalized with UV-activated anti-human IgG produced in goat via the PIT and blocked with a solution of casein. Details of the protocols and materials are reported in Section 4.B.1.
Covering up all the surface of the chips is essential to prevent a-specific attachment of the antigen via physisorption. The blocking with a small protein (e.g. BSA, casein) after the functionalization is a viable solution. In particular, for the experiment reported in this work the blocking is a crucial step to ensure the specificity (the specificity experiment is reported in Section 4.B.2).
To understand the reason why the blocking is needed we can look at Fig. 4.12 that depicts a comparison between the ΔR_{pp} signal measured at a fixed angle (70.8 degree) for the immobilization of IgG on a bare chip and for the subsequent blocking with casein. The chip used is the one selected in Section 4.4.2: Au9.9 nm/Co 5.2 nm/Au 15.5 nm/TiO_2 3 nm. The blue signal (orange signal) reported in Fig. 4.12 corresponds to the difference between the value of ΔR_{pp} before the immobilization of IgG (blocking with casein) and after the immobilization of IgG (blocking with casein). The immobilization of IgG takes place in pure water while the casein solution is in PBS buffer. Therefore, the casein signal in Fig. 4.12 refers to the signal level reached after the blocking and a subsequent washing step with water. For both the procedures the substrate are integrated in a microfluidic system (for details see Section 4.A) The signal due to the blocking is almost one-half of the signal due to the immobilization of IgG. This implies that relatively large areas on the chip are still empty after the functionalization with IgG. The inefficiency of the coating with IgG is mostly ascribable to the fluidic system which was not optimized during the conducted experiments. A further optimization would increase the amount of antibodies on the surface of the chip. This aspect will be recalled in the conclusions of this chapter (Section 4.6). Finally, it worth noticing that Fig. 4.12 displays the ΔR_{pp} signal measured during the functionalization steps and not the TMOKE signal $\Delta R_{pp}/R_{pp}$. Indeed, the TMOKE signal is not suitable for the comparison because it is saturated by the shift caused by the functionalization.

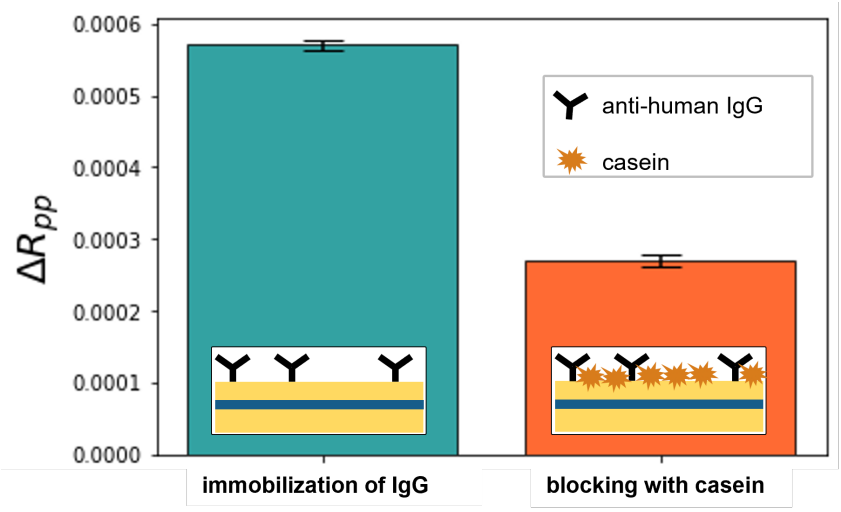

Figure 4.12: Comparison of shift of the signal ΔR_{pp} caused by the immobilization of IgG on the bare surface of the chip. The blue signal corresponds to difference between the value of ΔR_{pp} before the immobilization of IgG and after the immobilization of IgG in pure water. The orange signal refer to difference between the value of ΔR_{pp} before the blocking with casein and after the blocking in pure water.

4.5 Biosensing application

4.5.1 Specificity test

To ascertain the sensor specificity, we functionalized the surface of a magnetoplasmonic device following the protocol explained in Section 4.4.4 and then measured the response of the immunosensor to 500 ng/ml of anti-human IgG and 1 μg/ml of anti-*Salmonella*. Fig. 4.13 and Fig. 4.14 depict the comparison of the response signals to these analytes with the one obtained against the proper target human IgG at the same of concentration of the anti-*Salmonella* IgG. For completeness we show the results with the TMOKE signal (Fig. 4.13) $\Delta R_{pp}/R_{pp,M=0}$ and ΔR_{pp} signal (Fig. 4.14). The error on each response is estimated by propagating the errors of the considered signal in the equilibrium states in pure water before and after the analyte flow. The error of signal at an equilibrium state is estimated as the standard deviation of the measured values in a time interval of approximately four minutes. In both cases the response signals to these concentrations are negligible compared to the one obtained against the target analyte human IgG.

The specificity of the immunosensor is consequence of the biorecognition properties of the antibodies and confirm the effectiveness of the blocking procedure. Without a proper blocking, antibodies may attach to the empty areas on the sensor surface via physical adsorption.

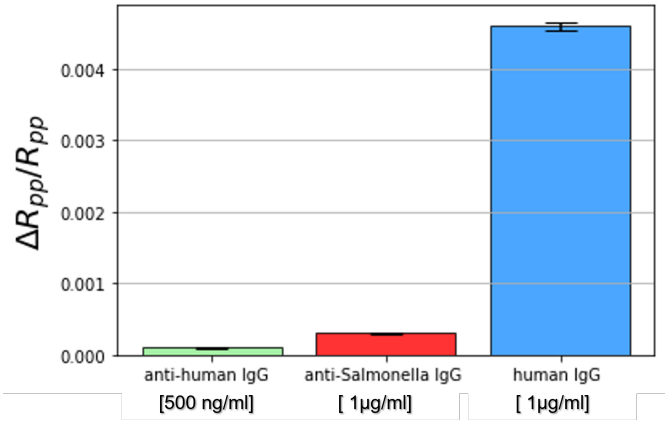

Figure 4.13: Response signal ($\Delta R_{pp}/R_{pp}$)of the MOSPR immunosensor to target analyte human IgG [1 μg/ml] (blue), to analyte different from the target: 500 ng/ml of anti-human IgG, 1 μg/mlof anti-*Salmonella*.

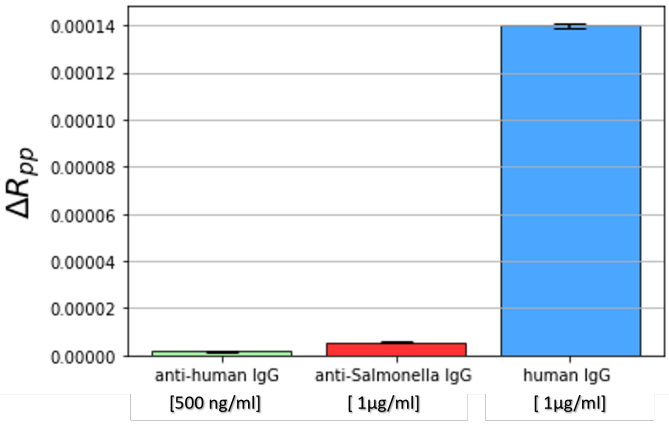

Figure 4.14: Response signal (ΔR_{pp})of the MOSPR immunosensor to the target analyte human IgG [$1\mu g/ml$] (blue), to analytes different from the target: 500 ng/mlof anti-human IgG,1 μg/ml of anti-*Salmonella*.

4.5.2 Detection of human IgG

The dependence of the TMOKE signal $\Delta R_{pp,M}/R_{pp}$ on the analyte concentration for the realized immunosensor is shown in Fig. 4.15. The data are fitted by the Hill's curve [153]:

$$f([x]) = \frac{V_{max}[x]^n}{K^n + [x]^n}, \tag{4.24}$$

where V_{max}, K and n three kinetic parameters. In particular V_{max} represents the maximum binding rate, K is the concentration at which the signal is equal to half of its maximum value, and n is the so-called Hill's coefficient. The best-fit parameter values are reported in Table 4.2.

Best-fit parameters	
V_{max}	$7.910^{-3} \pm 210^{-4}$
K	(5.0 ± 2) nM
n	3.8 ± 0.3
χ^2	1.2
LOD	1.6 nM

Table 4.2: Best-Fit Parameter Values and LOD obtained by fitting the experimental data in Fig. 4.15 with the Hill's curve (4.24).

Fig. 4.16 shows an example of a real-time monitoring of the antigen detection at several concentration of human IgG, sub-sequentially conveyed on the sensor's surface from 0.66 nM to 16.7 nM. In the figure the vertical black lines separate the minutes of

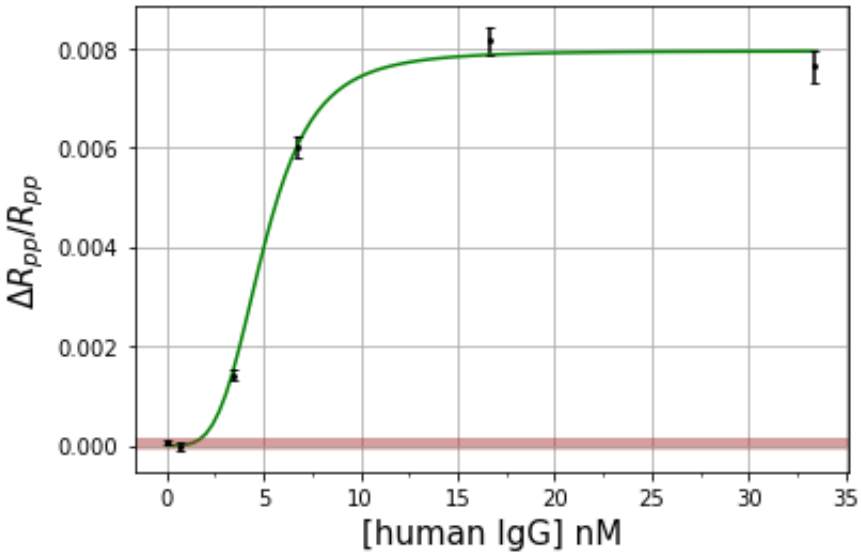

Figure 4.15: TMOKE signal $\Delta R_{pp}/R_{pp}$ as a function antigen (human IgG) concentration in pure water (calibration curve). The best fit curve (solid green line) is the Hill's curve (4.24). The shaded region represents the LOD level (1.6 nM).

stability and washing in pure water from the detection dynamics. The measurement was

conducted with a constant flow rate of 15 μl/min. The first concentration that gives a signal different from zero (i.e. the second level in water is higher than the previous level) is 3.3 nM. From the signal to noise ratio we deduce that it should be possible to detect a lower concentration and that the system is suffering from the inefficiency of the fluidic system. As regarding the higher concentrations injected (6.7 nM, 16.7 nM), the response signal due to each of them is given by the sum of the one given by the corresponding dynamic and the ones given by the previous dynamics (Fig. 4.16). Other details on the experimental procedure are reported in Section 4.4.3 and Section 4.4.4. Examples of the experimental angular scans of the reflectivity R_{pp}, the ΔR_{pp} signals and the $\Delta R_{pp}/R_{pp}$ signals acquired during a biosensing experiment are reported in Fig. 4.17.

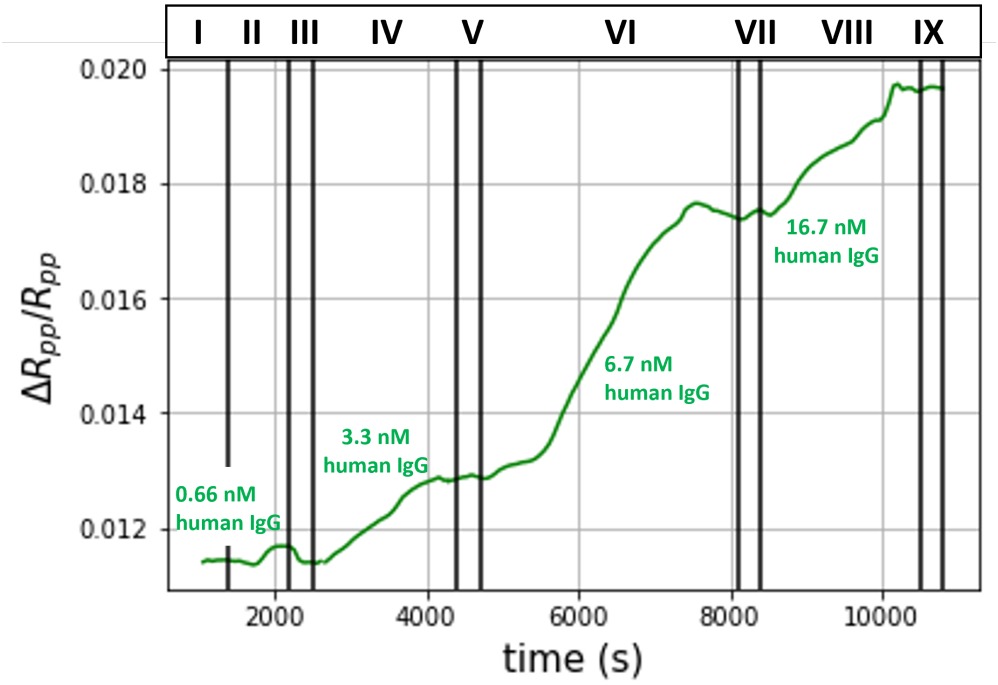

Figure 4.16: Real-time monitoring of human IgG detection. The black vertical line separate the washing steps in pure water ((I),(III),(V),(VII),(IX)) from the steps in which the selected concentrations of the target analyte human IgG (0.66 nM,3.3 nM,6.7 nM, 16.7 nM) are flowing on the sensor chip with a flux rate of 15 μl/min ((II),(IV),(VI),(VIII))

.

The error on each experimental point of the dose response curve is estimated by propagating the errors of the TMOKE signal $\Delta R_{pp,M}/R_{pp}$ in the equilibrium states (in water) before and after the analyte flow. The error of the signal at the equilibrium is estimated as the standard deviation of the measured values in the time interval of the equilibrium (few minutes).
The experimental points reported in the dose-response curve (Fig. 4.15) were retrieved by the experiment in Fig. 4.16, and other two different experiments with two different chips: one experiment was performed for the blank injection that corresponds to the first point of the dose-response curve, and one other for the maximum concentration).
The limit of detection (LOD) was estimated as the concentration at which the fitting

curve gives a signal equal to three times the standard deviation of a blank measurement 3σ and the results is LOD $\approx 1.6\,\mathrm{nM}$.

The dose-response curve exhibits a signal saturation at concentrations larger than $\approx 16.7\,\mathrm{nM}$ ($2.5\,\mu\mathrm{g/ml}$), thus showing that the dynamic range of the immunosensor corresponds to a decade of concentrations $\approx 1.6\,\mathrm{nM} - 16\,\mathrm{nM}$.

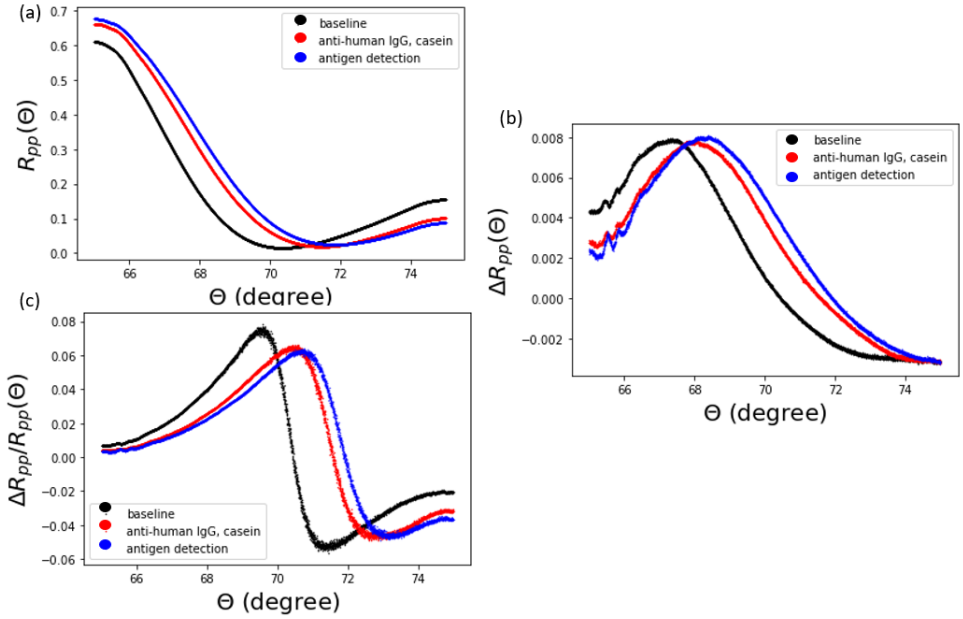

Figure 4.17: Biosensing measurements performed with the chip Au 9.9 nm/Co 5.2 nm/Au 15.5 nm/TiO_2 3 nm: (a) angular-scans of the reflectivity, (b) $\Delta R_{pp}(\theta)$ signals, (c) MOSPR signals $\Delta R_{pp}(\theta)/R_{pp}$ measured in pure water (black lines) (ii) after the biofunctionalization (anti-human IgG and casein solution) (red lines) (iii) after the detection of the human IgG at $5\,\mu\mathrm{g/ml}$ (blue lines).

4.6 Conclusions

Nowadays, label-free optical biosensors are widely employed for the real-time monitoring and detection of biological and chemical species with high sensitivity and selectivity. Among the label-free optical biosensors, SPR sensors devices, based on the excitation of SPP at a metal/dielectric interface , have turned into basic tools for biomarkers detection and for assessing the kinetics of the molecular interactions [18], finding application in a wide variety of fields from environmental monitoring to medical diagnostic ([194],[195]). Innovative solutions to improved the SPR performances in low concentrations detection are continuously proposed ([196]). Generally the aim is to improve the sensitivity while keeping the SPR advantages for biosensing applications. In this regard, magneto-optic surface-plasmon-resonance (MOSPR) biosensor based on simultaneous excitation of SPP and magneto-optic effects have been proposed [17] as SPR modulation configuration.
Compared to the conventional SPR sensor, the MOSPR need a magnetoplasmonic transducer instead of the thin gold chip typically employed in SPR systems and a low field electromagnet. The simplest magnetoplasmonic structures that one can conceive are multilayered structures made of noble and ferromagnetic metals layers [197] such as a thin ferromagnetic layer sandwiched between two gold layers. Other more complicated nanostructures have been conceived, but their fabrication certainly complicate the whole realization of the sensing device ([166, 198]).

In the last decade few works proved MOSPR biosensor based on multilayered nanostructures of noble metals and ferromagnetic film can increase by a three time factor the limit of detection of the SPR [169] or four times the signal to noise ratio [174].
Here we applied for the first time the PIT [12] to a MOSPR (and SPR) sensing platform. This technique allows to immobilize antibodies as bioreceptors easily and quickly (in few minutes). Since the excitation of SPPs is confined to the chip/sample interface, the proximity of the recognized analytes to the metal surface could play an important role into the MOSPR sensitivity. In this regard the PIT (Photochemical Immobilization Technique, [12], Section 1.1.2) can positively affects the sensitivity of the device. In fact, with this technique PIT the antibodies are immobilized directly on the metals surface and with one Fab exposed to the solution, thus giving rise to an antibodies thin layer of about 5 nm on the sensing surface [12].
We investigated the performance of MOSPR biosensor based on the a trilayer nanostructure Au/Co/Au as sensing platform. The thicknesses of the layers were chosen according to an experimental optimization of the MOSPR sensing signal. The performances of the MOSPR biosensor were tested in water against human IgG. The real-time monitoring of the antigen detection shows high stability in water. The specificity of the response to the analytes has been proved by specificity tests. The dose-response curve reveals a low LOD of about 1.6 nM and a dynamic range of about one decade of concentrations (1.6 nM − 16 nM). We are confident that an optimization of the fluidic system would allow to easily improve the LOD. Moreover this result has been achieved employing and easy and versatile functionalization technique and therefore it can be easily extended to other analytes. A future perspective would be also applying this MOSPR biosensor in combination with core@shell magnetic nanoparticles already employed as amplification tool in the biosensor described in Chapter 1 [1, 5].

Appendix

4.A Fluidic chamber

The microfluidic chambers consist of a double-sided adhesive polymer layer (ARseal 8939, Adhesive Research, Ireland), designed with AutoCAD software and cut with a cutting plotter (Silhouette portrait 2, Silhouette, Spain) (Fig. 4.18. The microfluidic chamber is sealed with a transparent poly(methyl methacrylate) layer (ME303016, Goodfellow, Spain) cut with the inlet and outlet ports that are connected to mini Luer connectors and tubings (microfluidic ChipShop, Germany). During the experiments (both the functionalization and the detection of antigens) the volume of solution in contact with the magnetoplasmonic substrate was approximately 10 μl. The output channel is connected with a syringe-pump (the syringe used is 3 ml) used for injecting the liquids.

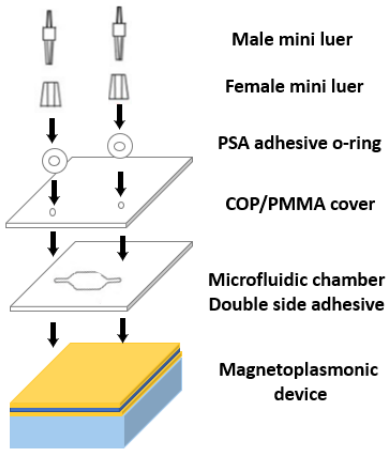

Figure 4.18: Schematic representation of the microfluidic device. PSA refers to pressure sensitive adhesive, COP refer to cyclic olefin polymer and and PMMA refer to poly(methylmethacrylate). Adapted from [199].

4.B Protocols

4.B.1 Surface biofunctionalization

Immobilization of Antibodies

Gold surface functionalization with anti-human IgG produced in goat was realized through the PIT (Section 1.1.2). The aqueous solution containing anti-human IgG (25 μg/ml concentration) was UV-irradiated for 30 s (6 W at 254 nm) and conveyed onto the surface of the substrate. The flux velocity used is 15 μl/s. The procedure consist in injecting 200 μl of antibodies solution immediately after the UV-irradiation and repeat the procedure three-times. It is convenient to split the volume solution so to exploit the maximum activation of the antibodies after the UV irradiation that lasts 5 min (Section 1.1.2, [12]).

Blocking

The blocking procedure was performed with a 1% casein solution in PBS for blocking (Blocker Casein in PBS, 37528, Thermofisher). The solution was conveyed onto the magnetoplasmonic device's surface for 40 min. The suggested time for most applications is between 30min and 2 hours (data sheet of the blocker solution used). The efficiency of the blocking was proven by the absence of non-specific signal, as we saw Section 4.5.1.

4.B.2 Fabrication of Au/Co/Au trilayers

The plasmonic material chosen for the experiments was a trilayer of gold-cobalt-gold (Au/Co/Au) deposited on glass with an intermediate adhesive layer TiO_2. The top gold layer can prevent the oxidation of Co and also offer a proper surface for the biofunctionalization with the PIT (Section 1.1.2). The metal layers were deposited 170 μm thick glass substrates. Before the deposition the BK7 substrate were cleaned in an ultrasonic bath using acetone and isopropanol as solvents, 5 min each, and rinsed with water.

Deposition of metal layers

All layers were deposited in the vacuum chamber of an evaporator (Oerlikon-UNIVEX 350/EPVD75 Kurt J. Lesker Company at CIC nanoGUNE centre) at room temperature with a pressure of 10^{-7} mbar. Gold and cobalt layers were deposited with thermal and electron-beam evaporation, respectively. Under these pressure conditions all the constituents layers are polycrystalline and the Co layer has in-plane magnetization. The thickness of the metal layers were calibrated using X-Ray Reflectivity measurements (X'Pert PRO PANalytical X-ray diffractometer, at CIC nanoGUNE centre). The deposition rate for was 0.8 Å/s and 0.2 Å/s for gold and cobalt layers, respectively.

Deposition of the adhesive layer

Gold and silver are commonly used as the plasmonic metal nanostructures. Since they are both noble metals, an adhesion layer is normally needed to ensure the stability of the metal layer on the substrate. As a common solution is adding thin layers of metals

as and chromium (Cr), titanium (Ti). However, high losses induced by these adhesion metals can add a significant damping effects affecting the performance of the plasmonic nanostructure, broadening the SPR resonance [177] and worsening the sensitivity of the MOSPR signal [17]. To avoid damping effects caused by the adhesion layer, it is possible to use oxides such as TiO_2, and Cr_2O_3 [190, 191, 177]. In this work we adopted TiO_2 with 3 nm of thickness. The thickness is the minimum at which we obtained a good adhesion (visible with a typical scotch-tape test). After cleaning the glass substrate, as explained above, the deposition of the TiO_2 layer was performed with a magnetron sputtering system (ATC series AJA Sputtering System, at CIC nanoGUNE centre) in a clean room environment. The thickness was calibrated with X-Ray Reflectivity measurements (X'Pert PRO PANalytical X-ray diffractometer, at CIC nanoGUNE centre). Then, the samples were inserted into the vacuum-chamber of the evaporator used for metal depositions. A plasma cleaning is performed inside the chamber with Argon gas before the metal deposition.

Final remarks

In the last few decades, outstanding progresses in nanotechnology allowed the development of a wide variety of nanostructures with novel interesting properties whose applications are increasingly spreading in more and more fields (to cite a few, integrated circuitry [200], photovoltaics [201], ultrasensitive molecule detection [11], optoelectronics [202]). Emerging nanomaterials have also given the opportunity to design novel classes of biosensors, addressing challenging quests in biosensors devising.

This thesis explores the potentiality of three types of magnetic and plasmonic nanomaterials in biosensing applications with three different approaches: (i) core@shell MNPs consisting of a magnetite core coated with gold (Fe_3O_4@AuNPs) were adopted in a ME biosensor (ii) a two-dimensional plasmonic nanostructure consisting of branch pattern of AuNPs immobilized on a glass slice was adopted in a PEF based biosensor (iii) and a magnetoplasmonic trilayer of gold and cobalt (Au/Co/Au) was adopted in a MOSPR biosensor. The potential applications in biosensing of these nanomaterials is explored in combination with the Photochemical Immobilization Technique (PIT), a novel functionalization method that allows a rapid, effective and well-oriented immobilization of antibodies on noble metals surfaces (Section 1.1.2, [12]). Remarkably, for all the above mentioned magnetic and plasmonic nanomaterials the PIT was tested and implemented in an immunosensing scheme for the first time.

The core@shell magnetic nanoparticles (Fe_3O_4@AuNPs) were adopted as innovative signal amplification method in a ME sensor [1]. As a proof of concept the performances of the device were tested against human IgG in water achieving a LOD of 0.66 nM. The results obtained with MNPs have been compared with those obtained with AuNPs, showing that the magnetic character of the former plays a crucial role for improving the sensing performances. We showed with a simple theoretical model that the advantages of the magnetic nanoparticles relies on their coupling with the local magnetic field, which leads to an increase of the local density of MNPs in proximity of the surface of the ME transducers. For futuristic scopes, MNPs could be employed both for extracting the target molecule from complex matrices and for carrying out the detection coupled with a ME transducer. Moreover, after this application, we successfully employed MNPs decorated with gold and functionalized with PIT in a magnetoresistive biosensor not reported in this thesis [5]. It worth noticing that the idea of taking advantage of the magnetic interaction between magnetite nanoparticles and ME ribbons has already been employed in the past to detect bacteria [93]. In that case, Fe_3O_4 nanoparticles were modified by using chitosan, a linear polysaccharide, so that their surface was charged positively. In this way, in specific conditions, the nanoparticles bind to negatively charged bacteria as Escherichia coli and therefore, thanks to magnetic attraction, they also bind to the sur-

face of the ME sensor giving rise to a signal enhancement. This approach has several drawbacks. Firstly, the chitosan coating and the Escherichia coli binding process are expensive and time consuming (several hours); and furthermore, the whole procedure must be carried out under controlled conditions, this preventing the application to complex matrices. Secondly, since the adhesion between bacteria and nanoparticles results from the electrostatic interaction between bacteria and the chitosan, it is expected that the specificity will be greatly compromised when other gram-negative bacteria are present in the sample. In our work, we functionalized the gold surface of Fe_3O_4@AuNPs with the antibodies targeting antigen, in this way a high specificity for the nanoparticle-antigen interaction is achieved (Section 2.4.3).

The second nanomaterial investigated is a novel double-resonant plasmonic substrate suitable as nanostructure in PEF-based biosensing. The substrate consists of an assembly of AuNPs hexagonally arranged along branch patterns together with sprinkled AuNPs. As a case-study, the substrate was implemented in detecting a malaria biomarker PfLDH in human whole blood achieving a LOD down to 260 fM. The PfLDH was simultaneously detected by two fluorophores coupled with the double-resonance of the nanostructure as proof of concept for simultaneous multiplexed analysis. The measured average values of the fluorescence enhancement FE were 160 with one fluorophore (5-FAM dye) and 4500 with the other (Cy5 dye). We proved that these results are consistent with those simulated by considering branch patterns of rough AuNPs and that the roughness of the AuNPS is crucial. As futuristic scopes, multi-resonant devices may be also conceived by combining different metal nanoparticles so to active additional plasmonic modes. Moreover, sharp nanoparticles may further augment the electromagnetic field by at least one order of magnitude as compared to smooth nanoparticles as simulations revealed [2]. The potential biosensing applications of the proposed approach are far-reaching, for not only multi-analyte detection but also biomarker panel identification with double signal redundancy.

Finally, it worth comparing these results with those in the literature, focusing on other recently reported platform-based biosensors conceived for multiplexed analysis. It is remarkable to note that in many applications, the multiplexing scheme was realized by performing parallel measurements on one platform containing different chips, each of them devoted to one analyte of interest. However, although such an approach constitutes a smart strategy to achieve multiplexed analysis without sophisticate multi-response chips, it may require complex microfluidic systems or an increase of specimen amount and costs [133, 134]. On the contrary, chips exhibiting multi-responsivity only need one specimen to carry out multiplexed analysis thereby reducing materials and costs [203, 204].

Eventually, a magnetoplasmonic multilayered nanostructure of gold and cobalt thin films (Au/Co/Au) was adopted as transducer in a MOSPR biosensor. In the last decade few works proved MOSPR biosensor based on multilayered nanostructures of noble metals and ferromagnetic films can increase by a three time factor the LOD of the SPR [169] or four times the signal to noise ratio [174]. This type of nanostructure is the simplest magnetoplasmonic platform that can be conceived. Other more complicated nanostructures can be considered, but their fabrication certainly complicate the whole realization of the sensing device ([166, 198]). In this work we applied for the first time the PIT [12] to a MOSPR (and SPR) sensing platform. Since the excitation of SPPs is confined to the chip/sample interface, the proximity of the recognized analytes to the metal surface could

play an important role into the MOSPR sensitivity. In this regard the PIT can positively affects the sensitivity of the device since antibodies are immobilized directly on the metals surface giving rise to an antibodies thin layer of about 5 nm on the chip's surface [12]. With this in mind, we investigated the performance of MOSPR biosensor based on the a trilayer nanostructure Au/Co/Au/TiO_2 as sensing platform. The thicknesses of the metallic layers were chosen according to an experimental optimization of the MOSPR sensing signal (Section 4.4.2). As a proof of concept we tested the performances of the MOSPR biosensor in water against human-IgG. We achieved a LOD of 1.6 nM. This LOD is four times lower than the best LOD reported for MOSPR biosensor based on the same type of platform (i.e. based on a multilayers of ferromagnetic and noble metal thin films [169]). The preliminary results were obtained with a non-optimized fluidics system which negatively affected the LOD. In particular, the fluidics affected the amount of antibodies per surface area attached during the functionalization. Thus, with a further optimization the results can be easily improved. Moreover the immunosensing application has been performed employing an easy and versatile functionalization technique. Therefore, if IgG are used as bioreceptors the results can be easily extended to a wide variety of analytes. This will also facilitate a general comparison between the performance of MOSPR sensors and SPR sensors (implemented with the same experimental setup) in real applications against interesting analytes.

Bibliography

[1] R. Campanile, E. Scardapane, A. Forente, C. Granata, R. Germano, R. Di Girolamo, A. Minopoli, R. Velotta, B. Della Ventura, and V. Iannotti. "Core-shell magnetic nanoparticles for highly sensitive magnetoelastic immunosensor". In: *Nanomaterials* 10.8 (2020), p. 1526.

[2] A. Minopoli, E. Scardapane, B. Della Ventura, J. A Tanner, A. Offenäusser, D. Mayer, and R. Velotta. "Double-Resonant Nanostructured Gold Surface for Multiplexed Detection". In: *ACS applied materials & interfaces* 14.5 (2022), pp. 6417–6427.

[3] A. Minopoli, E. Scardapane, A. Acunzo, R. Campanile, B. Della Ventura, and R. Velotta. "Analysis of the optical response of a SARS-CoV-2-directed colorimetric immunosensor". In: *AIP Advances* 11.6 (2021), p. 065319.

[4] A. Acunzo, E. Scardapane, M. De Luca, D. Marra, R. Velotta, and A. Minopoli. "Plasmonic Nanomaterials for Colorimetric Biosensing: A Review". In: *Chemosensors* 10.4 (2022).

[5] R. Campanile, A. Acunzo, E. Scardapane, A. Minopoli, V. C. Martins, R. Di Girolamo, S. Cardoso, R. Velotta, B. Della Ventura, and V. Iannotti. "Multifunctional Core@ Satellite Magnetic Particles for Magnetoresistive Biosensors". In: *ACS Omega* 7.41 (2022), pp. 36543–36550.

[6] L. C. Clark and C. Lyons. "Electrode systems for continuous monitoring in cardiovascular surgery". In: *Annals of the New York Academy of sciences* 102.1 (1962), pp. 29–45.

[7] C. I. Justino, A. C. Freitas, R. Pereira, A. C. Duarte, and T. A.P. R. Santos. "Recent developments in recognition elements for chemical sensors and biosensors". In: *TrAC Trends in Analytical Chemistry* 68 (2015), pp. 2–17.

[8] T. Lavecchia, A. Tibuzzi, and M. T. Giardi. "Biosensors for functional food safety and analysis". In: *Bio-Farms for Nutraceuticals: Functional Food and Safety Control by Biosensors* (2010), pp. 267–281.

[9] N. Bhalla, Y. Pan, Z. Yang, and A. F. Payam. "Opportunities and challenges for biosensors and nanoscale analytical tools for pandemics: COVID-19". In: *ACS nano* 14.7 (2020), pp. 7783–7807.

[10] M. Oliverio, S. Perotto, G. C. Messina, L. Lovato, and F. De Angelis. "Chemical functionalization of plasmonic surface biosensors: a tutorial review on issues, strategies, and costs". In: *ACS applied materials & interfaces* 9.35 (2017), pp. 29394–29411.

[11] J. N. Anker, W. P. Hall, O. Lyandres, N. C. Shah, J. Zhao, and R. P. Van Duyne. "Biosensing with plasmonic nanosensors". In: *Nature materials* 7.6 (2008), pp. 442–453.

[12] B. Della Ventura, M. Banchelli, R. Funari, A. Illiano, M. De Angelis, P. Taroni, A. Amoresano, and . Matteini P.and Velotta. "Biosensor surface functionalization by a simple photochemical immobilization of antibodies: experimental characterization by mass spectrometry and surface enhanced Raman spectroscopy". In: *Analyst* 144.23 (2019), pp. 6871–6880.

[13] E. Katz. *Magnetic nanoparticles*. 2020.

[14] E. Katz. "Synthesis, properties and applications of magnetic nanoparticles and nanowires—A brief introduction". In: *Magnetochemistry* 5.4 (2019), p. 61.

[15] J.B. González-Díaz, A. García-Martín, G. Armelles, J.M. García-Martín, C. Clavero, A. Cebollada, R.A. Lukaszew, J.R. Skuza, D.P. Kumah, and R. Clarke. "Surface-magnetoplasmon nonreciprocity effects in noble-metal/ferromagnetic heterostructures". In: *Physical Review B* 76.15 (2007), p. 153402.

[16] E. Ferreiro-Vila, J. B. González-Díaz, R. Fermento, M. U. González, A. García-Martín, J.M. García-Martín, A. Cebollada, G.r Armelles, D. Meneses-Rodríguez, and E. M. Sandoval. "Intertwined magneto-optical and plasmonic effects in Ag/Co/Ag layered structures". In: *Physical review B* 80.12 (2009), p. 125132.

[17] B. Sepúlveda, A. Calle, L. M. Lechuga, and G. Armelles. "Highly sensitive detection of biomolecules with the magneto-optic surface-plasmon-resonance sensor". In: *Opt. Lett.* 31.8 (2006), pp. 1085–1087.

[18] J. Homola. "Surface plasmon resonance sensors for detection of chemical and biological species". In: *Chemical reviews* 108.2 (2008), pp. 462–493.

[19] B. D. Malhotra, R. Singhal, A. Chaubey, S.K. Sharma, and A. Kumar. "Recent trends in biosensors". In: *Current Applied Physics* 5.2 (2005), pp. 92–97.

[20] S. Aydin. "A short history, principles, and types of ELISA, and our laboratory experience with peptide/protein analyses using ELISA". In: *Peptides* 72 (2015), pp. 4–15.

[21] L. Garibyan and N. Avashia. "Research techniques made simple: polymerase chain reaction (PCR)". In: *The Journal of investigative dermatology* 133.3 (2013), e6.

[22] R. Funari, B. Della Ventura, C. Altucci, A. Offenhausser, D. Mayer, and R. Velotta. "Single molecule characterization of UV-activated antibodies on gold by atomic force microscopy". In: *Langmuir* 32.32 (2016), pp. 8084–8091.

[23] S. K. Vashist and J. H.T. Luong. "Antibody immobilization and surface functionalization chemistries for immunodiagnostics". In: *Handbook of Immunoassay Technologies*. Elsevier, 2018, pp. 19–46.

[24] M. Rabe, D. Verdes, and S. Seeger. "Understanding protein adsorption phenomena at solid surfaces". In: *Advances in colloid and interface science* 162.1-2 (2011), pp. 87–106.

[25] J. M. Fowler, M.C. Stuart, and Danny K.Y. Wong. "Self-assembled layer of thiolated protein G as an immunosensor scaffold". In: *Analytical chemistry* 79.1 (2007), pp. 350–354.

[26] A. Makaraviciute and A. Ramanaviciene. "Site-directed antibody immobilization techniques for immunosensors". In: *Biosensors and Bioelectronics* 50 (2013), pp. 460–471.

[27] A. Makaraviciute and A. Ramanaviciene. "Site-directed antibody immobilization techniques for immunosensors". In: *Biosensors and Bioelectronics* 50 (2013), pp. 460–471.

[28] M. T. Neves-Petersen, Z. Gryczynski, J. Lakowicz, P. Fojan, S. Pedersen, E. Petersen, and S. Bjørn Petersen. "High probability of disrupting a disulphide bridge mediated by an endogenous excited tryptophan residue". In: *Protein Science* 11.3 (2002), pp. 588–600.

[29] T.R. Ioerger, C. Du, and D.S. Linthicum. "Conservation of cys–cys trp structural triads and their geometry in the protein domains of immunoglobulin superfamily members". In: *Molecular immunology* 36.6 (1999), pp. 373–386.

[30] A.R. Shafiqa, A. Abdul Aziz, and B. Mehrdel. "Nanoparticle optical properties: size dependence of a single gold spherical nanoparticle". In: *Journal of Physics: Conference Series* 1083.1 (2018), p. 012040.

[31] B. Della Ventura, M. Iannaccone, R. Funari, M. Pica Ciamarra, C. Altucci, R. Capparelli, S. Roperto, and R. Velotta. "Effective antibodies immobilization and functionalized nanoparticles in a quartz-crystal microbalance-based immunosensor for the detection of parathion". In: *PLoS One* 12.2 (2017), e0171754.

[32] M. Cimafonte, A. Fulgione, R. Gaglione, M. Papaianni, .R. Capparelli, A. Arciello, S. Bolletti Censi, G. Borriello, R. Velotta, and B. Della Ventura. "Screen printed based impedimetric immunosensor for rapid detection of Escherichia coli in drinking water". In: *Sensors* 20.1 (2020), p. 274.

[33] A. Minopoli, N. Sakač, B. Lenyk, R. Campanile, D. Mayer, A. Offenhäusser, R. Velotta, and B. Della Ventura. "LSPR-based colorimetric immunosensor for rapid and sensitive 17β-estradiol detection in tap water". In: *Sensors and Actuators B: Chemical* 308 (2020), p. 127699.

[34] M. Iarossi, C. Schiattarella, I. Rea, L. De Stefano, R. Fittipaldi, A. Vecchione, R. Velotta, and B. Della Ventura. "Colorimetric immunosensor by aggregation of photochemically functionalized gold nanoparticles". In: *ACS Omega* 3.4 (2018), pp. 3805–3812.

[35] S. P. Gubin. *Magnetic nanoparticles*. John Wiley & Sons, 2009.

[36] D. Cullity B and C.D. Graham. *Introduction to magnetic materials*. John Wiley & Sons, 2008.

[37] F.E. Luborsky. "Development of elongated particle magnets". In: *Journal of Applied Physics* 32.3 (1961), S171–S183.

[38] C.P. Bean and I.S. Jacobs. "Magnetic granulometry and super-paramagnetism". In: *Journal of applied Physics* 27.12 (1956), pp. 1448–1452.

[39] C.P. Bean and J.M. Livingston. "Superparamagnetism". In: *Journal of Applied Physics* 30.4 (1959), S120–S129.

[40] P. Majewski and B. Thierry. "Functionalized magnetite nanoparticles—synthesis, properties, and bio-applications". In: *Critical Reviews in Solid State and Materials Sciences* 32.3-4 (2007), pp. 203–215.

[41] N. Malhotra, J.S. Lee, R. A. D. Liman, J. M. S. Ruallo, O. B. Villaflores, T. R. Ger, and C.D. Hsiao. "Potential toxicity of iron oxide magnetic nanoparticles: a review". In: *Molecules* 25.14 (2020), p. 3159.

[42] M. L. Bruschi and Lucas de Alcântara Sica de Toledo. "Pharmaceutical applications of iron-oxide magnetic nanoparticles". In: *Magnetochemistry* 5.3 (2019), p. 50.

[43] Xiao-Shui Li, Gang-Tian Zhu, Yan-Bo Luo, Bi-Feng Yuan, and Yu-Qi Feng. "Synthesis and applications of functionalized magnetic materials in sample preparation". In: *TrAC Trends in Analytical Chemistry* 45 (2013), pp. 233–247.

[44] L. Gloag, M. Mehdipour, D. Chen, R. D. Tilley, and J. J. Gooding. "Advances in the application of magnetic nanoparticles for sensing". In: *Advanced Materials* 31.48 (2019), p. 1904385.

[45] F.A. Blyakhman, S. Y. Sokolov, A. P. Safronov, O. A. Dinislamova, T. F Shklyar, A. Y. Zubarev, and G. V. Kurlyandskaya. "Ferrogels ultrasonography for biomedical applications". In: *Sensors* 19.18 (2019), p. 3959.

[46] D. Xiao, T. Lu, R. Zeng, and Y. Bi. "Preparation and highlighted applications of magnetic microparticles and nanoparticles: a review on recent advances". In: *Microchimica Acta* 183 (2016), pp. 2655–2675.

[47] J. J. Gooding and S. Ciampi. "The molecular level modification of surfaces: from self-assembled monolayers to complex molecular assemblies". In: *Chemical Society Reviews* 40.5 (2011), pp. 2704–2718.

[48] M. Ali Dheyab, A. Abdul Aziz, M. S. Jameel, and P. Moradi Khaniabadi. "Recent advances in synthesis, medical applications and challenges for gold-coated iron oxide: Comprehensive study". In: *Nanomaterials* 11.8 (2021), p. 2147.

[49] S. A. Maier. *Plasmonics: fundamentals and applications*. Vol. 1. Springer, 2007.

[50] J.D. Jackson. *Classical electrodynamics*. American Association of Physics Teachers, 1999.

[51] H. U. Yang, J. D'Archangel, M. L. Sundheimer, E. Tucker, G. D. Boreman, and M. B. Raschke. "Optical dielectric function of silver". In: *Physical Review B* 91.23 (2015), p. 235137.

[52] C. Kittel. *Introduction to solid state physics Eighth edition*. John Wiley & Sons, 2005.

[53] A. Otto. "Excitation of nonradiative surface plasma waves in silver by the method of frustrated total reflection". In: *Zeitschrift für Physik A Hadrons and nuclei* 216.4 (1968), pp. 398–410.

[54] E. Kretschmann and H. Raether. "Notizen: Radiative Decay of Non Radiative Surface Plasmons Excited by Light". In: *Zeitschrift für Naturforschung A* 23.12 (1968), pp. 2135–2136.

[55] V. Giannini, A. I. Fernández-Domínguez, S. C. Heck, and S. Maier. "Plasmonic nanoantennas: fundamentals and their use in controlling the radiative properties of nanoemitters". In: *Chemical reviews* 111.6 (2011), pp. 3888–3912.

[56] K.M. Mayer and J.H. Hafner. "Localized surface plasmon resonance sensors". In: *Chemical reviews* 111.6 (2011), pp. 3828–3857.

[57] J. A. Stratton. *Electromagnetic theory*. Vol. 33. John Wiley & Sons, 2007.

[58] C. F. Bohren and D. R. Huffman. *Absorption and scattering of light by small particles*. John Wiley & Sons, 2008.

[59] Y. R. Zhen, K. H. Fung, and C. T. Chan. "Collective plasmonic modes in two-dimensional periodic arrays of metal nanoparticles". In: *Physical Review B - Condensed Matter and Materials Physics* 78.3 (2008).

[60] E. Prodan and P. Nordlander. "Plasmon Hybridization in Spherical Nanoparticles". In: *Journal of Chemical Physics* 120.11 (2004), pp. 5444–5454.

[61] P. Nordlander, C. Oubre, E. Prodan, K. Li, and M.I. Stockman. "Plasmon hybridization in nanoparticle dimers". In: *Nano letters* 4.5 (2004), pp. 899–903.

[62] S. Sheikholeslami, Y. W. Jun, P. K. Jain, and A. P. Alivisatos. "Coupling of optical resonances in a compositionally asymmetric plasmonic nanoparticle dimer". In: *Nano Letters* 10.7 (2010).

[63] P. K. Jain, S. Eustis, and M. A. El-Sayed. "Plasmon coupling in nanorod assemblies: Optical absorption, discrete dipole approximation simulation, and exciton-coupling model". In: *Journal of Physical Chemistry B* 110.37 (2006).

[64] T. S. Deng, J. Parker, Y. Yifat, N. Shepherd, and N. F. Scherer. "Dark Plasmon Modes in Symmetric Gold Nanoparticle Dimers Illuminated by Focused Cylindrical Vector Beams". In: *Journal of Physical Chemistry C* 122.48 (2018).

[65] S. K. Ghosh and T. Pal. "Interparticle coupling effect on the surface plasmon resonance of gold nanoparticles: from theory to applications". In: *Chemical reviews* 107.11 (2007), pp. 4797–4862.

[66] P. K. Jain, W. Huang, and M. A. El-Sayed. "On the universal scaling behavior of the distance decay of plasmon coupling in metal nanoparticle pairs: A plasmon ruler equation". In: *Nano Letters* 7.7 (2007).

[67] P. K. Jain and M. A. El-Sayed. "Plasmonic coupling in noble metal nanostructures". In: *Chemical Physics Letters* 487.4-6 (2010).

[68] A. Minopoli, A. Acunzo, B. Della Ventura, and R. Velotta. "Nanostructured Surfaces as Plasmonic Biosensors: A Review". In: *Advanced Materials Interfaces* 9.2 (2022).

[69] V. C. Romao, S. A.M. Martins, J. Germano, F.A. Cardoso, S. Cardoso, and P.P. Freitas. "Lab-on-chip devices: gaining ground losing size". In: *ACS nano* 11.11 (2017), pp. 10659–10664.

[70] C. A. Grimes, S.C. Roy, S. Rani, and Q. Cai. "Theory, instrumentation and applications of magnetoelastic resonance sensors: a review". In: *Sensors* 11.3 (2011), pp. 2809–2844.

[71] K. Zhang, L. Fu, L. Zhang, Z. Cheng, and T. Huang. "Magnetostrictive particle based biosensors for in situ and real-time detection of pathogens in water". In: *Biotechnology and bioengineering* 111.11 (2014), pp. 2229–2238.

[72] X. Guo, J. Wang, Y. Zhao, R. Liu, Z. Zhang Q.and Yuan, and S. Sang. "A wireless magnetoelastic DNA-biosensor amplified by AuNPs for the detection of a common mutated DNA causing β-thalassaemia". In: *Biochemical Engineering Journal* 156 (2020), p. 107498.

[73] M.L. Johnson, O. LeVar, S.H. Yoon, J. Park, S. Huang, D. Kim, Z. Cheng, and B. A. Chin. "Dual-cathode method for sputtering magnetoelastic iron-boron films". In: *Vacuum* 83.6 (2009), pp. 958–964.

[74] P. G. Saiz, D. Gandia, A. Lasheras, A. Sagasti, I. Quintana, M. L. Fdez-Gubieda, J. Gutiérrez, M. I. Arriortua, and A.C. Lopes. "Enhanced mass sensitivity in novel magnetoelastic resonators geometries for advanced detection systems". In: *Sensors and Actuators B: Chemical* 296 (2019), p. 126612.

[75] M. Barsan M, T. A. Enache, N. Preda, G. Stan, N. G. Apostol, E. Matei, A. Kuncser, and V. C. Diculescu. "Direct immobilization of biomolecules through magnetic forces on Ni electrodes via Ni nanoparticles: applications in electrochemical biosensors". In: *ACS Applied Materials & Interfaces* 11.22 (2019), pp. 19867–19877.

[76] K. S. Kim and J. Park. "Magnetic force-based multiplexed immunoassay using superparamagnetic nanoparticles in microfluidic channel". In: *Lab on a Chip* 5.6 (2005), pp. 657–664.

[77] C. Duarte, T. Costa, R. Carneiro C.and Soares, A. Jitariu, S. Cardoso, M. Piedade, R. Bexiga, and P. Freitas. "Semi-quantitative method for streptococci magnetic detection in raw milk". In: *Biosensors* 6.2 (2016), p. 19.

[78] R. Soares, V. C Martins, R. Macedo, F. A. Cardoso, M. Martins S. A, D. M Caetano, P. H. Fonseca, V. Silvério, S. Cardoso, and P.P. Freitas. "Go with the flow: advances and trends in magnetic flow cytometry". In: *Analytical and bioanalytical chemistry* 411.9 (2019), pp. 1839–1862.

[79] F. A. Blyakhman, N. A. Buznikov, T. F Sklyar, A. P. Safronov, E. V. Golubeva, A.V. Svalov, S. Y. Sokolov, G. Y. Melnikov, I. Orue, and G. V. Kurlyandskaya. "Mechanical, electrical and magnetic properties of ferrogels with embedded iron oxide nanoparticles obtained by laser target evaporation: Focus on multifunctional biosensor applications". In: *Sensors* 18.3 (2018), p. 872.

[80] C. A. Grimes, C. S. Mungle, K. Zeng, M. K. Jain, W. R. Dreschel, M. Paulose, and K. G. Ong. "Wireless magnetoelastic resonance sensors: A critical review". In: *Sensors* 2.7 (2002), pp. 294–313.

[81] A. García-Arribas, J. Gutiérrez, G. V. Kurlyandskaya, J. M. Barandiarán, A. Svalov, E. Fernández, A. Lasheras, David De Cos, and I. Bravo-Imaz. "Sensor applications of soft magnetic materials based on magneto-impedance, magneto-elastic resonance and magneto-electricity". In: *Sensors* 14.5 (2014), pp. 7602–7624.

[82] N.B. Ekreem, A.G. Olabi, A. Prescott T.and Rafferty, and M.S.J. Hashmi. "An overview of magnetostriction, its use and methods to measure these properties". In: *Journal of Materials Processing Technology* 191.1-3 (2007), pp. 96–101.

[83] A. K. Varshneya and J.C. Mauro. *Fundamentals of Inorganic Glasses*. Harcourt Brace & Company, 1994.

[84] G. Herzer. "Modern soft magnets: Amorphous and nanocrystalline materials". In: *Acta Materialia* 61.3 (2013), pp. 718–734.

[85] D. M. Miskovic, K. J. Laws, and M Ferry. "Metallic glasses". In: *Structural Biomaterials*. Elsevier, 2021, pp. 275–300.

[86] L. Landau and E.M. Lifshitz. *Course of Theoretical Physics Vol. 7: Theory of Elasticity*. Pergamon Press, Oxford, 1987.

[87] F. Brailsford. "Applied Magnetism: A Study in Quantities". In: *Electron. Power*. CRC Press, 1966. DOI: https://doi.org/10.1049/ep.1966.0297.

[88] L. Lanotte, G. Ausanio, M. Carbucicchio, V. Iannotti, and M. Muller. "Coexistence of very soft magnetism and good magnetoelastic coupling in the amorphous alloy Fe62.5Co6Ni7.5Zr6Cu1Nb2B15". In: *Journal of Magnetism and Magnetic Materials* 215-216 (2000), pp. 276–279.

[89] G. Ausanio, V. Iannotti, and L. Lanotte. "Magnetoelastic stress and strain sensors". In: *Encyclopedia of Sensors*. American Scientific Publishers, 2006.

[90] C. Liang, S. Morshed, and B. C. Prorok. "Correction for longitudinal mode vibration in thin slender beams". In: *Applied physics letters* 90.22 (2007), p. 221912.

[91] S. Huang, J. Hu, J. Wan, M.L. Johnson, H. Shu, and B.A. Chin. "The effect of annealing and gold deposition on the performance of magnetoelastic biosensors". In: *Materials Science and Engineering: C* 28.3 (2008), pp. 380–386.

[92] B. Della Ventura, M. Gelzo, E. Battista, A. Alabastri, Andrea Schirato, G. Castaldo, G. Corso, F. Gentile, and R. Velotta. "Biosensor for point-of-care analysis of immunoglobulins in urine by metal enhanced fluorescence from gold nanoparticles". In: *ACS Applied Materials & Interfaces* 11.4 (2019), pp. 3753–3762.

[93] H. Lin, Q. Lu, S. Ge, Q. Cai, and C. A. Grimes. "Detection of pathogen Escherichia coli O157: H7 with a wireless magnetoelastic-sensing device amplified by using chitosan-modified magnetic Fe3O4 nanoparticles". In: *Sensors and Actuators B: Chemical* 147.1 (2010), pp. 343–349.

[94] I. Langmuir. "The adsorption of gases on plane surfaces of glass, mica and platinum." In: *Journal of the American Chemical society* 40.9 (1918), pp. 1361–1403.

[95] K. S. Kim and J. Park. "Magnetic force-based multiplexed immunoassay using superparamagnetic nanoparticles in microfluidic channel". In: *Lab on a Chip* 5.6 (2005), pp. 657–664.

[96] E. P. Furlani. *Permanent magnet and electromechanical devices: materials, analysis, and applications*. Academic press, 2001.

[97] G. Samourgkanidis and D. Kouzoudis. "Characterization of magnetoelastic ribbons as vibration sensors based on the measured natural frequencies of a cantilever beam". In: *Sensors and Actuators A: Physical* 301 (2020), p. 111711.

[98] W. Shen, Sibel Cetinel, K.i Sharma, E. R. Borujeny, and C. Montemagno. "Peptide-functionalized iron oxide magnetic nanoparticle for gold mining". In: *Journal of Nanoparticle Research* 19.2 (2017), pp. 1–12.

[99] M. J. Pollitt, G. Buckton, R. Piper, and S. Brocchini. "Measuring antibody coatings on gold nanoparticles by optical spectroscopy". In: *Rsc Advances* 5.31 (2015), pp. 24521–24527.

[100] N. T.K. Haiss W.and Thanh, J. Aveyard, and D.G. Fernig. "Determination of size and concentration of gold nanoparticles from UV- Vis spectra". In: *Analytical chemistry* 79.11 (2007), pp. 4215–4221.

[101] J.-F. Li, C.-Y. Li, and R. F. Aroca. "Plasmon-enhanced fluorescence spectroscopy". In: *Chemical Society Reviews* 46.13 (2017), pp. 3962–3979.

[102] R. Ranjan, E.N. Esimbekova, M. A. Kirillova, and V. A. Kratasyuk. "Metal-enhanced luminescence: Current trend and future perspectives-A review". In: *Analytica Chimica Acta* 971 (2017), pp. 1–13.

[103] M. F. Cardinal, E. Vander Ende, R. A Hackler, M.O. McAnally, P.C. Stair, G. C. Schatz, and R. P. Van Duyne. "Expanding applications of SERS through versatile nanomaterials engineering". In: *Chemical Society Reviews* 46.13 (2017), pp. 3886–3903.

[104] X. Yang, Z. Sun, T. Low, H. Hu, X. Guo, F. J. García de Abajo, P. Avouris, and Q. Dai. "Nanomaterial-Based Plasmon-Enhanced infrared spectroscopy". In: *Advanced Materials* 30.20 (2018), p. 1704896.

[105] M. A. Badshah, N. Y. Koh, A. W. Zia, N. Abbas, Z. Zahra, and M.W. Saleem. "Recent developments in plasmonic nanostructures for metal enhanced fluorescence-based biosensing". In: *Nanomaterials* 10.9 (2020), p. 1749.

[106] J.B. Khurgin and G. Sun. "Enhancement of optical properties of nanoscaled objects by metal nanoparticles". In: *JOSA B* 26.12 (2009), B83–B95.

[107] E. Lucas, R. Knoblauch, M. Combs-Bosse, S. E. Broedel Jr, and C. D. Geddes. "Low-concentration trypsin detection from a metal-enhanced fluorescence (MEF) platform: Towards the development of ultra-sensitive and rapid detection of proteolytic enzymes". In: *Spectrochimica Acta Part A: Molecular and Biomolecular Spectroscopy* 228 (2020), p. 117739.

[108] Y. Chen, K. Munechika, and D. S. Ginger. "Dependence of fluorescence intensity on the spectral overlap between fluorophores and plasmon resonant single silver nanoparticles". In: *Nano letters* 7.3 (2007), pp. 690–696.

[109] M. Li, S. K. Cushing, and N. Wu. "Plasmon-enhanced optical sensors: a review". In: *Analyst* 140.2 (2015), pp. 386–406.

[110] S. Bhaskar, P. Das, V. Srinivasan, S. B. N. Bhaktha, and S. S. Ramamurthy. "Plasmonic-silver sorets and dielectric-Nd2O3 nanorods for ultrasensitive photonic crystal-coupled emission". In: *Materials Research Bulletin* 145 (2022), p. 111558.

[111] S. Bhaskar, N.C. S.S. Kowshik, S. P. Chandran, and S. S. Ramamurthy. "Femtomolar detection of spermidine using au decorated SiO2 nanohybrid on plasmon-coupled extended cavity nanointerface: a smartphone-based fluorescence dequenching approach". In: *Langmuir* 36.11 (2020), pp. 2865–2876.

[112] A. Camposeo, L. Persano, R. Manco, Y. Wang, P Del Carro, C. Zhang, Z. Y. Li, D. Pisignano, and Y. Xia. "Metal-enhanced near-infrared fluorescence by micropatterned gold nanocages". In: *ACS nano* 9.10 (2015), pp. 10047–10054.

[113] K.X. Xie, Q. Liu, S.S. Jia, and X.X. Xiao. "Fluorescence enhancement by hollow plasmonic assembly and its biosensing application". In: *Analytica Chimica Acta* 1144 (2021), pp. 96–101.

[114] F. Zang, Z. Su, L. Zhou, K. Konduru, G. Kaplan, and S. Y. Chou. "Ultrasensitive Ebola virus antigen sensing via 3D nanoantenna arrays". In: *Advanced Materials* 31.30 (2019), p. 1902331.

[115] B. Du, Cheng Tang, Dan Zhao, H. Zhang, D. Yu, Miao Yu, K. C Balram, H. Gersen, B. Yang, and W. Cao. "Diameter-optimized high-order waveguide nanorods for fluorescence enhancement applied in ultrasensitive bioassays". In: *Nanoscale* 11.30 (2019), pp. 14322–14329.

[116] J. Luan, J. J. Morrissey, Z. Wang, H. G. Derami, K.K. Liu, S. Cao, Q. Jiang, C. Wang, E.D. Kharasch, and R. R. Naik. "Add-on plasmonic patch as a universal fluorescence enhancer". In: *Light: Science & Applications* 7.1 (2018), pp. 1–13.

[117] M. Moronshing and C. Subramaniam. "Room temperature, multiphasic detection of explosives, and volatile organic compounds using thermodiffusion driven soret colloids". In: *ACS Sustainable Chemistry & Engineering* 6.7 (2018), pp. 9470–9479.

[118] S. Bhaskar, P. Das, M. Moronshing, A. Rai, C. Subramaniam, S.B.N. Bhaktha, and S. S. Ramamurthy. "Photoplasmonic assembly of dielectric-metal, Nd2O3-Gold soret nanointerfaces for dequenching the luminophore emission". In: *Nanophotonics* 10.13 (2021), pp. 3417–3431.

[119] S. Bhaskar, P. Jha, C. Subramaniam, and S. S. Ramamurthy. "Multifunctional hybrid soret nanoarchitectures for mobile phone-based picomolar Cu2+ ion sensing and dye degradation applications". In: *Physica E: Low-dimensional Systems and Nanostructures* 132 (2021), p. 114764.

[120] T.A. Kelf, Y. Sugawara, R.M. Cole, J.J. Baumberg, M.E. Abdelsalam, S. Cintra, S. Mahajan, A.E. Russell, and P.N. Bartlett. "Localized and delocalized plasmons in metallic nanovoids". In: *Physical Review B* 74.24 (2006), p. 245415.

[121] S. Bhaskar, M. Moronshing, V. Srinivasan, P. K. Badiya, C. Subramaniam, and S. S. Ramamurthy. "Silver soret nanoparticles for femtomolar sensing of glutathione in a surface plasmon-coupled emission platform". In: *ACS Applied Nano Materials* 3.5 (2020), pp. 4329–4341.

[122] L. Zhou, F. Ding, H. Chen, W. Ding, W. Zhang, and S. Y. Chou. "Enhancement of immunoassay's fluorescence and detection sensitivity using three-dimensional plasmonic nano-antenna-dots array". In: *Analytical chemistry* 84.10 (2012), pp. 4489–4495.

[123] V. Flauraud, R. Regmi, P.M. Winkler, D. T.L. Alexander, H. Rigneault, N. F. Van Hulst, M. F García-Parajo, J. Wenger, and J. Brugger. "In-plane plasmonic antenna arrays with surface nanogaps for giant fluorescence enhancement". In: *Nano letters* 17.3 (2017), pp. 1703–1710.

[124] A. Kinkhabwala, Z. Yu, S. Fan, Y. Avlasevich, K. Müllen, and W.E. Moerner. "Large single-molecule fluorescence enhancements produced by a bowtie nanoantenna". In: *Nature photonics* 3.11 (2009), pp. 654–657.

[125] A. Puchkova, C. Vietz, E. Pibiri, B. Wünsch, M. Sanz Paz, G.P. Acuna, and P. Tinnefeld. "DNA origami nanoantennas with over 5000-fold fluorescence enhancement and single-molecule detection at 25 μM". In: *Nano letters* 15.12 (2015), pp. 8354–8359.

[126] Y. Jeong, Y.M. Kook, K. Lee, and W.G. Koh. "Metal enhanced fluorescence (MEF) for biosensors: General approaches and a review of recent developments". In: *Biosensors and Bioelectronics* 111 (2018), pp. 102–116.

[127] D. Kawasaki, H. Yamada, Kenichi Maeno, K. Sueyoshi, H. Hisamoto, and T. Endo. "Core–shell-structured gold nanocone array for label-free DNA sensing". In: *ACS Applied Nano Materials* 2.8 (2019), pp. 4983–4990.

[128] K. Loza, J. Diendorf, C. Sengstock, L. Ruiz-Gonzalez, J.M. Gonzalez-Calbet, M. Vallet-Regi, M. Köller, and M. Epple. "The dissolution and biological effects of silver nanoparticles in biological media". In: *Journal of Materials Chemistry B* 2.12 (2014), pp. 1634–1643.

[129] X. Zhang. "Gold nanoparticles: recent advances in the biomedical applications". In: *Cell biochemistry and biophysics* 72.3 (2015), pp. 771–775.

[130] G. Chen, D. Wang, W. Hong, L. Sun, Y. Zhu, and X. Chen. "Fluorescence enhancement on large area self-assembled plasmonic-3D photonic crystals". In: *Small* 13.9 (2017), p. 1602612.

[131] S. Bhaskar, N.S. Visweswar Kambhampati, K.M. Ganesh, and S. S. Srinivasan V.and Ramamurthy. "Metal-free, graphene oxide-based tunable soliton and plasmon engineering for biosensing applications". In: *ACS Applied Materials & Interfaces* 13.14 (2021), pp. 17046–17061.

[132] S. Kasani, K. Curtin, and N. Wu. "A review of 2D and 3D plasmonic nanostructure array patterns: fabrication, light management and sensing applications". In: *Nanophotonics* 8.12 (2019), pp. 2065–2089.

[133] A. N. Masterson, T. Liyanage, H. Kaimakliotis, H. Gholami Derami, F. Deiss, and R. Sardar. "Bottom-up fabrication of plasmonic nanoantenna-based high-throughput multiplexing biosensors for ultrasensitive detection of microRNAs directly from cancer patients' plasma". In: *Analytical Chemistry* 92.13 (2020), pp. 9295–9304.

[134] Z. Liao, Y. Zhang, Y. Li, Y. Miao, F. Gao S.and Lin, Y. Deng, and L. Geng. "Microfluidic chip coupled with optical biosensors for simultaneous detection of multiple analytes: A review". In: *Biosensors and Bioelectronics* 126 (2019), pp. 697–706.

[135] R. Glass, M. Möller, and J. P. Spatz. "Block copolymer micelle nanolithography". In: *Nanotechnology* 14.10 (2003), p. 1153.

[136] A. Minopoli, B. Della Ventura, B. Lenyk, F. Gentile, J. A. Tanner, A. Offenhäusser, D. Mayer, and R. Velotta. "Ultrasensitive antibody-aptamer plasmonic biosensor for malaria biomarker detection in whole blood". In: *Nature communications* 11.1 (2020), pp. 1–10.

[137] A. Minopoli, B. Della Ventura, R. Campanile, J. A Tanner, A. Offenhäusser, D. Mayer, and R. Velotta. "Randomly positioned gold nanoparticles as fluorescence enhancers in apta-immunosensor for malaria test". In: *Microchimica Acta* 188.3 (2021), pp. 1–9.

[138] R. W. Snow. "Global malaria eradication and the importance of Plasmodium falciparum epidemiology in Africa". In: *BMC medicine* 13.1 (2015), pp. 1–3.

[139] J. R. Lakowicz. "Radiative decay engineering: biophysical and biomedical applications". In: *Analytical biochemistry* 298.1 (2001), pp. 1–24.

[140] J. R. Lakowicz. *Principles of fluorescence spectroscopy*. Springer, 2006.

[141] L. Novotny and B. Hecht. *Principles of nano-optics*. Cambridge university press, 2012.

[142] J. Wenger. "Fluorescence enhancement factors on optical antennas: enlarging the experimental values without changing the antenna design". In: *International Journal of Optics* 2012 (2012).

[143] G. M. Akselrod, C. Argyropoulos, T. B. Hoang, C. Ciracì, C. Fang, J. Huang, D. R Smith, and M. H. Mikkelsen. "Probing the mechanisms of large Purcell enhancement in plasmonic nanoantennas". In: *Nature Photonics* 8.11 (2014), pp. 835–840.

[144] D. V. Guzatov, S. V. Vaschenko, V. V. Stankevich, A.Y. Lunevich, Y. F. Glukhov, and S. V. Gaponenko. "Plasmonic enhancement of molecular fluorescence near silver nanoparticles: theory, modeling, and experiment". In: *The Journal of Physical Chemistry C* 116.19 (2012), pp. 10723–10733.

[145] D.V. Guzatov, S.V. Gaponenko, and H.V. Demir. "Plasmonic enhancement of electroluminescence". In: *AIP Advances* 8.1 (2018), p. 015324.

[146] S. Klimov. *Nanoplasmonics*. Taylor & Francis Group, 2013.

[147] H. Chew. "Transition rates of atoms near spherical surfaces". In: *The Journal of chemical physics* 87.2 (1987), pp. 1355–1360.

[148] K. Q. Le. "Nanoplasmonic enhancement of molecular fluorescence: theory and numerical modeling". In: *Plasmonics* 10.2 (2015), pp. 475–482.

[149] H. Aouani, O. Mahboub, E. Devaux, H. Rigneault, T. W. Ebbesen, and J. Wenger. "Large molecular fluorescence enhancement by a nanoaperture with plasmonic corrugations". In: *Optics Express* 19.14 (2011), pp. 13056–13062.

[150] D. K.G. de Boer, M.A. Verschuuren, K. Guo, A. F. Koenderink, J. G. Rivas, and S. R. Rodriguez. "Directional sideward emission from luminescent plasmonic nanostructures". In: *Optics Express* 24.2 (2016), A388–A396.

[151] C. Jiang, S. Markutsya, and V.V. Tsukruk. "Collective and individual plasmon resonances in nanoparticle films obtained by spin-assisted layer-by-layer assembly". In: *Langmuir* 20.3 (2004), pp. 882–890.

[152] J. A. Jenkins, Y. Zhou, S. Thota, X. Tian, X. Zhao, S. Zou, and J. Zhao. "Blue-shifted narrow localized surface plasmon resonance from dipole coupling in gold nanoparticle random arrays". In: *The Journal of Physical Chemistry C* 118.45 (2014), pp. 26276–26283.

[153] S. Goutelle, M. Maurin, F. Rougier, X. Barbaut, L. Bourguignon, M. Ducher, and P. Maire. "The Hill equation: a review of its capabilities in pharmacological modelling". In: *Fundamental & clinical pharmacology* 22.6 (2008), pp. 633–648.

[154] Y. Li, Y. Wang, G. Huang, and J. Gao. "Cooperativity principles in self-assembled nanomedicine". In: *Chemical reviews* 118.11 (2018), pp. 5359–5391.

[155] D. Turgut-Balik, E. Akbulut, D. K. Shoemark, V. Celik, K. M. Moreton, R. B Sessions, J. J. Holbrook, and R. L. Brady. "Cloning, sequence and expression of the lactate dehydrogenase gene from the human malaria parasite, Plasmodium vivax". In: *Biotechnology letters* 26.13 (2004), pp. 1051–1055.

[156] Y.W. Cheung, R. M. Dirkzwager, W.C. Wong, J. Cardoso, J. Costa, and J. A. Tanner. "Aptamer-mediated Plasmodium-specific diagnosis of malaria". In: *Biochimie* 145 (2018), pp. 131–136.

[157] H. Chen, X. Wang, J. Li, and X. Wang. "Cotton derived carbonaceous aerogels for the efficient removal of organic pollutants and heavy metal ions". In: *Journal of Materials Chemistry A* 3.11 (2015), pp. 6073–6081.

[158] Y. Huang, Y. Chen, L.-L. Wang, and E. Ringe. "Small morphology variations effects on plasmonic nanoparticle dimer hotspots". In: *Journal of Materials Chemistry C* 6.36 (2018), pp. 9607–9614.

[159] V. A. Povedailo, I. L. Lysenko, A. Tikhomirov S, D. L. Yakovlev, D. A. Tsybulsky, A. S. Kruhlik, F. Fan, Y. V. Martynenko-Makaev, O. L. Sharko, P. V. Duong, P. H. Minh, and V. V. Shmanai. "Fluorescent Properties of Carboxyfluorescein Bifluorophores". In: *Journal of Fluorescence* 30.3 (2020), pp. 629–635.

[160] R. B. Mujumdar, L. A. Ernst, S. R. Mujumdar, and Christopher J. Lewis. "Cyanine Dye Labeling Reagents: Sulfoindocyanine Succinimidyl Esters". In: *Bioconjugate Chemistry* 4 (2 1993).

[161] E. C. Le Ru, E. Blackie, M. Meyer, and P. G. Etchegoint. "Surface enhanced raman scattering enhancement factors: A comprehensive study". In: *Journal of Physical Chemistry C* 111.37 (2007).

[162] J. P. Bérenger. "Perfectly Matched Layer (PML) for computational electromagnetics". In: *Synthesis Lectures on Computational Electromagnetics* 8 (2007).

[163] W. Lee, S. Lee, R. Briber, and O. Rabin. "Self-assembled SERS substrates with tunable surface plasmon resonances". In: *Advanced Functional Materials* 21.18 (2011).

[164] N. Maccaferri, A. Berger, S. Bonetti, V. Bonanni, M. Kataja, Q. H. Qin, S. van Dijken, Z. Pirzadeh, A. Dmitriev, and J. Nogués. "Tuning the magneto-optical response of nanosize ferromagnetic Ni disks using the phase of localized plasmons". In: *Physical review letters* 111.16 (2013), p. 167401.

[165] K. Lodewijks, N. Maccaferri, T. Pakizeh, R. K Dumas, I. Zubritskaya, J. Åkerman, P. Vavassori, and A. Dmitriev. "Magnetoplasmonic design rules for active magneto-optics". In: *Nano letters* 14.12 (2014), pp. 7207–7214.

[166] C. Rizal, M. G. Manera, D. O Ignatyeva, J. R. Mejía-Salazar, R. Rella, V. I Belotelov, F. Pineider, and N. Maccaferri. "Magnetophotonics for sensing and magnetometry toward industrial applications". In: *Journal of Applied Physics* 130.23 (2021), p. 230901.

[167] J. Homola, S. S. Yee, and G. Gauglitz. "Surface plasmon resonance sensors". In: *Sensors and actuators B: Chemical* 54.1-2 (1999), pp. 3–15.

[168] D. O Ignatyeva, G. A. Knyazev, P. O Kapralov, G. Dietler, S. K. Sekatskii, and V. I. Belotelov. "Magneto-optical plasmonic heterostructure with ultranarrow resonance for sensing applications". In: *Scientific reports* 6.1 (2016), pp. 1–7.

[169] M.G. Manera, E. Ferreiro-Vila, J. M. Garcia-Martin, A. Garcia-Martin, and R. Rella. "Enhanced antibody recognition with a magneto-optic surface plasmon resonance (MO-SPR) sensor". In: *Biosensors and Bioelectronics* 58 (2014), pp. 114–120.

[170] M. G. Manera, G. Montagna, E Ferreiro-Vila, L. González-García, JR S., A. R. González-Elipe, A. Cebollada, J. M. Garcia-Martin, A. García-Martín, and G. Armelles. "Enhanced gas sensing performance of TiO 2 functionalized magneto-optical SPR sensors". In: *Journal of Materials Chemistry* 21.40 (2011), pp. 16049–16056.

[171] M.G. Manera and R. Rella. "Improved gas sensing performances in SPR sensors by transducers activation". In: *Sensors and Actuators B: Chemical* 179 (2013), pp. 175–186.

[172] C. Clavero, K. Yang, J. R. Skuza, and R. A. Lukaszew. "Magnetic field modulation of intense surface plasmon polaritons". In: *Opt. Express* 18.8 (2010), pp. 7743–7752.

[173] D. Regatos, D. Farina, A. Calle, A. Cebollada, B. Sepúlveda, G Armelles, and L.M. Lechuga. "Au/Fe/Au multilayer transducers for magneto-optic surface plasmon resonance sensing". In: *Journal of Applied Physics* 108.5 (2010), p. 054502.

[174] D. Regatos, B. Sepúlveda, D. Fariña, L. G. Carrascosa, and L. M. Lechuga. "Suitable combination of noble/ferromagnetic metal multilayers for enhanced magneto-plasmonic biosensing". In: *Optics express* 19.9 (2011), pp. 8336–8346.

[175] K. Kämpf, S. Kübler, F. Wilhelm Herberg, and A. Ehresmann. "Magneto-optic surface plasmon resonance optimum layers: simulations for biological relevant refractive index changes". In: *Journal of Applied Physics* 112.3 (2012), p. 034505.

[176] T.J. Wang, K.H. Lee, and T.T. Chen. "Sensitivity enhancement of magneto-optic surface plasmon resonance sensors with noble/ferromagnetic metal heterostructure". In: *Laser Physics* 24.3 (2014), p. 036001.

[177] T. G Habteyes, S. Dhuey, E. Wood, D. Gargas, S. Cabrini, P. J. Schuck, A. P. Alivisatos, and S. R. Leone. "Metallic adhesion layer induced plasmon damping and molecular linker as a nondamping alternative". In: *ACS nano* 6.6 (2012), pp. 5702–5709.

[178] T. Kaihara, H. Shimizu, A. Cebollada, and G. Armelles. "Magnetic field control and wavelength tunability of SPP excitations using Al2O3/SiO2/Fe structures". In: *Applied Physics Letters* 109.11 (2016), p. 111102.

[179] M. Faraday. "I. Experimental researches in electricity.—Nineteenth series". In: *Philosophical Transactions of the Royal Society of London* 136 (1846), pp. 1–20.

[180] J. Kerr. "On rotation of the plane of polarization by reflection from the pole of a magnet". In: *The London, Edinburgh, and Dublin Philosophical Magazine and Journal of Science* 3.19 (1877), pp. 321–343.

[181] M. Freiser. "A survey of magnetooptic effects". In: *IEEE Transactions on magnetics* 4.2 (1968), pp. 152–161.

[182] K. Shinagawa. "Faraday and Kerr effects in ferromagnets". In: *Magneto-optics*. Springer, 2000, pp. 137–177.

[183] A. K. Zvezdin and V. A. Kotov. *Modern magnetooptics and magnetooptical materials*. CRC Press, 1997.

[184] V. V. Temnov, G. Armelles, U. Woggon, D. Guzatov, A. Cebollada, A. Garcia-Martin, J. Garcia-Martin, T. Thomay, A. Leitenstorfer, and R. Bratschitsch. "Active magneto-plasmonics in hybrid metal–ferromagnet structures". In: *Nature Photonics* 4.2 (2010), pp. 107–111.

[185] A. Hartstein and E. Burstein. "Observation of magnetoplasma type surface polaritons on n-InSb". In: *Solid State Communications* 14.11 (1974), pp. 1223–1227.

[186] G. Armelles, A. Cebollada, A. García-Martín, and M. U. González. "Magnetoplasmonics: combining magnetic and plasmonic functionalities". In: *Advanced Optical Materials* 1.1 (2013), pp. 10–35.

[187] Š Višňovskỳ. "Optics of magnetic multilayers". In: *Czechoslovak journal of physics* 41.7 (1991), pp. 663–694.

[188] C. Dehesa-Martínez, L. Blanco-Gutierrez, M. Vélez, J. Diaz, L.M. Alvarez-Prado, and J.M. Alameda. "Magneto-optical transverse Kerr effect in multilayers". In: *Physical Review B* 64.2 (2001), p. 024417.

[189] R.F. Wallis, J.J. Brion, E. Burstein, and A. Hartstein. "Theory of surface polaritons in anisotropic dielectric media with application to surface magnetoplasmons in semiconductors". In: *Physical Review B* 9.8 (1974), p. 3424.

[190] F. Colas, D. Barchiesi, S. Kessentini, T. Toury, and M. L. De La Chapelle. "Comparison of adhesion layers of gold on silicate glasses for SERS detection". In: *Journal of Optics* 17.11 (2015), p. 114010.

[191] P. Sadri-Moshkenani, M. W. Khan, Md Shafiqul Islam, E. Montoya, I. Krivorotov, N. Bagherzadeh, and O. Boyraz. "Effect of magnesium oxide adhesion layer on resonance behavior of plasmonic nanostructures". In: *Applied Physics Letters* 116.24 (2020), p. 241601.

[192] P.B. Johnson and R.W. Christy. "Optical constants of transition metals: Ti, v, cr, mn, fe, co, ni, and pd". In: *Physical review B* 9.12 (1974), p. 5056.

[193] T. Siefke, S. Kroker, K. Pfeiffer, O. Puffky, K. Dietrich, D. Franta, I. Ohlídal, A. Szeghalmi, E.B. Kley, and A. Tünnermann. "Materials pushing the application limits of wire grid polarizers further into the deep ultraviolet spectral range". In: *Advanced Optical Materials* 4.11 (2016), pp. 1780–1786.

[194] J. Zhou, Q. Qi, C. Wang, G. Qian Y.and Liu, Y. Wang, and L. Fu. "Surface plasmon resonance (SPR) biosensors for food allergen detection in food matrices". In: *Biosensors and Bioelectronics* 142 (2019), p. 111449.

[195] Q. Wang, Z.H. Ren, W.M. Zhao, L. Wang, X. Yan, A. Zhu, F. Qiu, and K.K. Zhang. "Research advances on surface plasmon resonance biosensors". In: *Nanoscale* 14.3 (2022), pp. 564–591.

[196] Z. Mao, X. Peng, Y. Zhou, Y. Liu, K. Koh, and H. Chen. "Review of Interface Modification Based on 2D Nanomaterials for Surface Plasmon Resonance Biosensors". In: *ACS Photonics* 9.12 (2022), pp. 3807–3823.

[197] V.I. Safarov, V.A. Kosobukin, C. Hermann, G. Lampel, J. Peretti, and C. Marlière. "Magneto-optical effects enhanced by surface plasmons in metallic multilayer films". In: *Physical review letters* 73.26 (1994), p. 3584.

[198] B. Caballero, A. García-Martín, and J. C. Cuevas. "Hybrid magnetoplasmonic crystals boost the performance of nanohole arrays as plasmonic sensors". In: *Acs Photonics* 3.2 (2016), pp. 203–208.

[199] J. Etxebarria-Elezgarai, M. Mowat, E. Lopez, C. Rodríguez, I. Olaetxea, and A. Seifert. "Gaussian Beam Shaping and Multivariate Analysis in Plasmonic Sensing". In: *Analytical Chemistry* 92.24 (2020), pp. 16236–16244.

[200] Y. Fang and M. Sun. "Nanoplasmonic waveguides: towards applications in integrated nanophotonic circuits". In: *Light: Science & Applications* 4.6 (2015), e294–e294.

[201] V. E. Ferry, L.A. Sweatlock, D. Pacifici, and H. A. Atwater. "Plasmonic nanostructure design for efficient light coupling into solar cells". In: *Nano letters* 8.12 (2008), pp. 4391–4397.

[202] D.M. Koller, A. Hohenau, H. Ditlbacher, N. Galler, F. Reil, F.R. Aussenegg, A. Leitner, E.J.W. List, and J.R. Krenn. "Organic plasmon-emitting diode". In: *Nature Photonics* 2.11 (2008), pp. 684–687.

[203] K.X. Xie, Q Liu, X.L. Song, R.P. Huo, X.H. Shi, and Q.L. Liu. "Amplified fluorescence by hollow-porous plasmonic assembly: A new observation and its application in multiwavelength simultaneous detection". In: *Analytical Chemistry* 93.8 (2021), pp. 3671–3676.

[204] X. Luo, X. Zhao, G. Q. Wallace, M.-H. Brunet, K. J. Wilkinson, P. Wu, Chenxin Cai, C.G. Bazuin, and J.F. Masson. “Multiplexed SERS detection of microcystins with aptamer-driven core–satellite assemblies”. In: *ACS Applied Materials & Interfaces* 13.5 (2021), pp. 6545–6556.